Title

Four problems in stratified flows

Author

Konopliv, Nathan

Publication Date

2017

University of California
Santa Barbara

Four problems in stratified flows

A dissertation submitted in partial satisfaction
of the requirements for the degree

Doctor of Philosophy
in
Mechanical Engineering

by

Nathan Alexander Konopliv

Committee in charge:

Professor E. Meiburg, Chair
Professor P. Garaud
Professor P. Luzzatto-Fegiz
Professor J. Moehlis

January 2018

The Dissertation of Nathan Alexander Konopliv is approved.

Professor P. Garaud

Professor P. Luzzatto-Fegiz

Professor J. Moehlis

Professor E. Meiburg, Committee Chair

December 2017

Four problems in stratified flows

Reprinted excerpt with permission from

Schulte, B., Konopliv N. and Meiburg E., *Physical Review Fluids*, **1**, 012301, 2016.

Copyright (2016) by the American Physical Society.

`dx.doi.org/10.1103/PhysRevFluids.1.012301`

Reprinted excerpt with permission from

Konopliv, N., Llewellyn Smith, S., McElwaine, J., and Meiburg, E., *J. Fluid Mech.*, **789**, 806-829, 2016.

Copyright (2016) by Cambridge University Press.

`dx.doi.org/10.1017/jfm.2015.755`

Reprinted excerpt with permission from

Konopliv, N., and Meiburg, E., *J. Fluid Mech.*, **797**, 729-764, 2016.

Copyright (2016) by Cambridge University Press.

`dx.doi.org/10.1017/jfm.2016.300`

Dedicated to Mom and Dad.

Acknowledgements

The first person I would like to thank is my advisor, Eckart Meiburg. I have learned a lot about fluid mechanics, numerics and how to do research from him. I also appreciate the level of trust and patience he has showed me. My time is as a Ph.D. student was far less stressful and more enjoyable because of it. Having talked with plenty of other Ph.D. students about their advisors, I feel like I got pretty lucky.

Although I am listed as the only author for my thesis, there were meaningful contributions from my coauthors on the papers that we published together during my time as a Ph.D. student. Aside from my advisor, my coauthors were Stefan Llewellyn Smith, Lutz Lesshafft and Bartho Schulte. There were also meaningful contributions through conversations with Jim Rottman, Pascale Garaud, Rama Govindarajan and Timour Radko.

I also want to thank my labmates and visiting students. We've been through some crazy experiences together. I think it's probably more fun to look back on some of those super long hikes than actually doing them. Concerning academics, I want to thank Peter Burns and Senthil Radhakrishnan in particular for taking the time to teach me a lot about numerics and fluid mechanics in general when I first started. I would've wasted a lot of time doing things completely wrong if they hadn't offered to help me. It was also a pleasure to work with Bartho Schulte, who I mentioned already and was a talented and motivated visiting student. I also want to thank Thomas Köllner, who introduced me to the concept of adjoint-based optimization, which is something I find to be really neat.

I should also mention our supercomputing resources. Some of the simulations were carried out at the Beach supercomputing facility at the University of Colorado at Boulder. Additional computational resources were provided by the Extreme Science and Engineering Discovery Environment (XSEDE), which is supported by National Science Foundation Grant No. TG-CTS150053.

I am also thankful for the support I received from my homegroup from church, and my church, Santa Barbara Community Church, as a whole. I feel like I am known, flaws included, and accepted. I'm glad that I will get to stay in Santa Barbara after I graduate. I was beginning to dread leaving this church, even though I suppose I would have been fine in the long run.

Of course, I have to mention my family. I feel like I can't mention everybody, so I'll stick with immediate family here. I'm thankful for the closeness I have with my parents and the freedom I feel to be completely honest with them and talk about anything. That is a very valuable thing to have in general, not to mention graduate school. I'm also thankful for my sisters and the silliness-infused friendships we have, as well as the freedom to step on each other's toes without fear because we'll always get over it.

Curriculum Vitæ

Nathan Alexander Konopliv

Education

2017	Ph.D. in Mechanical Engineering (Expected), University of California, Santa Barbara.
2012	B.S. in Chemical Engineering, University of California, San Diego.

Experience

2012–2017	Graduate Student Researcher Computational Fluid Dynamics Laboratory University of California, Santa Barbara
2013–2015	Teaching Assistant Department of Mechanical Engineering University of California, Santa Barbara
2010–2011	Undergraduate Student Researcher Biomolecular Materials and Nanoscale Assembly Laboratory University of California, San Diego
Summer 2011	Summer Intern Air Liquide Delaware Research and Technology Center Newark, DE
Summer 2010	Eugene and Ruth Roberts Summer Student Academy Participant City of Hope Duarte, CA
Summer 2009	Summer Intern Jet Propulsion Laboratory Pasadena, CA

Publications

1. N. Konopliv and E. Meiburg. Double-diffusive and settling-driven instabilities in two-component, stably stratified fluids: The influence of shear. *In preparation for submission to J Fluid Mechanics*
2. N. Konopliv and E. Meiburg. Double-diffusive lock-exchange gravity currents. *J Fluid Mechanics*. 797. 729–764. (2016)
3. N. Konopliv and E. Meiburg. Modeling gravity currents without an energy closure. *J Fluid Mechanics*. 789. 806–829. (2016)
4. B. Schulte, N. Konopliv and E. Meiburg. Clear salt water above sediment-laden fresh water: Interfacial instabilities. *Physical Review Fluids*. 1. 012301. (2016)

5. A.M. Hung, N.A. Konopliv, and J.N. Cha. Solvent-Based Assembly of CdSe Nanorods in Solution. *Langmuir*. 27. 12322–12328. (2011)

Abstract

Four problems in stratified flows

by

Nathan Alexander Konopliv

We extend the vorticity-based modeling approach of Borden & Meiburg [1] to non-Boussinesq gravity currents and derive an analytical expression for the Froude number without the need for an energy closure. Via detailed comparisons with simulation results, we assess the validity of three key assumptions underlying both our as well as earlier models, *viz.* i) steady-state flow in the moving reference frame; ii) inviscid flow; and iii) horizontal flow sufficiently far in front of and behind the current. The current approach does not require an assumption of zero velocity in the current.

Double-diffusive lock-exchange gravity currents in the fingering regime are explored via two- and three-dimensional Navier-Stokes simulations in the Boussinesq limit. The front velocity of these currents exhibits a nonmonotonic dependence on the diffusivity ratio and the initial stability ratio due to the competing effects of increased buoyancy and increased drag. Scaling arguments based on the simulation results suggest that even low Reynolds number double-diffusive gravity currents are governed by a balance of buoyancy and turbulent drag.

The stability of an interface separating less dense, clear salt water above from more dense, sediment-laden fresh water below is explored via direct numerical simulations. We find that the destabilizing effects of double-diffusion and particle settling amplify each other above the diffusive interface, whereas they tend to cancel each other below. For large settling velocities, plume formation below the interface is suppressed. We identify the dimensionless parameter that determines in which regime a given flow takes place.

The effects of shear on double-diffusive fingering and on the settling-driven instability are assessed by means of a transient growth analysis. Shear is seen to dampen both instabilities, which is consistent with previous findings by other authors. The shear damping is more pronounced for parameter values that produce larger unsheared growth. These trends can be explained in terms of instantaneous linear stability results for the unsheared case. For both double-diffusive and settling-driven instabilities, low Pr-values result in less damping and an increased importance of the Orr mechanism, for which a quantitative scaling law is obtained.

Contents

Curriculum Vitae **vii**

Abstract **ix**

1 Overview **1**

2 A vorticity model for non-Boussinesq gravity currents **4**
2.1 Introduction 4
2.2 Non-Boussinesq gravity currents: Theory 9
2.3 Numerical simulations 14
2.4 Simulation results and discussion 23
2.5 Summary 33

3 Double-diffusive lock-exchange gravity currents **37**
3.1 Introduction 37
3.2 Physical problem 39
3.3 Numerical approach 43
3.4 Results 45
3.5 Force balances 81
3.6 Comparison of two- and three-dimensional simulations 88
3.7 Conclusions 92

4 Interfacial instabilities in clear salt water above sediment-laden fresh water **95**
4.1 Introduction 95
4.2 Governing equations, initial and boundary conditions 97
4.3 Direct numerical simulations 99
4.4 Discussion 101

5 Two-component instabilities and shear **110**
5.1 Introduction 110
5.2 Problem Formulation 111

5.3 Optimization Procedure 117
5.4 Results 123
5.5 Discussion and Conclusions 147

A 2D flow solver **149**
A.1 Boussinesq 149
A.2 Non-Boussinesq 156
A.3 Parallelization and Performance Considerations 157

B Additional vorticity model calculations **161**
B.1 Extension of the non-Boussinesq vorticity model to 3D flows 161
B.2 Vorticity flux deviations for the primitive variable approach 163

C Derivation of energy budget **167**

Bibliography **169**

Chapter 1

Overview

This work can be divided into four studies on four topics, each of which has something to do with gravity currents, two-component instabilities, shear or some combination of the three. Because each study is fairly distinct from the other ones, they will each be introduced separately, in addition to the brief overview given here.

Gravity currents occur when heavy fluid flows underneath light fluid, driven by gravity. Depending on the relative density difference of the two fluids, a gravity-driven flow may be classified as Boussinesq or non-Boussinesq. Boussinesq flows occur when the relative density difference is small, and are more common in nature. Because of the simplifications afforded by the Boussinesq approximation, Boussinesq flows are easier to model than non-Boussinesq flows. In chapter 2, the vorticity model developed by Borden & Meiburg [1] for Boussinesq gravity currents is extended to the case of a non-Boussinesq gravity current. The validity of the key assumptions in the creation of this model are also checked numerically. The citation for this work is [2].

In chapter 3, the focus is shifted back to Boussinesq gravity currents, but driven by density differences caused by two components instead of one. Specifically, the case of hot and salty water flowing over heavier cold and fresh water is considered. In this situation, the salt is unstably stratified and the heat is stably stratified. This double stratification is unstable to the double-diffusive fingering instability, which is driven by the release of the potential energy stored in the salinity field. The release of the potential energy stored in the salinity field causes the current to become more buoyant, but it also results in additional drag on the current due to the fluid motion from the fingering instability. These effects are analyzed as a function of two governing parameters – the diffusivity ratio between heat and salt and the ratio of the density contributions from heat and salt. Most of the simulations are done in two dimensions to minimize cost, but a three dimensional simulation is performed as well for comparison. The citation for this work is [3].

We then shift from gravity currents to an analysis of a purely two-component gravity-driven instability in chapter 4. A two-layer setup of fresh, particle-laden water below salty, clear water is considered. In this situation, the differing diffusivities of the salinity and particle concentration cause plumes to form on both sides of the interface, while particle settling causes plumes to form only above the interface. A model is developed that is able to predict whether settling or diffusion will be the dominant effect, which will determine if plumes are present below the interface as well as above it. One potential application for this work concerns “heavy” river outflows. If a river is exceptionally muddy, either due to freak erosion events or generally high erosion in the area, the sediment in the river can make the fresh river water heavier than the surrounding ocean water and the river outflow will run along the bottom of the ocean. This is the same stratification as our study. The main differences are the presence of shear and the scale or size of the problem, but the model from our study still may be able to help predict the amount of mixing in the current by predicting the presence of plumes below the interface. The citation for this work is [4].

Finally, in chapter 5 we move back to the fingering instability and examine the effect of shear on it using Kelvin waves. This transient growth analysis predicts that shear will dampen the fingering instability, which is consistent with a wide array of previous work, discussed in section 5.1. We then extend this analysis to the settling-driven instability first identified by Alsinan *et al.*[5], and find that it too is dampened by shear. We look closely at the mechanisms driving this instability and use that to explain the damping effect of shear. In the case of either instability, we find that shear can occaisonally have an amplifying effect. This is due to the previously known Orr mechanism, and we develop a formula to quantify its effect. If the effect of the Orr mechanism is subtracted, shear dampened both instabilities for every parameter combination tested.

Chapter 2

A vorticity model for non-Boussinesq gravity currents

2.1 Introduction

Three quarters of a century ago, von Kármán [6] introduced the idealized gravity current model shown in figure 2.1a. He considered the flow in the reference frame moving with the current front, and invoked three main simplifying assumptions: i) the flow is steady in this reference frame; ii) the flow is inviscid; and iii) the fluid inside the current is at rest. By neglecting the flow in the ambient and applying Bernoulli's law along the streamlines C-O and O-A, *i.e.*, by assuming that the mechanical energy is conserved along these streamlines, he obtained for the Froude number

$$F_h = \frac{U}{\sqrt{g'h}} = \sqrt{\frac{2}{\sigma}}\ . \tag{2.1}$$

Here, U denotes the front velocity of the gravity current, h represents its height, $g' = g(\rho_1 - \rho_2)/\rho_1$ indicates the reduced gravity, and $\sigma = \rho_2/\rho_1$ refers to the density ratio.

Benjamin [7] objected to von Kármán's analysis on the grounds that Bernoulli's equation should not be assumed to hold along streamline O-A, due to the dissipation that occurs in this interfacial region as a result of the velocity shear between the current and

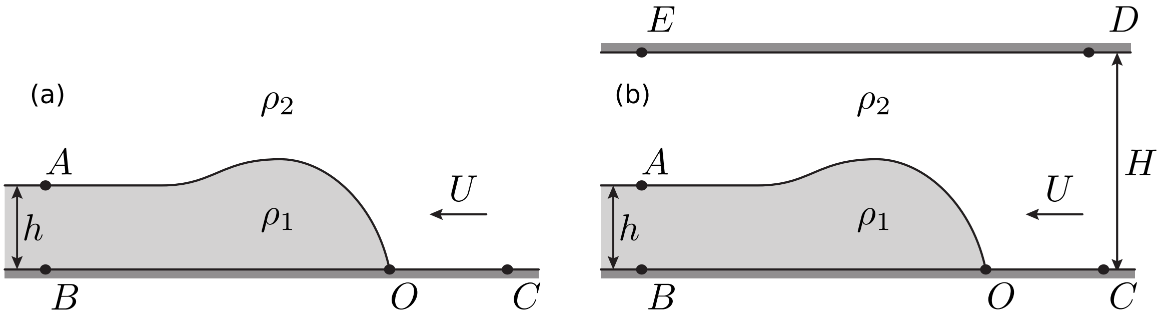

Figure 2.1: Idealized gravity current in a deep ambient (a) and a channel (b).

the ambient, which causes the development of Kelvin-Helmholtz billows and turbulence. Benjamin instead considered a corresponding gravity current in a channel of finite depth H, as shown in figure 2.1b. By applying the same three simplifying assumptions as von Kármán, and also considering the pressure distributions far up- and downstream of the current front to be hydrostatic, Benjamin was able to write the conservation laws for mass and horizontal momentum flux as

$$UH = U_2(H-h) \tag{2.2}$$

$$p_C H + \rho_2 U^2 H = p_B H + \tfrac{1}{2} g\left(\rho_1-\rho_2\right) h^2 - g\left(\rho_1-\rho_2\right) H h + \rho_2 U_2^2 \left(H-h\right) \ . \tag{2.3}$$

For a given set of values for current thickness, channel height and density ratio, the above relationships represent two equations for the three unknowns U, U_2 and $p_B - p_C$, so that one additional equation is required. To close the problem, Benjamin followed von Kármán's approach and applied Bernoulli's law; however, he did so along the bottom wall C-B of the channel, rather than along the interface as von Karman had done. For a current of fractional height $\alpha = h/H$, Benjamin thus obtained for the Froude number

$$F_{H,b} = \frac{U}{\sqrt{g'H}} = \left[\frac{\alpha(1-\alpha)(2-\alpha)}{\sigma(1+\alpha)}\right]^{1/2} \ . \tag{2.4}$$

Note that the Froude number F_h based on the current height is related to the Froude number F_H based on the channel height by $F_h = F_H \alpha^{-1/2}$.

For Boussinesq gravity currents, Borden & Meiburg [1] showed that invoking an energy closure assumption such as Bernoulli's equation in Benjamin's model becomes unnecessary if the conservation of vertical momentum is enforced, along with the conservation of mass and horizontal momentum. This approach bypasses the controversy between Benjamin and von Kármán entirely, as the conservation of energy or head loss arguments are not required. While there is no flow of vertical momentum into or out of the control volume $BCDE$, the importance of vertical momentum conservation inside the control volume is clear. The ambient fluid is first accelerated and then decelerated in the vertical direction, which affects the pressure profiles along the top and bottom walls. In turn, these profiles determine the pressure jump $p_B - p_C$ across the current front, for which the need of an additional equation originally arose. Borden & Meiburg [1] showed that the conservation of vertical momentum can be accounted for by considering the linear combination of the differential versions of the steady-state, inviscid, horizontal and vertical momentum equations, in the form of the Boussinesq vorticity equation

$$\boldsymbol{u} \cdot \boldsymbol{\nabla} \omega = -g' \frac{\partial \rho}{\partial x} \ , \tag{2.5}$$

where $\omega = \frac{\partial v}{\partial x} - \frac{\partial u}{\partial y}$ denotes the vorticity, and x and y represent the horizontal and vertical directions, respectively. By integrating (2.5) over the control volume, we obtain a relation governing the total circulation around the control volume

$$\oint \omega \boldsymbol{u} \cdot \boldsymbol{n} \, \mathrm{d}S = \iint -g' \frac{\partial \rho}{\partial x} \, \mathrm{d}A \ . \tag{2.6}$$

Equation (2.6) states that for incompressible flows in the Boussinesq limit the flow of vorticity into and out of the control volume is balanced by the baroclinic generation of vorticity inside the control volume. For a sharp interface, the area integral of the baroclinic term becomes $g'h$. Furthermore, no vorticity enters the control volume, and the flow of vorticity out of the control volume is confined to the vortex sheet between the current and the ambient. The vorticity flux carried by this sheet equals the vortex sheet strength, $\gamma = U_2$, multiplied by the sheet's principal velocity, $u_{PV} = U_2/2$ [8, 9]. Equation (2.6) thus reduces to

$$\frac{1}{2}U_2^2 = g'h \ . \tag{2.7}$$

Combining the vorticity conservation relationship (2.7) with the continuity equation (2.2) produces

$$F_{H,c} = \sqrt{2\alpha}(1-\alpha) \ , \tag{2.8}$$

where the subscript 'c' refers to 'circulation model.' Borden & Meiburg [1] showed that with regard to the vorticity flux of Boussinesq currents this relationship between the Froude number and the current height results in better agreement with DNS simulation results than Benjamin's relationship (2.4). However, even Benjamin's model prediction is found to be quite close to the DNS data, which indicates that his zero-headloss assumption closely approximates the situation in the simulated flow field. We note that in the above analysis, the pressure jump $p_B - p_C$ across the current front has become decoupled from the problem of determining U and U_2, which were determined from the conservation of mass and vorticity alone. Up to this point, we have used the conservation of horizontal momentum only in linear combination with the conservation of vertical momentum, *i.e.*, as the vorticity equation. Consequently, if desired, the pressure jump $p_B - p_C$ across the current front can now be determined from the horizontal momentum equation, as was shown by Borden & Meiburg [1]. The decoupling of the pressure in the above analysis is analogous to employing the streamfunction-vorticity formulation of the Navier-Stokes equations, which allows for the numerical simulation of incompressible flow fields without having to calculate the pressure explicitly. As explained earlier, by accounting for the conservation of mass, horizontal and vertical momentum, the above analysis did not have to invoke any assumptions about energy conservation. Rather, individual terms in the energy equation can now be evaluated, so that the overall loss of energy can be calculated *a posteriori*, rather than assumed *a priori*.

We remark that both Benjamin's model and the vorticity model assume that the flow is inviscid. However, the role of viscosity in a real flow affects the two models differently. Benjamin invokes the assumption of inviscid flow in order to apply Bernoulli's equation to a streamline along which he expects dissipation to be minimal. We expect that any small amount of viscosity, and hence dissipation, will cause a loss of mechanical energy, so that Bernoulli's equation will no longer hold exactly. The vorticity model, on the other hand, invokes the assumption of inviscid flow in the context of the vorticity equation, so that it can model the vorticity field as an infinitely thin sheet. A small amount of viscous diffusion in the flow will cause the sheet to attain a finite thickness. However, for the parallel flow field far behind the current front a small amount of viscosity will not affect the vorticity flux, which remains the same for a thin but finite vorticity layer as it is for a vortex sheet. Hence we would expect the vorticity model to be less sensitive to small amounts of viscosity than Benjamin's model. The only caveat concerns the stagnation point O, where even a small amount of viscosity might potentially lead to a diffusive loss of vorticity out of the control volume.

As mentiond above, the investigation by Borden & Meiburg [1] was limited to Boussinesq gravity currents. In the following, we extend their results to non-Boussinesq liquid gravity currents,such as the ones investigated experimentally by Lowe *et al.*[10] and computationally by Birman *et al.*[11]. In this chapter, we will investigate in detail the significance of the three key assumptions invoked by all of the above authors, *viz.* steady-state flow, inviscid flow, and gravity current fluid at rest.

2.2 Non-Boussinesq gravity currents: Theory

In the following, we will present two alternate ways of extending the above analysis to liquid non-Boussinesq flows. The first approach, which more closely follows the work of Borden & Meiburg [1] by focusing on the vorticity variable, will consider the problem under the standard assumptions of steady-state inviscid flow, with the gravity current fluid at rest. The second, alternative approach starts from the conservative form of the momentum equations for primitive variables. It will be shown that, with this approach, it is possible to relax some of the standard assumptions. The relationship between the two approaches will be discussed briefly towards the end of the section.

2.2.1 Vorticity approach

In order to extend the modeling approach by Borden & Meiburg [1] to non-Boussinesq gravity currents, we begin with the steady-state Euler equation

$$\boldsymbol{u} \cdot \boldsymbol{\nabla} \boldsymbol{u} = -\frac{1}{\rho} \boldsymbol{\nabla} P + \mathbf{g} \, . \tag{2.9}$$

By taking the curl, we obtain the steady-state, inviscid, non-Boussinesq vorticity transport equation

$$\boldsymbol{u} \cdot \boldsymbol{\nabla} \omega = -\boldsymbol{\nabla} \times \left(\frac{1}{\rho} \boldsymbol{\nabla} P \right) \, . \tag{2.10}$$

Integrating over the control volume and using the divergence theorm on the left hand side yields an expression analogous to the Boussinesq case (2.6)

$$\oint \omega \boldsymbol{u} \cdot \boldsymbol{n} \, \mathrm{d}S = -\iint \boldsymbol{\nabla} \times \left(\frac{1}{\rho} \boldsymbol{\nabla} P \right) \mathrm{d}A \; = -\int \frac{1}{\rho} \boldsymbol{\nabla} P \cdot \mathrm{d}\mathbf{l} \; . \tag{2.11}$$

The final integral is a contour integral along the boundary taken in the positive sense. Unlike the Boussinesq version of the problem, the pressure no longer decouples from the vorticity transport equation. However, since the density is taken to be piecewise constant, in each layer we may take the density out of the integral and reduce the right-hand side of (2.11) to $(\rho_2^{-1} - \rho_1^{-1})(P_O - P_A)$, which depends only on the difference in pressures between O and A. Taking the fluid in the current to be at rest leads to $P_O = P_B = P_A + \rho_1 g h$. We have not assumed anything about the pressure distribution in fluid 2 upstream or downstream. From (2.11), we thus obtain for non-Boussinesq currents

$$\oint \omega \boldsymbol{u} \cdot \boldsymbol{n} \, \mathrm{d}S = \frac{g' h}{\sigma} \; . \tag{2.12}$$

As for the Boussinesq case, there is no vorticity flux entering the control volume and the vorticity leaving the control volume is confined to a vortex sheet with strength U_2 and principal velocity $U_2/2$. The vorticity balance can then be written as

$$\frac{1}{2} U_2^2 = \frac{g' h}{\sigma} \; . \tag{2.13}$$

Combining this with the continuity equation produces an expression for the Froude number

$$F_{H,c} = \sqrt{\frac{2\alpha}{\sigma}} (1 - \alpha) \; . \tag{2.14}$$

In the limit of small density contrasts $\sigma \approx 1$, so that the Boussinesq result is recovered.

2.2.2 Primitive variable approach

Alternatively, we can begin with the steady-state, two-dimensional Euler equation in conservative form

$$\boldsymbol{\nabla} \cdot (\rho \boldsymbol{u}\boldsymbol{u}) + \boldsymbol{\nabla} P = \rho \mathbf{g} \ , \tag{2.15}$$

where y is the vertical direction, so that $\mathbf{g} = (0, -g)$ and the velocity vector has components $\boldsymbol{u} = (u, v)$. We also assume that $\boldsymbol{\nabla} \cdot \boldsymbol{u} = 0$. Taking the z-component of the curl of this equation gives a scalar equation that can be written as the divergence of a vector field

$$L = \boldsymbol{\nabla} \cdot \mathbf{q} = \boldsymbol{\nabla} \cdot \begin{pmatrix} g\rho + \partial_x(\rho u v) + \frac{1}{2}\partial_y \left[\rho(v^2 - u^2)\right] \\ -\partial_y(\rho u v) + \frac{1}{2}\partial_x \left[\rho(v^2 - u^2)\right] \end{pmatrix} = 0 \ . \tag{2.16}$$

After integrating over the control volume $BCDE$ and applying the divergence theorem, we are left with integrals over q_y along the top and bottom walls, and integrals over q_x along the in- and outflow boundaries. Along the top and bottom walls we have $v = 0$, so that

$$q_y = -\rho u \partial_y v - \rho u \partial_x u - \tfrac{1}{2} u^2 \partial_x \rho = -\tfrac{1}{2} u^2 \partial_x \rho \ , \tag{2.17}$$

where the last equality follows from $\boldsymbol{\nabla} \cdot \boldsymbol{u} = 0$. Along the top there are no density gradients, so that the last term is zero. Along the bottom, if $x = 0$ denotes the front location, the velocity in the vicinity of the front will scale as $u \propto U\sqrt{x/h}$. This was shown first by von Kármán [6] for the flow in the ambient, assuming that the current was stationary, and later extended by McElwaine [12], who demonstrated that it also holds in the current. We expect the local density profile near the front to be approximately of error function shape $\rho = (\rho_1 + \rho_2)/2 - (\rho_1 - \rho_2)\,\mathrm{erf}(x/W)/2$, where W is a (small) width. Multiplying this by the velocity and integrating gives a contribution proportional to $(\rho_1 - \rho_2)U^2 W/h^2$ for the right hand side of equation (2.17), which is small provided that W is much less than the current height h.

Along the in- and outflow boundaries we have the q_x-term to consider. When integrating, we can use $v = 0$ along the top and bottom walls to obtain

$$\int_0^H q_x \, dy = g \int_0^H \rho \, dy + \int_0^H \partial_x(\rho u v) \, dy - \frac{1}{2}\rho u^2 \Big|_0^H . \tag{2.18}$$

This result is general in the sense that it holds for any density field, as well as any divergence free velocity field such that v vanishes on the upper surface.

We now limit ourselves to flows in which W/h is small, so that the $\int q_y \, dx$ contribution discussed above is negligible. Furthermore, we assume that $\partial_x(\rho u v) = 0$ sufficiently far in front of and behind the front. The implications of this assumption will be discussed in more detail below.

The shapes of the inflow and outflow velocity profiles are not important since, when we integrate, only the top and bottom values contribute. The driving term is then seen as the difference in the integral of density between the inflow and outflow boundaries:

$$g \int_0^H \left[\rho_{BE}(y) - \rho_{CD}(y)\right] dy = \frac{1}{2}\left[u_E^2 \rho_E - u_B^2 \rho_B - u_D^2 \rho_D + u_C^2 \rho_C\right] . \tag{2.19}$$

In the case considered in detail in this paper, we have $u_E = U_2$, $u_B = 0$ and $u_D = u_C$, so that

$$gh(\rho_1 - \rho_2) = \tfrac{1}{2} U_2^2 \rho_2. \tag{2.20}$$

For general velocity profiles but piecewise constant density, equation (2.19) yields

$$\begin{aligned} \rho_2 \left[Hg - \tfrac{1}{2}u_D^2 + \frac{1}{2}u_C^2\right] &= \rho_2 \left[(H-h)g - \tfrac{1}{2}u_E^2\right] + \rho_1 h g, & (2.21) \\ u_E^2 - u_D^2 + u_C^2 &= 2hg(\rho_1/\rho_2 - 1) = 2hg'/\sigma \ . & (2.22) \end{aligned}$$

When $u_D = u_C$, this relation gives a Froude number condition

$$F_{H,c} = \sqrt{\frac{2\alpha}{\sigma}}(1-\alpha) \ , \tag{2.23}$$

which is identical to the result obtained with the vorticity approach in (2.14). However, in the case when $u_D \neq u_C$, there is no natural choice for the front velocity to define the Froude number.

The result can be extended to integration along a streamline rather than just $y = 0$ or $y = H$. Integrating from A to B to C and then back along a streamline just outside the current to A gives

$$u_A^2 = 2hg' \ . \tag{2.24}$$

This suggests that perhaps the best measure of velocity to use is actually the velocity u_A taken just outside the current.

The above analysis holds for general input and output velocity profiles. Details regarding the extension of the primitive variable approach to three-dimensional flows are presented in appendix B.1.

In the following, we analyze the implications of assuming

$$\int_0^H \frac{\partial}{\partial x}(\rho u v)\,\mathrm{d}y = 0 \tag{2.25}$$

in the above derivation. Consider the inviscid, steady-state, vertical momentum equation in conservative form

$$\frac{\partial}{\partial x}(\rho u v) + \frac{\partial}{\partial y}(\rho v^2) = -\frac{\partial P}{\partial y} - \rho g \ , \tag{2.26}$$

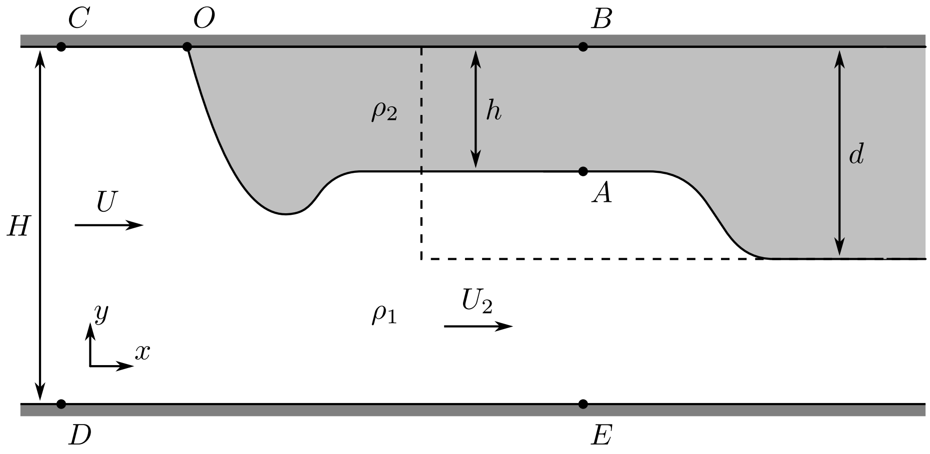

Figure 2.2: Schematic of a non-Boussinesq lock-exchange gravity current. The Navier-Stokes simulations focus on the buoyant current along the top wall, which more closely corresponds to a quasisteady flow in the moving reference frame than a negatively buoyant bottom current.

and integrate from C to D, using $v_C = v_D = 0$

$$\int_C^D \frac{\partial}{\partial x}(\rho u v)\,\mathrm{d}y + (\rho_D v_D^2 - \rho_C v_C^2) = (P_C - P_D) - \rho_2 g H \ . \tag{2.27}$$

This demonstrates that the assumption (2.25) corresponds to requiring that P_C and P_D are hydrostatic relative to one another, which also had been assumed as part of the vorticity approach in the previous section. Corresponding considerations apply to the outflow boundary, provided that $v_A = 0$, *i.e.*, that the interface at the outflow boundary is flat.

2.3 Numerical simulations

In order to assess the relative accuracy of Benjamin's and the vorticity model, we compare their predictions to two-dimensional Navier-Stokes simulations of lock-exchange gravity currents. The setup of the simulations is shown in figure 2.2, with the dashed line indicating the initial lock configuration. If the lock depth d is equal to (less than) the height H of the domain, the resulting flow is referred to as a full depth (partial depth) current.

During each simulation, one positively buoyant current is generated that propagates to the left along the top wall, and one negatively buoyant current propagating to the right. For full depth locks, this negatively buoyant current has the form of a gravity current along the bottom wall, whereas for partial depth locks, it is a bore traveling along the density interface. As will be seen below, the light current along the top wall generally can be approximated more accurately by a quasisteady flow in the reference frame moving with the current tip, so that it will be more suitable for assessing the validity of the various models. For light currents, Benjamin's analysis yields

$$F_{H,b} = \frac{U}{\sqrt{g'H}} = \left[\frac{\alpha(1-\alpha)(2-\alpha)}{1+\alpha}\right]^{1/2} , \tag{2.28}$$

instead of equation (2.4) for dense currents, while the vorticity model results in

$$F_{H,c} = \sqrt{2\alpha}(1-\alpha) , \tag{2.29}$$

rather than the corresponding relationship (2.14) for dense currents.

2.3.1 Governing equations

We follow the simulation approach of Birman *et al.*[11] and employ the incompressible, non-Boussinesq Navier-Stokes equations in two dimensions. As long as there is minimal diffusion, the velocity field can be considered divergence free, as the flow consists of two separate incompressible fluids. For a discussion of the effects of diffusion on the continuity equation and their quantitative assessment, we refer the reader to the work of

Chen & Meiburg [13]. The dynamic viscosities of the two fluids are taken to be equal, and the density field evolves based on a convection-diffusion equation. To minimize mixing, we employ small diffusivities. Referring to figure 2.2 and letting a star symbol denote a dimensionless quantity, we nondimensionalize the equations with the lock height d, the buoyancy velocity $U_b = \sqrt{g'd}$, where $g' = g(\rho_1 - \rho_2)/\rho_1$ is the reduced gravity, the dynamic pressure $\rho_1 U_b^2$ and the ambient fluid density ρ_1 to obtain

$$\boldsymbol{\nabla} \cdot \boldsymbol{u}^* = 0 \tag{2.30}$$

$$\frac{\mathrm{D}\boldsymbol{u}^*}{\mathrm{D}t^*} = -\frac{1}{\rho^*}\boldsymbol{\nabla} P^* + \frac{1}{\rho^* Re}\nabla^2 \boldsymbol{u}^* + \frac{1}{1-\sigma}\mathbf{e}_g \tag{2.31}$$

$$\frac{\mathrm{D}\rho^*}{\mathrm{D}t^*} = \frac{1}{ReSc}\nabla^2 \rho^* \tag{2.32}$$

Here $\mathrm{D}/\mathrm{D}t^*$ denotes the material derivative and $\mathbf{e}_g$ is the unit vector in the direction of gravity. The nondimensional parameters are then

$$Re = \frac{\rho_1 U_b d}{\mu}, \quad Sc = \frac{\mu}{\rho_1 \kappa}, \quad \sigma = \frac{\rho_2}{\rho_1} \ , \tag{2.33}$$

where μ represents the dynamic viscosity and κ indicates the molecular diffusivity of the density field. Alternatively, we can employ the Péclet number $Pe = Re\,Sc$. We recast the momentum equation (2.31) into the vorticity form

$$\frac{\mathrm{D}\omega^*}{\mathrm{D}t^*} = \frac{\rho_y^*}{\rho^*}\frac{\mathrm{D}u^*}{\mathrm{D}t^*} - \frac{\rho_x^*}{\rho^*}\frac{\mathrm{D}v^*}{\mathrm{D}t^*} + \frac{1}{\rho^* Re}\nabla^2\omega^* - \frac{\rho_x^*}{(1-\sigma)\rho^*} \ , \tag{2.34}$$

where the velocity is defined as

$$\boldsymbol{u}^* = \begin{pmatrix} u^* \\ v^* \end{pmatrix} . \tag{2.35}$$

We employ free-slip and no-flux conditions along all walls, so that the vorticity vanishes along the boundaries. We emphasize that this does not necessarily translate into a symmetry boundary condition for the vorticity field. To clarify this issue, consider the flow along the top wall in the vicinity of the stagnation point. Applying the boundary conditions $\omega^* = 0$ and $\rho^*_y = 0$ yields

$$\omega^*_{yy} = \frac{Re}{1-\sigma}\rho^*_x \ , \tag{2.36}$$

so that $\omega^*_{yy} \neq 0$ in regions with horizontal density gradients.

2.3.2 Computational approach

The unsteady simulations are performed in a streamfunction-vorticity formulation, by integrating equations (2.34) and (2.32) with an explicit third order, low storage Runge-Kutta scheme [14]. The time derivatives $\frac{\partial u^*}{\partial t^*}$ and $\frac{\partial v^*}{\partial t^*}$ appearing on the right hand side of (2.34) are evaluated iteratively at each Runge-Kutta substep. A pseudospectral method in the x-direction and a eigth order compact finite difference scheme in the y-direction are employed for the spatial discretization. As mentioned above, symmetry boundary conditions cannot be applied along the top and bottom walls, so that we instead employ right at the boundary a one-sided third order scheme for the concentration and a fourth-order scheme for the vorticity, along with a centered fourth order scheme one point away from the boundary.

An equation for pressure can be found by taking the divergence of (2.31)

$$\nabla^2 P^* = -2\rho^* \left[\left(\frac{\partial u^*}{\partial x^*} \right)^2 + \frac{\partial u^*}{\partial y^*}\frac{\partial v^*}{\partial x^*} \right] - \frac{\partial \rho^*}{\partial x^*}\frac{\mathrm{D}u^*}{\mathrm{D}t^*} - \frac{\partial \rho^*}{\partial y^*}\left(\frac{\mathrm{D}v^*}{\mathrm{D}t^*} + \frac{1}{1-\sigma} \right) \ . \tag{2.37}$$

Since this pressure relation is decoupled from the vorticity and density equations, the

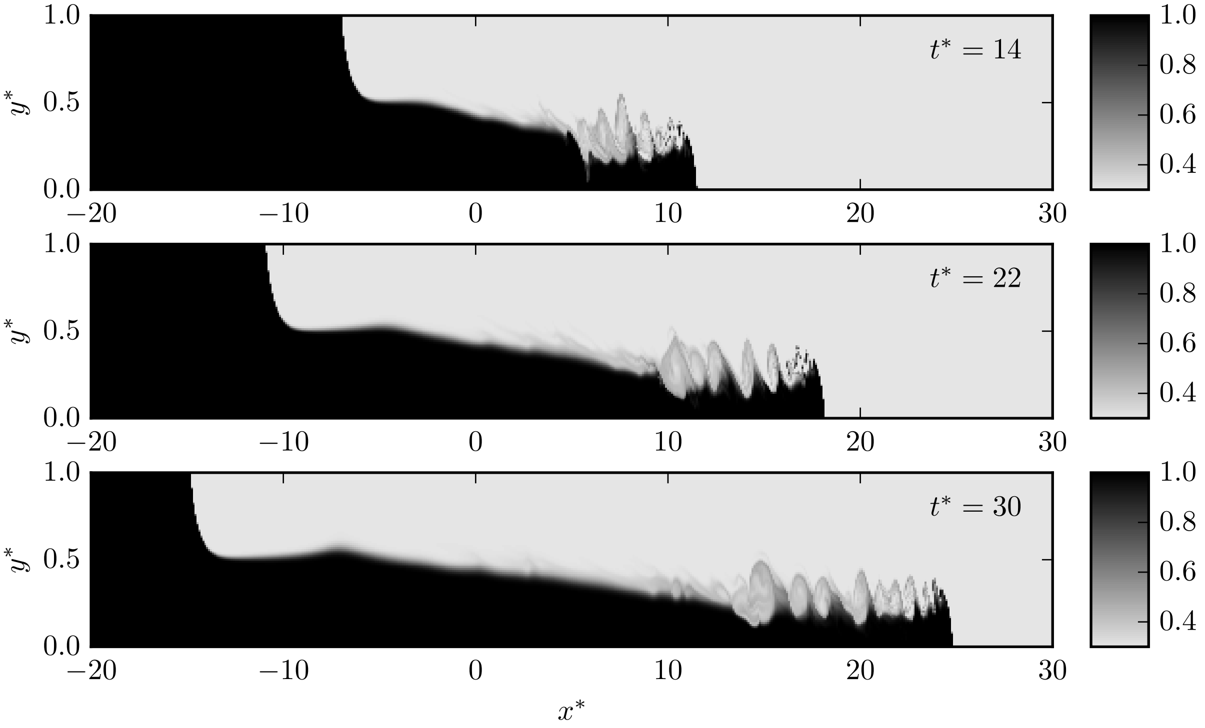

Figure 2.3: Simulation results for the density field of a full depth, non-Boussinesq flow with $Re = 5,000$, $Pe = 50,000$ and $\sigma = 0.3$.

pressure field can be evaluated during a postprocessing step after the simulation has finished.

2.3.3 Diagnostic tools

Figure 2.3 shows a representative full depth simulation at various times. The computational grid employs $16,384 \times 512$ points, with a time step of $O(5 \times 10^{-4})$, although its exact size varies according to the CFL condition. The figure confirms that the buoyant current propagating to the left along the top wall is more amenable to quasisteady modeling than the bottom current. Nevertheless, below we will discuss comparisons between DNS simulation results and model predictions for both the upper and the lower current.

The simulation is performed in the laboratory frame, and the results are then shifted to the reference frame moving with the current front during postprocessing. Towards this

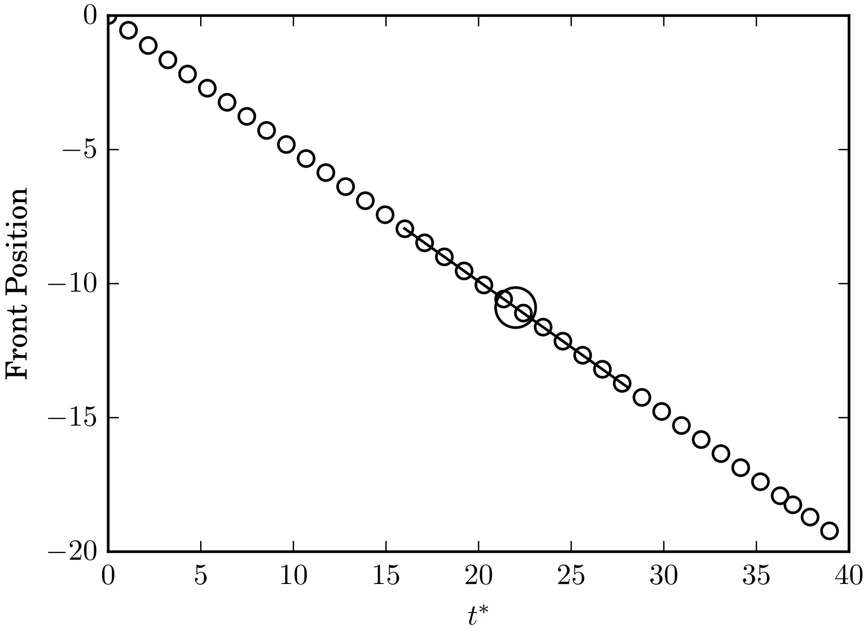

Figure 2.4: Calculation of the quasisteady front velocity U for the full depth top current with $Re = 5,000$, $Pe = 50,000$ and $\sigma = 0.3$. The small circles represent the tip location at every $2,000^{\text{th}}$ time step. In order to evaluate the front velocity at a given time, e.g., the large circle, we employ a local linear best fit of the front locations, as indicated by the line.

end, we employ linear interpolation to find the tip of the upper current as the location where $\rho^* = \frac{\sigma+1}{2}$ along the top wall. The front velocity U^* is then determined via linear regression on the front location *vs.* time data, (*cf.* Figure 2.4). To shift the results to the moving reference frame, U^* is subtracted from the laboratory frame velocity field.

The height $h^*(x^*, t^*)$ of the top current is defined as

$$h^*(x^*, t^*) = \frac{H}{d} - \int_0^{H/d} \frac{\rho^*(x^*, y^*, t^*) - \sigma}{1 - \sigma} \mathrm{d}y^* \ . \tag{2.38}$$

For the flow of figure 2.3, the current height is shown as a function of the distance behind the current tip in figure 2.5, at selected times. This confirms that the steady-state approximation holds with good accuracy near the front of the buoyant current.

In order to assess the validity of Benjamin's and the current model, we will primarily

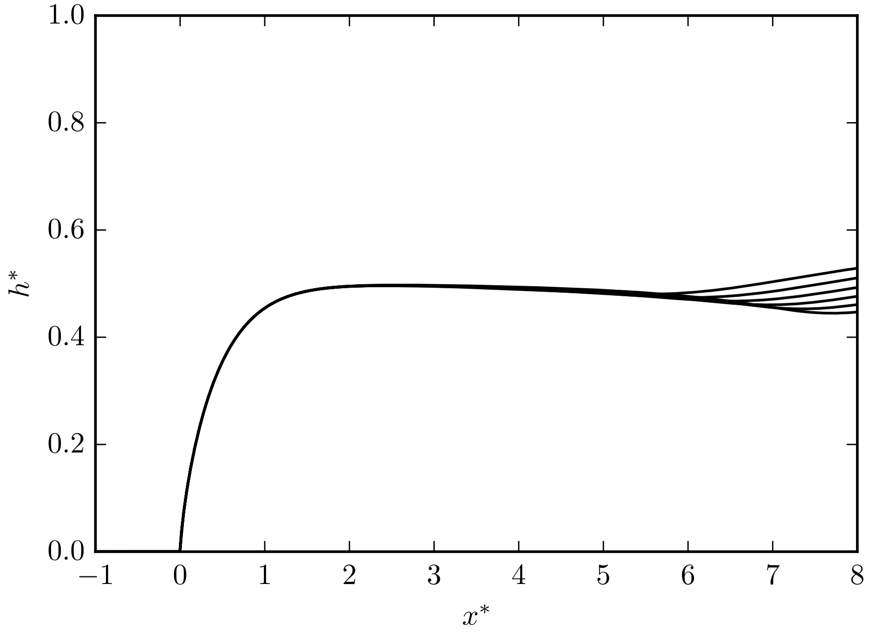

Figure 2.5: Current height as a function of distance behind the front for a full depth top current with $Re = 5,000$, $Pe = 50,000$ and $\sigma = 0.3$, at $t^* = 20, 22, 24, 26, 28$ and 30. The steady-state approximation is seen to be valid in the vicinity of the current tip.

compare their predictions for the vorticity flux as a function of location with corresponding simulation results. Borden & Meiburg [1] discuss the reasons for focusing on the vorticity flux, rather than the front velocity, due primarily to the difficulty in identifying a single representative value for the current height to use in (2.4) and (2.14). In the past, different authors have employed such measures as the first maximum in the current height behind the front, the current height at the gate location, a spatially averaged value for this purpose or the center of mass [15]. Depending on which value is selected to represent the current height, the predicted front velocities can vary appreciably, so that the front velocity is ill-suited for determining which model is more accurate.

The vorticity flux Ω_B predicted by the Benjamin model can be found by using (2.28), along with the conservation of mass

$$\frac{\Omega_B}{g'd} = \Omega_B^* = \frac{h}{d} \; \frac{2-\alpha}{2-2\alpha^2} \tag{2.39}$$

The corresponding vorticity flux predicted by the current model is

$$\frac{\Omega_C}{g'd} = \Omega_C^* = \frac{h}{d} \;, \tag{2.40}$$

cf. also equations (16) and (18) in Borden & Meiburg [1]. Both models predict identical fluxes for $\alpha = \frac{1}{2}$ and in the limit $\alpha \to 0$, *i.e.*, for currents that either occupy half the channel height or are much smaller than the channel height. The ratio between the two predicted vorticity fluxes reaches a maximum of approximately 1.07 at $\alpha = 2 - \sqrt{3} \approx 0.268$.

The origin of vorticity flux discrepancies between simulation results and theoretical predictions will be discussed here for the vorticity approach, with a corresponding discussion for the primitive variable approach given in appendix B.2. If we had kept the viscous and unsteady terms when deriving (2.11), we would have obtained

$$\Omega^* = \Omega_C^* + E_P^* - E_t^* - E_\mu^* \;, \tag{2.41}$$

where Ω^* represents the instantaneous dimensionless vorticity flux out of the domain. Ω_C^* indicates the dimensionless vorticity flux predicted by the vorticity model for the steady, inviscid case in which the gravity current fluid is at rest. E_P^*, E_t^* and E_μ^* denote the deviations from this idealized model due to, respectively, fluid motion within the gravity current, unsteadiness and viscous effects

$$\begin{aligned} E_P^* &= \iint -\boldsymbol{\nabla} \times \left(\frac{1}{\rho^*} \boldsymbol{\nabla} P^* \right) \mathrm{d}A^* - \Omega_C^* \ , && (2.42) \\ E_t^* &= \iint \boldsymbol{\nabla} \times \left(\frac{\partial \boldsymbol{u}^*}{\partial t^*} \right) \mathrm{d}A^* \ , && (2.43) \\ E_\mu^* &= -\frac{1}{Re} \iint \boldsymbol{\nabla} \times \left(\frac{1}{\rho^*} \nabla^2 \boldsymbol{u}^* \right) \mathrm{d}A^* \ , && (2.44) \end{aligned}$$

where the integration is carried out over the control volume $BCDE$. The discrepancies derived in appendix B.2 for the primitive variable approach are closely related to (2.42), (2.43) and (2.44). For this reason, we will in the following section limit our discussion of the discrepancies between theoretical model predictions and simulation results to terms (2.42), (2.43) and (2.44).

We furthermore remark that, if we assume a hydrostatic pressure profile along the downstream boundary B-A-E of the control volume, E_P^* can alternatively be evaluated as

$$E_P^* = (P_O^* - P_B^*) \frac{\sigma - 1}{\sigma} \ . \qquad (2.45)$$

The difference between evaluating E_P^* via (2.42) and (2.45) thus provides information on how close to hydrostatic the pressure profile is along B-A-E. The pressure difference $P_O^* - P_B^*$ can be found by integrating the x-momentum equation from O to B in the simulation. The x-momentum equation yields

$$\begin{aligned} P_O^* - P_B^* &= \frac{\sigma U_B^{*2}}{2} - \sigma E_{\mu,B}^* - \sigma E_{t,B}^* && (2.46) \\ E_{\mu,B}^* &= \frac{1}{\sigma Re} \int_O^B \nabla^2 u^* \mathrm{d}x^* && (2.47) \\ E_{t,B}^* &= -\int_O^B \frac{\partial u^*}{\partial t^*} \mathrm{d}x^* && (2.48) \end{aligned}$$

Note that $E^*_{\mu,B}$ and $E^*_{t,B}$ can be thought of as partial evaluations of E^*_μ and E^*_t after using Stokes' theorem. By substituting (2.46) into (2.45), one obtains

$$E^*_P = (1-\sigma)\left(-\frac{U^{*2}_B}{2} + E^*_{\mu,B} + E^*_{t,B}\right) \tag{2.49}$$

For $E^*_{\mu,B} \approx E^*_\mu$ and $E^*_{t,B} \approx E^*_t$, E^*_P, E^*_μ and E^*_t will tend to cancel each other out partially in (2.41). This effect will be greatest when σ and the fluid motion inside the current U^*_B are both small. As $\sigma \to 1$, $E^*_P \to 0$, which is consistent with the Boussinesq vorticity model, which did not require any assumptions regarding the pressure profile inside the current.

2.4 Simulation results and discussion

2.4.1 Full Depth Lock Releases

Figure 2.6 compares the model predictions to the vorticity flux in the simulation for the full depth current with $Re = 5,000$, $Pe = 50,000$ and $\sigma = 0.3$, as a function of the distance behind the current tip. We note that both model predictions are very close to the simulation result, and also to each other. This is perhaps not unexpected in light of the fact that for a full depth current $\alpha \approx 0.5$, and that for $\alpha = 0.5$ the vorticity model (2.40) and Benjamin's model (2.39) predict identical vorticity flux values.

We now analyze the magnitude of the terms that account for the deviation between the simulation result and the prediction by the vorticity model, i.e., E^*_P, E^*_t and E^*_μ. Figure 2.7a shows the values of the integrals in (2.42), (2.43) and (2.44) as functions of the distance x^* of the control volume boundary B-A-E behind the current front. The figure indicates that close to the current tip the assumption of steady flow is very accurate. Further downstream, the influence of the unsteadiness increases, which is consistent with

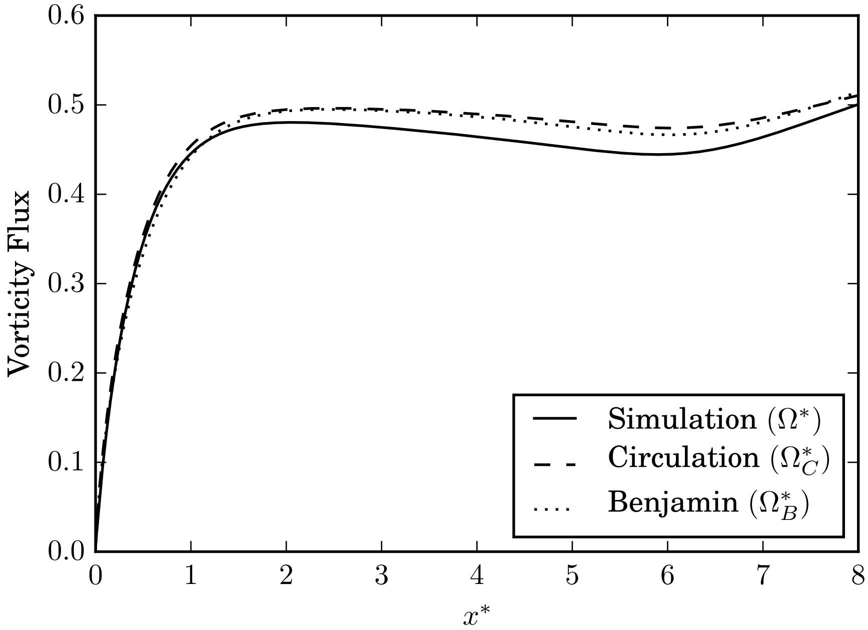

Figure 2.6: Vorticity flux normalized by $g'd$ *vs.* distance x^* behind the current head for the full depth curent with $Re = 5,000$, $Pe = 50,000$ and $\sigma = 0.3$ at $t^* = 22$. The values predicted by Benjamin's model (2.39) and the circulation model (2.40) are close to each other, and to the simulation results.

the graphs of the current heights at various times shown in figure 2.5. The influence of viscous diffusion is significant near the tip of the current, but very small further downstream. The fluid motion inside the gravity current plays a significant role near the current tip, and farther downstream where the current height varies more strongly with x^*. Figure 2.7b confirms that if the vorticity model prediction is augmented by the three terms E^*_P, E^*_t and E^*_μ, the correct simulation result for the vorticity flux is recovered.

Figure 2.8 shows the magnitude of the pressure term E^*_P as a function of the distance x^* of the downstream control volume boundary *B*-*A*-*E* behind the current tip. The open symbols are obtained by direct integration of the integral in (2.42) from the simulation pressure field, while the solid line assumes a hydrostatic pressure profile along *B*-*A*-*E* and evaluates (2.45). The results are shown to be in good agreement everywhere except near the current tip, which reflects the non-hydrostatic nature of the pressure field in this

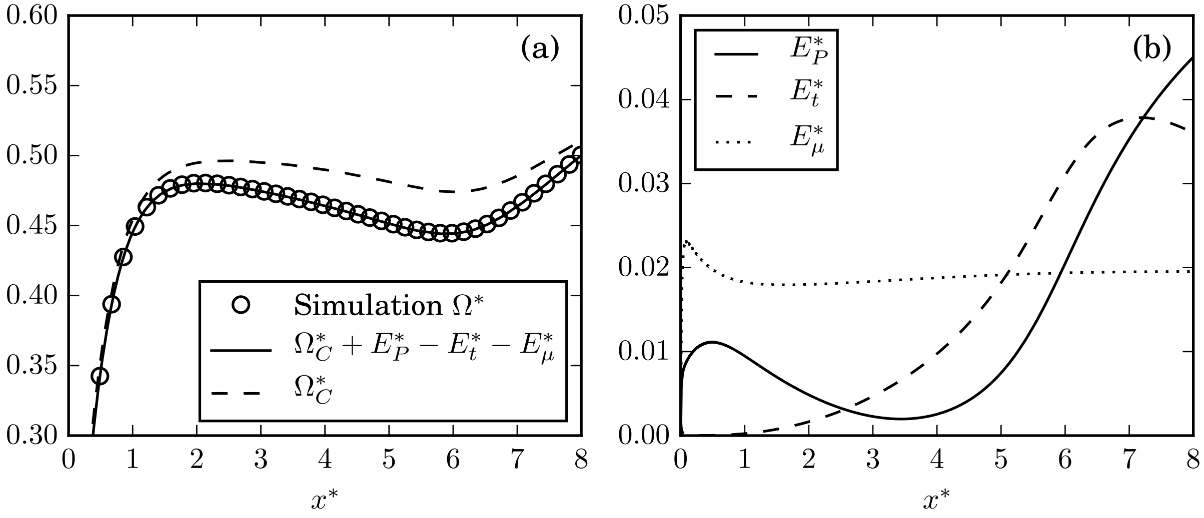

Figure 2.7: (a) Simulation vorticity flux Ω^* along with Ω_C^* and $\Omega_C^* + E_P^* - E_t^* - E_\mu^*$ as functions of x^*, for the full depth curent with $Re = 5,000$, $Pe = 50,000$ and $\sigma = 0.3$ at $t^* = 22$. All quantities are evaluated directly from the simulation data, and made dimensionless by $g'd$. The discrepancy between the vorticity flux Ω_C^* predicted by the vorticity model and the simulation result Ω^* is due to the quantities E_P^*, E_t^* and E_μ^*. Here E_P^* is evaluated using (2.42). (b) Components of the difference between the vorticity flux predicted by the circulation model and the flux observed in the simulation, stemming from the three assumptions of motionless fluid inside the current (E_P^*), steady state (E_t^*) and inviscid flow (E_μ^*).

region. Recall that the non-Boussinesq vorticity model made two assumptions about the pressure: (a) it assumed that the pressure distribution at the downstream boundary of the control volume is hydrostatic; and (b) it assumed that as a result of the current fluid being at rest, $P_O - P_B = 0$. Figure 2.8 indicates that far behind the current front (a) is very accurate, so that (b) is largely responsible for the discrepancy between simulation results and model predictions for the vorticity flux.

Figure 2.9 analyzes the dependence of E_P^*, E_t^* and E_μ^* on the density ratio σ and on Re. We observe that increases in σ or Re tend to reduce the magnitude of all three of these terms, which indicates that predictions by the vorticity model become more accurate as the flow is less viscous and closer to Boussinesq. The decrease in E_P^* for larger σ is consistent with (2.49) and reflects the fact that the pressure profile inside the

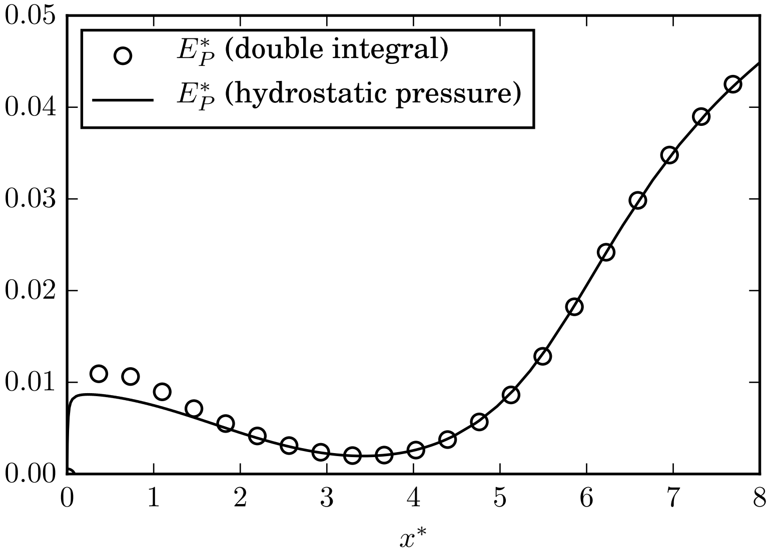

Figure 2.8: Pressure-related deviation E_P^* evaluated using (2.42) and (2.45), for the full depth curent with $Re = 5,000$, $Pe = 50,000$ and $\sigma = 0.3$ at $t^* = 22$. The difference near the tip reflects the non-hydrostatic nature of the pressure in this region, since (2.45) implied a hydrostatic pressure distribution. Farther behind the current tip, the assumption of hydrostatic pressure is very accurate. All quantities are made dimensionless by $g'd$.

current becomes less influential as the flow approaches Boussinesq conditions. In order to understand the decrease in E_P^* for larger Re-values, it is important to realize that for higher Re the shear layer between the current and the ambient becomes thinner, so that the ambient stream drags less current fluid with it. Consequently, the counterflow along the top wall inside the current required to replenish the loss of current fluid in the mixing layer is reduced in strength for larger Re, which is confirmed by figure 2.10. Hence, the streamwise pressure gradient inside the current is weaker for higher Re, so that E_P^* is reduced.

The weaker flow inside the current for larger σ and higher Re also lowers any unsteady effects, thereby reducing E_t^*. Finally, (2.47) indicates that E_μ^* scales with $\frac{1}{\sigma Re}$, so that it should decrease for larger values of σ and Re, which is confirmed by figure 2.9.

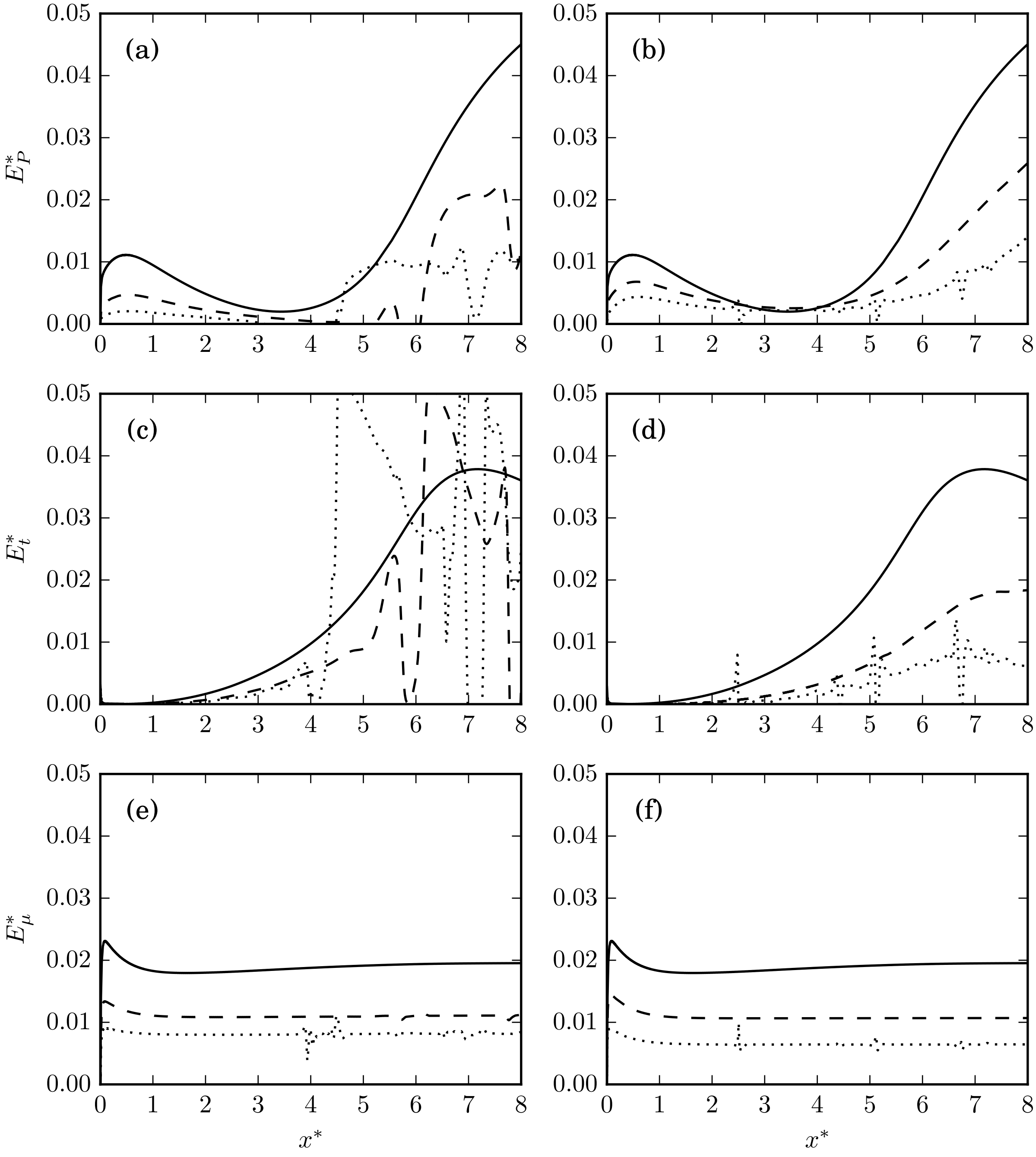

Figure 2.9: Effect of σ and Re on E_P^*, E_t^* and E_μ^*: (a,c,e) $Re = 5000$ and $\sigma = 0.3$ (solid line), 0.5 (dashed line) and 0.7 (dotted line); (b,d,f) $\sigma = 0.3$ and $Re = 5000$ (solid line), $Re = 10,000$ (dashed line) and $Re = 20,000$ (dotted line). All three of E_P^*, E_t^* and E_μ^* get smaller for lower viscosity and reduced density contrast, as explained in the text.

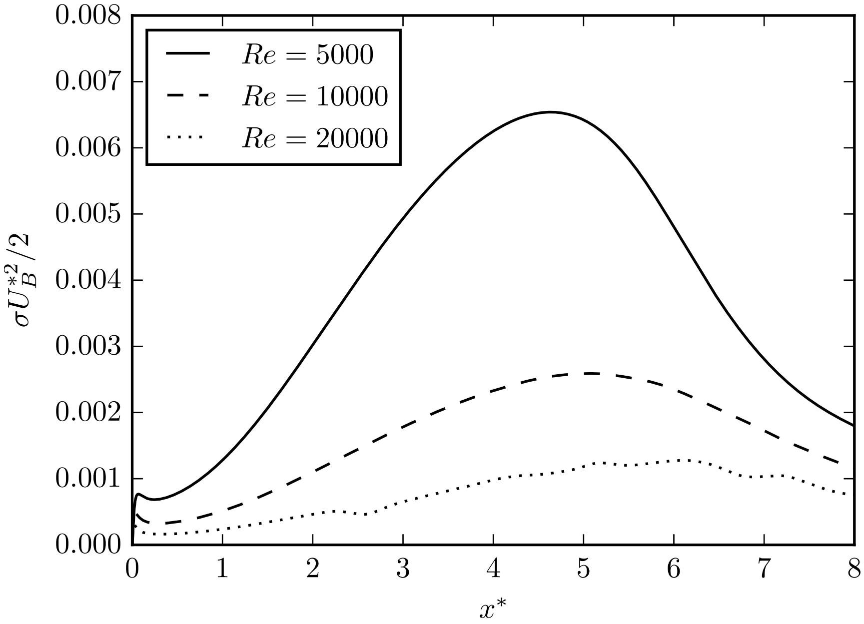

Figure 2.10: Streamwise velocity along the top wall inside the current, as a function of the distance x^* behind the current front, for $\sigma = 0.3$. For increasing Re-values, the flow inside the current is reduced.

2.4.2 Partial Depth Lock Releases

Figure 2.11 shows the evolution of a partial depth gravity current from a lock with $d/H = \frac{1}{2}$. The front of the buoyant current is not as smooth as that of the corresponding full depth current discussed earlier, as a result of instabilities that emerge along the interface. Nevertheless, figure 2.12 indicates that for both values of σ tested, the vorticity model predicts the vorticity flux accurately near the front. Benjamin's model, while not quite as close to the DNS results as the vorticity model, nevertheless shows good quantitative agreement with the simulation data, which indicates that his zero-headloss assumption closely approximates the situation in the simulated flow. This is confirmed by figure 2.13, which demonstrates that (for the present case of slip walls) the headloss along the wall is limited to about 3-4% of the free stream kinetic energy.

The reasons for the good agreement between the vorticity model predictions and the simulation data become clear from figure 2.14, which shows the fluid velocity along the

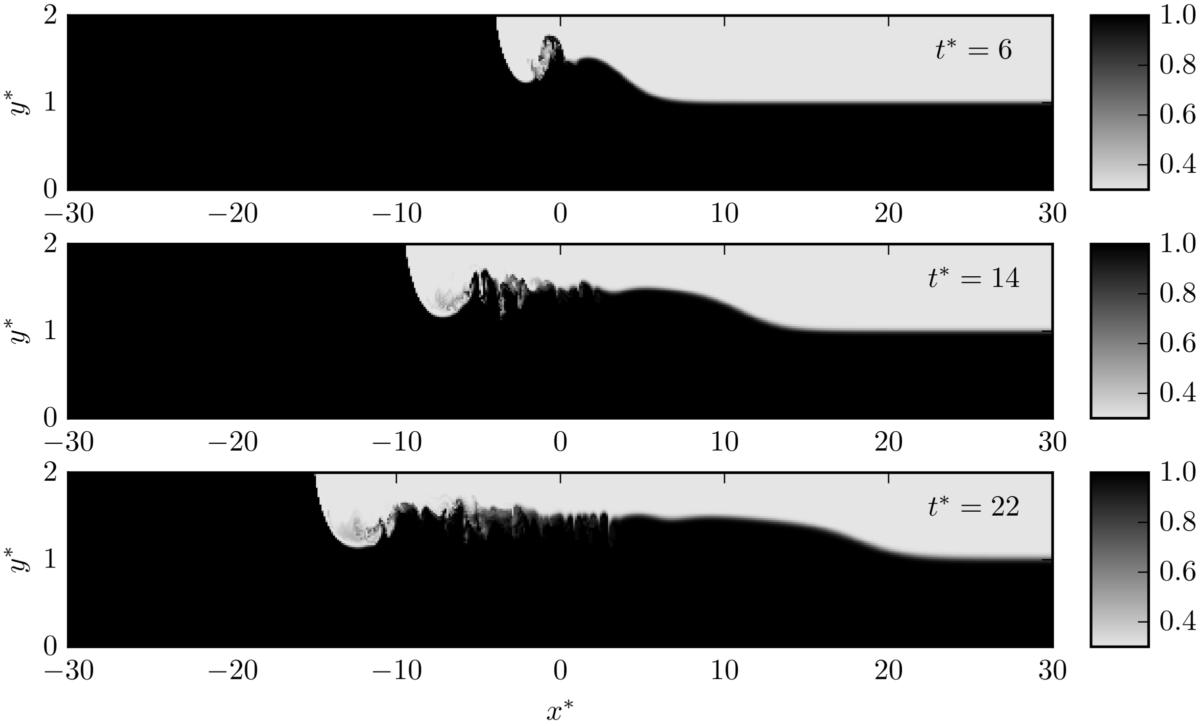

Figure 2.11: Density field of a partial depth, non-Boussinesq gravity current with $Re = 5,000$, $Pe = 50,000$, $\sigma = 0.3$ and $d/H = 0.5$.

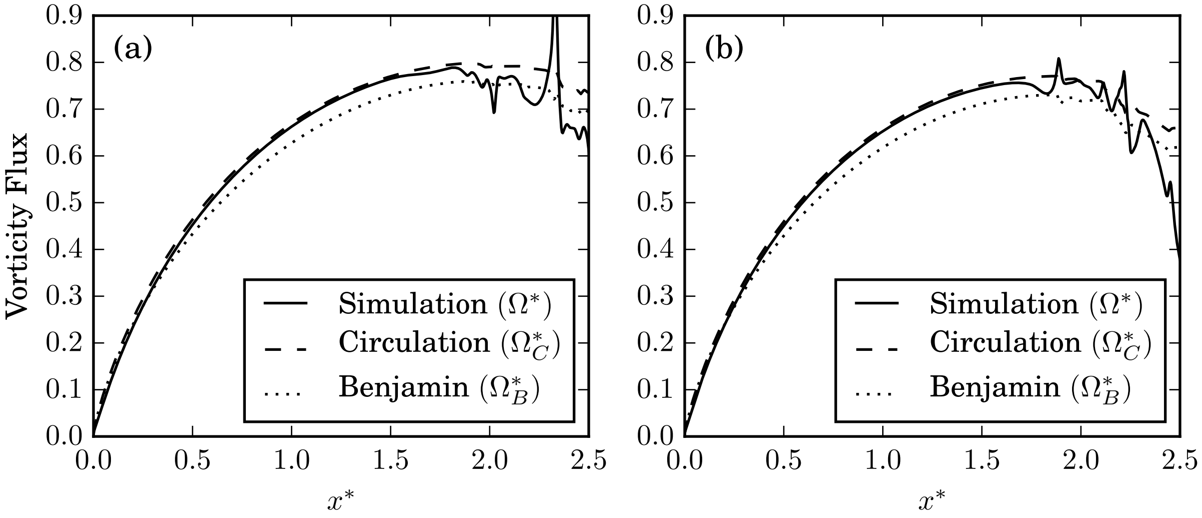

Figure 2.12: Vorticity flux *vs.* distance behind the current tip for the partial depth current with $Re = 5,000$, $Pe = 50,000$, $d/H = 0.5$ and (a) $\sigma = 0.2$ and (b) $\sigma = 0.3$ at $t^* = 6$. For both density ratios, the circulation model (2.40) is seen to agree very closely with the simulation results. Benjamin's model (2.39), while not quite as close, nevertheless also yields good quantitative agreement.

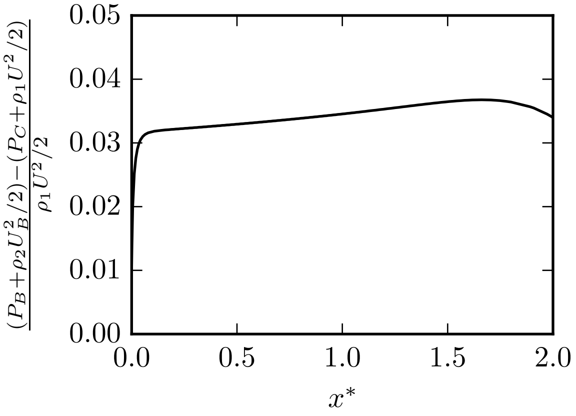

Figure 2.13: Headloss inside the current along the top wall, for the partial depth current with $Re = 5,000$, $Pe = 50,000$, $d/H = 0.5$ and $\sigma = 0.3$ at $t^* = 6$. The headloss is limited to about 3-4% of the free stream kinetic energy, which explains the good quantitative agreement between Benjamin's model predictions and the simulation results.

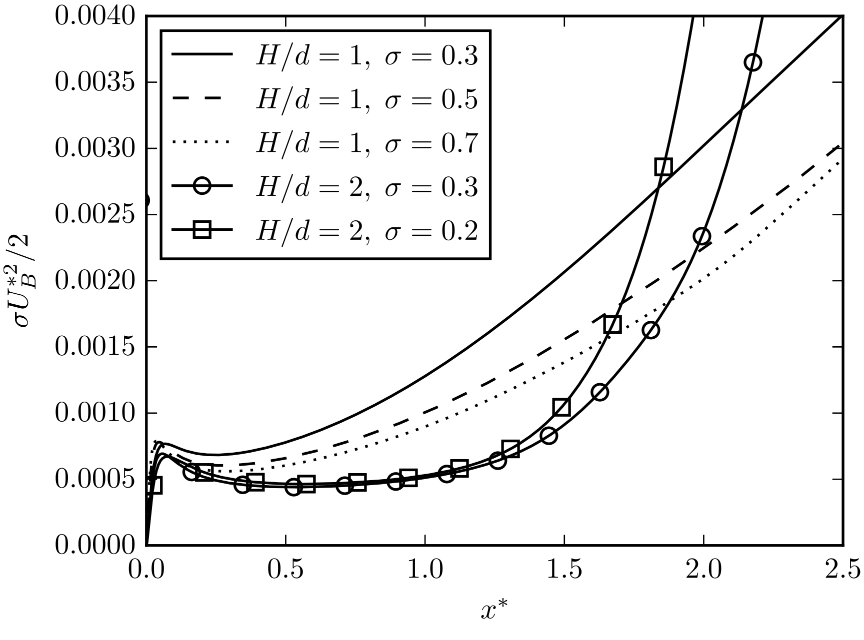

Figure 2.14: Fluid velocity inside the current along the top wall. Near the current tip, partial depth currents (shown at $t^* = 6$) exhibit smaller velocities than full depth currents (shown at $t^* = 22$).

top wall inside the current, for several full and half depth currents. The partial depth currents generally give rise to smaller velocities inside the current. This is a consequence of the weaker acceleration of the ambient fluid around the tip of partial depth currents,

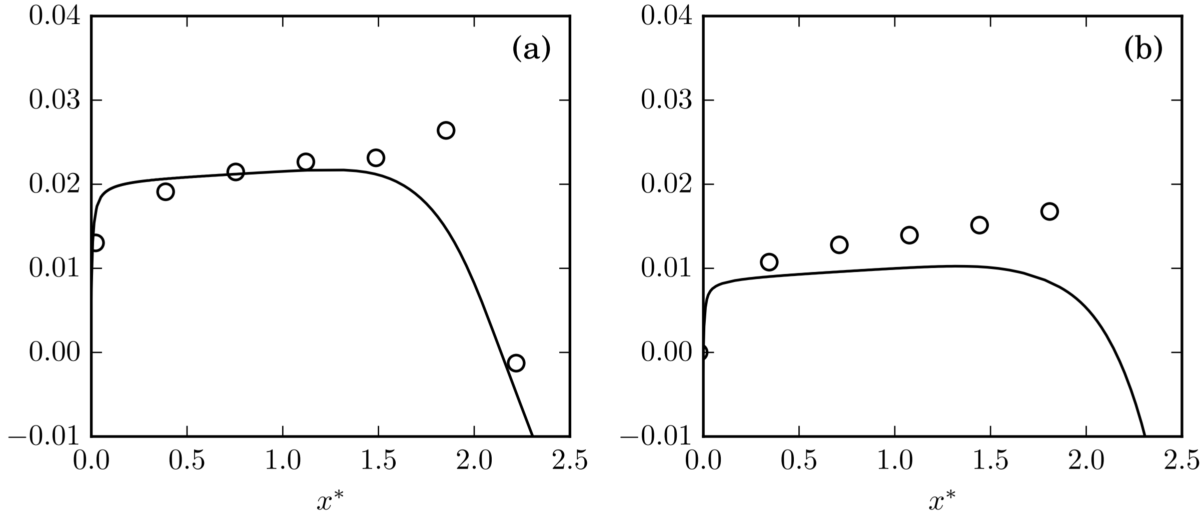

Figure 2.15: Deviation E_P^* due to the fluid motion inside the gravity current, evaluated from (2.42) (circles) and (2.45) (solid line), respectively. The simulations are the same as in figure 2.11 at $t^* = 6$ with (a) $\sigma = 0.2$ and (b) $\sigma = 0.3$, and all quantities are made dimensionless by $g'd$.

so that partial depth currents experience less shear and a lower momentum transfer. Equation (2.49) indicates that the weaker values of U_B^* associated with half depth currents enhance the partial cancellation of E_P^* by E_μ^* and E_t^*, thereby resulting in improved model predictions.

Figure 2.15 shows the deviation E_P^* due to the fluid motion inside the gravity current, evaluated from (2.42) and (2.45), respectively. Both results agree closely with each other in the vicinity of the current tip, which demonstrates that the pressure is approximately hydrostatic there, despite the interfacial instabilities. Consistent with our earlier observations for full depth currents, the deviation decreases for larger σ. Furthermore, the values of E_P^* and E_μ^* as a fraction of Ω_C^* are only about half as large as for the full depth current. This also contributes to the good agreement observed in figure 2.12.

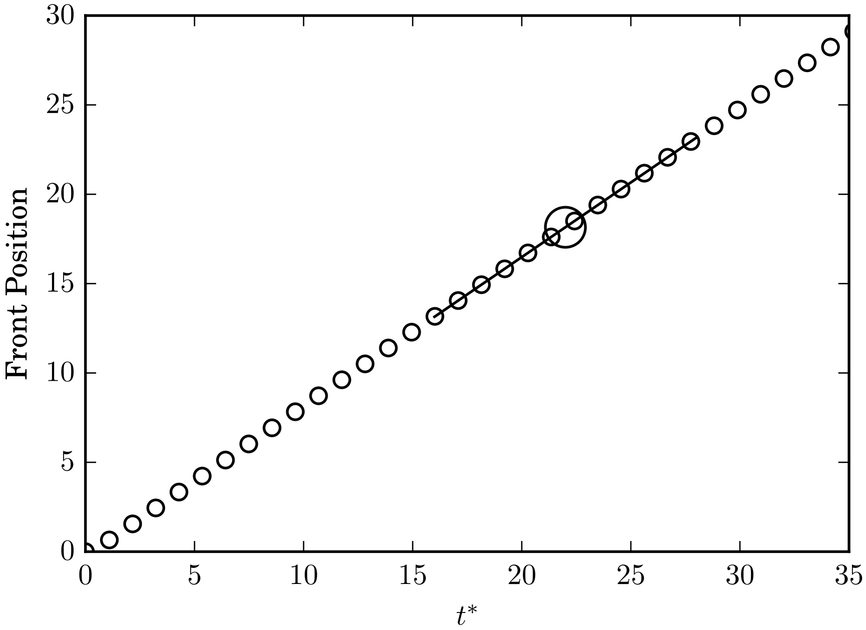

Figure 2.16: Calculation of the quasisteady front velocity U for the full depth bottom current with $Re = 5,000$, $Pe = 50,000$ and $\sigma = 0.3$. The small circles represent the tip location at every $2,000^{\text{th}}$ time step. In order to evaluate the front velocity at a given time, e.g., the large circle, we employ a local linear best fit of the front locations, as indicated by the line.

2.4.3 Dense Currents

We now focus on the dense current moving towards the right along the bottom wall in figure 2.3. Figure 2.16 indicates that this current also has a steady front velocity. Figure 2.17 shows the bottom current heights for several times, corresponding to figure 2.5 for the top current. While a steady-state region again develops near the tip, it is much shorter than that for the top current, as a result of the turbulent billows. Figure 2.18 compares DNS results and model predictions for the vorticity flux in this region. The model predictions are given in (2.50) and (2.51).

$$\frac{\Omega_B}{g'd} = \Omega_B^* = \frac{h}{d} \quad \frac{2-\alpha}{2\sigma(1-\alpha^2)} \tag{2.50}$$

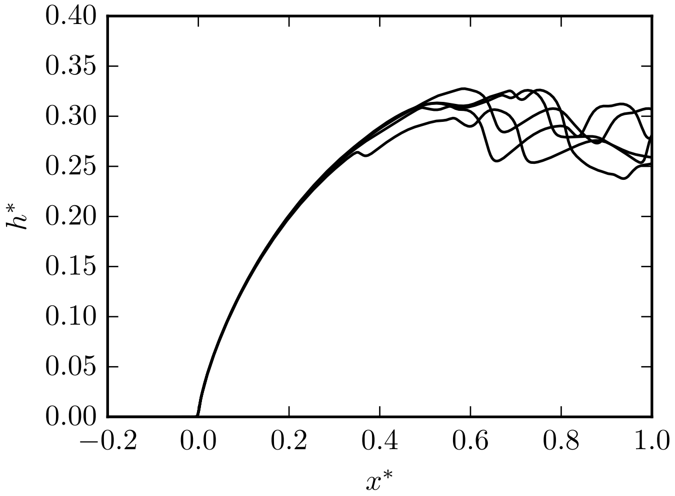

Figure 2.17: Current height as a function of distance behind the front for a full depth bottom current with $Re = 5,000$, $Pe = 50,000$ and $\sigma = 0.3$, at $t^* = 20, 22, 24, 26, 28$ and 30. The steady-state approximation is seen to be valid in the vicinity of the current tip, although this region steady-state region is significantly shorter than that for the top current.

The corresponding vorticity flux predicted by the current model is

$$\frac{\Omega_C}{g'd} = \Omega_C^* = \frac{h}{d}\ \frac{1}{\sigma} \tag{2.51}$$

These predictions differ by (2.39) and (2.40) by a factor of $1/\sigma$. Good agreement is seen for both models, in spite of the fact the hydrostatic pressure assumption may not be very accurate so close to the tip.

2.5 Summary

In the present investigation we have extended the vorticity-based modeling approach by Borden & Meiburg [1] to non-Boussinesq gravity currents. This approach enables us to arrive at a closed form solution for the Froude number without having to invoke an energy-based closure assumption, such as had been required in the analyses by von

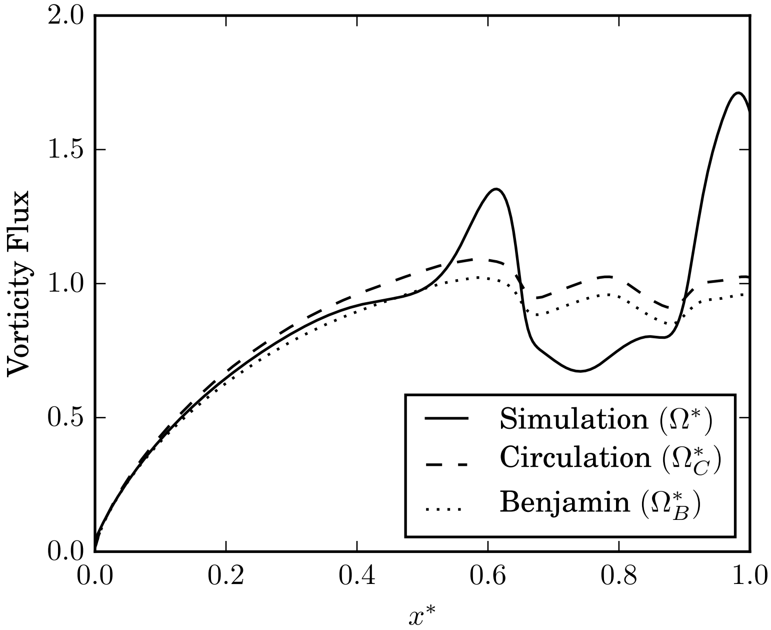

Figure 2.18: Vorticity flux normalized by $g'd$ *vs.* distance x^* behind the current head, for the full depth bottom current with $Re = 5,000$, $Pe = 50,000$ and $\sigma = 0.3$ at $t^* = 22$. In the steady-state region near the tip, the values predicted by Benjamin's model (2.50) and the circulation model (2.51) are close to each other, and to the simulation results.

Kármán [6] and Benjamin [7]. Hence the vorticity approach bypasses the discussion among those authors as to which energy closure provides the optimal fit with experimental and simulation data.

In the Boussinesq limit, it had been possible to decouple the pressure entirely from the conservation equations for mass and vorticity, so that no assumptions whatsoever had been required regarding the pressure. For non-Boussinesq currents, on the other hand, the pressure does not decouple from the vorticity transport equation, so that a certain amount of information regarding the pressure is needed for the exact integration of the vorticity equation over a finite control volume. Towards this end, we stipulate that the pressure distributions inside the current is hydrostatic. Furthermore, we assume the pressure inside the current to be constant along the wall, since the current fluid is considered to be at rest. On this basis we obtain a closed-form solution for the Froude number of non-Boussinesq gravity currents that reduces to the correct expression derived for the Boussinesq limit.

In order to assess the accuracy of the predictions by the various models for non-Boussinesq flows, we analyze the rate at which vorticity is convected out of the control volume. For full-depth currents, the prediction by the vorticity model is close to that of Benajmin's model, and both are very close to corresponding high-resolution simulation data. For partial depth currents, the vorticity model agrees closely with simulation data. We show that Benjamin's model predictions also reproduce the DNS results with good accuracy, which indicates that the simulated flow satisfies Benjamin's assumption of vanishing headloss to a good approximation. Hence, the key contribution of the vorticity model should be seen in its ability to predict the front velocity without any energy-based closure assumptions, rather than in its improved accuracy.

We furthermore discuss the influence of the three main assumptions underlying all of the above models, including the present vorticity-based model, regarding the nature of the flow, *viz.* i) the flow is steady in the reference frame moving with the current front; ii) the flow is inviscid; and iii) the fluid inside the current is at rest. We find the quasisteady flow assumption to be very accurate in the neighborhood of the front of the top current, although unsteady effects increase farther downstream. The influence of viscosity is significant near the front, but very small further downstream. The effects of the fluid motion inside the current are small at an intermediate distance of a few current heights behind the tip, but they increase both farther downstream and in the immediate neighborhood of the tip. For a constant density ratio, the model predictions generally improve with increasing Reynolds number, while for a constant Reynolds number they improve for weaker density contrasts. We furthermore show that the effects of the above three assumptions partially cancel each other out with regard to the predicted vorticity flux, which explains the good agreement with simulation data across the entire range of

Reynolds numbers and density ratios investigated.

Chapter 3

Double-diffusive lock-exchange gravity currents

3.1 Introduction

Recent decades have seen rapid growth in our understanding of the dynamics of single-component gravity currents [7, 16, 17, 18], based on laboratory experiments [19], field observations ([20] and references therein), high-resolution numerical simulations [21, 22, 23], and novel theoretical approaches [1]. These investigations have elucidated the dynamical force balances governing the various stages of single-component gravity current flows, as well as their front velocity, mixing properties and energy budgets. By comparison, multicomponent gravity currents remain much less well understood, in spite of their importance in natural settings and engineering applications, such as river plumes [24], oceanic overflows [25] and desalination plants [26]. Most of the research on two-component gravity currents to date has focused on the influence of a particulate phase, and on the role of particle settling in triggering buoyancy reversal in such flows [27, 28]. On the other hand, very few investigations have focused on the effects of double-diffusion on the dynamics of gravity currents driven by temperature and salinity differences.

Double-diffusion is known to give rise to a host of complex dynamical phenomena in nominally stably stratified thermohaline systems [29]. At the most basic level, the experiments of Huppert & Turner [30] demonstrate that a fingering interface forms when the slowly diffusing component is unstably stratified, while a diffusive interface emerges for an unstable stratification of the faster diffusing component. The subsequent evolution of the convective flow can produce such interesting features as collective fingering instabilities, staircases and horizontal intrusions [31, 32]. To date, double-diffusive convection has primarily been explored for base states in which the fluid is at rest. On the other hand, for base states in the form of gravity currents, characterized by sharp fronts, pronounced temperature and salinity gradients, as well as strong shear, we might expect the evolution of double-diffusive convection to proceed quite differently. This was confirmed in the laboratory experiments of double diffusive gravity currents by Maxworthy [33], who explored the scaling laws and force balances governing both fixed volume and constant flow rate double-diffusive currents and intrusions. The experiments by Yoshida *et al.*[34], while similar in nature, focused on double-diffusive gravity currents with small density differences, and on the ways in which such currents evolve differently from their single-diffusive counterparts.

Laboratory experiments are commonly constrained by the choice of salt, sugar and heat as the diffusing scalars, so that it is difficult to explore the influence of the diffusivity ratio on double-diffusive phenomena in a systematic fashion. At the same time, it is challenging to obtain detailed time-dependent information on velocity and scalar concentration fields from laboratory experiments. Numerical simulations, on the other hand, are free to vary the diffusivity ratio within a wider range that is effectively bounded only by resolution requirements. Consequently, the present investigation focuses on exploring the interplay between gravity current flows and double-diffusion, and on quantifying the dynamics of such flow fields as a function of the diffusity and stability ratios. Section 3.2 will define the physical set-up, and formulate the governing equations and dimensionless parameters. Section 3.3 briefly reviews the computational approach, while section 3.4 focuses on the simulation results. It discusses the dependence of the gravity current velocity and thickness on the governing parameters, as well as the structure of the resulting density and velocity fields. The convective and diffusive fluxes of heat and salinity out of the current will be quantified, along with the various components of the energy budget. In order to estimate the turbulent drag acting on the current, and its role in the overall force balance, we will analyze the momentum flux across the current/ambient interface. Some interesting aspects will be highlighted regarding the late-stage dynamics of double-diffusive gravity currents. Section 3.5 provides information on the force balances governing double-diffusive gravity currents, while section 3.6 compares the results of two- and three-dimensional simulations. Lastly, section 3.7 summarizes the findings of this chapter.

3.2 Physical problem

We perform direct numerical simulations of full-depth, double-diffusive lock exchange gravity currents, as sketched in figure 3.1. The left half of the domain initially contains the lighter, hot and salty fluid of density ρ_1, whereas the heavier, cold and fresh fluid of density ρ_2 is located on the right. In dimensionless units, the domain extends from $x = -30$ to $x = 30$, and it has a height of one. When the lock is released, the lighter fluid forms a buoyant current that propagates towards the right along the top wall, whereas the denser fluid propagates towards the left along the bottom wall. In the absence of any symmetry-breaking perturbations, these currents develop symmetrically to each other with regard to the center of the domain at $(0, 0.5)$. The simulations are terminated when the currents approach the endwalls.

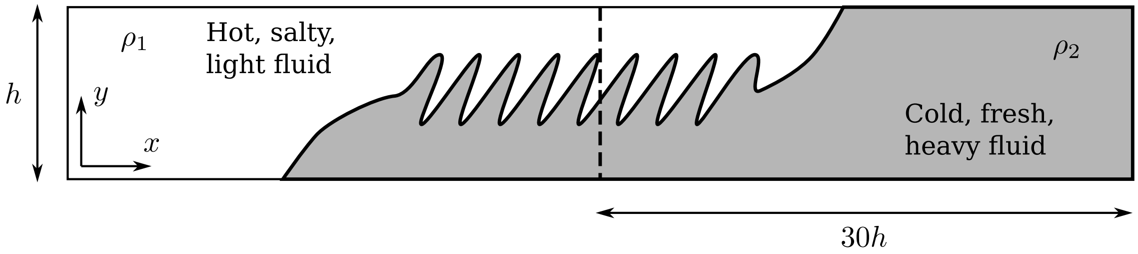

Figure 3.1: Sketch of the lock exchange flow under consideration. The left reservoir is initially filled with light, hot and salty fluid, while the right reservoir contains dense, cold and fresh fluid. Upon removal of the gate (represented by the dashed line), the hot and salty fluid forms a right-moving buoyant current along the top wall, while the cold and fresh fluid propagates to the left along the bottom wall. The interface separating the two currents may be subject to double-diffusive fingering.

3.2.1 Governing equations and dimensionless parameters

We employ the Navier-Stokes equations in the Boussinesq approximation, along with convection-diffusion equations for heat and salinity. In order to nondimensionalize these equations, we introduce the following scales for velocity, length and time, respectively

$$\mathbf{u} = U_b \tilde{\mathbf{u}} \quad , \quad \mathbf{x} = h \tilde{\mathbf{x}} \quad , \quad t = \frac{h}{U_b} \tilde{t} \; . \tag{3.1}$$

Here the tilde symbol indicates a dimensionless quantity. h represents the height of the domain and U_b denotes the buoyancy velocity

$$U_b \equiv \sqrt{g' h} \quad , \quad g' \equiv \frac{\Delta \rho_0}{\rho_0} g \; , \tag{3.2}$$

where the reduced gravity g' is defined based on the initial density difference $\Delta\rho_0 = \rho_2 - \rho_1$ and the average density $\rho_0 = (\rho_1 + \rho_2)/2$.

Pressure, temperature, salinity and density are rendered dimensionless according to

$$P = \rho_0 U_b^2 \tilde{P} \quad , \quad \tilde{T} = \frac{T - T_2}{T_1 - T_2} \quad , \quad \tilde{S} = \frac{S - S_2}{S_1 - S_2} \quad , \quad \tilde{\rho} = \frac{\rho - \rho_1}{\rho_2 - \rho_1} \; . \tag{3.3}$$

The following discussion will focus on dimensionless quantities, so that we now drop the tilde symbols for convenience. The governing equations take the form

$$\begin{aligned}
\boldsymbol{\nabla}\cdot\mathbf{u} &= 0\,, && (3.4)\\
\frac{\partial\mathbf{u}}{\partial t}+\mathbf{u}\cdot\boldsymbol{\nabla}\mathbf{u} &= -\boldsymbol{\nabla}P+\frac{1}{Re}\nabla^2\mathbf{u}-\rho\hat{\mathbf{y}}\,, && (3.5)\\
\frac{\partial T}{\partial t}+\mathbf{u}\cdot\boldsymbol{\nabla}T &= \frac{1}{Pe_T}\nabla^2 T\,, && (3.6)\\
\frac{\partial S}{\partial t}+\mathbf{u}\cdot\boldsymbol{\nabla}S &= \frac{1}{Pe_S}\nabla^2 S\,, && (3.7)\\
\rho &= -c_1T+c_2S+c_3\,. && (3.8)
\end{aligned}$$

The constants c_1, c_2 and c_3 in the equation of state depend on the initial conditions, as will be discussed below. The governing dimensionless parameters

$$Re\equiv\frac{U_bh}{\nu}\quad,\quad Pe_T\equiv\frac{U_bh}{k_T}\quad,\quad Pe_S\equiv\frac{U_bh}{k_S}\quad,\quad \tau\equiv\frac{k_S}{k_T}\equiv\frac{Pe_T}{Pe_S} \qquad (3.9)$$

have the form of a Reynolds and two Péclet numbers. Additionally, it is convenient to define the diffusivity ratio τ. Here ν denotes the kinematic viscosity of the fluid, while k_T and k_S represent the diffusivities of heat and of salt, respectively. We remark that, even when we vary the value of τ, we will employ the terms 'salt' ('heat') for the more slowly (rapidly) diffusing scalar.

An additional dimensionless parameter arises through the initial conditions, in the form of the stability ratio

$$R_{\rho 0}=\frac{c_1}{c_2}\,. \qquad (3.10)$$

Keeping in mind that the initial dimensionless temperature and salinity differences are unity, $R_{\rho 0}$ denotes the ratio of the initial density contributions due to heat and salt, respectively. Our interest focuses on situations in which the warm, salty fluid in the left reservoir is lighter than the cold, fresh fluid in the right one, so that the temperature density contribution exceeds that of salinity, resulting in $R_{\rho 0} > 1$. The constants c_1, c_2 and c_3 in (3.8) and (3.10) can now be expressed as functions of $R_{\rho 0}$. The dimensionless density of the warm, salty fluid is zero

$$0 = -c_1 + c_2 + c_3 \ , \tag{3.11}$$

whereas that of the cold, fresh fluid is one

$$1 = c_3 \ . \tag{3.12}$$

Equations (3.10), (3.11) and (3.12) hence yield

$$c_1 = \frac{R_{\rho 0}}{R_{\rho 0} - 1} \quad , \quad c_2 = \frac{1}{R_{\rho 0} - 1} \ . \tag{3.13}$$

As will be discussed in section 3.4.4, at later times the effective dimensionless temperature and salinity values of the top (T_t, S_t) and bottom (T_b, S_b) currents can be different from their reservoir values, so that it is useful to define the time-varying stability ratio

$$R_\rho(t) = R_{\rho 0} \frac{\Delta T(t)}{\Delta S(t)} \tag{3.14}$$

where $\Delta T(t) = T_t(t) - T_b(t)$ and $\Delta S(t) = S_t(t) - S_b(t)$ represent the time-dependent temperature and salinity differences between the currents.

We furthermore define $\gamma(t)$ as the ratio of the time-dependent density difference between the currents to the initial density difference between the reservoirs

$$\gamma(t) \equiv \frac{\Delta\rho(t)}{\Delta\rho_0} = \frac{R_{\rho 0}}{R_{\rho 0} - 1} \Delta T(t) - \frac{1}{R_{\rho 0} - 1} \Delta S(t) \tag{3.15}$$

where the initial density difference is $\Delta\rho_0 = 1$.

We assume slip boundaries along all walls, as well as no-flux conditions for the temperature and salinity. As will be discussed below, the present investigation primarily focuses on the influence of the initial stability ratio $R_{\rho 0}$ and the diffusivity ratio τ on the gravity current dynamics.

3.3 Numerical approach

We integrate the Navier-Stokes equations in two dimensions in the streamfunction-vorticity formulation, which allows us to analyze strongly double-diffusive flows in the regime $\tau \ll 1$. As usual, the streamfuction ψ is defined via

$$u = \frac{\partial \psi}{\partial y} \quad , \quad v = -\frac{\partial \psi}{\partial x} \ , \tag{3.16}$$

while the vorticity ω is given as

$$\omega = \frac{\partial v}{\partial x} - \frac{\partial u}{\partial y} \ . \tag{3.17}$$

The equations are discretized in the x-direction via a pseudospectral method, and in the y-direction by means of sixth order compact finite differences [35]. A typical mesh consisted of 8,192 × 257 grid points. The pressure can be calculated in a post-processing step from the Poisson equation

$$\nabla^2 P = 2\left(\frac{\partial u}{\partial x}\frac{\partial v}{\partial y} - \frac{\partial u}{\partial y}\frac{\partial v}{\partial x}\right) - \frac{\partial \rho}{\partial y} \ , \tag{3.18}$$

subject to homogeneous Neumann boundary conditions at the left and right walls in conjunction with

$$\frac{\partial P}{\partial y} = -\rho \tag{3.19}$$

along the top and bottom boundaries. Equation (3.18) is solved by means of a Fourier approach in the x-direction, combined with sixth order compact finite differences in y. Because all of the boundary conditions for the pressure are of Neumann type, we set the average pressure to zero.

Detailed validation results for the code are discussed by Burns & Meiburg [36]. In addition, we performed a number of convergence tests for various governing parameter combinations, to ensure a sufficiently fine grid resolution.

The three-dimensional simulation to be discussed below was performed with the flow solver IMPACT, whose implementation and validation details have been published elsewhere [36, 37]. IMPACT uses a primitive variable formulation on a structured mesh. Within a single cell, the variables are staggered, with velocity nodes centred on the face normal to their direction of propagation and pressure/scalars located at the cell centre. The solver uses central finite differences in all spatial directions with the accuracy capability ranging from second order up to tenth order compact. For the present work, a non-compact sixth-order scheme is chosen for the three-dimensional simulation. The improved accuracy and spectral resolution characteristics of staggered grids [35] dictate that compact schemes are unnecessary. For temporal differencing, the low-storage third-order Runge-Kutta/Crank-Nicolson scheme of [38] is used. The pressure is solved using the Schur complement formulation, and at each Runge-Kutta substep a Richardson iteration is used to ensure convergence of the pressure field. Linear systems are solved by the BiCGStab algorithm with a multigrid preconditioner.

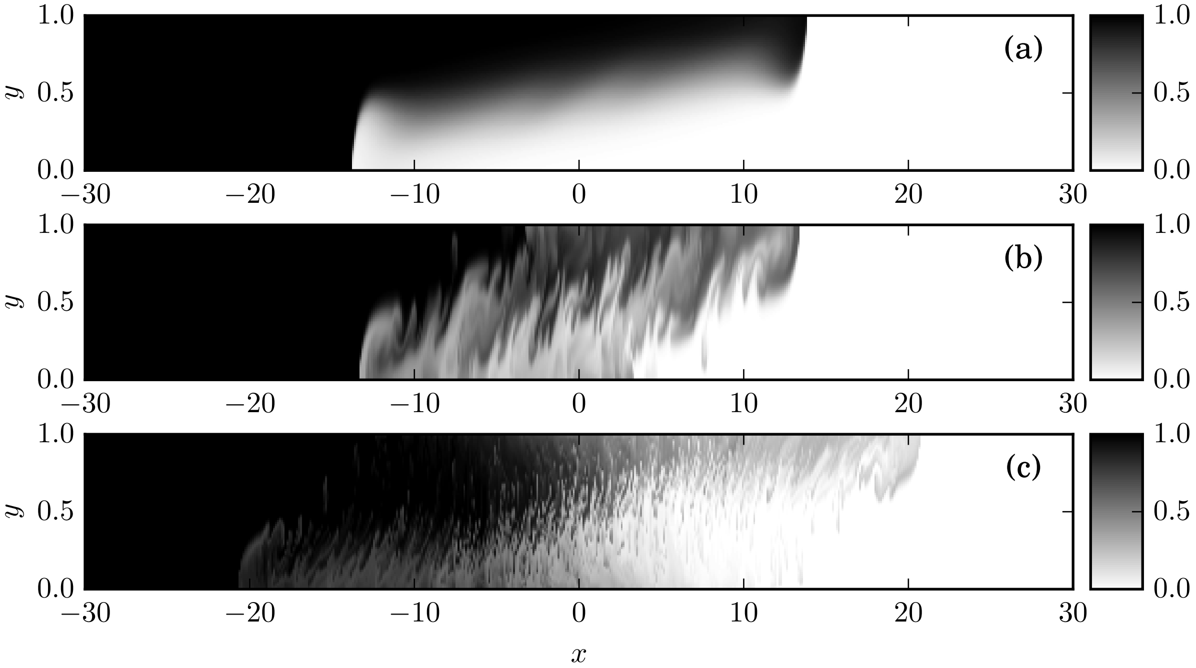

Figure 3.2: Salinity concentration for (a) a single-diffusive case with a diffusivity ratio $\tau = 1$, (b) a mildly double-diffusive case with $\tau = 2/3$, and (c) a strongly double-diffusive case with $\tau = 1/8$. All flows have $R_{\rho 0} = 1.07$ and are shown for $t = 30$. At lower diffusivity ratios, the double-diffusive fingers are smaller and more numerous. Even for the mildly double-diffusive case with $\tau = 2/3$, the flow structure is quite different from that of a single-diffusive current, although the front velocity remains similar.

3.4 Results

In the following, we will discuss results from a parametric study that we conducted by means of two-dimensional simulations. Subsequently, we will present a comparison with a representative three-dimensional simulation, in order to assess the importance of the third dimension. A few comments are in order regarding the range of dimensionless parameter values in the simulations. While numerical simulations can provide flexibility in the diffusivity and stability ratios to be investigated, it is usually prohibitively expensive to perform a parametric study for the very disparate diffusivities characteristic of heat/salt systems. For this reason, we are unable to directly compare our results with those of Maxworthy [33] and Yoshida *et al.*[34]. Nevertheless, the simulations to be discussed below will serve to identify scaling laws in the current dynamics as a function of the dimensionless parameter values, and in some cases we will observe asymptotic behavior. This will allow us to draw conclusions that also apply to much smaller diffusivity ratios.

We will begin with an overview of how the main features of the currents, such as their structure, front velocity and thickness, depend on the governing dimensionless parameters. Subsequently, we will discuss the detailed physical mechanisms responsible for the observed behavior.

Figure 3.2 shows representative results for three configurations with identical parameter values $Re = 10^3$, $Pe_T = 10^3$ and $R_{\rho 0} = 1.07$, but different diffusivity ratios $\tau = 1$ (single-diffusive, top), 2/3 (weakly double-diffusive, middle) and 1/8 (strongly double-diffusive, bottom). All flow fields are shown for $t = 30$. The density difference between the lighter fluid in the left reservoir and the heavier fluid in the right one is seen to drive opposing gravity currents along the top and bottom walls. Superimposed on the primarily horizontal motion of these light (warm, salty) and dense (cold, fresh) gravity currents, double-diffusion gives rise to strong fingering in the vertical direction. These fingers are driven by the release of potential energy stored in the unstable salinity stratification. While a fraction ξ of this potential energy released by the salt is converted into potential energy of upwardly lifted colder fluid, linear stability investigations and nonlinear simulations of classical double-diffusive convection suggest that $\xi < 1$ [29]. As will be demonstrated in more detail below, double-diffusion thus effectively reduces the density of the light top current, while increasing that of the heavy bottom current. As expected, lower diffusivity ratios (more disparate diffusivities) result in more intense double-diffusive fingering, and hence in the pronounced acceleration of the gravity currents for $\tau = 1/8$.

In figure 3.2 we note that the single-diffusive gravity current for $Re = 10^3$ and $\tau = 1$ is laminar. It is stable towards shear instabilities, and no Kelvin-Helmholtz instabilities

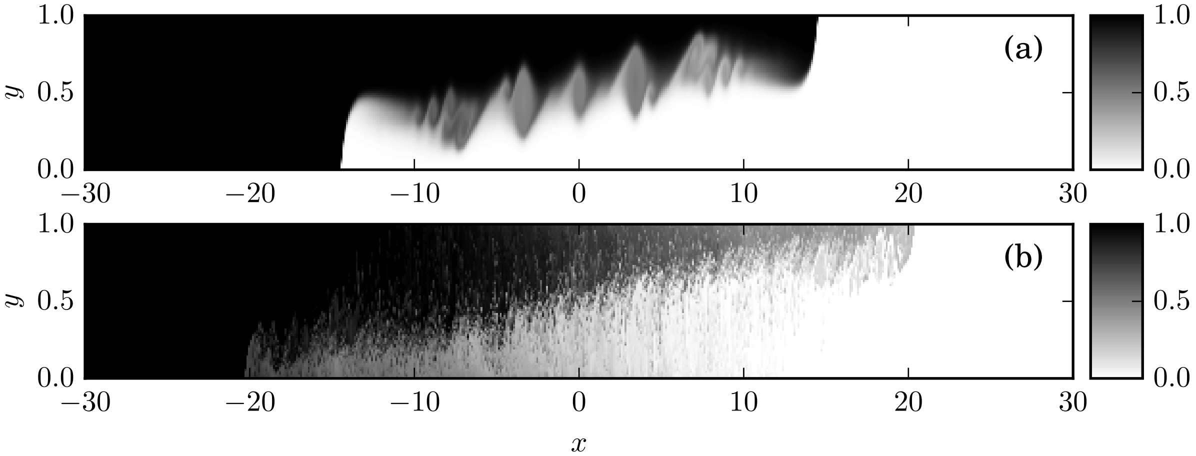

Figure 3.3: Salinity concentration for (a) a single-diffusive case with a diffusivity ratio $\tau = 1$ and (b) a strongly double-diffusive case with $\tau = 1/8$. Both flows have $R_{\rho 0} = 1.07$ and are shown for $t = 30$. Here $Re = 4000$, compared to figure 3.2, where $Re = 1000$.

form, as a suitably defined Richardson number would be above 0.25. For $Re = 4 \times 10^3$, on the other hand, the single-diffusive current does form Kelvin-Helmholtz instabilities, as shown in figure 3.3a, although their effect on the front velocity is small. For $\tau = 1/8$, the flow is dominated by double-diffusive fingering for both values of Re, and Kelvin-Helmholtz instabilities can be identified at most in the vicinity of the current tip, where the fingering is less intense, as will be discussed in section 3.4.7.

This brief, qualitative description of the fundamental mechanisms at work suggests a strong coupling between the predominantly horizontal motion of the gravity currents and the primarily vertical double-diffusive fingering. To quantify the coupled dynamics as a function of the key governing dimensionless parameters $R_{\rho 0}$ and τ represents the main goal of the present investigation. Towards this end, we perform a parametric study involving diffusivity ratio values $\tau = 2/3, 1/2, 1/3, 1/4, 1/6, 1/8$ and stability ratio values $R_{\rho 0} = 1.05, 1.07, 1.1, 1.15, 1.2, 1.3, 1.5$. All simulations employ a fixed Reynolds number of 10^3, along with a temperature Peclet number of 10^3. For all parameter combinations with either $R_{\rho 0} = 1.07$ or $\tau = 1/4$, we perform ten simulations with slightly different random

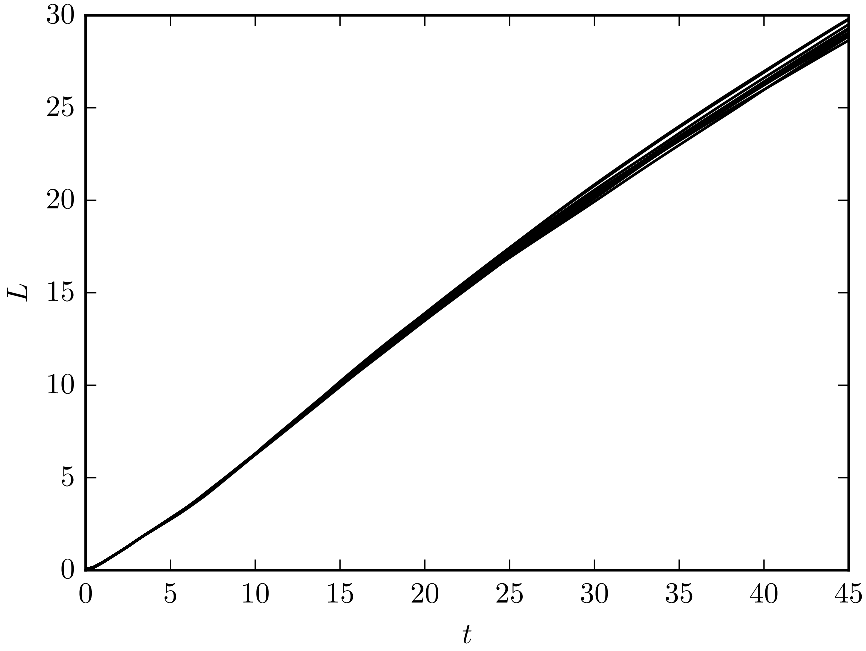

Figure 3.4: Current length *vs.* time for ten individual simulations with $R_{\rho 0} = 1.07$ and $\tau = 1/8$. Each simulation was initiated with a different random initial perturbation.

initial perturbations, so that we can obtain smoother data via ensemble averaging.

We initiate the simulations with an initial perturbation of white noise with an amplitude of 0.027 that is superimposed on an error function-shaped background initial condition

$$T, S(x, y, t = 0) = 1 - \operatorname{erf}\left(\frac{x + 0.027^{*}\text{rand}[-0.5, 0.5](y)}{0.03}\right) \tag{3.20}$$

While the flow fields of individual simulations for identical dimensionless parameter combinations exhibit similar qualitative behavior, the ensemble averaging of ten simulations allows us to obtain smoother quantitative information.

3.4.1 Current length

We define the length $L(t)$ of the rightward propagating buoyant top current as the distance from the gate to the current tip, which is taken as the most advanced location with a dimensionless temperature of at least 0.05. Figure 3.4 shows $L(t)$ for all 10 simulations with $R_{\rho 0} = 1.07$ and $\tau = 1/8$. We observe that up until $t \approx 15 - 20$ the currents undergo a slight acceleration, whereas they tend to slow down moderately thereafter. At $t = 45$, the individual current lengths differ by up to 4%.

For a constant initial stability ratio $R_{\rho 0} = 1.07$, figure 3.5a displays the ensemble-averaged current length $L(t)$ as function of τ. Keeping in mind that $\tau = 1$ corresponds to classical, single-diffusive gravity currents, we find that strongly double-diffusive currents propagate up to 50% faster than classical currents. We expect double-diffusion to affect the current velocity via two opposing mechanisms: On one hand, double-diffusion can modify the density contrast between a current and its ambient environment, which in turn will affect the current velocity. At the same time, double-diffusive fingering will increase the turbulent drag acting on the current, which should have a retarding effect. Interestingly, figure 3.5a indicates that the current velocity does not vary monotonically with τ. For τ-values slightly less than one, i.e. for weakly double-diffusive currents, we observe the current length to grow more slowly than for single-diffusive currents, whereas for strongly double-diffusive currents it grows more rapidly. This suggests that τ affects the balance between buoyancy and turbulent drag in a nonlinear fashion.

The above observations are consistent with earlier findings by Kimura and Smyth [39], and Smyth and Kimura [40, 41] on the interaction of double-diffusion with shear. Those authors showed that for small values of τ the effective diffusivity of momentum is significantly smaller than that of the scalars.

A similar picture emerges regarding the influence of the initial stability ratio $R_{\rho 0}$ when τ is held constant, cf. figure 3.5b. Buoyant currents with $R_{\rho 0} \to 1$ contain large quantities of both heat and salinity. Hence they are strongly double-diffusive and quickly release substantial amounts of salt, so that their density decreases and they accelerate. Larger values of $R_{\rho 0}$, on the other hand, correspond to more weakly double-diffusive currents,

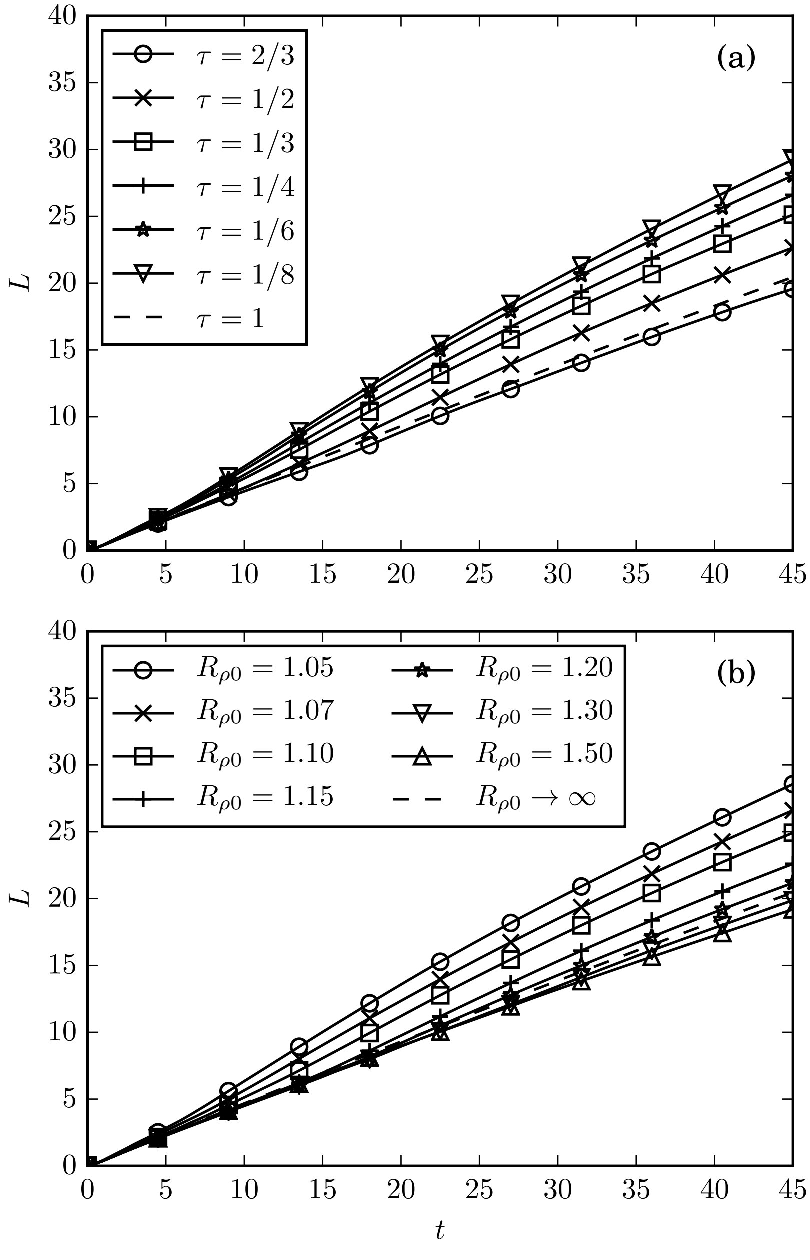

Figure 3.5: Current length *vs.* time for $R_{\rho 0} = 1.07$ with varying τ (a), and for $\tau = 1/4$ with varying $R_{\rho 0}$ (b). Smaller values of τ or $R_{\rho 0}$, i.e., more strongly double-diffusive currents, result in larger front velocities. The single-diffusive case corresponds to $\tau = 1$ in (a), and to $R_{\rho 0} \to \infty$ in (b).

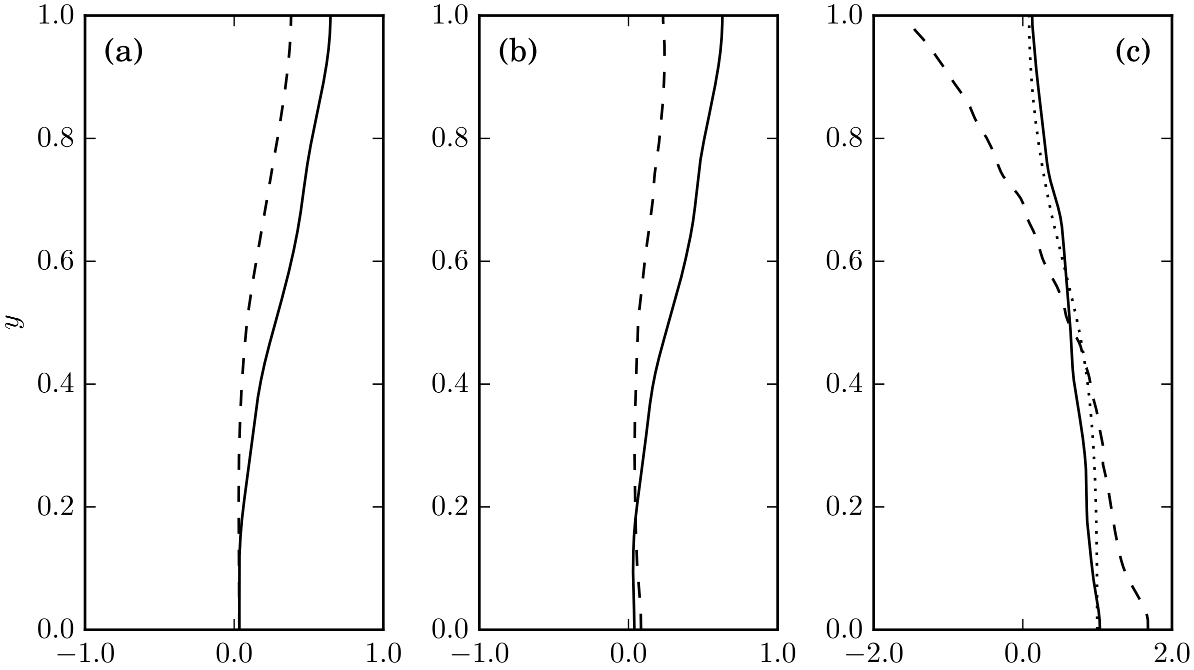

Figure 3.6: Profiles averaged horizontally over the current length for (a) temperature T, (b) salinity S, and (c) density ρ, at time $t = 45$ with $\tau = 2/3$ (solid line), $\tau = 1/8$ (dashed line) and $\tau = 1$ (dotted line). All simulations have the same stability ratio $R_{\rho 0} = 1.07$. Strongly double-diffusive currents lose their salinity more rapidly than their heat, in spite of the lower molecular diffusivity of salinity, so that the density difference driving the current increases.

for which the balance between buoyancy and turbulent drag becomes more complex, as will be discussed in more detail below. The limit $R_{\rho 0} \to \infty$ corresponds to the classical, single-diffusive case.

3.4.2 Current structure: temperature, salinity, density and velocity

In order to provide quantitative evidence for the scenario outlined above, we now discuss the effective temperature and salinity profiles of the current. Towards this end, figures 3.6a and 3.6b display vertical T- and S-profiles averaged in the streamwise direction from the gate position to the location half a channel height behind the current front.

These figures demonstrate that the strongly double-diffusive top curent ($\tau = 1/8$) loses both heat and salt more rapidly than its weakly double-diffusive counterpart ($\tau = 2/3$). In addition, it loses salt more quickly than heat, so that its effective density decreases. This is confirmed by the density profiles displayed in figure 3.6c, which indicate that the dimensionless density of the strongly double-diffusive top current can reach values as low as -1.5 near the upper boundary, far below the left reservoir value of $\rho = 0$. Similarly, the current density near the lower wall significantly exceeds the value $\rho = 1$ in the right reservoir. The weakly double-diffusive current, on the other hand, loses heat and salinity at approximately the same rate, so that its effective density varies from $\rho = 1$ near the bottom wall to $\rho = 0$ near the top wall, similar to the single-diffusive gravity current. This increased buoyancy for the strongly double-diffusive current is consistent with the results shown in figure 3.2, where the strongly double-diffusive gravity current was seen to propagate much faster than its weakly double-diffusive counterpart. However, to fully understand the behavior shown in figure 3.2, we will also have to consider the potentially higher drag acting on the strongly double-diffusive current, as a result of the fingering. We will return to this point further below.

The influence of $R_{\rho 0}$ is consistent with the above arguments. Again, the strongly double-diffusive top current ($R_{\rho 0} = 1.05$) loses both salt and heat much more rapidly than its weakly double-diffusive counterpart ($R_{\rho 0} = 1.50$), cf. figures 3.7a and 3.7b. It also loses salt faster than heat, so that its effective density decreases, as confirmed by the density profiles in figure 3.7c.

For $R_{\rho 0} = 1.07$, figure 3.8 compares the density fields of single-diffusive ($\tau = 1$), weakly double-diffusive ($\tau = 2/3$) and strongly double-diffusive ($\tau = 1/8$) currents. While the reservoir densities are identical for all flow fields, the current densities exhibit very different properties. The density of the single-diffusive current has to fall in between the reservoir densities, which is not true for the double-diffusive currents. The theoretical

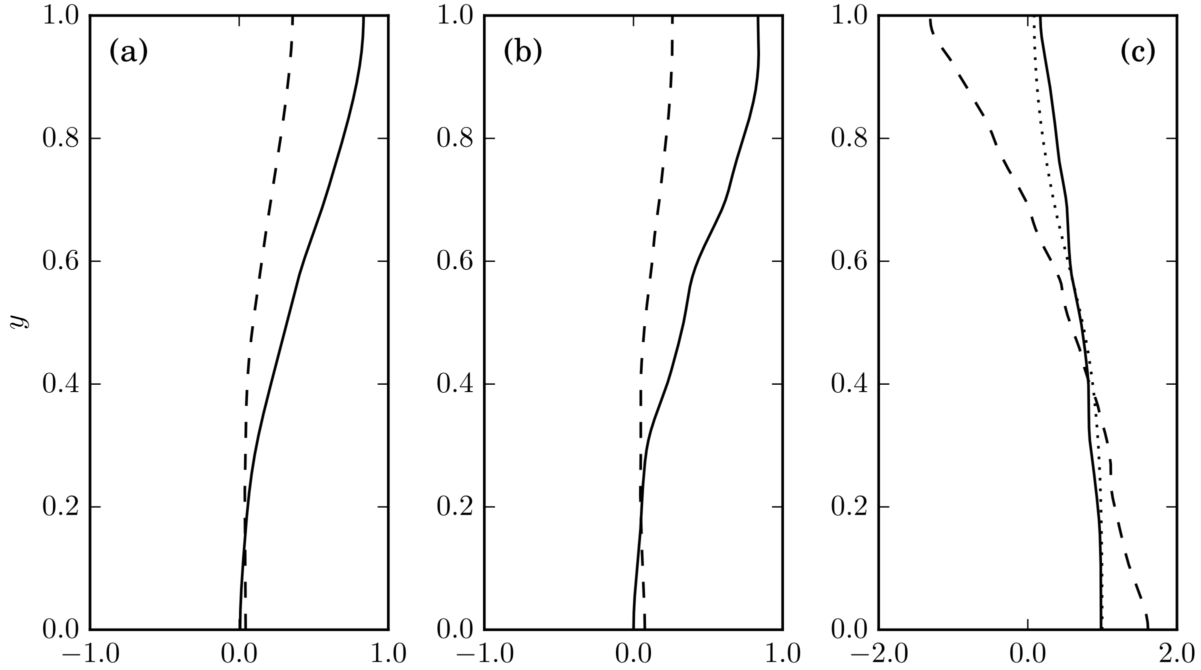

Figure 3.7: Profiles averaged horizontally over the current length for (a) temperature T, (b) salinity S, and (c) density ρ, at time $t = 45$ with $R_{\rho 0} = 1.50$ (solid line), $R_{\rho 0} = 1.05$ (dashed line) and $R_{\rho 0} \to \infty$ (dotted line). All simulations have the same diffusivity ratio $\tau = 1/4$. Again, strongly double-diffusive currents lose their salinity more rapidly than their heat, so that the density difference driving the current increases.

density limits for the light and heavy double-diffusive currents are given by

$$\rho(T=1, S=0) = 1 - \frac{R_{\rho 0}}{R_{\rho 0} - 1} = -14.3 \, , \tag{3.21}$$

$$\rho(T=0, S=1) = 1 + \frac{1}{R_{\rho 0} - 1} = 15.3 \, , \tag{3.22}$$

respectively. For the strongly double-diffusive case $\tau = 1/8$, we notice that the minimum and maximum fluid densities in the entire flow field appear near the upper and lower walls, in the neighborhood of the gate location.

The formation of this pool of high-density fluid along the bottom wall, which is confirmed by figure 3.9, strongly modifies the structure of the flow field. Since this fluid is significantly denser than the fluid in the right reservoir, it tends to spread horizontally

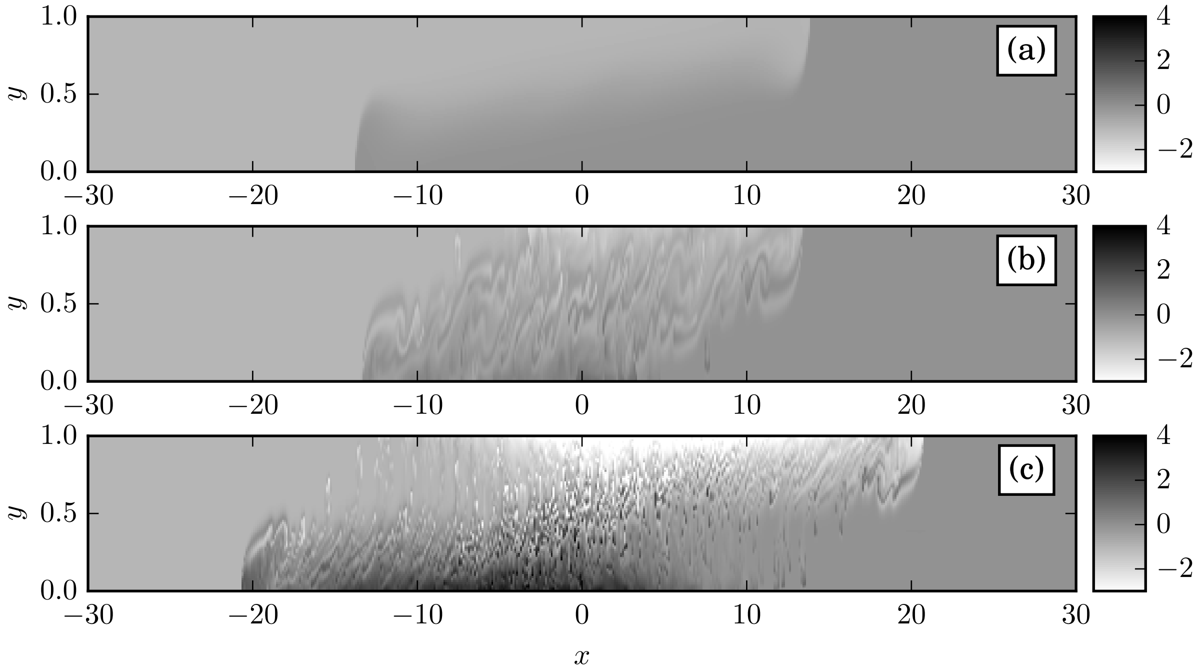

Figure 3.8: Density fields at $t = 30$ for simulations with $R_{\rho 0} = 1.07$ and (a) $\tau = 1$ (single-diffusive), (b) $\tau = 2/3$ (mildly double-diffusive), and (c) $\tau = 1/8$ (strongly double-diffusive). For the single-diffusive flow, the range of possible densities is bracketed by the reservoir values of 0 and 1. Double-diffusive flows, on the other hand, can give rise to local density values outside this range. Strongly double-diffusive flows display a local density maximum (minimum) near the bottom (top) center of the domain.

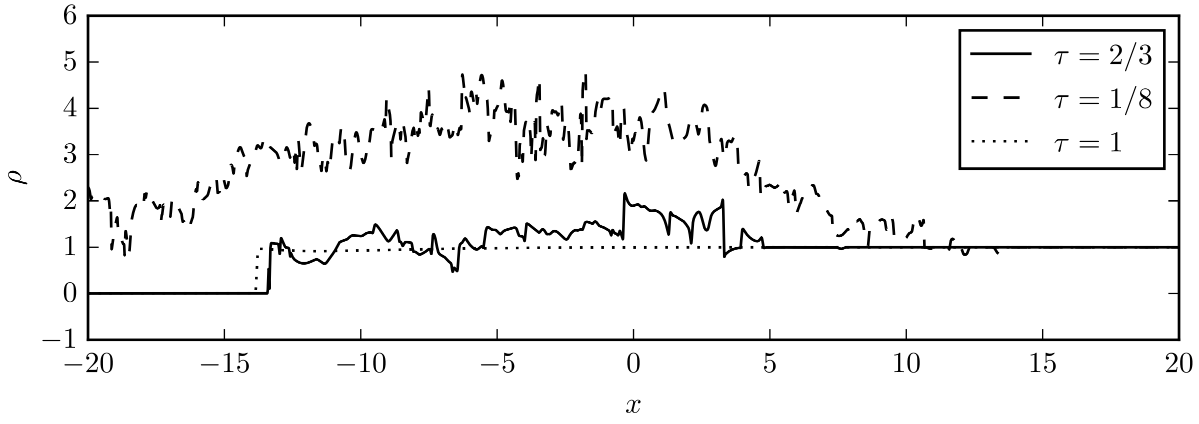

Figure 3.9: Density profiles along the bottom wall for the simulations with $R_{\rho 0} = 1.07$ at $t = 30$. For the single-diffusive current the density values have to fall in between the reservoir values of 0 and 1, respectively, while for the strongly double-diffusive current density values in excess of 4 appear near the gate location at $x = 0$.

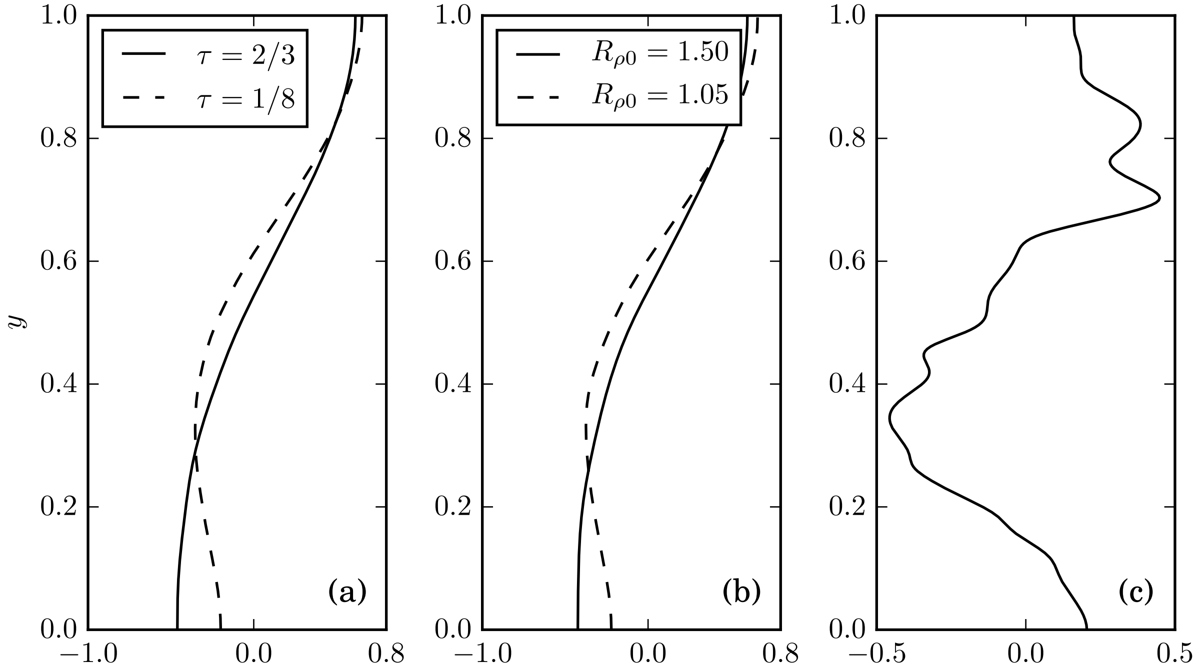

Figure 3.10: Horizontally averaged u-profiles at $t = 45$: (a) for $\tau = 2/3$ and $1/8$, with $R_{\rho 0} = 1.07$, and (b) for $R_{\rho 0} = 1.50$ and 1.05, with $\tau = 1/4$. In each frame, the more strongly double-diffusive current develops a pronounced three-layer structure. Frame (c) shows the u-profile at $x = 3$ for a simulation with $R_{\rho 0} = 1.07$ and $\tau = 1/8$. The right-moving, very dense current next to the bottom wall is clearly visible, while the left-moving current containing fluid from the right reservoir has been deflected upwards, and away from the wall.

along the bottom wall in both directions, and *below* the fluid of the right reservoir. Consequently, it deflects the left-moving current of right reservoir fluid upwards and away from the bottom wall. In this fashion, the flow field to the right of the original gate location acquires an effective three-layer structure, with a right-moving, light current along the top wall made up of warm and increasingly less salty fluid, a left-moving intermediate density current in the center of the channel, and a pool of very dense, cold and salty fluid spreading horizontally along the bottom wall.

This emerging three-layer structure for strongly double-diffusive gravity currents ($\tau = 1/8$) is confirmed by the horizontally averaged u-velocity profiles shown in figure 3.10a. The weakly double-diffusive gravity current ($\tau = 2/3$), on the other hand, exhibits a clear

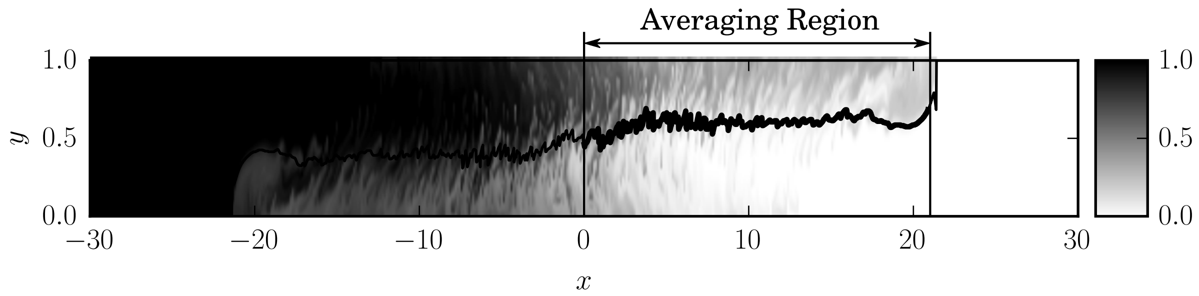

Figure 3.11: Salinity concentration for a current with $R_{\rho 0} = 1.07$ and $\tau = 1/4$, at $t = 35$. The current interface, evaluated as described in the text, is drawn as a solid line. To obtain effective current properties such as temperature, salinity and thickness, we average from the gate location to half a channel height behind the current tip.

two-layer structure, with a light top current moving to the right, and a dense bottom current moving to the left. Again, the influence of the parameter $R_{\rho 0}$ is found to be consistent with these observations, as seen in figure 3.10b. The weakly double-diffusive current for $R_{\rho 0} = 1.50$ displays a two-layer structure, while its strongly double-diffusive counterpart for $R_{\rho 0} = 1.05$ clearly has three distinct layers. The right-moving, dense current along the bottom wall can be clearly recognized in the local velocity profile of figure 3.10c.

3.4.3 Current thickness

We now proceed to analyze the thickness of the buoyant top current. In order to be able to do so, we need to distinguish the current from the ambient. Towards this end, we define the interface location separating the top current from the ambient fluid below as the y-location above which the horizontal volume flux in the positive x-direction reaches a maximum. The condition of zero net horizontal volume flux implies that this y-location also maximizes the horizontal volume flux in the negative x-direction below. For a representative current with $R_{\rho 0} = 1.07$ and $\tau = 1/4$, figure 3.11 shows that the y-position of the interface remains nearly constant over the length of the current. Consequently, we can evaluate an effective top current thickness by averaging the local thickness over the streamwise direction. In order to eliminate artifacts due to the current front, we take this streamwise average from the gate location to the position half a channel height behind the current front. We furthermore remark that, due to the initial transient flow evolution, a meaningful current thickness can be identified only after $t \approx 5$.

Figure 3.12a displays the current thickness as a function of time for $R_{\rho 0} = 1.07$ and various values of τ. During the acceleration phase until $t \approx 15 - 20$, the current thickness decreases slightly, whereas subsequently it shows a mild increase as the current decelerates. While weakly double-diffusive currents have a thickness similar to that of single-diffusive currents, more strongly double-diffusive currents are seen to be increasingly thinner, as a result of the transition from a two-layer to a three-layer structure of the flow field, as described above. This trend is observed both for lower values of τ (figure 3.12a) and for lower values of $R_{\rho 0}$ (figure 3.12b). We remark that the double-diffusive fingering also strongly affects the dissipation associated with the current.

It would be desirable to develop simplified, conceptual models in the spirit of Benjamin [7] and/or Borden & Meiburg [1] for predicting the velocity of double-diffusive currents as a function of their height. However, it is not obvious how those earlier models of steady, conservative currents could be extended to non-conservative, double-diffusive currents whose effective heat and salinity vary with time.

3.4.4 Temperature and salinity difference between the current and the ambient

We obtain the effective temperature and salinity of the buoyant top current by averaging over the area of the current, i.e., over the area above the interface from the gate location to the position half a channel height behind the tip. In order to quantify the

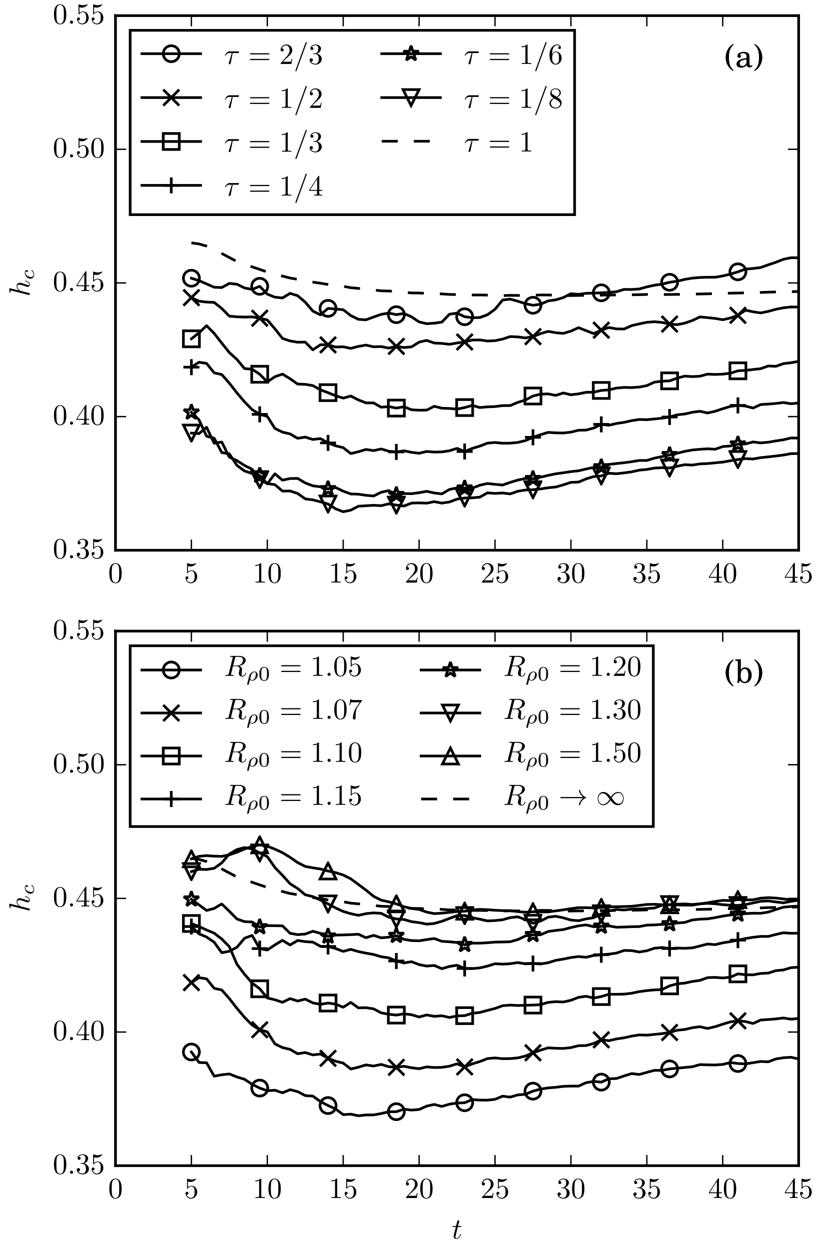

Figure 3.12: Current thickness *vs.* time for $R_{\rho 0} = 1.07$ with varying τ (a), and for $\tau = 1/4$ with varying $R_{\rho 0}$ (b). Smaller values of τ or $R_{\rho 0}$, i.e. stronger double-diffusion, lead to thinner currents. The single-diffusive case corresponds to $\tau = 1$ or $R_{\rho 0} \to \infty$.

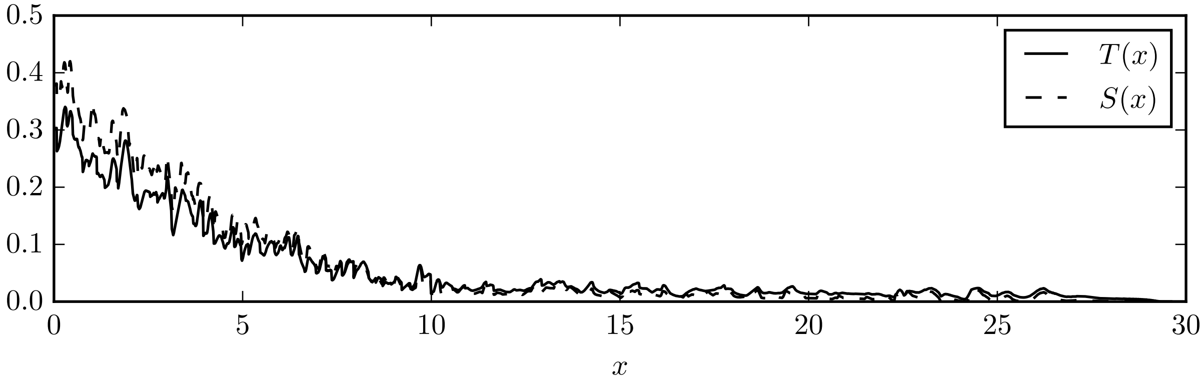

Figure 3.13: Vertically averged temperature and salinity in the ambient as a function of x, for a current with $R_{\rho 0} = 1.07$ and $\tau = 1/8$ at $t = 45$. Over much of the length of the current, T and S in the ambient are close to zero.

temperature and salinity differences ΔT and ΔS between the current and the ambient, we need to identify representative values for the temperature and salinity of the ambient. Towards this end, figure 3.13 shows the temperature and salinity, vertically averaged over the region below the interface, as functions of the streamwise x-location for a representative flow. While the ambient has acquired significant amounts of heat and salinity near the gate location, its temperature and salinity values are close to zero over much of the length of the top current. For this reason, we assume the effective temperature and salinity values of the ambient to be zero, so that the ΔT- and ΔS-values between current and ambient are taken to be equal to the temperature and salinity of the current itself.

Figure 3.14 shows the resulting, ensemble averaged results for $\Delta T(t)$ and $\Delta S(t)$, for the weakly double-diffusive current with $R_{\rho 0} = 1.50$ and $\tau = 1/4$. These indicate that the temperature difference between the current and the ambient decays faster than the salinity difference, i.e., the weakly double-diffusive current loses heat more rapidly than salt. To identify the reasons for this behavior, we evaluate the diffusive and convective fluxes of heat and salinity out of the current into the ambient according to

$$F_{q,conv}(t) = -\frac{1}{L(t) - 0.5} \int_0^{L(t)-0.5} vq \, \mathrm{d}x \ , \tag{3.23}$$

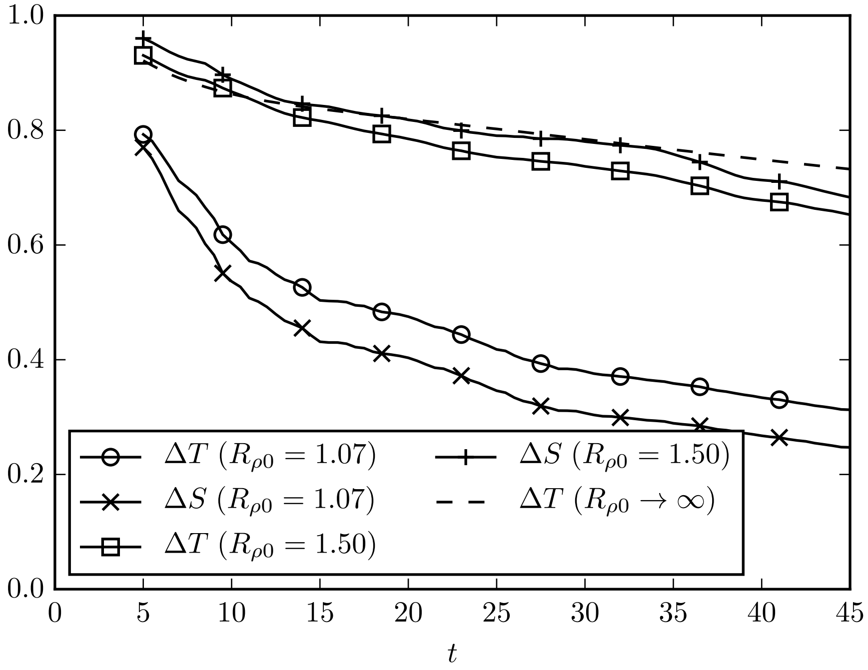

Figure 3.14: Current temperature and salinity *vs.* time for a weakly double-diffusive current with $R_{\rho 0} = 1.50$ and $\tau = 1/4$, and for a strongly double-diffusive current with $R_{\rho 0} = 1.07$ and $\tau = 1/4$. The weakly double-diffusive current is seen to lose heat faster than salinity, which reflects the larger molecular diffusivity of heat, as compared to salt. The strongly double-diffusive current, on the other hand, loses salinity more rapidly than heat, as a result of the stronger turbulent diffusivity of salt, as compared to heat.

$$F_{q,diff}(t) = \frac{1}{Pe_q(L(t) - 0.5)} \int_0^{L(t)-0.5} \frac{\partial q}{\partial y} \, \mathrm{d}x \ , \qquad (3.24)$$

where q represents T or S, and the integrals are evaluated along an effective interface y-location, which is taken as the actual y-location of the interface averaged over the length of the current and from $t = 5$ to $t = 45$. Figure 3.15a demonstrates that for the weakly double-diffusive current with $R_{\rho 0} = 1.50$ and $\tau = 1/4$ the diffusive outflow of heat outweighs the diffusive outflow of salt for all times, as a result of the higher molecular diffusivity of heat as compared to salt. On the other hand, the convective fluxes of heat and salinity are nearly identical for early times, and mostly due to coherent vortical structures such as Kelvin-Hemlholtz vortices, rather than double-diffusive fingering. At late times, fingering causes the convective outflow of salt to outweigh that of heat, and the combined diffusive and convective fluxes of heat and salt are nearly the same.

A very different picture emerges for the strongly double-diffusive current with $R_{\rho 0} = 1.07$ and $\tau = 1/4$, also shown in figure 3.14. In contrast to the weakly double-diffusive current the salinity difference now decays faster than the temperature difference, indicating that the current loses salt more rapidly than heat, in spite of the larger molecular diffusvity of heat. The reason for this becomes clear when we analyze the convective and diffusive fluxes of heat and salt out of the current, cf. figure 3.15b. As expected, the diffusive outflow of heat from the current is larger than that of salt, due to the larger molecular diffusivity. However, this effect is outweighed by the larger convective outflow of salt, due to strong double-diffusive fingering. Hence, the effective turbulent diffusivity of salt is larger than that of heat, in spite of its molecular diffusivity being smaller.

Figure 3.16 shows ensemble averaged results for $\Delta T(t)$ as function of τ and $R_{\rho 0}$, respectively. Corresponding plots of $\Delta S(t)$ exhibit the same qualitative behavior. Both parts of figure 3.16 indicate that $\Delta T(t)$ decreases more quickly as the strength of the double-diffusive fingering increases. In the limit of $\tau \to 0$, $\Delta T(t)$ reaches an asymptotic limit. This reflects the fact that the effective diffusivity of heat depends on its molecular diffusivity as well as on the strength of the fingering, with the latter reaching an asymptotic limit as the molecular diffusivity of salt approaches zero, cf. also the analysis by Burns & Meiburg [36]. It is not immediately clear if a similar limit exists for $R_{\rho 0} \to 1$. We conclude that the presence of double-diffusive fingering strongly affects the temporal decay of temperature and salinity in the current, and thus the current's driving force.

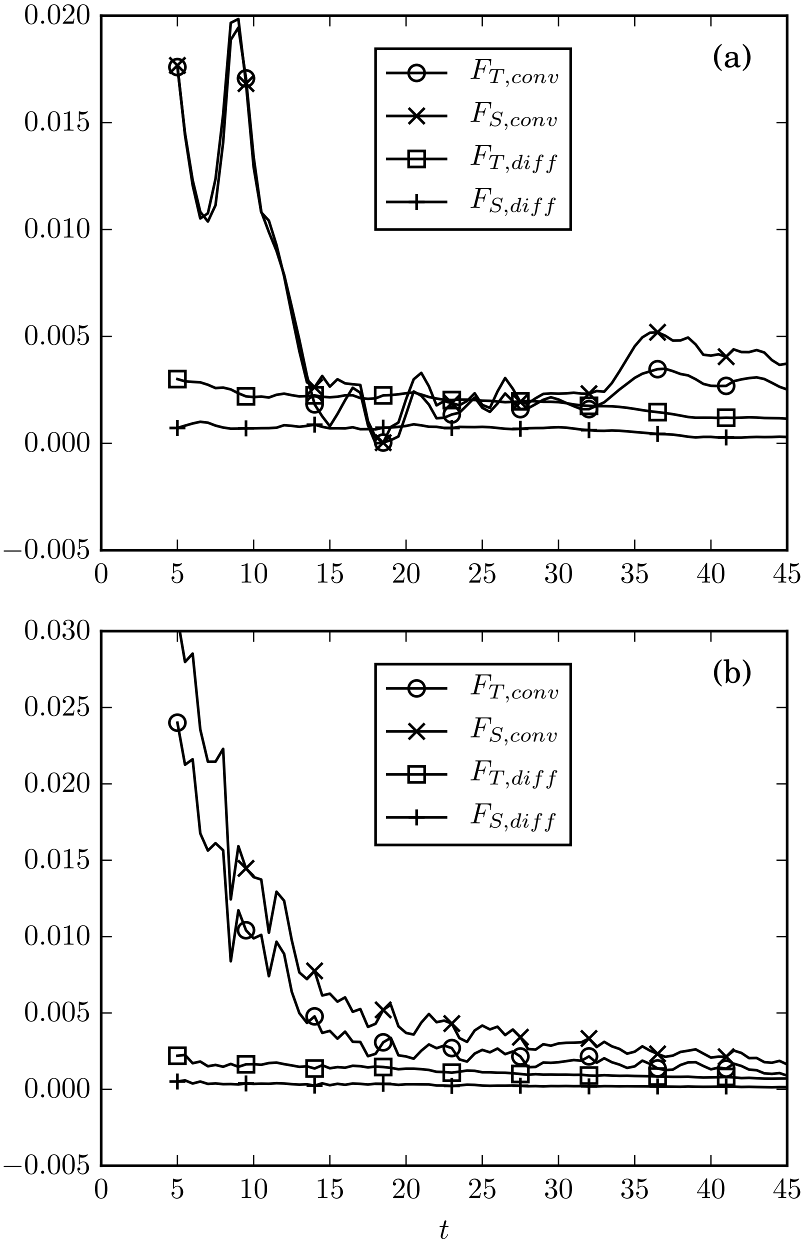

Figure 3.15: Diffusive and convective heat and salinity fluxes out of the top current, averaged from $x = 0$ to $x = x_{tip} - 0.5$ for (a) a weakly double-diffusive current with $\tau = 1/4$ and $R_{\rho 0} = 1.50$, and (b) a strongly double-diffusive current with $\tau = 1/4$ and $R_{\rho 0} = 1.07$. For both currents, the diffusive outflow of heat is larger than that of salinity. However, for the strongly double-diffusive current this effect is outweighed by the larger convective outflow of salt as compared to heat.

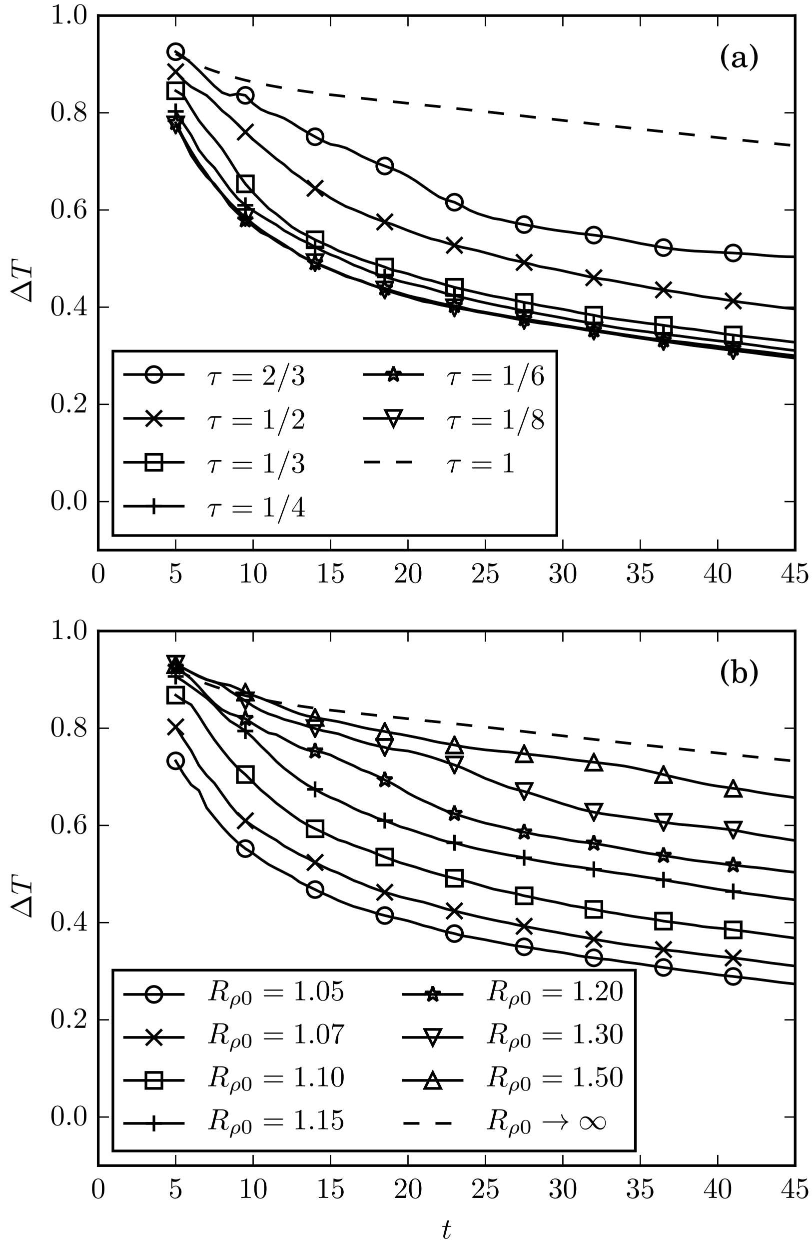

Figure 3.16: ΔT *vs.* time for (a) $R_{\rho 0} = 1.07$ with varying τ, and (b) varying $R_{\rho 0}$ with $\tau = 1/4$. The diffusivity of heat is the same in all simulations. Lower values of τ or $R_{\rho 0}$ give rise to more intense double-diffusive fingering, which causes ΔT to decay more rapidly. The single-diffusive case corresponds to $\tau = 1$ or $R_{\rho 0} \to \infty$.

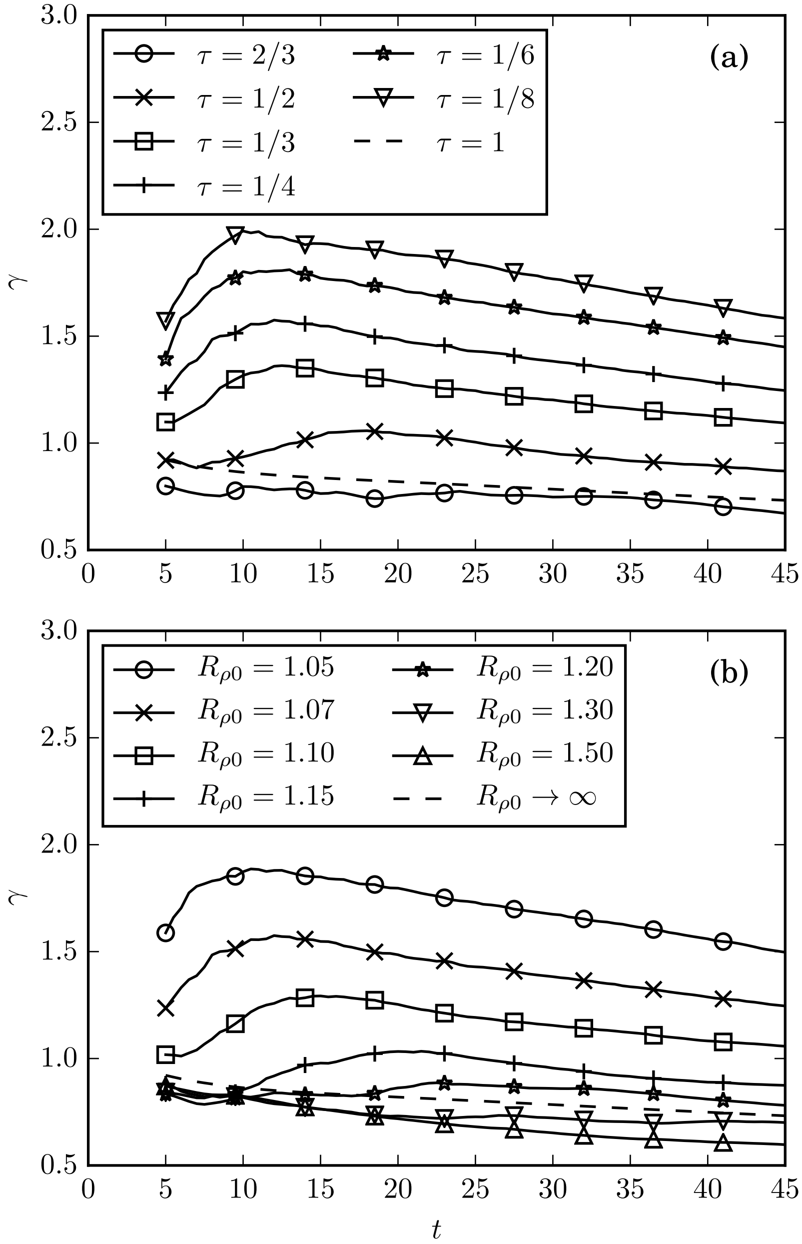

Figure 3.17: Density difference γ *vs.* time for (a) $R_{\rho 0} = 1.07$ and varying τ, and (b) varying $R_{\rho 0}$ with $\tau = 1/4$. For strongly double-diffusive currents, the density difference can climb to twice the value of the reservoir fluids.

3.4.5 Effective buoyancy

We can now employ (3.15) to calculate the effective density of the buoyant current, based on the results for ΔT and ΔS from section 3.4.4. Figure 3.17a indicates that, for constant $R_{\rho 0}$ and varying τ, weakly double-diffusive currents are slightly less buoyant than single-diffusive currents. This is consistent with our earlier observation that they lose heat more rapidly than salt as a result of molecular diffusion, cf. figure 3.14. On the other hand strongly double-diffusive currents are significantly more buoyant than single-diffusive currents, since fingering causes them to lose salt much more rapidly than heat, as was also seen in figure 3.14. These findings are also consistent with our earlier observation that weakly double-diffusive currents propagate slightly more slowly than single-diffusive currents, whereas strongly double-diffusive currents advance much more rapidly. The results shown in figure 3.17b for varying $R_{\rho 0}$ and constant τ confirm this scenario.

3.4.6 Energy budget

As shown in appendix C, the mechanical energy balance for a Boussinesq flow can be written as

$$K + E_p + W_c + W_d = \text{const.} \tag{3.25}$$

Here the kinetic energy K is defined as

$$K = \int \frac{u_i^2}{2} \mathrm{d}A \ , \tag{3.26}$$

while the gravitational potential energy E_p has the form

$$E_p = \int \rho x_2 \mathrm{d}A \ , \tag{3.27}$$

and the energy lost to viscous dissipation is obtained as

$$W_d = \frac{1}{Re} \int_0^t \int (\partial_j u_i)(\partial_j u_i) \, \mathrm{d}A\mathrm{d}t \ . \tag{3.28}$$

The term

$$W_c = -\int_0^t \int x_2 \frac{\mathrm{D}\rho}{\mathrm{D}t} \mathrm{d}A\mathrm{d}t \tag{3.29}$$

deserves some extra discussion, as it reflects the ways in which the diffusion of heat and salt affect the energy budget. Absent such diffusion, in an incompressible flow field each fluid particle maintains its density, so that $W_c = 0$. The way in which the diffusion of heat and salt influence the flow field via W_c can be understood by exploring their role under simplified conditions. Imagine a stably stratified configuration of fluid at rest, consisting of a layer of warm fluid above a layer of colder fluid. In the absence of any initial perturbations, the fluid will stay at rest for all times, and the only transport that occurs is the downward diffusion of heat. This downward diffusion of heat implies that the density of fluid particles in the upper (lower) layer increases (decreases), giving a negative value of W_c. In the energy equation (3.25), the negative W_c is balanced by a positive change of E_p, corresponding to an increase in potential energy. Winters *et al.*[42] interpret W_c in terms of the conversion of internal energy into potential energy via irreversible molecular processes, while Tailleux [43] discusses W_c in terms of the Boussinesq limit of the work performed due to fluid compression.

Now consider a stably stratified configuration consisting of a layer of warm, salty, lighter fluid above a layer of cold, fresh, denser fluid. In the absence of fluid motion, the only transport is the downward diffusion of heat and salt. As we saw above, the downward diffusion of heat gives a negative value of W_c. On the other hand, the downward diffusion of salt reduces (increases) the density of the upper (lower) layer, thereby resulting in a

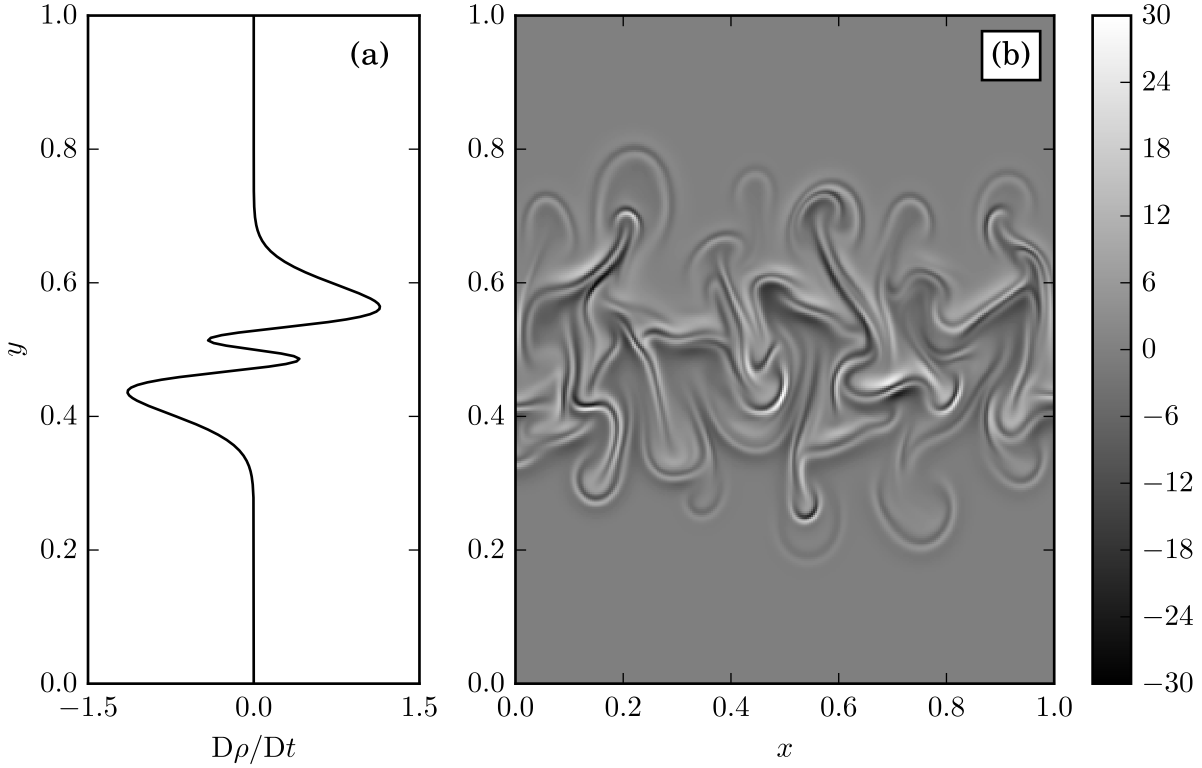

Figure 3.18: Material density derivative $D\rho/Dt$ for hot, salty, light fluid above cold, fresh, dense fluid. (a) molecular diffusion only, (b) with double-diffusive fingering. In each case, a pronounced four-layer pattern is observed along the interface.

positive value of W_c. However, due to the larger molecular diffusivity of heat as compared to salt, the material density derivative due to the diffusion of heat outweighs that due to the diffusion of salinity, so that we expect the net effect of molecular diffusion to result in negative W_c values. This is confirmed by figure 3.18a, which shows a pronounced four-layer structure for $D\rho/Dt$ at the interface. Figure 3.18b indicates that even in the presence of strong double-diffusive fingering, this four-layer structure of the material density derivative along the interface is maintained.

In order to clarify the effect of vertical convective transport on W_c, let us inspect the integral in (3.29) more closely. In a closed system such as the present one, the integral over $\mathrm{D}\rho/\mathrm{D}t$ vanishes. Now imagine a downward moving finger carrying hot and salty fluid. As this fluid loses heat to its environment, it becomes increasingly denser, resulting in positive values of $\mathrm{D}\rho/\mathrm{D}t$. At the same time, however, neighboring fluid elements that absorb the heat released by the finger will see their density decrease. Conversely, upward moving fingers become increasingly lighter as they absorb heat, leading to negative values of $\mathrm{D}\rho/\mathrm{D}t$, while the surrounding fluid becomes denser. For hot and salty fluid at rest above cold and fresh fluid, figure 3.18a demonstrates that the four-layer structure results in W_c being negative. Since figure 3.18b shows that this four-layer structure is maintained for double-diffusive fingering, we expect W_c to remain negative even in the presence of flow. This is confirmed by figure 3.19, which shows the temporal evolution of all terms in (3.25) for a weakly and a strongly double-diffusive simulation, respectively, along with their sum. Here, all terms are scaled by the potential energy difference between the initial state and a hypothetical final state in which the upper half of the domain contains the lighter, hot and salty fluid, whereas the denser, cold and fresh fluid is located in the lower half. This limiting state would be reached for long times in the absence of any molecular diffusion of heat and salt. We refer to this energy difference as the 'initially available potential energy' APE_0. We observe that the sum of all energy components is preserved with very good accuracy for both flows.

For the weakly double-diffusive current in figure 3.19a, we find that about 40% of APE_0 is lost in the course of the simulation, and an approximately equal amount of kinetic energy is generated. An amount equivalent to about 60% of APE_0 is dissipated by viscous forces, and roughly the same amount of mechanical energy is introduced into the flow field via the term W_c.

A qualitatively different picture emerges for the strongly double-diffusive current in figure 3.19b. Here the amount of lost potential energy far exceeds APE_0, which indicates that the buoyant, hot and salty current must have released some of the potential energy stored in the salinity field. In this context, it is useful to realize that the potential energy difference between the initial state and the theoretical limit of a layer of hot, fresh

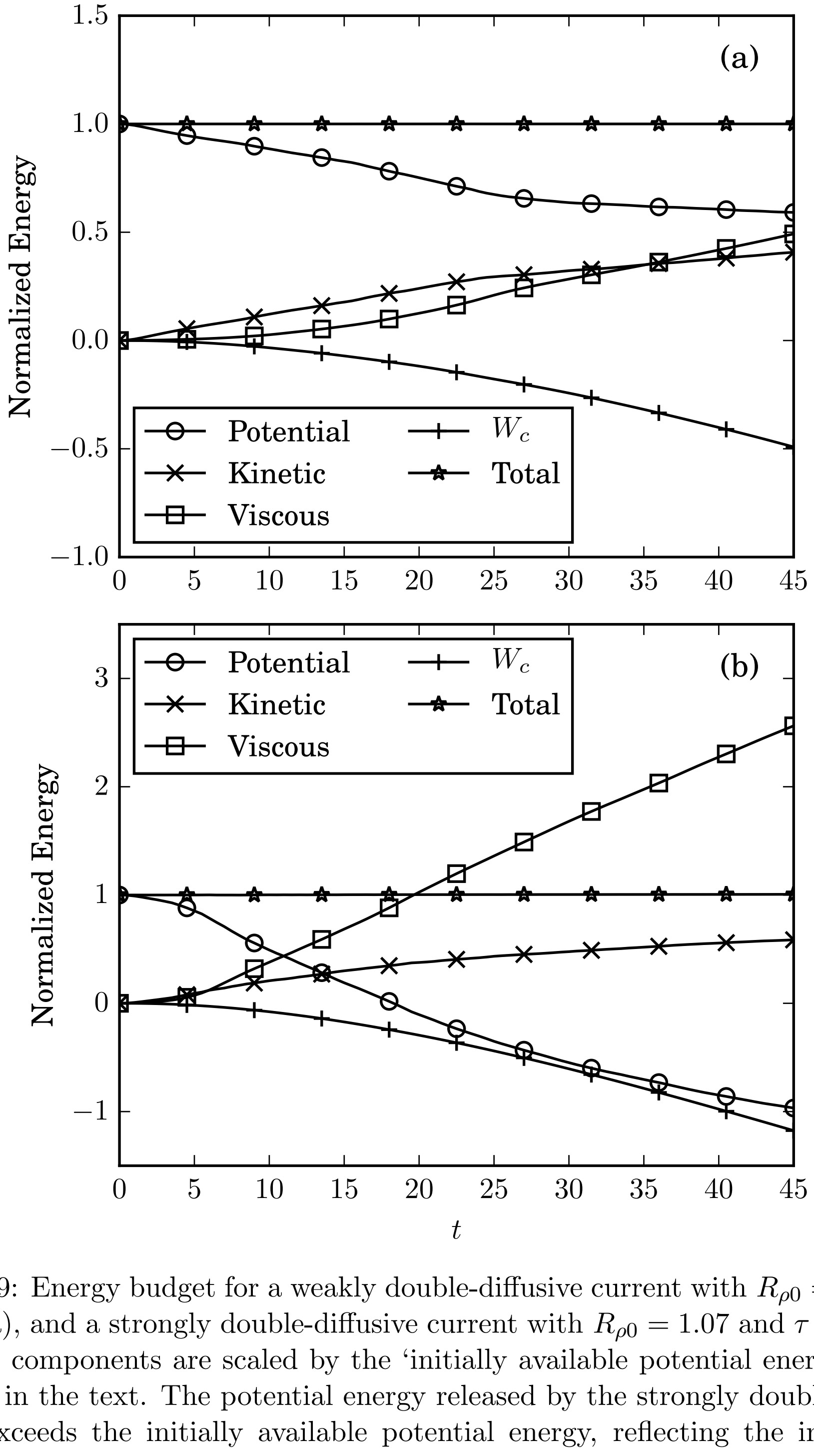

Figure 3.19: Energy budget for a weakly double-diffusive current with $R_{\rho 0} = 1.07$ and $\tau = 2/3$ (a), and a strongly double-diffusive current with $R_{\rho 0} = 1.07$ and $\tau = 1/8$ (b). All energy components are scaled by the 'initially available potential energy' APE_0, as defined in the text. The potential energy released by the strongly double-diffusive flow far exceeds the initially available potential energy, reflecting the influence of double-diffusive fingering.

water above cold, salty water is $\frac{R_{\rho 0}+1}{R_{\rho 0}-1}$ times APE_0. The amount of mechanical energy introduced into the flow by W_c also exceeds APE_0. By the end of the simulation, nearly three times APE_0 has been dissipated.

Figure 3.20a shows a comparison of the time evolution of gravitational potential energy for $\tau = 2/3$ and various $R_{\rho 0}$. As explained earlier in section 3.4.4, for strong double-diffusive fingering the convective downward flux of salinity outweighs that of heat, resulting in a larger release of potential energy. Consequently, the current becomes lighter and propagates faster. As $R_{\rho 0}$ increases, the dynamics of the current is governed by two competing effects. The intensity of the fingering decreases, which slows down the rate at which the potential energy of the salt is released. The fingering becomes very weak at $R_{\rho 0} = 1.20$ and nonexistent at $R_{\rho 0} = 1.30$, so that the potential energy budget becomes dominated by diffusion. The current now loses its heat faster than its salinity, so that it retains more of its potential energy than a single-diffusive current, and it propagates more slowly. As $R_{\rho 0}$ increases further, the density contribution of the salinity decreases as compared to that of heat, and the current propagates faster again. Eventually, for large values of $R_{\rho 0}$ its behavior approaches that of a single-diffusive current.This observation is consistent with figure 3.5b, which showed that the current is slowest for intermediate values of $R_{\rho 0}$.

Figure 3.20b shows the corresponding graph for $\tau = 1/8$, where all of the currents exhibit strong fingering. In this case, changing $R_{\rho 0}$ changes the release of gravitational potential energy in a monotonic way because the effect from fingering is always stronger than bulk diffusion. It is interesting to note that the presence of double diffusive fingering enables more potential energy to be released than a single diffusive current would have theoretically available. This is because some potential energy in the salinity field can be released in addition to the release of potential energy in the temperature field due to the motion of the current.

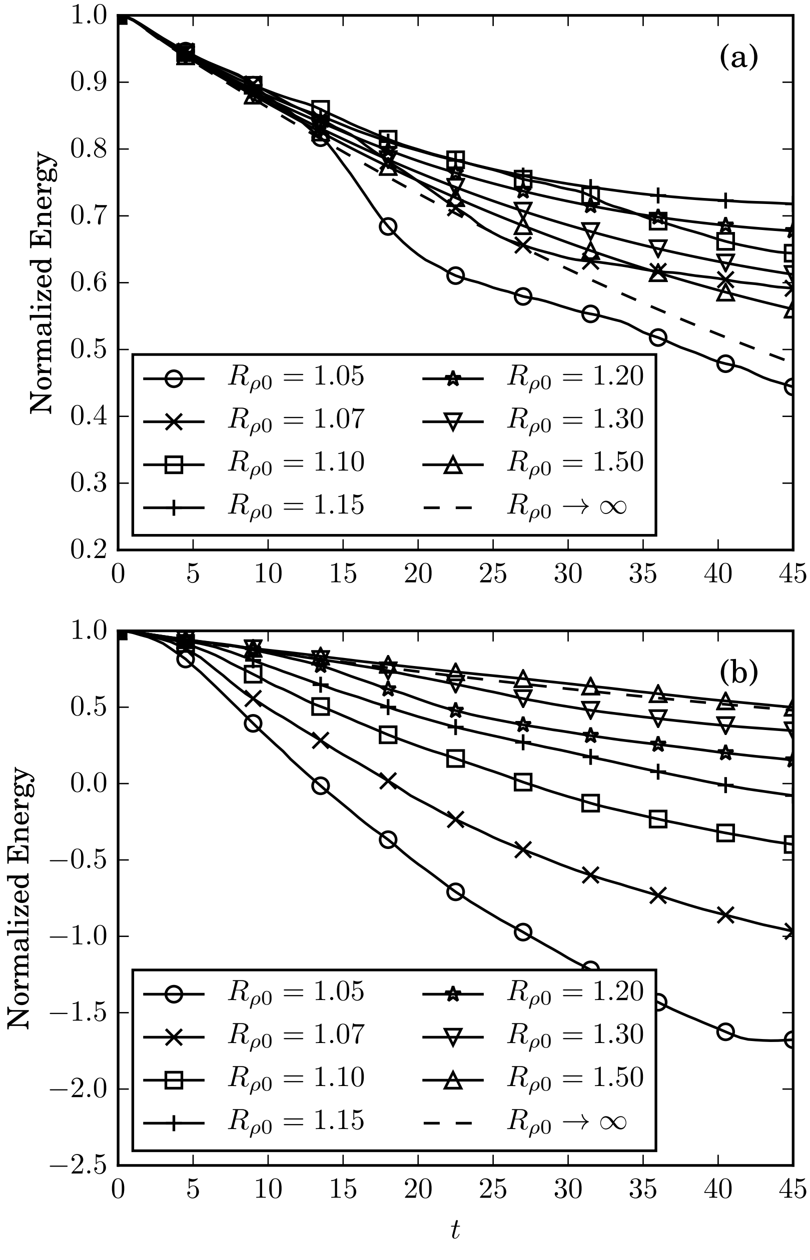

Figure 3.20: Potential energy *vs.* time for $\tau = 2/3$ (a), and $\tau = 1/8$ (b). In (a), when $R_{\rho 0}$ is low enough to cause significant fingering, the fingering works to separate T and S, resulting in the release of more potential energy. When $R_{\rho 0}$ is too high for fingering, further increases in $R_{\rho 0}$ result in more potential energy being released because the salinity remaining in the current will contribute less to the density of the current and the current will spread faster. In (b), fingering is always strong, so decreasing $R_{\rho 0}$ results in the release of more potential energy.

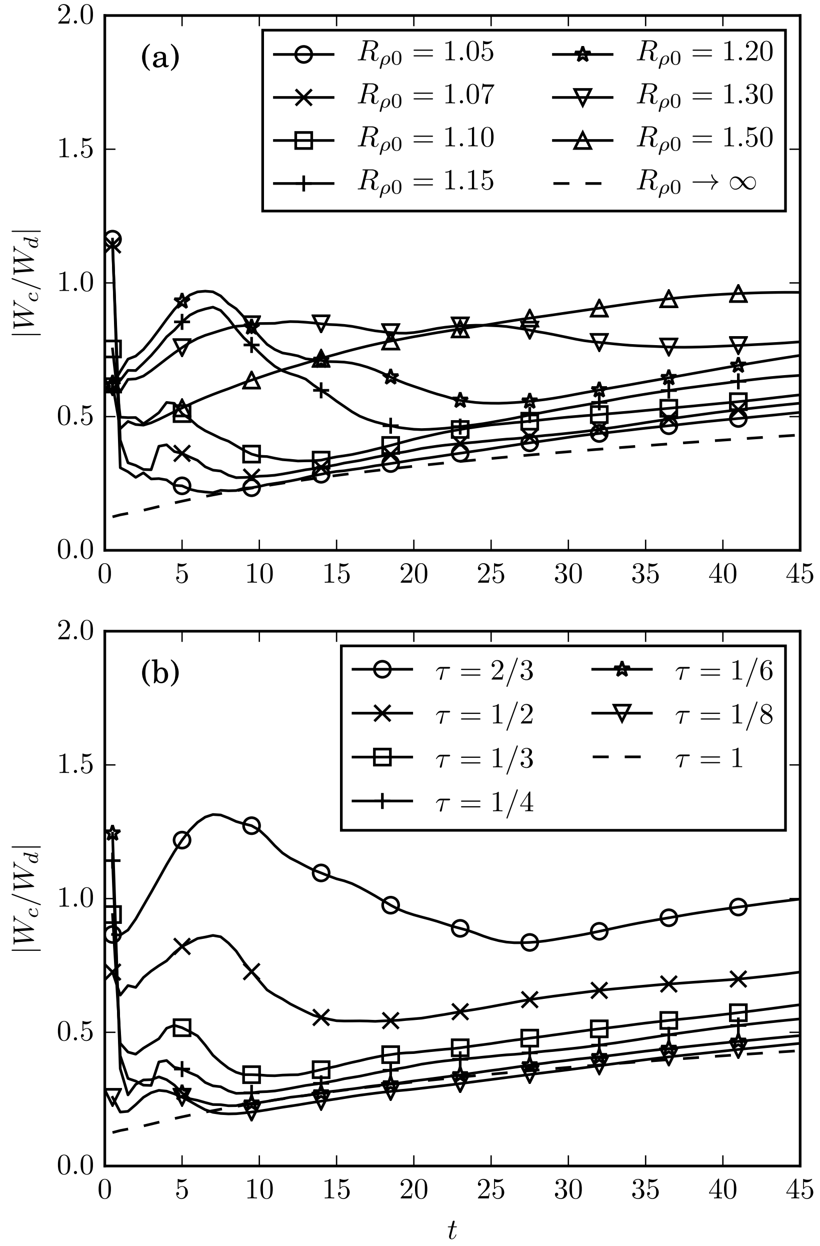

Figure 3.21: The ratio of W_c/W_d *vs.* time for (a) $R_{\rho 0} = 1.07$ with varying τ, and (b) varying $R_{\rho 0}$ with $\tau = 1/4$. Strongly double-diffusive currents give rise to about the same ratio as single-diffusive currents, whereas weakly double-diffusive currents are characterized by a larger ratio.

While double-diffusive currents generate more dissipation than their single-diffusive counterparts, i.e., they transfer more kinetic energy into internal energy, they also give rise to larger W_c, so that they transfer more internal energy to potential energy. The magnitude of $|W_c/W_d|$ provides insight into whether there is a net gain or loss of internal energy. Figure 3.21 displays this ratio for the usual parameter combinations. It is seen to be less than one for most currents, although for the weakly diffusive current with $R_{\rho 0} = 1.07$ and $\tau = 2/3$ it exceeds this value for some period of time. Here it is important to keep in mind that not all of W_c is necessarily converted into available potential energy. In the simple case of static cold fluid underneath warm fluid, heat diffuses downward, thereby increasing the potential energy. At the same time there is no dissipation, so that $|W_c/W_d|$ becomes infinite. The system remains in a state of minimum potential energy, and no potential energy is available for conversion into kinetic energy. Most interestingly, figure 3.21 indicates that the ratio $|W_c/W_d|$ is about the same for single-diffusive currents as for strongly double-diffusive currents, which suggests that strong fingering increases W_c and W_d by proportional amounts.

3.4.7 Stability ratio

From the instantaneous temperature and salinity values of the current, we can calculate its effective stability ratio R_ρ as a function of time. The ensemble-averaged results for R_ρ shown in figure 3.22 are consistent with the earlier discussion in section 3.4.4. Strong double-diffusive fingering releases salt from the current more rapidly than heat, so that the stability ratio increases with time. However, this growth of R_ρ tends to slow down over time since, as R_ρ increases, the intensity of the double diffusive fingering decreases. Conversely, in the absence of double-diffusive fingering, the current loses heat faster than salt, so that R_ρ decreases with time. This is the case initally for $\tau = 1/4$

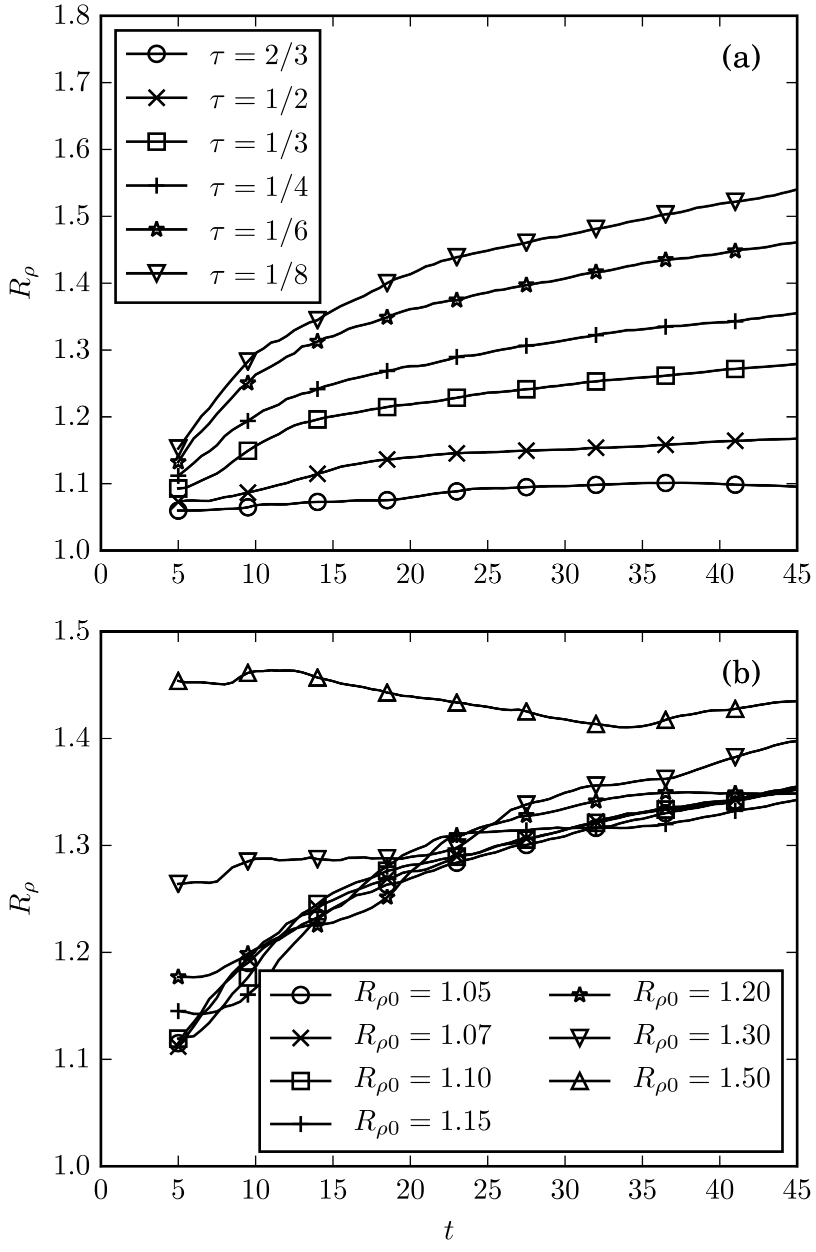

Figure 3.22: Stability ratio R_ρ *vs.* time for (a) $R_{\rho 0} = 1.07$ with varying τ, and (b) varying $R_{\rho 0}$ with $\tau = 1/4$. Note that for $\tau = 1/4$, the stability ratio for all currents approaches 1.4 for long times, independent of the initial stability ratio $R_{\rho 0}$. On the other hand, for $R_{\rho 0} = 1.07$, different values of τ result in different R_ρ-values for long times.

and $R_{\rho 0} = 1.50$. This decrease in R_ρ tends to promote double-diffusive fingering, which in turn will slow down any further decrease of R_ρ. As a result of these counterbalancing effects, we find that for $\tau = 1/4$ all currents approach a stability ratio near 1.4 for long times, independent of their initial stability ratio. In figure 3.22a, different values of τ lead to different long term balances for the same $R_{\rho 0}$. Changing the value of τ modifies the strength of the effects of fingering and diffusion, which dictate the long term balance, while changing $R_{\rho 0}$ merely alters the initial condition. This effect applies not only in time, but also spatially, as fluid near the current front has had more time to adjust the local R_ρ to reflect a balance of fingering and diffusive fluxes.

3.4.8 Vertical velocity

In order to quantify the fingering intensity and the turbulent drag acting on the current, we evaluate the average magnitude V of the vertical velocity along the interface from the gate location to 0.5 dimensionless units behind the current tip

$$V(t) = \frac{1}{N} \sum_{x_i=0}^{x_i \leq \text{tip}-0.5} |v(x_i, \text{interface}(x_i), t)| \tag{3.30}$$

where N indicates the number of grid points included in the summation. Figure 3.23 shows representative, ensemble-averaged results for V as a function of time.

For early times, parameter combinations giving rise to strong double-diffusive fingering result in larger values of V. As either $R_{\rho 0}$ or τ is held constant and the value of the other parameter is decreased to produce more intense fingering, $V(t)$ approaches an asymptotic relation. For constant $R_{\rho 0}$, this suggests that as τ is decreased, $R_\rho(t)$ increases in such a way that the overall fingering intensity remains about the same, which is consistent with figure 3.22a. For constant τ, the existence of the asymptote reflects the fact that $R_\rho(t)$ approaches a constant value for all initial $R_{\rho 0}$, as had been seen in

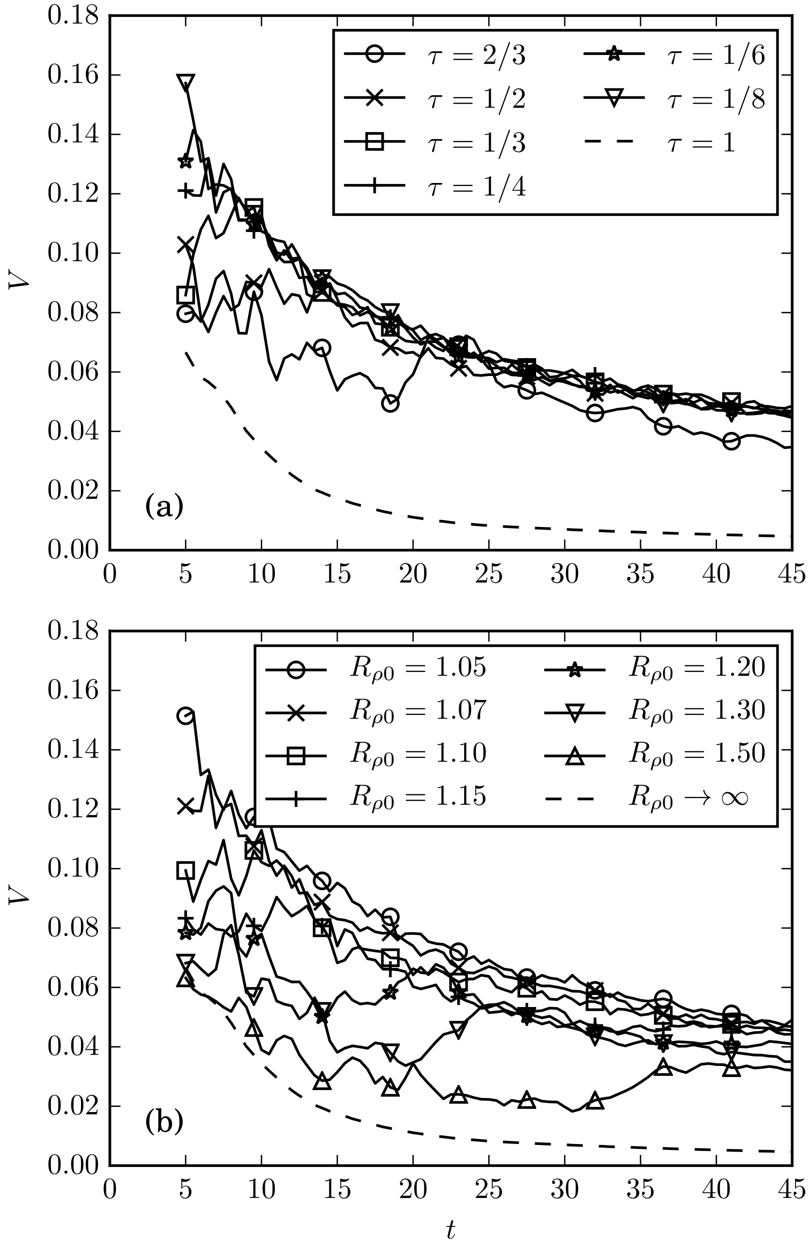

Figure 3.23: Average vertical velocity magnitude V *vs.* time for (a) $R_{\rho 0} = 1.07$ with varying τ, and (b) varying $R_{\rho 0}$ with $\tau = 1/4$. Lower τ- or $R_{\rho 0}$-values (more intense double-diffusive fingering) initially produce larger vertical velocities, whereas for long times the velocity magnitude depends only weakly on $R_{\rho 0}$ and τ.

figure 3.22b. For long times $V(t)$ decays for all currents, in line with the observations in section 3.4.7.

We remark that vertical velocities along the interface can be generated not only by double-diffusive fingering, but also as a result of the local thickening of the current behind the tip, as well as due to Kelvin-Helmholtz instabilities. For this reason even the single-diffusive current in figure 3.23a displays non-zero values of V, although for all but the smallest times these are much lower than those due to double-diffusive fingering.

3.4.9 Late-stage dynamics

Currents with sufficiently strong fingering to yield the three-layer structure described in section 3.4.2 exhibit long-term dynamics fundamentally different from the early stages. We will now discuss this for the representative case of $R_{\rho 0} = 1.05$ and $\tau = 1/8$ shown in figures 3.24 and 3.25. We conducted a single large simulation with these parameters in an extended domain $x \in [-120, 120]$. The streamline pattern indicates that already at $t = 25$ the pools of hot fresh fluid at the center of the top wall, and cold salty fluid near the center of the bottom wall have gained enough strength to deflect the original gravity current pattern, thereby resulting in the three-layer structure discussed above. However, the overall dynamics of the flow at this time is still governed by the right-moving top current and the left-moving bottom current.

By time $t = 75$, these localized pools along the top and bottom walls have become sufficiently strong to dominate the dynamics in the central region $-20 \leq x \leq 20$. Due to their strong density difference relative to the surrounding fluid, these pools tend to spread horizontally along their respective walls and give rise to new density fronts that propagate in the direction opposite to the original currents, so that a secondary, left-propagating top current emerges, along with secondary, right-propagating current along the bottom

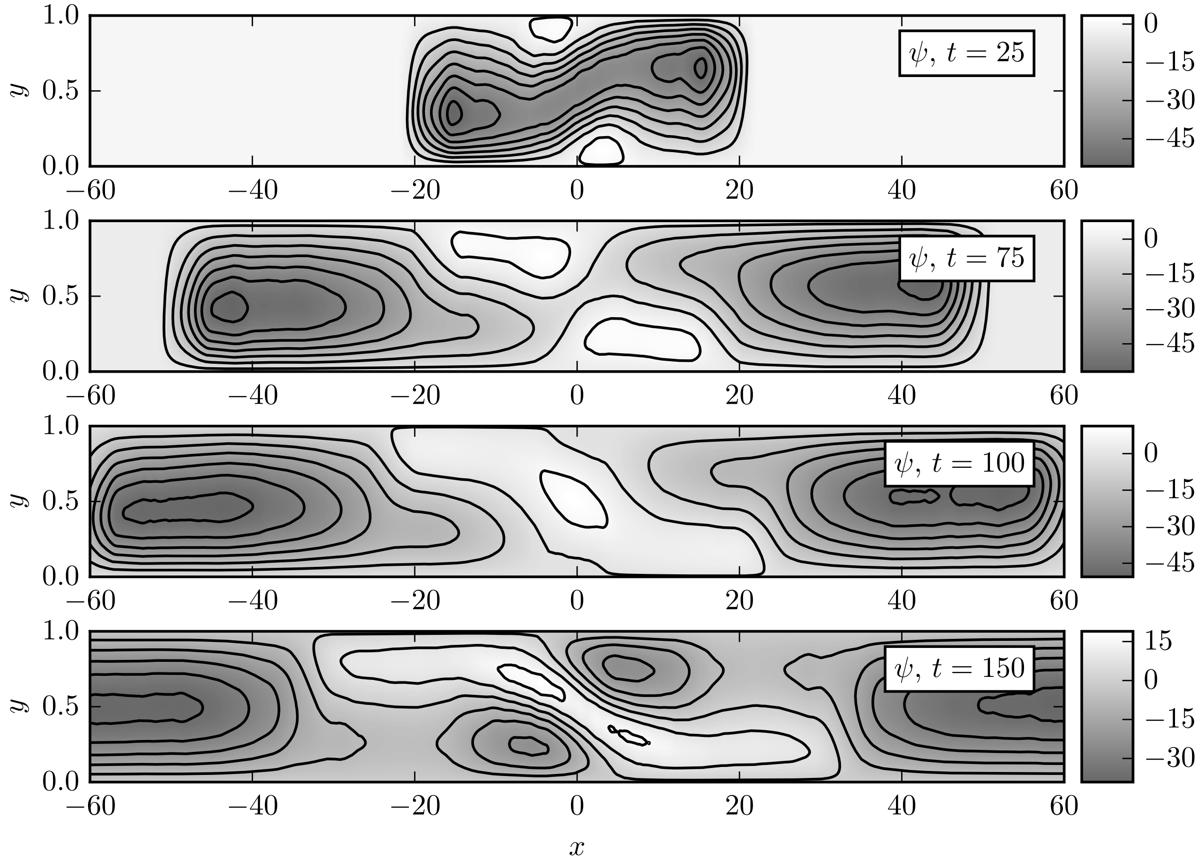

Figure 3.24: Streamlines in the laboratory reference frame at $t = 25$, $t = 75$, $t = 100$ and $t = 150$. Velocity fields were smoothed using a moving average window with a width of 3 in x. No smoothing was done in y. A current with $R_{\rho 0} = 1.05$ and $\tau = 1/8$ is shown. The size of the domain was $x \in [-120, 120]$, but only $x \in [-60, 60]$ is shown.

wall. Initially, the fluid displaced by the secondary, left-moving top current forms a countercurrent immediately below that feeds into the original right-moving current along the same wall, as sketched in the streamline pattern in figure 3.26a. A symmetric situation emerges along the bottom wall. By $t = 100$, however, the nature of the flow field has undergone a qualitative change due to a topological transition of the streamline pattern: The currents associated with the secondary fronts now form a closed recirculation zone in the central region that has cut off the primary currents from their original reservoirs, cf. figure 3.26b. As a result, in the central region of the channel the local flow direction at $t = 150$ is opposite to what it was at $t = 25$.

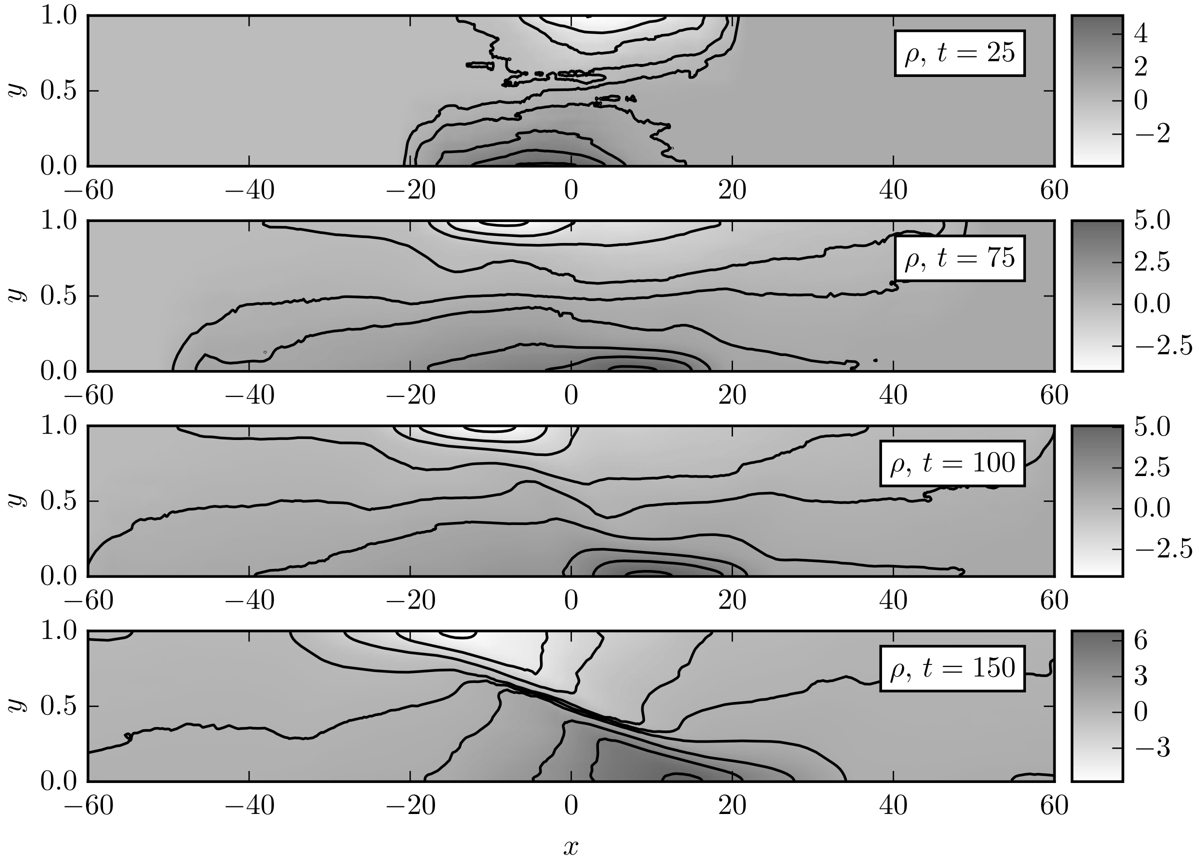

Figure 3.25: Density contours at $t = 25$, $t = 75$, $t = 100$ and $t = 150$. Density fields were smoothed using a moving average window with a width of 3 in x. No smoothing was done in y. A current with $R_{\rho 0} = 1.05$ and $\tau = 1/8$ is shown. The size of the domain was $x \in [-120, 120]$, but only $x \in [-60, 60]$ is shown.

This closed recirculation region occupying the central section of the channel pushes hot and salty fluid underneath cold and fresh fluid, as shown in figure 3.27. A comparison of figure 3.27 to figure 3.25 confirms that in this region the hot, salty fluid is denser than the cold and fresh one, as it has lost more of its original heat than salinity. Hence this region becomes unstable to the 'diffusive' variant of the double-diffusive instability. The rapid upward diffusion of heat creates a layer of hot and fresh fluid just above the interface, along with cold and salty fluid just below it. These layers then drive 'diffusive convection' [44], [45], which transports light fluid containing more heat than salinity upward, and dense fluid with more salinity than heat downward. As a result, the density

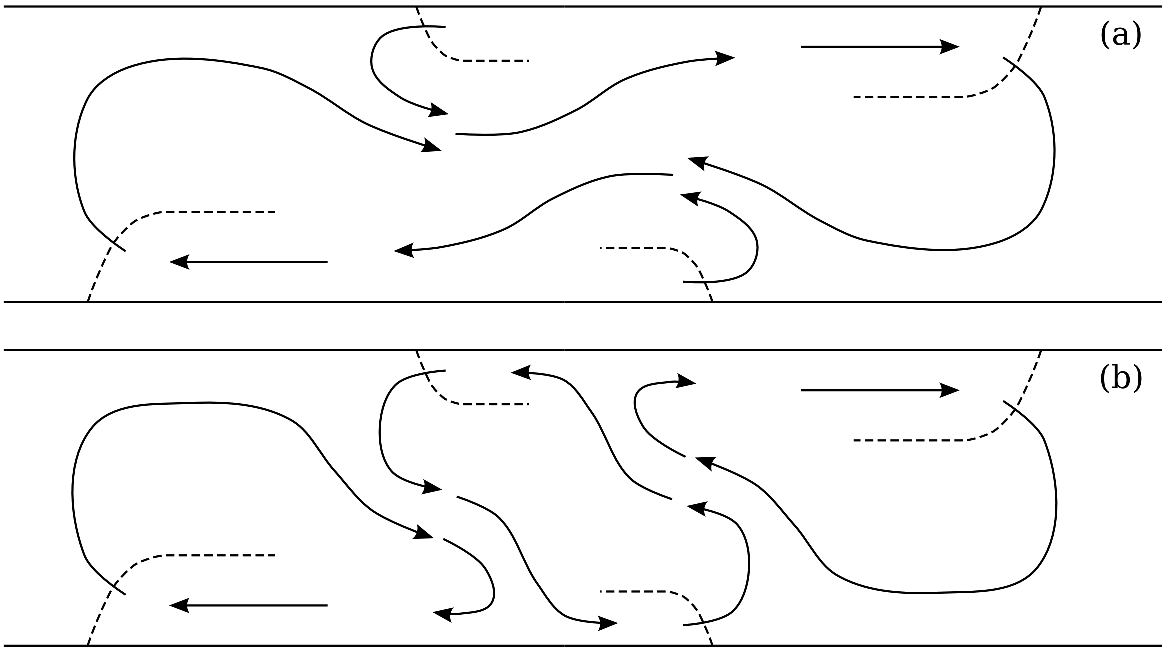

Figure 3.26: Sketches showing current fronts (dashed lines) and fluid motion (solid lines) before (a) and after (b) the transition to late stage dynamics.

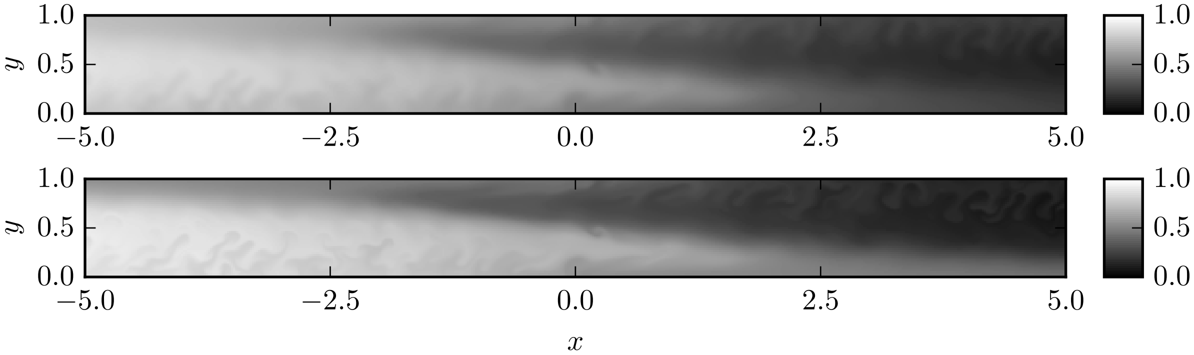

Figure 3.27: Heat (top) and salinity (bottom) near the center of the domain at $t = 100$ plotted with the true aspect ratio. In this region, denser hot and salty fluid exists under lighter cold and fresh fluid, leading to the diffusive instability.

gradient driving the secondary currents intensifies, cf. figure 3.25 at $t = 150$. Since the mixing above and below the interface is incomplete, some of the hot and salty fluid rises all the way to the top wall, where it forms a tertiary current flowing to the right, cf. figure 3.24 at $t = 150$. This current again displays the fingering instability, as seen in figure 3.27. In summary, in contrast to their single-diffusive counterparts, double-diffusive gravity currents display a much more complex long-term behavior, which is characterized by the repeated generation of new density fronts.

3.5 Force balances

We begin by developing dimensional scaling arguments for the force balances, and subsequently convert these into dimensionless criteria. Following the approach of Maxworthy [33], we consider buoyancy, inertial, viscous and turbulent drag forces acting on the current. The turbulent drag due to vertical transport of horizontal momentum as a result of double-diffusive fingering can be estimated as

$$F_{dd} \sim \rho_0 U V L \sim \rho_0 V L \frac{\mathrm{d}L}{\mathrm{d}t} \ , \tag{3.31}$$

where U represents the horizontal velocity scale. Here we use $U \sim \mathrm{d}L/\mathrm{d}t$, while Maxworthy [33] and Didden & Maxworthy [46] employed $U \sim L/t$. These two approaches are equivalent as long as the power law relationship between L and t remains constant for all times. By employing $U \sim \mathrm{d}L/\mathrm{d}t$, we gain some flexibility in terms of allowing for temporal changes in the magnitude of the forces acting on the current, which may cause a transition from one power law to another. The inertial force per Maxworthy [33] and Didden & Maxworthy [46] scales as

$$F_i \sim \rho_0 U^2 h_c \sim \rho_0 \left(\frac{\mathrm{d}L}{\mathrm{d}t}\right)^2 h_c \ . \tag{3.32}$$

The viscous force is discussed at length by Didden & Maxworthy [46]. For constant inflow, those authors develop spreading relations for top currents along slip boundaries, and for bottom currents along no-slip boundaries, governed by a balance of viscous and buoyancy forces. The currents are assumed to propagate into deep ambients, so that the drag on a bottom current is determined by the current thickness, while the drag on a top current is set by the growth of the shear layer into the ambient with time. In their experiments, however, the authors observe that even top currents seem to obey a no-slip boundary condition. They attribute this to impurities in the fluid, which cause the creation of a film on top of the current that effectively acts as a solid surface. Consequently, they assume that the viscous force scales with the current thickness even for a top current. While we have a clean, stress-free boundary in our numerical experiments, the ambient fluid layer is not deep, as the thickness of the current is roughly half the domain height. Consequently, the viscous force F_μ can be assumed to scale as

$$F_\mu \sim \mu \frac{U}{h_c} L \sim \mu \frac{L}{h_c} \frac{\mathrm{d}L}{\mathrm{d}t} \; . \tag{3.33}$$

The ratio of the double-diffusive to the viscous drag is thus given by

$$\frac{F_{dd}}{F_\mu} \sim \tilde{V} \tilde{h}_c Re \; , \tag{3.34}$$

where the tilde symbol indicates a dimensionless variable. Representative values for our numerically simulated currents are $\tilde{h}_c \approx 0.5$ and $\tilde{V} \approx 0.1$, cf. figure 3.23. For typical simulation values of $Re = 10^3$, we hence estimate that the fingering drag F_{dd} is roughly 50 times stronger than viscous drag F_μ.

The buoyancy force can be estimated by integrating the hydrostatic pressure difference between an idealized current shape and the ambient, as shown by Didden & Maxworthy [46] and Maxworthy [33]

$$F_b \sim \Delta \rho g h_c^2 \; . \tag{3.35}$$

For lock-release currents such as the ones considered here, the flow is always driven by the buoyancy force, which is balanced by one of the other forces. For currents driven by a supercritical forced inlet, Didden & Maxworthy [46] point out that the flow may be driven by inertia; however, that does not apply to the present situation.

3.5.1 Inertia-buoyancy balance

The spreading relationship for a current governed by an inertia-buoyancy balance can be derived by combining (3.32) and (3.35)

$$\rho_0 \left(\frac{\mathrm{d}L}{\mathrm{d}t} \right)^2 h_c \sim \Delta\rho g h_c^2 \; . \tag{3.36}$$

Consistent with our earlier numerical observations, we assume that the current thickness h_c is constant with time, while $\Delta\rho$ can vary with time. We thus obtain

$$\frac{\mathrm{d}L}{\mathrm{d}t} \sim \sqrt{\gamma(t) g' h_c} \; , \tag{3.37}$$

where $\gamma(t)$ represents the ratio of the instantaneous density difference driving the current to the initial density difference. By nondimensionalizing and integrating in time we obtain

$$\widetilde{L} \sim \int_0^{\widetilde{t}} \sqrt{\gamma(t')}\mathrm{d}t' \; . \tag{3.38}$$

The above differs from the analysis of Maxworthy [33] and Didden & Maxworthy [46] in two ways. Firstly, we allow for a time-dependent $\gamma(t)$, and secondly, we assume h_c is constant with time. In contrast, the earlier authors had assumed an additional relationship of the form

$$Qt^\alpha = Lh_c \; , \tag{3.39}$$

where Q indicates a constant.

3.5.2 Turbulent drag-buoyancy balance

We obtain the spreading relationship for a current governed by a fingering drag-buoyancy balance by combining (3.31) and (3.35)

$$\rho V L \frac{\mathrm{d}L}{\mathrm{d}t} \sim \Delta\rho g h_c^2 \; . \tag{3.40}$$

Nondimensionalizing and integrating gives

$$\widetilde{L}^2 - \widetilde{L}_s^2 \sim \int_{\widetilde{t}_s}^{\widetilde{t}} \frac{\gamma(\widetilde{t}')}{\widetilde{V}} \mathrm{d}\widetilde{t}' \; , \tag{3.41}$$

where $\widetilde{t}_s$ indicates the transition time beyond which (3.41) first becomes valid, and $\widetilde{L}_s$ represents the corresponding transition length. This balance corresponds to the one proposed by Maxworthy [33], except that here we assume h_c to be constant, as discussed in the previous section, and we employ $U \sim \mathrm{d}L/\mathrm{d}t$ instead of $U \sim L/t$.

3.5.3 Transition times

Hypothetically, if a certain force balance has been governing a current since $t = 0$ and the current length L obeys a power law relationship with t, the approximation

$$\frac{\mathrm{d}L}{\mathrm{d}t} \sim \frac{L}{t} \tag{3.42}$$

may be made and the proper scaling of L with t will be recovered. If it is assumed that $\gamma = 1$ is constant, (3.38) simplifies to

$$\widetilde{L} \sim \widetilde{t} \tag{3.43}$$

Assuming $\gamma = 1$ and $\widetilde{V}$ constant and solving (3.41) for L in a similar fashion, again using (3.42), gives

$$\widetilde{L} \sim \sqrt{\frac{\widetilde{t}}{\bar{\widetilde{V}}}} \tag{3.44}$$

Setting (3.44) equal to (3.43) and solving for t gives an estimate of the time of the transition of the current from a inertia-buoyancy balance to a turbulent drag-buoyancy balance

$$\widetilde{t} \sim \frac{1}{\bar{\widetilde{V}}} \tag{3.45}$$

This is consistent with how Maxworthy [33] estimated transition times for his force balances. In light of our numerical findings, which show $\tilde{V} \approx 0.1$ (figure 3.23), this gives values of $O(10)$ for $\widetilde{t}$.

3.5.4 Numerical evidence of force balances

Inertia-buoyancy balance

Figure 3.28 displays the ratio of the double-diffusive drag force (3.31) to the inertial force (3.32). We note that an inertia-buoyancy balance could at best be observed briefly for very early times, before the current becomes long enough for the fingering drag to dominate over inertia. However, as discussed above, the calculated current properties (T, S, γ) are less reliable during these early stages, so that we do not observe a clear inertia-buoyancy stage for any of the double-diffusive currents. The single-diffusive current

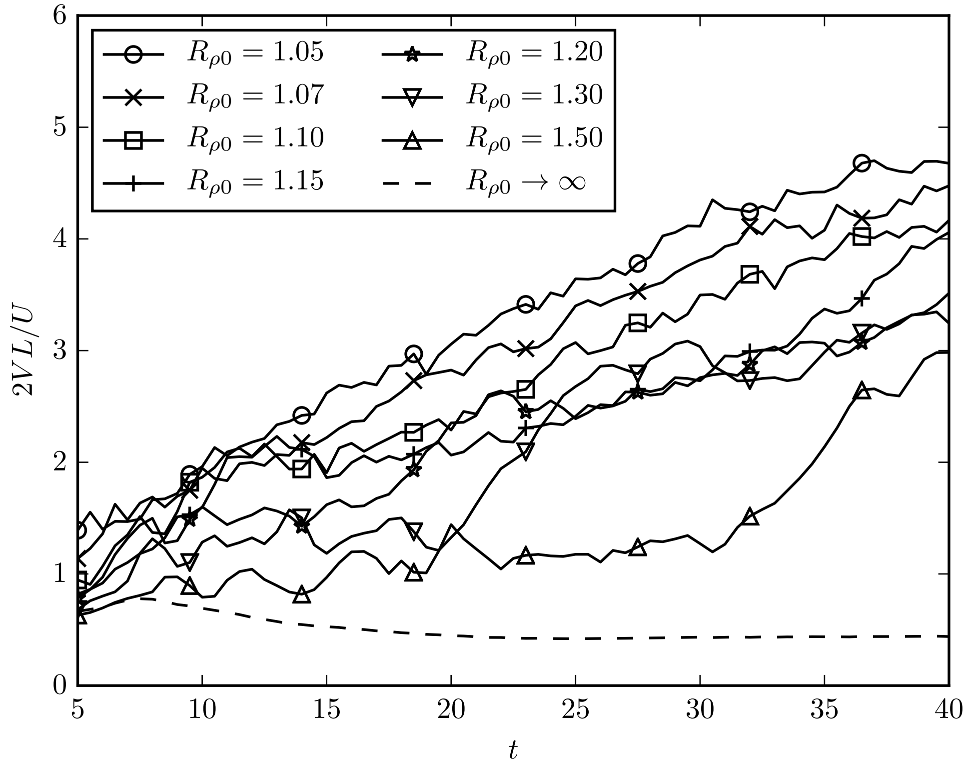

Figure 3.28: Ratio of fingering drag to inertia force for various simulations showing that a pure inertia-buoyancy balance will not exist for currents with these parameters.

included in figure 3.28, while not having genuine double-diffusive fingering, nevertheless gives rise to vertical velocities along its interface, so that the evaluation of (3.31) results in a non-zero value. However, this value is much smaller than for any of the double-diffusive currents. An inertia-buoyancy balance can be observed for this single-diffusive current, as shown in figure 3.29a, which plots the two sides of (3.38) against each other. The linear relationship through the origin for early times demonstrates the validity of (3.38).

Turbulent drag-buoyancy balance

Equation (3.45), with typical V-values in the range $[0.05, 0.10]$, provides an estimate of the transition time to a turbulent drag-buoyancy balance in the range $t \sim$ 10-20. In

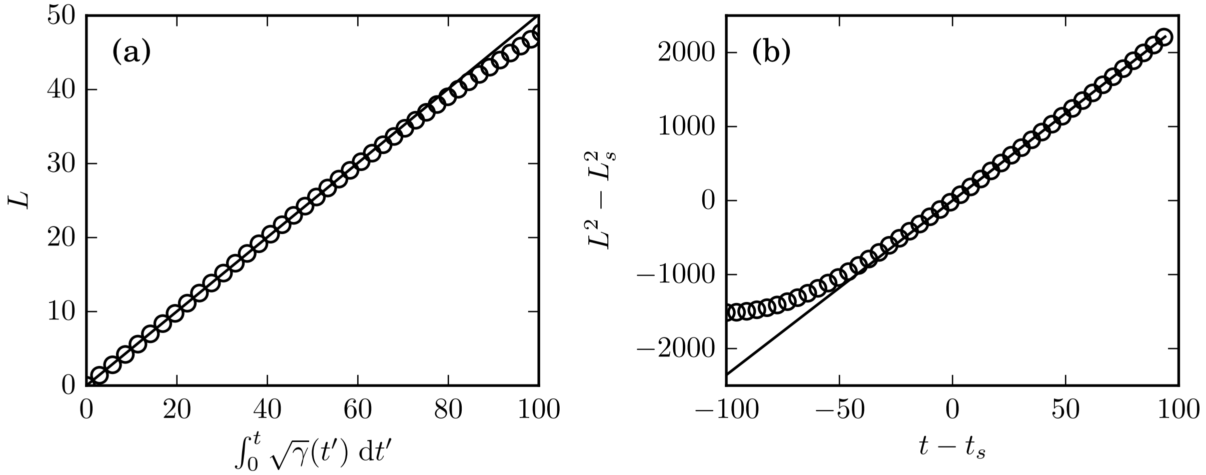

Figure 3.29: (a) Single-diffusive current: an inertia-buoyancy balance is observed, as indicated by the straight line, before viscous drag begins to become important. The circles represent the two sides of (3.38) plotted against each other. The solid line is a linear fit through the origin using data with $t \leq 50$. (b) Double-diffusive current: test for a turbulent drag-buoyancy balance at later times. In the figure, $t_s = 100$ and L_s is the length of the current at $t = t_s$. The fact that the data forms a straight line through the origin shows that (3.41) holds in this time range.

order to test for this turbulent drag-buoyancy balance, we carried out a long simulation until $t = 190$ in a large control volume $x \in [-60, 60]$, for parameter values $R_{\rho 0} = 1.50$ and $\tau = 1/8$, which result in a moderate amount of fingering. Figure 3.29b plots the two sides of (3.41) against each other, with the additional assumption that γ/V does not depend on time, which holds approximately for this simulation. In order to provide sufficient time for the transition to the turbulent drag-buoyancy balance to be completed, we choose $t_s = 100$, with $\tilde{L}_s$ denoting the current length at $t = t_s$. The agreement of the simulation data with the straight line through the origin in figure 3.29b confirms the turbulent drag-buoyancy balance for long times.

There may be interesting implications of the above regarding the dynamics of double-diffusive intrusions. Ruddick *et al.*[47] observed a constant Froude number for intrusions driven by sugar and salt, suggesting a balance of inertia and buoyancy. However, at a value of 0.005 the Froude number was surprisingly small, which could not be explained

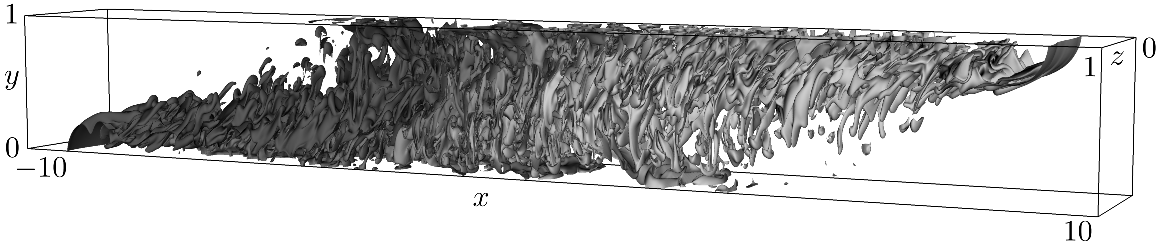

Figure 3.30: Three-dimensional isosurfaces of the salinity concentration for $R_{\rho 0} = 1.07$ and $\tau = 1/8$, at $t = 14$. From dark to light, the contour values are 0.1, 0.3, 0.5, 0.7 and 0.9.

by the authors. Although the diffusivities in the present simulations are much larger than those of sugar and salt, our results suggest that the intrusions of Ruddick *et al.*[47] could potentially have been driven by a buoyancy-fingering drag balance, with the appearance of a constant Froude number coming from an increase in the buoyancy of the intrusions over time. Because the length scales and velocities associated with the intrusions of Ruddick *et al.*[47] yield a much lower effective Re than in the present simulations, we also cannot exclude the possibility that buoyancy and viscous forces were in balance, in accordance with (3.34). Either way, constant buoyancy would give a spreading relationship of $L \sim \sqrt{t}$, whereas increasing buoyancy with time may result in a constant Fr.

3.6 Comparison of two- and three-dimensional simulations

All of the simulations discussed up to this point were two-dimensional in nature. In order to explore the qualitative and quantitative agreement between two- and three-dimensional flows, we conducted a single three-dimensional run for $R_{\rho 0} = 1.07$ and $\tau = 1/8$. A visualization of the salinity isosurfaces at $t = 14$ is shown in figure 3.30. Due to the high computational cost, this simulation employed a shorter domain in the x-

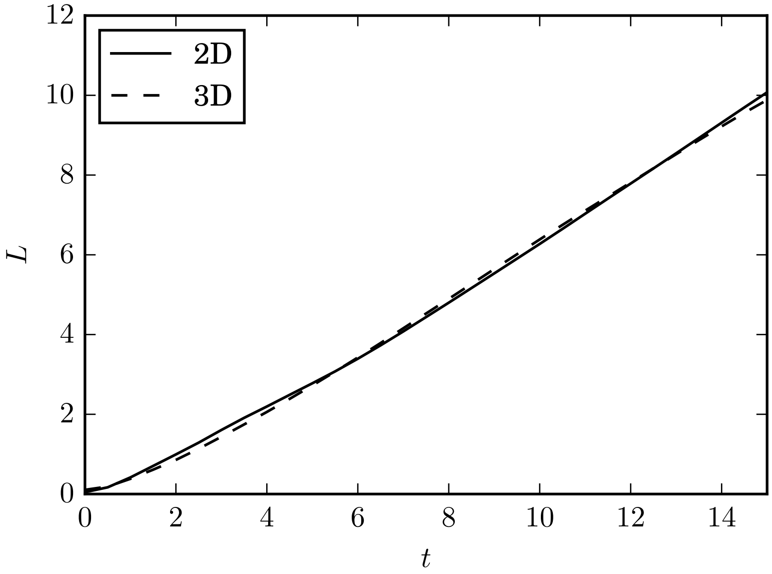

Figure 3.31: Comparison of the current length L vs. time t for the two- and three--dimensional simulations with $R_{\rho 0} = 1.07$ and $\tau = 1/8$. The results indicate that the front velocity is not strongly affected by the third dimension.

direction, $x \in [-10, 10]$, instead of $x \in [-30, 30]$ as in the two-dimensional simulations. The grid size was $2,049 \times 257 \times 257$. The simulation was carried out until $t = 15$, at which time the current front approached the endwall. The properties of the three-dimensional current including the current length L, the current thickness h_c and the temperature and salinity differences between the current and the ambient, ΔT and ΔS, were calculated from the spanwise average of the simulation data.

Over the time interval of the simulations, the two- and three-dimensional currents propagate at nearly identical velocities, as shown in figure 3.31. This is consistent with earlier findings for single-diffusive gravity currents [21] as well as turbidity currents [48]. Nevertheless, there are noticeable differences in the dynamics of the currents even at these relatively early times, as will be seen in the following. Figure 3.32a indicates that soon after the start of the flow the thickness of the three-dimensional current drops by about 20% compared to the equivalent two-dimensional current, which suggests that the fingering is considerably more intense in three than in two dimensions. This is

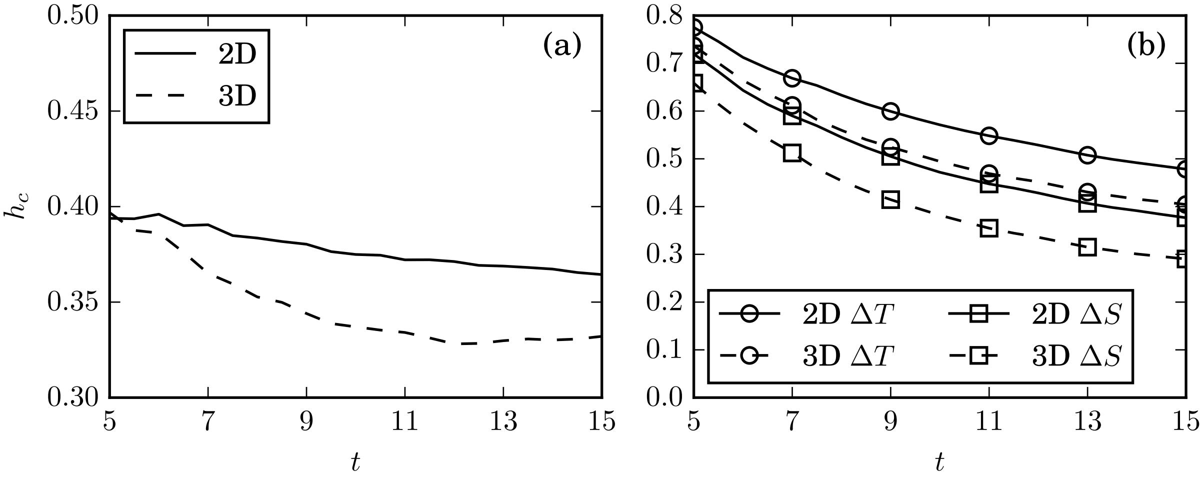

Figure 3.32: Noticeable differences emerge between the two- and three-dimensional currents regarding their thickness h_c (a), and their temperature and salinity difference with respect to the ambient, ΔT and ΔS (b). Parameter values are $R_{\rho 0} = 1.07$ and $\tau = 1/8$.

confirmed by figure 3.32b, which displays the temperature and salinity difference between current and ambient over time for both currents. The stronger fingering causes the three-dimensional current to exhibit a much more rapid decay of ΔT and ΔS. It is interesting to note that the front velocity remains nearly unchanged, in spite of the noticeable differences in current height, ΔT and ΔS.

The 3-layer structure discussed earlier in section 3.4.2 is seen to emerge again for three-dimensional currents, just as it had in two dimensions. Figure 3.33 compares streamwise averaged $u(y)$-profiles and local $u(y)$-profiles at $x = 1$ for the two- and three-dimensional simulations, where the three-dimensional flows have been averaged over the spanwise direction. The 3-layer structure is somewhat less pronounced in three dimensions, but clearly similar in nature.

Our finding that the three-dimensional current is similar to its two-dimensional counterpart but exhibits stronger fingering is consistent with results presented in Radko *et al.*[49] for flows with stochastic shear. These authors' work shows that fingering fluxes are larger in unsheared three-dimensional flows as compared to two dimensions, but that

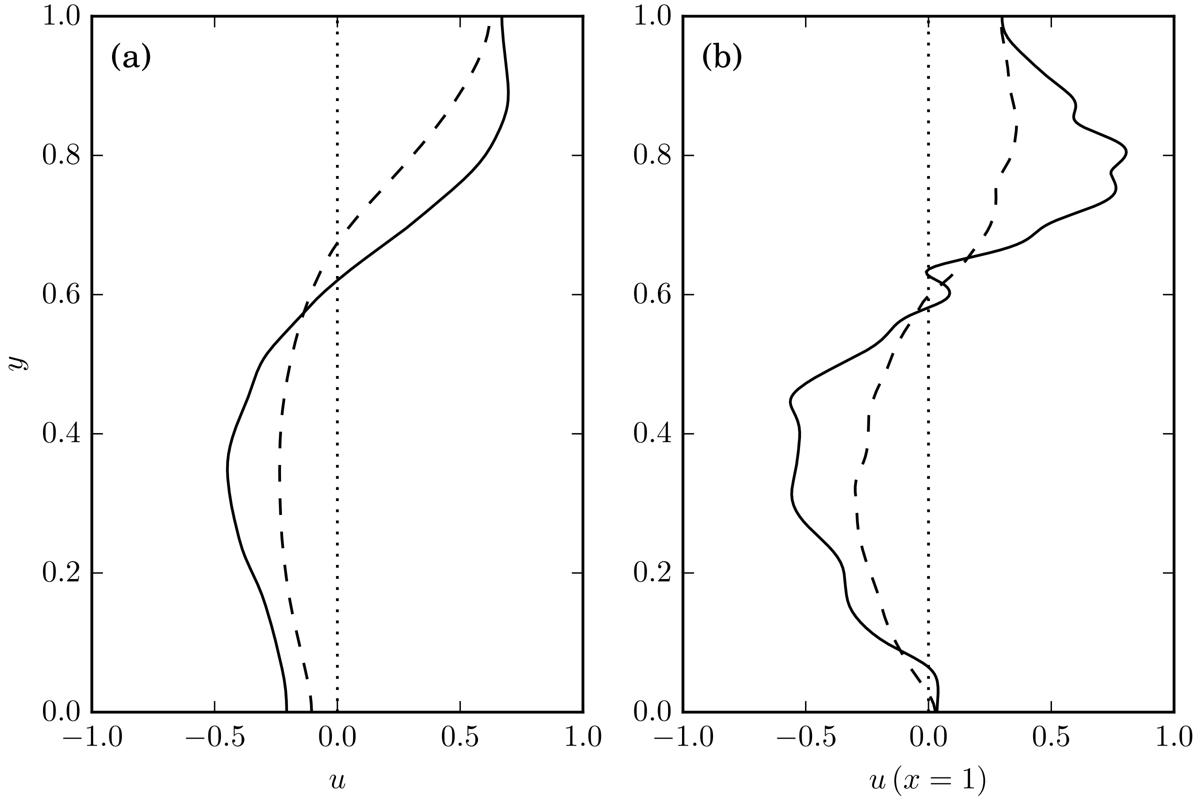

Figure 3.33: $u(y)$-profiles at $t = 15$ for 2D (solid line) and 3D (dashed line) simulations: (a) averaged over the streamwise extent of the current (and also over the spanwise direction for the three-dimensional flow), (b) local profile at $x = 1$ (averaged over the spanwise direction for the three-dimensional flow). Parameter values are $R_{\rho 0} = 1.07$ and $\tau = 1/8$. The 3-layer structure discussed earlier for two-dimensional flows emerges in three dimensions as well.

fluxes in a sheared three-dimensional environment are similar to two-dimensional fluxes in an unsheared environment. This is mainly due to the fact that shear causes three-dimensional fingers to align into salt sheets in the plane of the shear [50], since modes with nonzero wavenumber in this direction are damped. As a result, shear effectively reduces the dimensionality of the fingering from three to two dimensions, thereby reducing the flux by a factor of 2 to 3 [49]. In two-dimensional gravity currents, the lack of the third dimension prevents any sheets from forming, and only modes with nonzero wavenumbers in the streamwise direction can grow. However, these modes will be damped in comparison to three dimensions, so that fluxes will be lower in the sheared two-dimensional

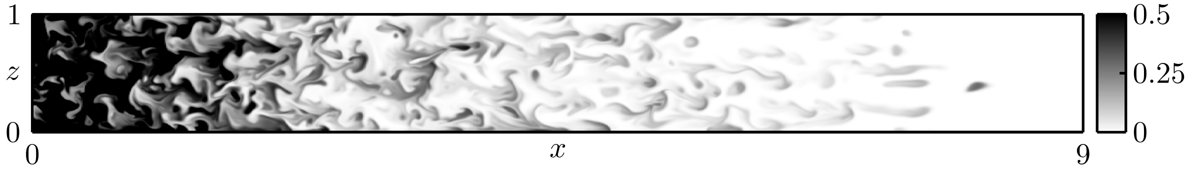

Figure 3.34: Slice of salinity concentration at $t = 14$ normal to the vertical at $y = 0.65$, which is roughly the location of the current interface shown in figure 3.32a.

environment.

The tendency of three-dimensional flows to form sheets is clearly visible in the horizontal slice of the salinity field displayed in figure 3.34. The slice shown is located at $y = 0.65$, which is roughly the height of the interface in figure 3.32a. The sheet-like nature of the structures is more pronounced near the front of the current, where the shear at this y-elevation may be more intense than near $x = 0$. In addition, this current section has been exposed to shear over a longer time interval, which may also contribute to its more sheet-like structure. A similar effect in horizontal cross sections of fingering in shear was also observed by Radko *et al.*[49].

3.7 Conclusions

The above simulations of lock-exchange flows in the Boussinesq regime demonstrate that strongly double-diffusive gravity currents in the fingering regime can exhibit quite different dynamics from their single-diffusive counterparts. Even at relatively modest Reynolds numbers, for which single-diffusive currents remain laminar, double-diffusive currents can give rise to pronounced small-scale fingering convection. By systematically varying the diffusivity ratio τ and the initial stability ratio $R_{\rho 0}$, we are able to quantify the influence of these parameters on the current evolution. Specifically, we notice that the propagation velocity of the current depends nonmonotonically on these parameters.

Strongly double-diffusive currents are seen to lose both heat and salinity more quickly than weakly double-diffusive ones. Furthermore, they lose salinity more quickly than heat, thereby increasing the initial density difference that drives them. This differential loss of heat and salinity results in the emergence of strong local density maxima and minima along the top and bottom walls in the gate region, which in turn promotes the formation of secondary, counterflowing currents along the walls. These secondary currents result in a pronounced three-layer structure of the flow. In the neighborhood of the gate region, the late stages of the flow are characterized by currents flowing in the opposite directions from the original ones, a phenomenon that bears some similarity to the buoyancy reversal observed for certain types of particulate gravity currents [27].

A detailed analysis of the energy budget shows that strongly double-diffusive currents can release several times their initially available potential energy. It furthermore elucidates the conversion of internal energy into mechanical energy via diffusion of the scalar fields. By quantifying the vertical fingering velocity, we are able to estimate the turbulent drag acting on the gravity current. Scaling arguments suggest that even at fairly low Reynolds numbers double-diffusive gravity currents are governed by a balance of buoyancy and turbulent drag, which is confirmed by the simulation results.

While the present simulations were motivated by thermohaline flows, the underlying model may also be applicable to flows in which one of the scalars contributing to the density is a particulate phase, as long as the influence of the settling velocity is small. For non-negligible settling velocities, on the other hand, novel phenomena can arise, as demonstrated in recent laboratory experiments [51], linear stability investigations [52, 53] and nonlinear simulations [54, 36]. Similar considerations also apply to bioconvection in stratified environments [55].

As a final remark, we note that a related problem concerns the evolution of double-diffusive intrusions [56, 57], for which the upper and lower interfaces may be subject to different instability modes. Work along these lines is currently under way.

Chapter 4

Interfacial instabilities in clear salt water above sediment-laden fresh water

4.1 Introduction

The recent investigations by Burns & Meiburg [52, 36] and Yu *et al.*[53, 54] address the instability of an interface separating a less dense layer of sediment-laden fresh water above, from a more dense layer of clear salt water below. This configuration is introduced as a conceptual model for buoyant river plumes or hypopycnal turbidity currents propagating along the ocean's surface, respectively. The evolution of the interface is found to be governed by the competition of two linear instability modes. On one hand, the unstable stratification of the more slowly diffusing particulate phase can trigger double-diffusive convection within the interfacial region. On the other hand, the downward settling of the particular phase prompts the formation of a maximum-density 'nose' layer of sediment-laden salt water along the interface, which can trigger the growth of a Rayleigh-Taylor instability along its lower boundary. Direct numerical simulations show that the effective thicknesses l_s and l_c of the salinity and sediment concentration interfaces grow proportionally to the square root of time, as does the nose layer thickness H, so that these processes can be modeled in terms of a turbulent diffusivity. For small values of $H/l_s < O(0.1)$ double-diffusive fingering is found to dominate, whereas for larger ratios $H/l_s > O(0.1)$ the dominant instability is of Rayleigh-Taylor type. This finding is consistent with the experimental observations by Parsons *et al.*[51].

It is well known that under exceptional discharge conditions some rivers can carry sufficiently high sediment loads to render them denser than the saline ocean water [58]. Under these conditions, the river plume will propagate along the seafloor ('hyperpycnal flow'), so that a layer of more dense, sediment-laden fresh water is situated below less dense, clear salt water, [27] cf. figure 4.1a. The downward particle settling velocity is now directed *away* from the interface, so that it favors the formation of a minimum-density nose region along the interface, with the potential for Rayleigh-Taylor instability along its upper boundary, as sketched in figure 4.1b. Furthermore, the differential diffusion of salt (fast) and sediment (slow) tends to create locally unstable density overhangs both along the upper and the lower boundaries of the interfacial region, which will give rise to gravitational instabilities. This regime of double-diffusive instability, in which the more slowly diffusing particular phase is stably stratified, is commonly referred to as the diffusive type, [59, 60, 30, 29] cf. figure 4.1c. Thus, the superposition of double-diffusive and settling effects amplifies the potential for Rayleigh-Taylor instability above the interface, and reduces it below, cf. figure 4.1d. The present investigation aims to explore the nonlinear competition among these instability modes via DNS simulations, with a particular focus on the conditions under which the gravitational instability below the interface will be suppressed. While we will generally refer to the more rapidly diffusing scalar as 'salt,' we note that similar considerations apply to the inflow of a denser, warm, sediment-laden river into a less dense, cold, fresh water lake.

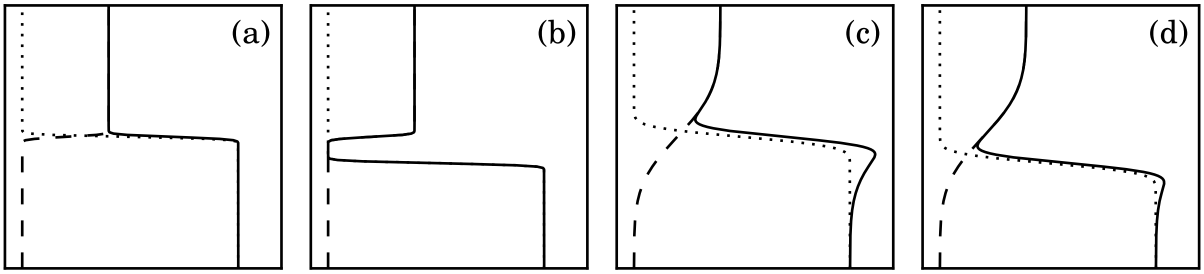

Figure 4.1: Qualitative shape of salinity (dashed line), sediment (dotted line) and total (solid line) density distributions under various conditions: (a) initial distribution; (b) later time, as a result of particle settling only; (c) later time, as a result of different diffusivities only; (d) later time, as a result of both settling and different diffusivities.

4.2 Governing equations, initial and boundary conditions

The governing equations are identical to the ones employed in Burns & Meiburg [36] and we refer the reader to this reference for the detailed derivation. The equations are made dimensionless using as salinity scale S_{max} the initial salinity in the upper layer, and as particle concentration scale C_{max} the initial concentration in the lower layer. In addition, we employ viscous scales for length $d = \left(\frac{\nu^2}{g\gamma C_{max}}\right)^{1/3}$, tiime d^2/ν and velocity ν/d, reflecting a balance of inertial, viscous and buoyancy forces. Here α and γ are the expansion coefficients for salinity and sediment concentration, respectively. In dimensionless form, the conservation equations for mass, momentum, salinity S and sediment concentration C are

$$\begin{aligned}
\boldsymbol{\nabla} \cdot \boldsymbol{u} &= 0 \,, && (4.1)\\
\frac{\partial \boldsymbol{u}}{\partial t} + \boldsymbol{u} \cdot \boldsymbol{\nabla} \boldsymbol{u} &= \nabla^2 \boldsymbol{u} - \boldsymbol{\nabla} P - (R_s C + S)\hat{\boldsymbol{y}} \,, && (4.2)\\
\frac{\partial S}{\partial t} + \boldsymbol{u} \cdot \boldsymbol{\nabla} S &= \frac{1}{Sc} \nabla^2 S \,, && (4.3)\\
\frac{\partial C}{\partial t} + V_p \frac{\partial C}{\partial y} + \boldsymbol{u} \cdot \boldsymbol{\nabla} C &= \frac{1}{\tau\, Sc} \nabla^2 C \,, && (4.4)
\end{aligned}$$

with the governing dimensionless parameters

$$V_p = \frac{v_s}{(\nu\, g\, \alpha\, S_{max})^{1/3}}\ ,\ Sc = \frac{\nu}{\kappa_s}\ ,\ \tau = \frac{\kappa_s}{\kappa_c}\ ,\ R_s = \frac{\gamma C_{max}}{\alpha S_{max}}\ . \tag{4.5}$$

Here the dimensionless settling velocity V_p represents the ratio of the Stokes settling velocity v_s and the characteristic viscous buoyancy velocity. Sc denotes the Schmidt number, which is based on the diffusivity of salinity κ_s. κ_c refers to the sediment diffusivity, and the diffusivity ratio $\tau > 1$. The upper layer being less dense than the lower layer, the stability ratio R_s, which represents the ratio of the density contributions of sediment and salt, is always larger than unity in the present investigation.

Based on a typical seawater salinity of 3.5%, a typical velocity scale in this problem is about 7 mm/s or less. In this study, we analyze a simulation with $V_p = 0.04$, which corresponds to a grain size of 9.0 μm, a fine silt, assuming a particle specific gravity of 2.6 along with Stokes law for the settling velocity. Depending on the sediment content of the fresh water, the stability ratio R_s can take on a range of values in nature. Here we employ $R_s = 2.5$, so that the sediment loading is 2.5 times larger than the salinity loading. While $Sc = 700$ for salt water, this value is too large to conduct DNS simulations, and we use a value of 1 instead. Estimates for the physical diffusivity of the particles as a function of their size are available in the literature [61]. Here, we use $\tau = 25$ and note that further increases in τ made little difference in the final results.

The present investigation employs two-dimensional simulations of the above equations. We note that for the case of fresh water with particles above salt water, Burns & Meiburg [36] had observed similar dynamics in two- and three-dimensional simulations, so that we can expect two-dimensional simulations to provide meaningful insight for the present case. Our simulations use periodic boundary conditions in the horizontal direction and slip walls with no flux at the top and bottom boundaries. The simulations are

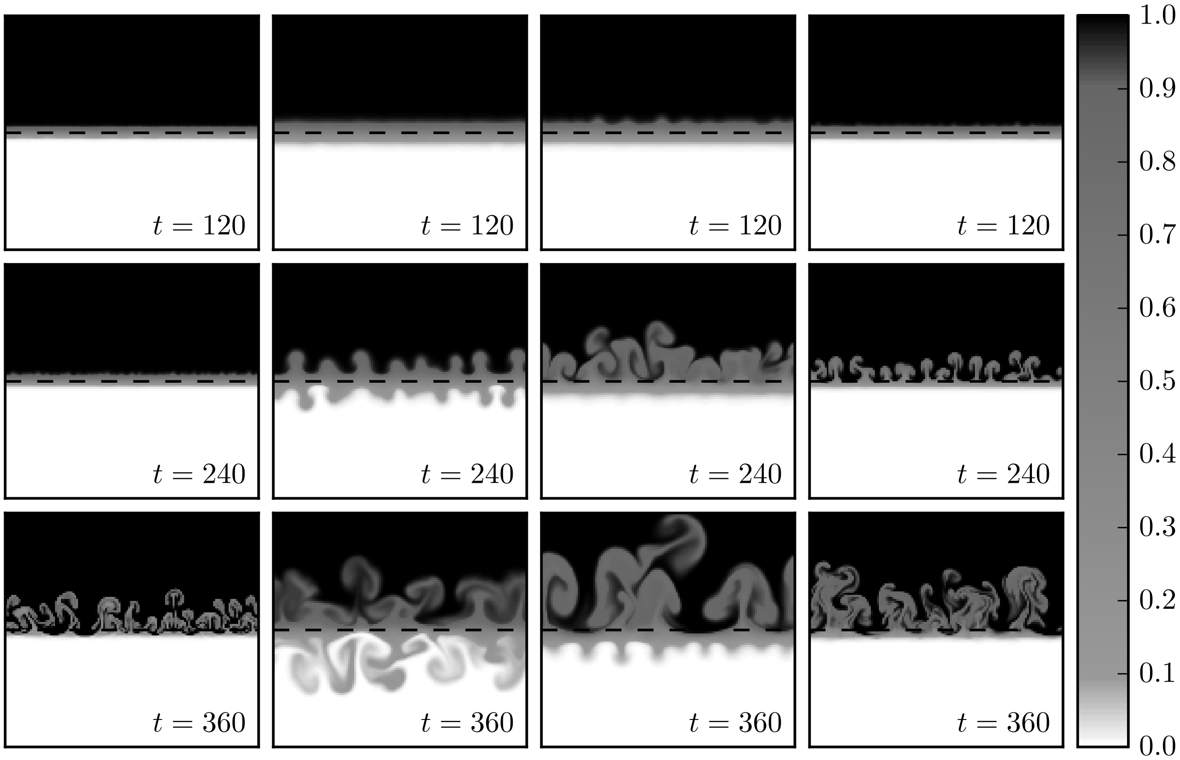

Figure 4.2: Snapshots of salinity concentration fields for four simulations with $R_s = 2.5$. (Left) The effect of settling only: $V_p = 0.04$, $Sc = 25$, $\tau = 1$; (center-left) the effect of double diffusion only: $V_p = 0$, $Sc = 1$, $\tau = 25$; (center-right) the combined effects of settling and double diffusion: $V_p = 0.04$, $Sc = 1$, $\tau = 25$; (right) the effect of settling is strong enough to eliminate plumes in the bottom half: $V_p = 0.04$, $Sc = 7$, $\tau = 25$. The domain shown extends from 0 to 700 in x and -300 to 300 in y, with the initial interface at $y = 0$ marked with a dashed line.

always terminated before any plumes reach these boundaries. The flow field is initialized from rest, with randomly perturbed, slightly smoothed step profiles for sediment and salinity.

4.3 Direct numerical simulations

In order to demonstrate the effects of settling and double diffusion in isolation, figures 4.2 and 4.3 present the salinity and sediment concentration fields for four repre-

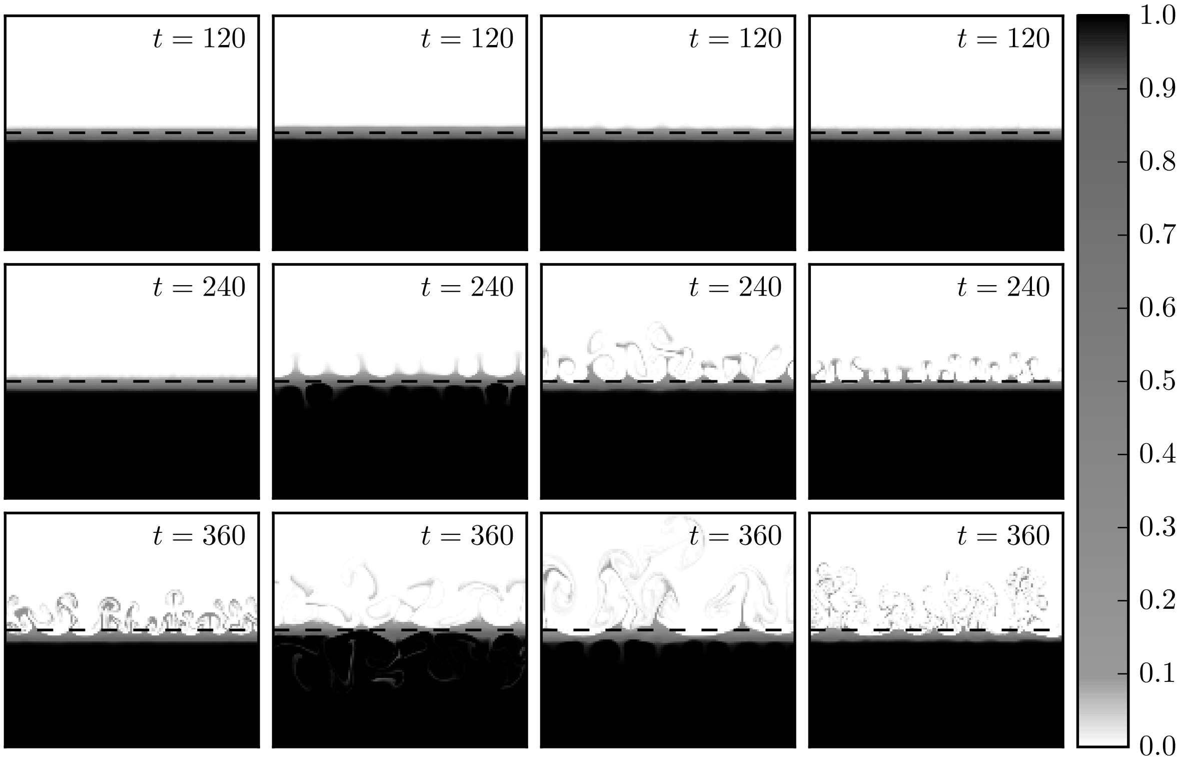

Figure 4.3: Snapshots of sediment concentration fields for three simulations with $R_s = 2.5$. (Left) The effect of settling only: $V_p = 0.04$, $Sc = 25$, $\tau = 1$; (center-left) the effect of double diffusion only: $V_p = 0$, $Sc = 1$, $\tau = 25$; (center-right) the combined effects of settling and double diffusion: $V_p = 0.04$, $Sc = 1$, $\tau = 25$; (right) the effect of settling is strong enough to eliminate plumes in the bottom half: $V_p = 0.04$, $Sc = 7$, $\tau = 25$. The domain extends from 0 to 700 in x and -300 to 300 in y, with the initial interface at $y = 0$ marked with a dashed line.

sentative simulations with $R_s = 2.5$, at three different times. While the full x-axis is displayed, the domain is truncated in the y-direction, so that we can focus on the most active region near the interface. The left column shows the case of particle settling in the absence of double diffusion, for $V_p = 0.04$, $Sc = 25$ and $\tau = 1$. Rising plumes can be identified in both the salinity and sediment concentration fields, as a result of a Rayleigh-Taylor instability that develops along the upper boundary of the interfacial region, in accordance with the sketch in figure 4.1b. By contrast, the second columns show the case of double-diffusive instability in the absence of particle settling, for $V_p = 0$,

$Sc = 1$ and $\tau = 25$. Consistent with the sketch in figure 4.1c, the flow exhibits a diffusively dominated central layer from which positively and negatively buoyant plumes of roughly equal size rise and descend into the upper and lower regions, as a result of the local density overhangs above and below the central layer, respectively. The third column shows the combined effects of double diffusion and sedimentation, for $V_p = 0.04$, $Sc = 1$ and $\tau = 25$. As expected from figure 4.1d, we recognize a combination of strong rising and weaker descending plumes, which indicates that sedimentation destroys the approximate symmetry of the pure double-diffusive instability. Finally, the right column shows a simulation for $V_p = 0.04$, $Sc = 7$ and $\tau = 25$, for which the settling is sufficiently strong to suppress the formation of plumes below the interfacial region. For those flows with $\tau = 25$, the sediment concentration gradients are much more pronounced than the salinity ones, due to the smaller diffusivity of the sediment. Taken together, figures 4.2 and 4.3 indicate that along the upper boundary of the central, diffusively dominated region the effects of double-diffusion and sedimentation amplify each other, whereas along its lower boundary they tend to cancel each other, possibly even to the point where instabilities in the lower fluid layer are completely suppressed, which is consistent with the sketches of figure 4.1.

4.4 Discussion

In the following, our analysis will focus on the simulation shown in the center-right columns of figures 4.2 and 4.3, where both sedimentation and double diffusion are influential. Figure 4.4a displays the horizontal rms-fluctuations of the salinity field, as a function of the vertical location and time. It confirms that the rising plumes above the interface are stronger and spread more rapidly than their descending counterparts below the interface. The analogous plot for the sediment concentration field (not shown)

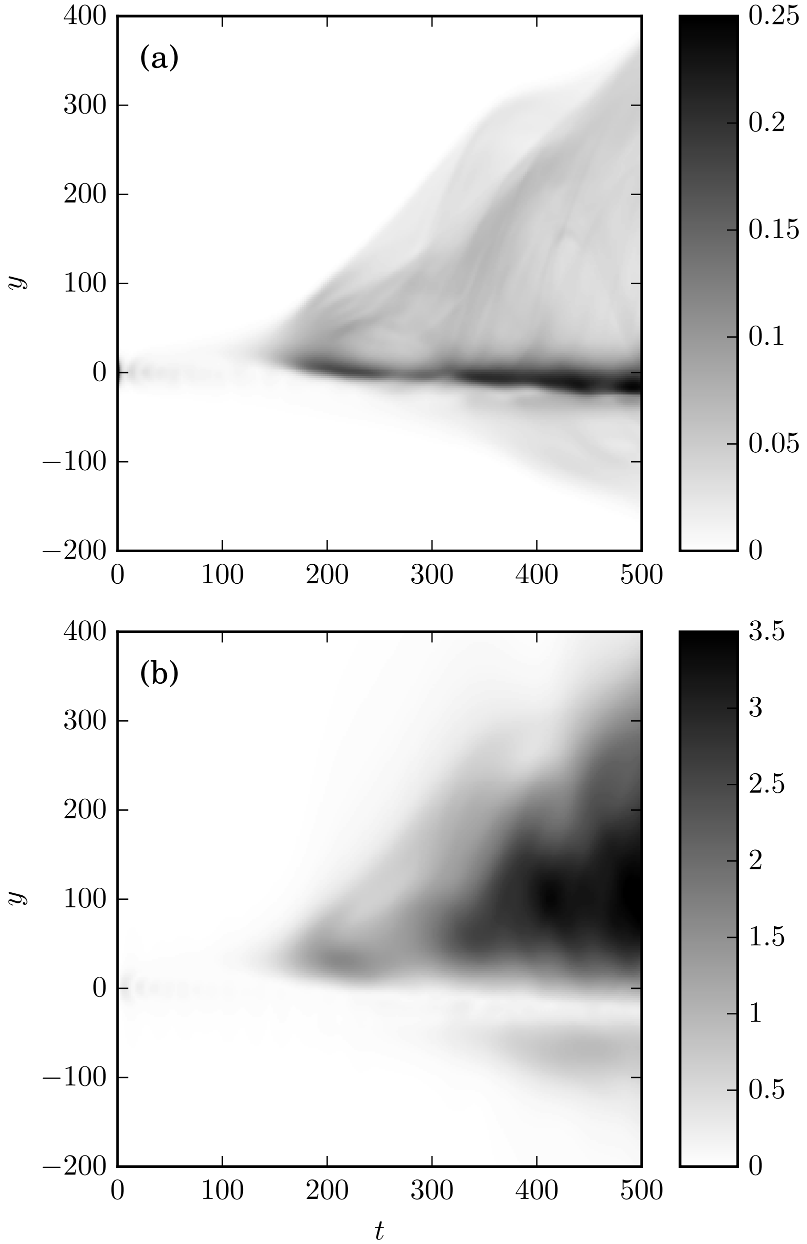

Figure 4.4: (a) Horizontal rms-fluctuations of the salinity concentration field, as function of the vertical coordinate and time. (b) Horizontal rms-fluctuations of the vertical velocity as function of the vertical coordinate and time. Parameters for this simulation were $Sc = 1$, $R_s = 2.5$, $\tau = 25$ and $V_p = 0.04$.

displays corresponding features. The horizontal rms-fluctuations of the vertical velocity field for the present case, shown in figure 4.4b, exhibit characteristics that are quite different from the configuration analyzed by Burns & Meiburg [36]. These fluctuations are seen to be very small in the slowly descending, central interfacial region, confirming that this region is dominated by diffusion rather than convection. This suggests that the flux of sediment across the central region will be a result of diffusion and settling only, while the transport of salinity will be purely diffusive, and the convective components are negligible.

These differences between the two configurations are confirmed by the temporal evolution of the sediment and salinity interface thicknesses, $l_c(t)$ and $l_s(t)$, as well as the corresponding interface locations, $y_c(t)$ and $y_s(t)$, cf. figure 4.5. These quantities are obtained by fitting the horizontally averaged concentration profiles, $\bar{S}(y,\, t)$ and $\bar{C}(y,\, t)$, to error functions, cf. Burns & Meiburg [36]. Equation (4.6) shows the form of the fitted function for salinity, with an identical expression holding for particle concentration

$$\bar{S}(y,\, t) = \frac{1}{2}\,\mathrm{erf}\left(\frac{y - y_s(t)}{l_s(t)}\right) \,. \tag{4.6}$$

The inflection point of the error function profile then indicates the interface location, while the error function width is taken as the effective interface thickness. Burns & Meiburg [36] had found that for sediment-laden fresh water above salt water both interface thicknesses grew proportionally to $t^{1/2}$ for all times, so that effective turbulent diffusivities could be defined. Their simulation results showed that, in spite of its much larger molecular diffusivity, the turbulent diffusivity of salt was smaller than that of sediment. Figure 4.5a demonstrates that, for the present configuration of clear salt water above sediment-laden fresh water, the salinity interface thickness grows diffusively only during the early stages of the flow. Once the convective instability sets in, both interface

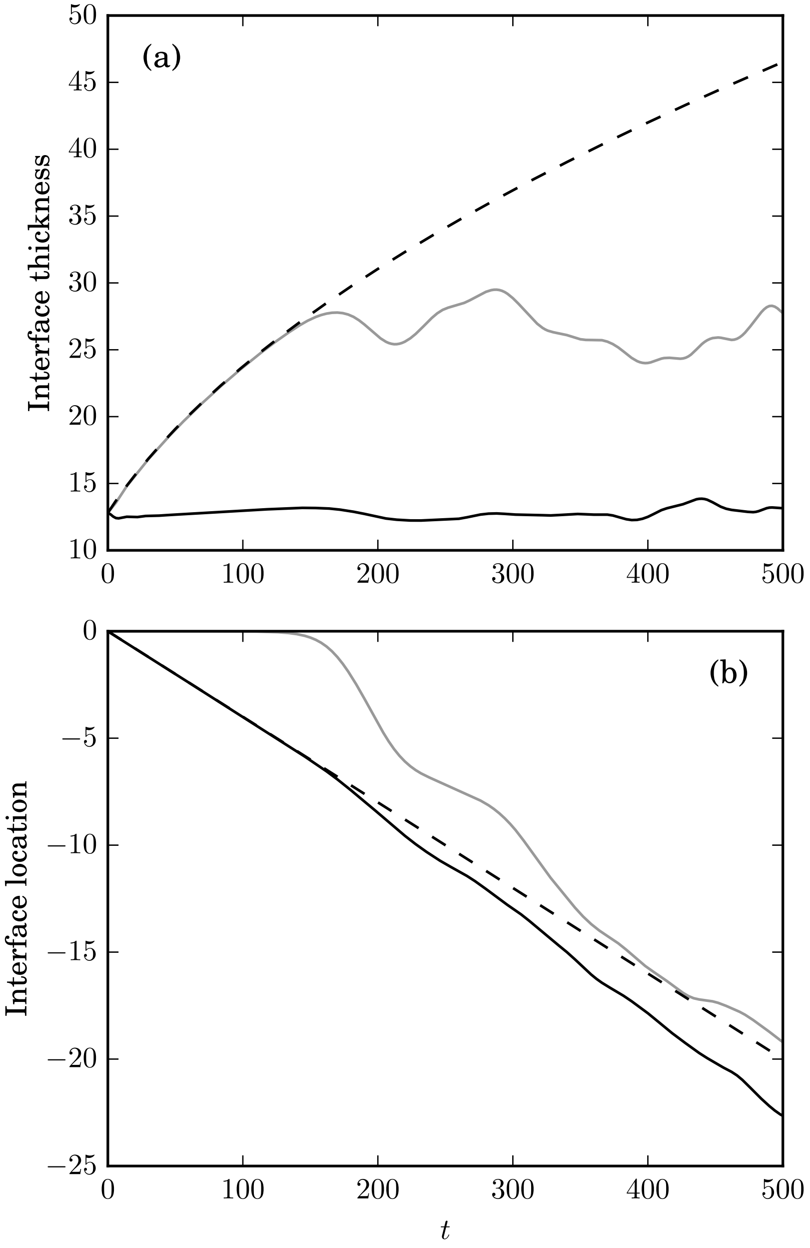

Figure 4.5: (a) Interface thicknesses for sediment (black) and salinity (grey) as functions of time. The dashed line represents the initial diffusive growth of the salinity interface thickness according to $\sqrt{4t/Sc}$. (b) Interface locations for sediment (black) and salinity (grey) as functions of time. The dashed line represents the Stokes settling velocity. Parameters for this simulation were $Sc = 1$, $R_s = 2.5$, $\tau = 25$ and $V_p = 0.04$.

thicknesses fluctuate around values that remain constant in time. This reflects a competition between diffusion, which tends to thicken the interface, and convection, which continuously sharpens it, analogous to a thermal boundary layer [30].

For sediment-laden fresh water above salt water, Burns & Meiburg [36] had found that the sediment interface location, after initially descending with the particle settling velocity, propagates downward at a reduced rate, while the salinity interface location moves upward. As a result, the distance between the salinity and particle interfaces, i.e., the 'nose thickness' H was seen to grow proportinally to $t^{1/2}$. A qualitatively different picture emerges for the configuration of clear salt water above sediment-laden fresh water, cf. figure 4.5b. Here the sediment interface propagates downward roughly with the settling speed for all times. We note that the downward velocity of the sediment interface is not to be confused with the effective particle settling velocity, which varies depending on whether or not downward moving plumes are present. The salinity interface location, after initially remaining stationary, subsequently tracks the sediment interface downward, so that the distance between the two remains approximately constant with time. This quasisteady nose thickness can be understood as the result of a balance between two competing effects: The continued settling of particles moves the sediment interface downward. This reduces the minimum density at the upper boundary of the interfacial region, which in turn increases the strength of the salinity convection above the interfacial region, thereby bringing the salinity interface downwards. Once the salinity interface approaches the sediment interface, the density difference driving the convection above the interfacial region is reduced, the downward motion of the salinity interface slows, and the downward propagating sediment interface increases the offset again.

In the following, we will formulate scaling relations that allow us to distinguish the two main flow regimes, *viz.* the regime characterized by plumes both above and below the interfacial region, and the one that exhibits plumes only above the interfacial region.

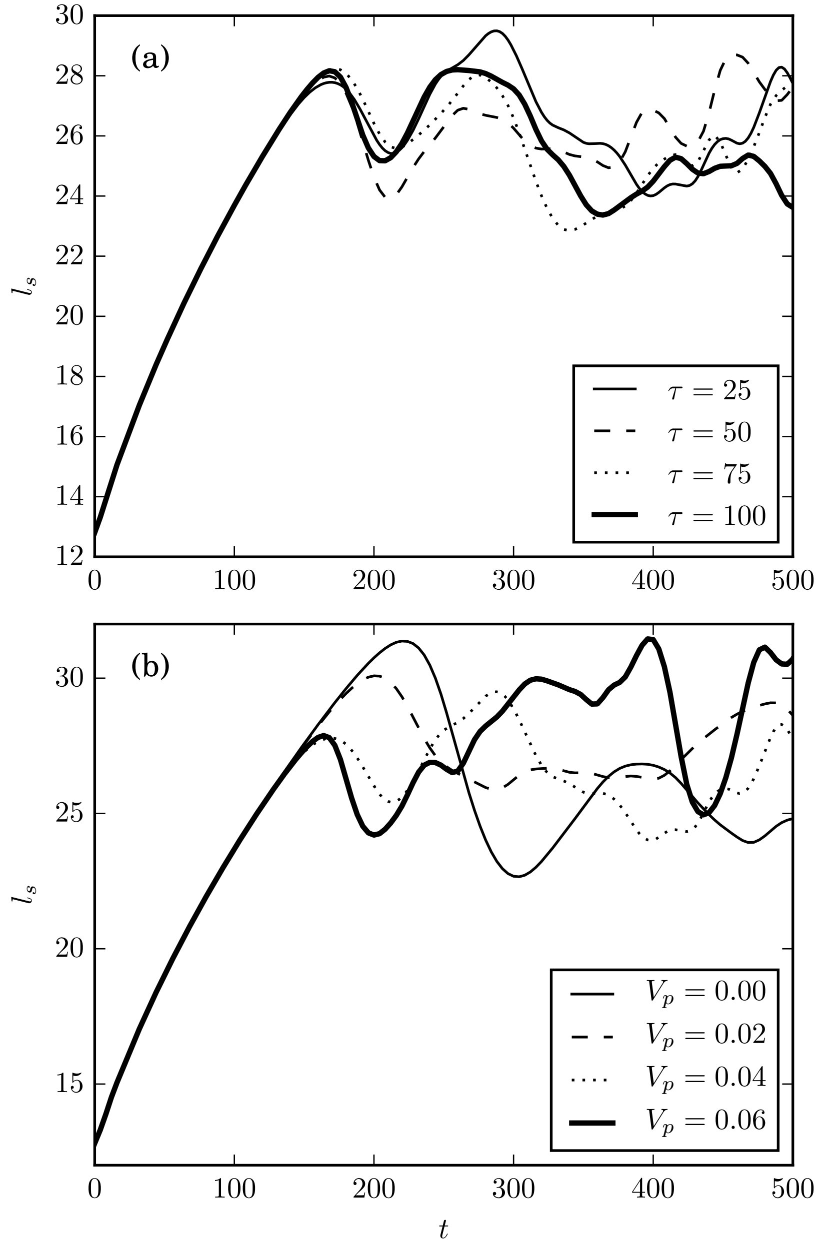

Figure 4.6: (a) Development of l_s over time for different values of τ. (b) Development of l_s over time for different settling velocities. Parameters: (a) $Sc = 1$, $R_s = 2.5$, $\tau = 25$, 50, 100, 200, (b) $Sc = 1$, $R_s = 2.5$, $\tau = 25$, $V_p = 0$, 0.02, 0.04, 0.06.

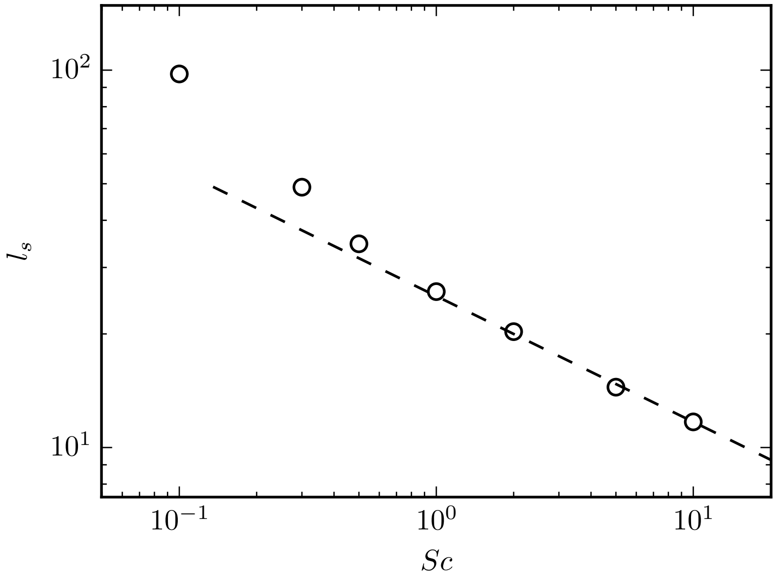

Figure 4.7: Quasisteady salinity interface thickness l_s for different values of the Schmidt number. Parameters: $Sc = 10, 5, 2, 1, 0.5, 0.3, 0.1$, $R_s = 2.5$, $\tau = 25$, $V_p = 0.04$. The dashed line has a slope of $-1/3$.

The generation of plumes below the interface is linked to the emergence of a local density maximum in this region. In other words, descending plumes will form if the downward diffusive flux of salinity $F_s \propto 1/(Sc\, l_s)$ across the interfacial region exceeds the downward sediment flux as a result of settling $F_c \propto V_p$.

While Sc and V_p are known input parameters, the quasisteady salinity interface thickness l_s is not, so that we have to obtain it from the numerical simulations. Towards this end, figure 4.6 shows a number of simulation results for $l_s(t)$ as a function of the diffusivity ratio τ and the settling velocity V_p. We find that, once convection sets in, l_s remains approximately constant in time and depends only weakly on τ and V_p for the regimes explored. On the other hand, l_s depends strongly on the Schmidt number. A log-log plot of the quasisteady l_s as a function of Sc shows that $l_s \propto Sc^{-1/3}$ for large Sc, cf. figure 4.7. A dimensional scaling argument in support of this relationship can be constructed along the following lines: The plumes emanating from the interface at discrete locations generate shear along the interface, thereby setting up a viscous boundary layer

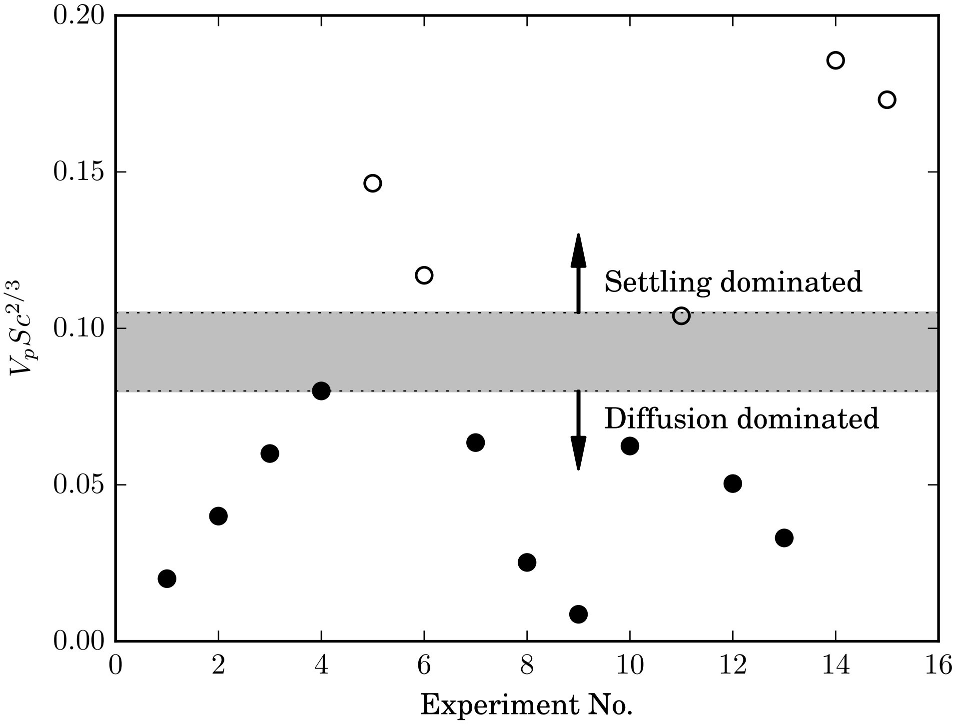

Figure 4.8: Value of the ratio of the sediment to salinity flux $V_p\ Sc\ l_s$ for 15 numerical simulations with $R_s = 2.5$, $\tau = 25$ and the Sc- and V_p-values listed in table 4.1. Blank markers indicate that plumes do not form below the interface, while solid markers reflect the existence of plumes in this region.

along the horizontal interface. Since we employed viscous scaling to derive the original set of governing equations, we have $u \propto \frac{\nu}{\delta}$ within this boundary layer. For large Sc the salinity boundary layer of thickness l_s will be much thinner than the viscous boundary layer of thickness δ. Hence we have a characteristic velocity of the salinity $u_s = \frac{u\,l_s}{\delta} = \frac{\nu\,l_s}{\delta^2}$. Balancing the dominant convective and diffusive terms in the salinity equation, $u_s\,\frac{\partial S}{\partial x}$ and $k_s\,\frac{\partial^2 S}{\partial y^2}$, respectively, then yields $\frac{l_s}{\delta} \propto (\frac{k_s}{\nu})^{1/3} = Sc^{-1/3}$, in agreement with the simulation data in figure 4.7. This scaling is only valid for moderate and large Sc, since when Sc is small salinity will tend to diffuse further than the viscous boundary layer and then the characteristic velocity of the salinity will no longer be $u_s \propto \frac{ul_s}{\delta}$.

In order to explore the existence of a critical value of $V_p\ Sc\ l_s$ beyond which the formation of plumes below the interface would be suppressed, we carried out simulations

Simulation No.	V_p	Sc
1	0.02	1.0
2	0.04	1.0
3	0.06	1.0
4	0.08	1.0
5	0.04	7.0
6	0.04	5.0
7	0.04	2.0
8	0.04	0.5
9	0.04	0.1
10	0.03	3.0
11	0.05	3.0
12	0.02	4.0
13	0.01	6.0
14	0.04	10.0
15	0.04	9.0

Table 4.1: Sc- and V_p-values of the simulations in figure 4.8.

for $R_s = 2.5$, $\tau = 25$ and the Sc- and V_p-values listed in table 4.1. Figure 4.8 indicates whether or not a specific simulation exhibits negatively buoyant plumes. The graph confirms that for $V_p\, Sc\, l_s \leq 2.5$ descending plumes form, whereas flows with $V_p\, Sc\, l_s \geq 2.5$ exhibit rising plumes only.

Chapter 5

Two-component instabilities and shear

5.1 Introduction

When the density of a stably stratified fluid is a function of two scalar fields with differing diffusivities, and one of these scalars is unstably stratified, there exists the potential for a double-diffusive instability to evolve [29]. A prominent example concerns the ocean, as heat diffuses one hundred times faster in water than salt. Even if the two scalars diffuse at identical rates, an instability can form if the unstably stratified scalar has a settling velocity associated with it [5, 62]. This situation can be encountered in buoyant river outflows, where sediment is unstably stratified while the overall density gradient is stable due to salinity [52, 36, 53, 54].

An important feature of river outflows is the presence of shear along the lower boundary of the river plume. The effect of this shear on the growth of double-diffusive fingering has been the subject of several studies [50, 40, 41, 49], which found it to dampen the instability growth along the direction of the shear, thereby resulting in the formation of salt sheets. In studying the influence of asymptotically weak Couette flow on double-diffusive fingering, Linden [50] found that for large Prandtl numbers shear had a damping influence. For small Prandtl numbers, on the other hand, shear may amplify the fingering instability. Smyth & Kimura [40, 41] employed hyperbolic tangent temperature, salinity and velocity profiles within a linear stability analysis as well as direct numerical simulations (DNS) to analyze the effect of shear on fingering. These authors examined fluxes, the dissipation ratio and growth rates, and arrived at the conclusion that shear dampens the fingering instability. Radko *et al.*[49] showed that in a DNS, fingering fluxes in the presence of shear are a factor of 2-3 times smaller than without shear. Here we will investigate the effects of finite-strength shear on both the double-diffusive and the settling-driven instability. Towards this end, we would like to employ an infinite domain to eliminate the effects of solid boundaries, as well as uniform shear profiles without inflection points to avoid the presence of competing shear instabilities. As we will see, all of these goals can be accomplished by means of a transient growth analysis, which has the added benefit of providing detailed insight into the physical mechanisms at work.

Section 5.2 will define the problem and derive the linearized equations describing the instability growth. In section 5.3, we describe the adjoint method employed for calculating the objective gradients for the optimization procedure. Section 5.4 presents the results of this analysis, along with their physical interpretation.

5.2 Problem Formulation

Several strategies may appear feasible for investigating the effect of shear on double-diffusive and settling-driven instabilities. Linden [50] performed a linear stability analysis for a vertically bounded Couette flow with linear temperature and salinity gradients, as sketched in figure 5.1. However, in trying to extend this approach to the settling-driven instability, we found the eigenvalues and eigenvectors to strongly depend on the size of the domain, and to be dominated by boundary effects. This difficulty cannot be

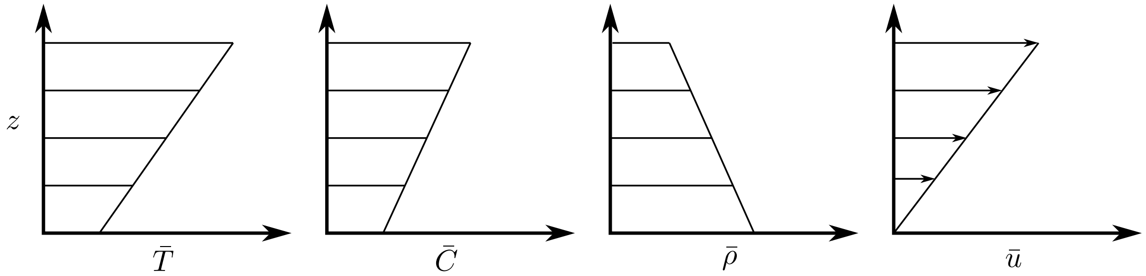

Figure 5.1: Background temperature $\bar{T}$, particle concentration $\bar{C}$, density $\bar{\rho}$ and x-velocity $\bar{u}$. Within the stable overall density stratification, the particle concentration is unstably stratified.

eliminated by considering a sedimenting particle concentration field in an unbounded error function-type background shear instead, as this set-up violates the quasi-steady base state approximation. For these reasons, we opt to solve an optimization problem in order to identify the maximum perturbation growth within a linearized framework. This approach no longer requires a quasi-steady state approximation, and it allows us to consider a wave-like perturbation with a time-dependent slope in an unbounded Couette flow. This concept is known as Kelvin waves, and it has been successfully employed in the study of the planar Couette flow [63, 64, 65, 66, 67].

Consider the Navier-Stokes equations in the Boussinesq approximation, along with convection-diffusion transport equations for temperature T^* and particle concentration C^*, a linear equation of state for the fluid density, and the continuity equation. With asterisks denoting dimensional quantities, these read

$$\begin{aligned}
\frac{\partial \mathbf{u}^*}{\partial t^*} + \mathbf{u}^* \cdot \boldsymbol{\nabla}^* \mathbf{u}^* &= -\frac{1}{\rho_0^*} \boldsymbol{\nabla}^* P^* + \nu^* \nabla^{*2} \mathbf{u}^* + \frac{\rho^*}{\rho_0^*} \mathbf{g}^* \ , && (5.1)\\
\frac{\partial T^*}{\partial t^*} + \mathbf{u}^* \cdot \boldsymbol{\nabla}^* T^* &= k_T^* \nabla^{*2} T^* \ , && (5.2)\\
\frac{\partial C^*}{\partial t^*} + \mathbf{u}^* \cdot \boldsymbol{\nabla}^* C^* &= k_C^* \nabla^{*2} C^* + V_{st}^* \frac{\partial C^*}{\partial z^*} \ , && (5.3)\\
\rho^* &= \rho_0^* (1 - \alpha^* (T^* - T_0^*) + \beta^* (C^* - C_0^*)) \ , && (5.4)\\
\boldsymbol{\nabla}^* \cdot \mathbf{u}^* &= 0 && (5.5)
\end{aligned}$$

Here $\mathbf{u}^* = (u^*, v^*, w^*)$ represents the velocity, ρ^* indicates the density, ρ_0^* is the density of a reference state with $T^* = T_0^*$ and $C^* = C_0^*$, P^* denotes the pressure, $\mathbf{g}^* = (0, 0, -g^*)$ the gravity vector, ν^* the kinematic viscosity, k_T^* and k_C^* represent the diffusivity of heat and particles, and α^* and β^* express the density dependence on temperature and particle concentration. V_{st}^* is the Stokes settling velocity

$$V_{st}^* = \frac{2 g^* r_p^{*2} (\rho_p^* - \rho_0^*)}{9 \mu^*} \ , \tag{5.6}$$

where r_p^* denotes the particle radius, ρ_p^* the particle density and μ^* the dynamic viscosity. Each variable q^* can be thought of as the sum of a background or base state $\bar{q}^*$, and the perturbation $q^{*\prime}$ from that state. We assume a background state of the form

$$\begin{aligned}
\bar{\mathbf{u}}^* &= (S^* z^*, 0, 0) \ , && (5.7)\\
\bar{T}^* &= \bar{T}_z^* z^* \ , && (5.8)\\
\bar{C}^* &= \bar{C}_z^* (z^* + V_{st}^* t^*) \ , && (5.9)\\
\frac{\partial \bar{P}^*}{\partial z^*} &= -\rho_0^* g^* \left[1 - \alpha^* (\bar{T}^* - T_0^*) + \beta^* (\bar{C}^* - C_0^*) \right] \ , && (5.10)
\end{aligned}$$

where $\bar{T}_z^*$ and $\bar{C}_z^*$ are positive constants, as sketched in figure 5.1. We remark that at a given location, the background particle concentration increases uniformly with time as a result of particle settling acting on the uniform background particle concentration z-gradient. The density contributions due to the background profiles, as well as the reference temperature and particle concentration, can be absorbed into the background pressure $\bar{P}^*$. By substituting $q^* = \bar{q}^* + q^{*\prime}$ into the governing equations, we obtain

$$\begin{aligned}
\frac{\mathrm{D}u^{*\prime}}{\mathrm{D}t^*} + S^* z^* \frac{\partial u^{*\prime}}{\partial x^*} + w^{*\prime} S^* &= -\frac{1}{\rho_0^*}\frac{\partial P^{*\prime}}{\partial x^*} + \nu^* \nabla^{*2} u^{*\prime} \ , && (5.11)\\
\frac{\mathrm{D}v^{*\prime}}{\mathrm{D}t^*} + S^* z^* \frac{\partial v^{*\prime}}{\partial x^*} &= -\frac{1}{\rho_0^*}\frac{\partial P^{*\prime}}{\partial y^*} + \nu^* \nabla^{*2} v^{*\prime} \ , && (5.12)\\
\frac{\mathrm{D}w^{*\prime}}{\mathrm{D}t^*} + S^* z^* \frac{\partial w^{*\prime}}{\partial x^*} &= -\frac{1}{\rho_0^*}\frac{\partial P^{*\prime}}{\partial z^*} + \nu^* \nabla^{*2} w^{*\prime} + g^*(\alpha^* T^{*\prime} - \beta^* C^{*\prime}) \ , && (5.13)\\
\frac{\mathrm{D}T^{*\prime}}{\mathrm{D}t^*} + S^* z^* \frac{\partial T^{*\prime}}{\partial x^*} &= k_T^* \nabla^{*2} T^{*\prime} - w^{*\prime}\frac{\partial \bar{T}^*}{\partial z^*} \ , && (5.14)\\
\frac{\mathrm{D}C^{*\prime}}{\mathrm{D}t^*} + S^* z^* \frac{\partial C^{*\prime}}{\partial x^*} &= k_C^* \nabla^{*2} C^{*\prime} - w^{*\prime}\frac{\partial \bar{C}^*}{\partial z^*} + V_{st}^* \frac{\partial C^{*\prime}}{\partial z^*} \ , && (5.15)\\
\boldsymbol{\nabla}^* \cdot \mathbf{u}^{*\prime} &= 0 \ , && (5.16)
\end{aligned}$$

where $\mathrm{D}/\mathrm{D}t = \partial/\partial t + \mathbf{u} \cdot \boldsymbol{\nabla}$ denotes the material derivative. We nondimensionalize the problem using the length, time, temperature and concentration scales according to Radko [29], where we replace salinity with particle concentration

$$d_c^* = \left(\frac{k_T^* \nu^*}{g^* \alpha^* |\bar{T}_z^*|}\right)^{1/4} \ , \quad t_c^* = \frac{(d_c^*)^2}{k_T^*} \ , \quad u_c^* = \frac{k_T^*}{d_c^*} \ , \quad P_c^* = \frac{\rho_0^* \nu^* k_T^*}{(d_c^*)^2} \ ,$$

$$T_c^* = d_c^* |\bar{T}_z^*| \ , \quad C_c^* = \frac{\alpha^*}{\beta^*} T_c^* \ . \tag{5.17}$$

Representative oceanic values of $\nu^* = 10^{-6}$ m/s^2, $k_T^* = \nu^*/7$, $|\bar{T}_z^*| = 0.01$ K/m and $\alpha^* = 2.07 \times 10^{-4}$ K^{-1} yield $d_c^* \approx 1$ cm and $t_c^* \approx 10^3$ s. After applying these scales and dropping the apostrophes, we obtain the nondimensional governing equations

$$\begin{aligned}
\frac{\partial u}{\partial t} + Sz\frac{\partial u}{\partial x} + wS + \mathbf{u}\cdot\boldsymbol{\nabla}u &= -Pr\frac{\partial P}{\partial x} + Pr\nabla^2 u\ , && (5.18)\\
\frac{\partial v}{\partial t} + Sz\frac{\partial v}{\partial x} + \mathbf{u}\cdot\boldsymbol{\nabla}v &= -Pr\frac{\partial P}{\partial y} + Pr\nabla^2 v\ , && (5.19)\\
\frac{\partial w}{\partial t} + Sz\frac{\partial w}{\partial x} + \mathbf{u}\cdot\boldsymbol{\nabla}w &= -Pr\frac{\partial P}{\partial z} + Pr\nabla^2 w + Pr(T-C)\ , && (5.20)\\
\frac{\partial T}{\partial t} + Sz\frac{\partial T}{\partial x} + w + \mathbf{u}\cdot\boldsymbol{\nabla}T &= \nabla^2 T\ , && (5.21)\\
\frac{\partial C}{\partial t} + Sz\frac{\partial C}{\partial x} + \frac{w}{R_\rho} + \mathbf{u}\cdot\boldsymbol{\nabla}C &= \frac{1}{\tau}\nabla^2 C + V_p\frac{\partial C}{\partial z}\ , && (5.22)\\
\boldsymbol{\nabla}\cdot\mathbf{u} &= 0\ . && (5.23)
\end{aligned}$$

Dimensionless parameters arise in the form

$$Pr = \frac{\nu^*}{k_T^*}\quad ,\quad \tau = \frac{k_T^*}{k_C^*}\quad ,\quad V_p = \frac{V_{st}^*}{u_c^*}\quad ,\quad R_\rho = \frac{\alpha^*\bar{T}_z^*}{\beta^*\bar{C}_z^*}\ . \tag{5.24}$$

Linearization around the background state, and using the continuity equation to eliminate pressure results in

$$\begin{aligned}
\frac{\partial}{\partial t}(\nabla^2 w) &= -Sz\frac{\partial}{\partial x}\nabla^2 w + Pr\nabla^4 w + Pr\left(\frac{\partial^2 T}{\partial x^2} + \frac{\partial^2 T}{\partial y^2}\right)\\
&\qquad -Pr\left(\frac{\partial^2 C}{\partial x^2} + \frac{\partial^2 C}{\partial y^2}\right)\ , && (5.25)\\
\frac{\partial}{\partial t}(T) &= -Sz\frac{\partial T}{\partial x} - w + \nabla^2 T\ , && (5.26)\\
\frac{\partial}{\partial t}(C) &= -Sz\frac{\partial C}{\partial x} - \frac{w}{R_\rho} + \nabla^2 C + V_p\frac{\partial C}{\partial z}\ . && (5.27)
\end{aligned}$$

We assume that the solution has the form of a plane wave with time-varying wavenumbers

$$q(x,y,z,t) = \widetilde{q}(t)\exp[ik(t)x + il(t)y + im(t)z]\ . \tag{5.28}$$

Substitution into (5.25)-(5.27) yields

$$\begin{aligned}
\frac{\mathrm{d}}{\mathrm{d}t}(K^2\widetilde{w}) + K^2\widetilde{w}\left(i\frac{\mathrm{d}k}{\mathrm{d}t}x + i\frac{\mathrm{d}l}{\mathrm{d}t}y + i\frac{\mathrm{d}m}{\mathrm{d}t}z\right) &= -ikSzK^2\widetilde{w} - PrK^4\widetilde{w} \\
&\quad + Pr(k^2+l^2)(\widetilde{T}-\widetilde{C}) \ , \quad (5.29) \\
\frac{\mathrm{d}}{\mathrm{d}t}(\widetilde{T}) + \widetilde{T}\left(i\frac{\mathrm{d}k}{\mathrm{d}t}x + i\frac{\mathrm{d}l}{\mathrm{d}t}y + i\frac{\mathrm{d}m}{\mathrm{d}t}z\right) &= -ikSz\widetilde{T} - \widetilde{w} - K^2\widetilde{T} \ , \quad (5.30) \\
\frac{\mathrm{d}}{\mathrm{d}t}(\widetilde{C}) + \widetilde{C}\left(i\frac{\mathrm{d}k}{\mathrm{d}t}x + i\frac{\mathrm{d}l}{\mathrm{d}t}y + i\frac{\mathrm{d}m}{\mathrm{d}t}z\right) &= -ikSz\widetilde{C} - \frac{\widetilde{w}}{R_\rho} - \frac{1}{\tau}K^2\widetilde{C} \\
&\quad + imV_p\widetilde{C} \ , \quad (5.31)
\end{aligned}$$

where

$$K^2(t) = k(t)^2 + l(t)^2 + m(t)^2 \ . \tag{5.32}$$

We would like to eliminate the terms with explicit dependence on z, so that we can transform the equations to wave space and assume an infinite domain for the perturbation fields. We do this by strategically choosing

$$\frac{\mathrm{d}k}{\mathrm{d}t} = 0 \ , \qquad \frac{\mathrm{d}l}{\mathrm{d}t} = 0 \ , \qquad \frac{\mathrm{d}m}{\mathrm{d}t} = -Sk \ . \tag{5.33}$$

Substitution into (5.29)-(5.31) and rearranging into matrix form yields

$$\frac{\mathrm{d}}{\mathrm{d}t}\begin{pmatrix} K^2\widetilde{w} \\ \widetilde{T} \\ \widetilde{C} \end{pmatrix} = \begin{pmatrix} -PrK^2 & Pr(k^2+l^2) & -Pr(k^2+l^2) \\ -K^{-2} & -K^2 & 0 \\ -R_\rho^{-1}K^{-2} & 0 & -\tau^{-1}K^2 + i(m_0 - Skt)V_p \end{pmatrix}\begin{pmatrix} K^2\widetilde{w} \\ \widetilde{T} \\ \widetilde{C} \end{pmatrix} \tag{5.34}$$

now with

$$K^2(t) = k^2 + l^2 + (m_0 - Skt)^2 \ , \tag{5.35}$$

where m_0 denotes the initial value of $m(t)$. We note that at a fixed time, (5.28) reduces to Fourier waves in space. Hence any perturbation can be represented by a superposition of these modes. Because the equations are linear, the solution to the PDEs is then given by the superposition of the solutions of the modes present in the initial condition. Just like in a traditional linear stability analysis, we consider one mode at a time, and then optimize to identify the fastest growing mode. We keep in mind that the growth may not be exponential in time, and that the spatial shape of the mode is time-dependent. The entire analysis can then be performed in wave space. For added convenience later on, we rewrite (5.34) as

$$\frac{\mathrm{d}}{\mathrm{d}t}\begin{pmatrix}\widetilde{w}\\ \widetilde{T}\\ \widetilde{C}\end{pmatrix} = \begin{pmatrix}\psi(t) & PrK^{-2}(k^2+l^2) & -PrK^{-2}(k^2+l^2)\\ -1 & -K^2 & 0\\ -R_\rho^{-1} & 0 & -\tau^{-1}K^2+i(m_0-Skt)V_p\end{pmatrix}\begin{pmatrix}\widetilde{w}\\ \widetilde{T}\\ \widetilde{C}\end{pmatrix}, \tag{5.36}$$

where the notation

$$\psi(t) = -PrK^2 + 2Sk(m_0 - Skt)K^{-2} \tag{5.37}$$

is employed to save space.

5.3 Optimization Procedure

We aim to identify the maximum of the gain

$$G = \frac{(|\widetilde{w}|^2 + |\widetilde{T}|^2 + |\widetilde{C}|^2)|_{t=t_{\text{end}}}}{(|\widetilde{w}|^2 + |\widetilde{T}|^2 + |\widetilde{C}|^2)|_{t=0}} \tag{5.38}$$

with respect to k, l, m_0, and the complex initial conditions for $\widetilde{w}$, $\widetilde{T}$ and $\widetilde{C}$. In the absence of shear ($S = 0$), the equations depend only on $k^2 + l^2$ instead of on k and l independently, so that we can set $l = 0$ without loss of generality. When shear is present, its influence is removed if $k = 0$ so that the unsheared result is recovered, although now as a function of l instead of k. In a linear stability analysis, growth rates for sheared double-diffusive fingering are generally lower for $k > 0$ than for $k = 0$ [50, 40], so that we expect the formation of "salt sheets" aligned in the direction of the shear, with $k = 0$. In the present investigation we set $l = 0$, so that we can isolate the effect of shear. We note that any problem with $l > 0$ can be converted to one with $l = 0$, although with different S- and k-values, by the transformation

$$k \leftarrow \sqrt{k^2 + l^2} \, , \tag{5.39}$$

$$S \leftarrow \frac{Sk}{\sqrt{k^2 + l^2}} \, . \tag{5.40}$$

In anticipation of findings to be discussed below, we remark that this transformation implies the following: If for $l = 0$, i.e. in the absence of spanwise perturbations, shear is observed to dampen the growth, we can conclude that the maximum sheared growth will likely occur for spanwise modes with $k = 0$, for which the unsheared growth results are recovered.

Since the ODE for which we optimize is linear, multiplying the initial condition by a complex constant will not affect the gain in (5.38). To remove this degree of freedom, we set

$$(|\widetilde{w}|^2 + |\widetilde{T}|^2 + |\widetilde{C}|^2)|_{t=0} = 1 \tag{5.41}$$

and optimize for

$$G = (|\widetilde{w}|^2 + |\widetilde{T}|^2 + |\widetilde{C}|^2)|_{t=t_{\text{end}}} \, . \tag{5.42}$$

We parameterize the initial condition constraint (5.41) by setting

$$\begin{aligned}
\widetilde{w}_{t=0} &= r_w e^{i\theta_w} \ , && (5.43)\\
\widetilde{T}_{t=0} &= r_T e^{i\theta_T} \ , && (5.44)\\
\widetilde{C}_{t=0} &= r_C e^{i\theta_C} \ . && (5.45)
\end{aligned}$$

Note that these three values can be multiplied by a factor of $e^{i\theta}$ for any θ without affecting (5.41). Consequently we set

$$\theta_w = 0 \tag{5.46}$$

and only optimize for θ_T and θ_C. Equation (5.41) yields

$$r_w^2 + r_T^2 + r_C^2 = 1 \ . \tag{5.47}$$

These three parameters and one constraint can be reduced to two free parameters ϕ_1 and ϕ_2 by using spherical coordinates

$$\begin{aligned}
r_w &= \cos(\phi_1)\cos(\phi_2) \ , && (5.48)\\
r_T &= \sin(\phi_1)\cos(\phi_2) \ , && (5.49)\\
r_C &= \sin(\phi_2) \ . && (5.50)
\end{aligned}$$

To summarize, we need to optimize over the four initial condition variables θ_T, θ_C, ϕ_1 and ϕ_2, from which the initial condition can be reconstructed by

$$\begin{aligned}
\widetilde{w} &= \cos(\phi_1)\cos(\phi_2) \ , && (5.51)\\
\widetilde{T} &= \sin(\phi_1)\cos(\phi_2)e^{i\theta_T} \ , && (5.52)\\
\widetilde{C} &= \sin(\phi_2)e^{i\theta_C} \ . && (5.53)
\end{aligned}$$

With $l = 0$ as discussed above, our goal is now to find the total derivative of G with respect to

$$\mathbf{p} = \begin{pmatrix} \phi_1 \\ \phi_2 \\ \theta_T \\ \theta_C \\ k \\ m_0 \end{pmatrix} \tag{5.54}$$

and then employ its gradient in a gradient-based optimization algorithm such as BFGS or nonlinear conjugate gradient, which is available in Matlab through the `fminunc()` function.

We calculate the gradient using the adjoint method, adapted from Gunzburger [68] and described in the following. We begin by defining a Lagrangian functional L

$$L = G + \int_0^{t_{\mathrm{end}}} (\mathbf{q}^+)^T \left(\frac{\mathrm{d}\mathbf{q}}{\mathrm{d}t} - A(t)\mathbf{q} \right) \, \mathrm{d}t \ , \tag{5.55}$$

where it is helpful to rewrite G as

$$G = \mathbf{q}(t_{\mathrm{end}})^T \mathbf{q}(t_{\mathrm{end}}) \ . \tag{5.56}$$

In (5.55), we define

$$A(t) = \begin{pmatrix} \mathbb{R}\mathrm{e}(B(t)) & -\mathbb{I}\mathrm{m}(B(t)) \\ \mathbb{I}\mathrm{m}(B(t)) & \mathbb{R}\mathrm{e}(B(t)) \end{pmatrix} \tag{5.57}$$

with

$$B(t) = \begin{pmatrix} -PrK^2 + 2Sk(m_0 - Skt)K^{-2} & PrK^{-2}(k^2+l^2) & -PrK^{-2}(k^2+l^2) \\ -1 & -K^2 & 0 \\ -R_\rho^{-1} & 0 & -\tau^{-1}K^2 + i(m_0 - Skt)V_p \end{pmatrix} \tag{5.58}$$

according to the system of ODEs in (5.36). The vector $\mathbf{q}$ and its initial condition $\mathbf{q}(0)$ are defined as

$$\mathbf{q}(t) = \begin{pmatrix} \mathbb{Re}(\widetilde{w}(t)) \\ \mathbb{Re}(\widetilde{T}(t)) \\ \mathbb{Re}(\widetilde{C}(t)) \\ \mathbb{Im}(\widetilde{w}(t)) \\ \mathbb{Im}(\widetilde{T}(t)) \\ \mathbb{Im}(\widetilde{C}(t)) \end{pmatrix}, \qquad \mathbf{q}(0) = \begin{pmatrix} \cos(\phi_1)\cos(\phi_2) \\ \sin(\phi_1)\cos(\phi_2)\cos(\theta_T) \\ \sin(\phi_2)\cos(\theta_C) \\ 0 \\ \sin(\phi_1)\cos(\phi_2)\sin(\theta_T) \\ \sin(\phi_2)\sin(\theta_C) \end{pmatrix} . \tag{5.59}$$

In (5.55), the Lagrange multiplier $\mathbf{q}^+$ can be chosen freely because we always enforce

$$\frac{\mathrm{d}\mathbf{q}}{\mathrm{d}t} - A(t)\mathbf{q} = 0 . \tag{5.60}$$

Because constraint (5.60) is always satisfied, we have

$$\frac{\mathrm{d}L}{\mathrm{d}\mathbf{p}} = \frac{\mathrm{d}G}{\mathrm{d}\mathbf{p}} . \tag{5.61}$$

Our goal now is to find this gradient $\mathrm{d}L/\mathrm{d}\mathbf{p}$ in such a way that we will not have to calculate $\mathrm{d}\mathbf{q}/\mathrm{d}\mathbf{p}$, except at $t = 0$, which is easily done using (5.59). We begin with

$$\frac{\mathrm{d}L}{\mathrm{d}\mathbf{p}} = \frac{\partial G}{\partial \mathbf{q}(t_{\text{end}})}\frac{\mathrm{d}\mathbf{q}(t_{\text{end}})}{\mathrm{d}\mathbf{p}} + \frac{\partial G}{\partial \mathbf{p}} + \int_0^{t_{\text{end}}} (\mathbf{q}^+)^T \left(\frac{\mathrm{d}}{\mathrm{d}\mathbf{p}}\frac{\mathrm{d}\mathbf{q}}{\mathrm{d}t} - A(t)\frac{\mathrm{d}\mathbf{q}}{\mathrm{d}\mathbf{p}} - \frac{\mathrm{d}A(t)}{\mathrm{d}\mathbf{p}}\mathbf{q} \right) \mathrm{d}t \tag{5.62}$$

and use integration by parts on the term containing $\mathrm{d}\mathbf{q}/\mathrm{d}t$

$$\begin{aligned}\int_0^{t_{\text{end}}} (\mathbf{q}^+)^T \frac{\mathrm{d}}{\mathrm{d}\mathbf{p}}\frac{\mathrm{d}\mathbf{q}}{\mathrm{d}t}\ \mathrm{d}t &= \left.\left((\mathbf{q}^+)^T\frac{\mathrm{d}\mathbf{q}}{\mathrm{d}\mathbf{p}}\right)\right|_{t=t_{\text{end}}} \\ &- \left.\left((\mathbf{q}^+)^T\frac{\mathrm{d}\mathbf{q}}{\mathrm{d}\mathbf{p}}\right)\right|_{t=0} \\ &- \int_0^{t_{\text{end}}} \left(\frac{\mathrm{d}\mathbf{q}^+}{\mathrm{d}t}\right)^T \frac{\mathrm{d}\mathbf{q}}{\mathrm{d}\mathbf{p}}\ \mathrm{d}t\ . \qquad (5.63)\end{aligned}$$

We substitute (5.63) into (5.62)

$$\begin{aligned}\frac{\mathrm{d}L}{\mathrm{d}\mathbf{p}} &= -\mathbf{q}^+(0)^T\frac{\mathrm{d}\mathbf{q}(0)}{\mathrm{d}\mathbf{p}} + \frac{\partial G}{\partial \mathbf{p}} - \int_0^{t_{\text{end}}} (\mathbf{q}^+)^T\frac{\mathrm{d}A(t)}{\mathrm{d}\mathbf{p}}\mathbf{q}\ \mathrm{d}t \\ &- \int_0^{t_{\text{end}}}\left(\left(\frac{\mathrm{d}\mathbf{q}^+}{\mathrm{d}t}\right)^T + (\mathbf{q}^+)^T A(t)\right)\frac{\mathrm{d}\mathbf{q}}{\mathrm{d}\mathbf{p}}\ \mathrm{d}t \\ &+ \left.\left[\left((\mathbf{q}^+)^T + \frac{\partial G}{\partial \mathbf{q}}\right)\frac{\mathrm{d}\mathbf{q}}{\mathrm{d}\mathbf{p}}\right]\right|_{t_{\text{end}}} \qquad (5.64)\end{aligned}$$

and pick $\mathbf{q}^+$ so that there is only dependence on $\mathrm{d}\mathbf{q}/\mathrm{d}\mathbf{p}$ at $t = 0$. This yields

$$\mathbf{q}^+(t_{\text{end}}) = -\left(\frac{\partial G}{\partial \mathbf{q}(t_{\text{end}})}\right)^T = -2\mathbf{q}(t_{\text{end}})\ , \qquad (5.65)$$

as well as an ODE for $\mathbf{q}^+$

$$\frac{\mathrm{d}\mathbf{q}^+}{\mathrm{d}t} = -A(t)^T\mathbf{q}^+\ , \qquad (5.66)$$

which we integrate from $t = t_{\text{end}}$ to $t = 0$. In combination with the fact that G has no explicit dependence on $\mathbf{p}$, this yields the gradient

$$\frac{\mathrm{d}G}{\mathrm{d}\mathbf{p}} = -\mathbf{q}^+(0)^T\frac{\mathrm{d}\mathbf{q}(0)}{\mathrm{d}\mathbf{p}} - \int_0^{t_{\text{end}}} (\mathbf{q}^+)^T\frac{\mathrm{d}A(t)}{\mathrm{d}\mathbf{p}}\mathbf{q}\ \mathrm{d}t\ . \qquad (5.67)$$

The method used to calculate the gradient is now as follows. For a given initial condition $\mathbf{q}(0)$, k and m_0, we integrate (5.60) in time from $t = 0$ to $t = t_{\text{end}}$. We then use the result $\mathbf{q}(t_{\text{end}})$ to calculate $\mathbf{q}^{+}(t_{\text{end}})$ using (5.65). With $\mathbf{q}^{+}(t_{\text{end}})$ as an initial condition, we integrate (5.66) from $t = t_{\text{end}}$ to $t = 0$. We then use $\mathbf{q}(t)$, $\mathbf{q}^{+}(t)$ and $\mathbf{q}(0)$ along with (5.59) to evaluate (5.67). We validated equation (5.67) using finite differences applied to direct compuations of G using (5.38).

5.4 Results

Figure 5.2 shows a representative set of optimization results for the fingering instability, with $Pr = 7$, $\tau = 100$, $R_\rho = 2$ and $V_p = 0$. It compares the case $S = 0.1$ with its no-shear counterpart. For the no-shear case, the dotted lines demonstrate the excellent agreement between the optimization results for large t_{end} and corresponding linear stability results. For small times $t_{\text{end}} \leq 5$, on the other hand, the optimization results deviate strongly from the linear stability results. In the following, we will first examine the reasons for this transient phenomenon in more detail, and then proceed to discuss the effects of Pr, τ, R_ρ and V_p on the fingering and-settling driven instabilities in the presence of shear.

5.4.1 Initial growth and the Orr mechanism

The initial fast growth seen in figure 5.2 occurs when $k \to 0$ and $m_0 \to 0$. It is present with and without shear, and as we will see below, it also exists for the settling-driven instability, cf. figure 5.8. In this limit, the system of ODEs (5.36) reduces to

$$\frac{\partial}{\partial t}\begin{pmatrix}\widetilde{w}\\ \widetilde{T}\\ \widetilde{C}\end{pmatrix} = \begin{pmatrix}0 & Pr & -Pr\\ -1 & 0 & 0\\ -R_\rho^{-1} & 0 & 0\end{pmatrix}\begin{pmatrix}\widetilde{w}\\ \widetilde{T}\\ \widetilde{C}\end{pmatrix}, \tag{5.68}$$

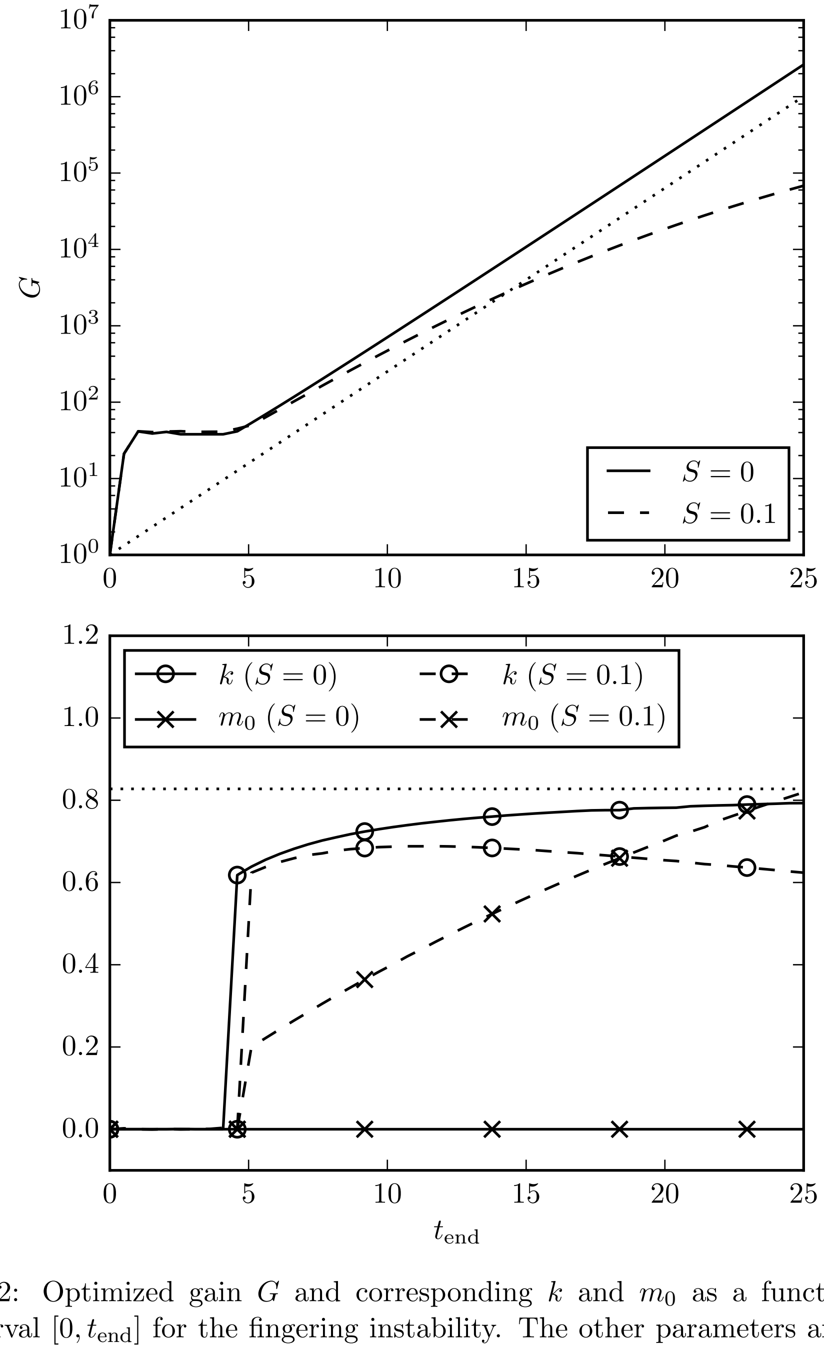

Figure 5.2: Optimized gain G and corresponding k and m_0 as a function of the time interval $[0, t_{\text{end}}]$ for the fingering instability. The other parameters are $Pr = 7$, $\tau = 100$, $R_\rho = 2$ and $V_p = 0$. The dotted lines correspond to linear stability results for the maximum growth rate and corresponding k-value, in the absence of shear.

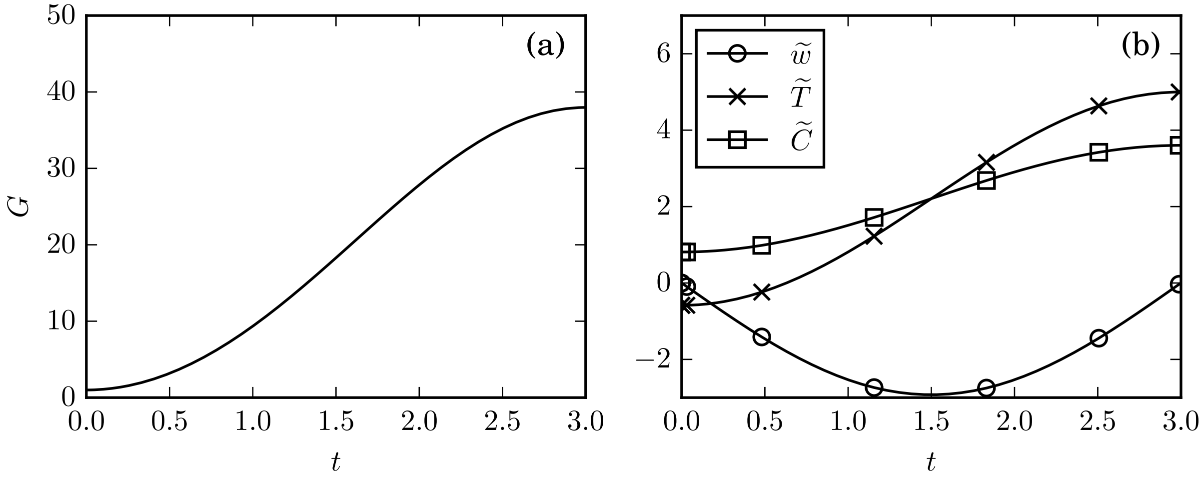

Figure 5.3: The optimally growing solution for $t_{\text{end}} = 3$ with $Pr = 7$, $\tau = 100$, $R_\rho = 2$, $V_p = 0$ and $S = 0$. a) the gain G, and b) the solution components. Here the solution is real.

so that S no longer appears. The fast initial growth occurs when $\widetilde{T}$ and $\widetilde{C}$ initially have opposite signs, so they act in phase on the density field, as higher $\widetilde{T}$ and lower $\widetilde{C}$ both reduce the overall density. As a result $\widetilde{w}$ grows strongly, which in turn will cause $\widetilde{T}$ and $\widetilde{C}$ to move in the same direction until they eventually are of the same sign and sufficiently large for the transient growth to decay. A representative example is shown in figure 5.3, which displays the overall gain and individual solution components as functions of time for the optimal solution with $t_{\text{end}} = 3$ and the same parameters as in figure 5.2. At first, $\widetilde{T}$ and $\widetilde{C}$ have opposite signs, which causes $\widetilde{w}$ to become negative. This negative $\widetilde{w}$ causes both $\widetilde{T}$ and $\widetilde{C}$ to increase. Since $R_\rho > 1$, $\widetilde{w}$ affects $\widetilde{T}$ more strongly than $\widetilde{C}$. When $\widetilde{T}$ and $\widetilde{C}$ cross, $\widetilde{w}$ stops growing and begins to decay. The overall gain continues to increase until the point where $\widetilde{w} = 0$, at which point $\widetilde{T}$ and $\widetilde{C}$ would begin to decrease.

This transient growth mechanism relies on the existence of density gradients, and it occurs whether or not shear is present. This is in contrast to the Orr mechanism [69], which requires shear and does not depend on density gradients. The Orr mechanism is related to the tilting of the plane perturbation vorticity wave by the background shear. If this wave is initially tilted against the shear, its vorticity contours are relatively close together. As m decreases with time due to the shear and the perturbation wave tilts into an upright position, the vorticity contours separate. Since the strength of the perturbation vorticity wave is conserved during this tilting process, the kinetic energy of the associated perturbation velocity field increases. As the background shear tilts the wave past the upright position, the perturbation vorticity contours come closer together again, and the associated kinetic energy decreases. The maximum gain due to this inviscid Orr mechanism can be found by considering the relationship between vorticity and vertical velocity, which can be derived from the definition of vorticity and continuity

$$\frac{\partial \omega}{\partial x} = \nabla^2 w \ . \tag{5.69}$$

By substituting the time dependent plane wave (5.28) into this equation, we obtain

$$\widetilde{w} = -\frac{ik}{k^2 + (m_0 - Skt)^2}\widetilde{\omega} \ . \tag{5.70}$$

The maximum $\widetilde{w}$ will occur when $t = m_0/(Sk)$, i.e. when $m = 0$ and the wave is vertical. The associated maximum gain is

$$G_w = \frac{|\widetilde{w}|^2|_{t=t_{\text{end}}}}{|\widetilde{w}|^2|_{t=0}} = \frac{(k^2 + m_0^2)^2}{k^4} \ , \tag{5.71}$$

where G_w differs from G in (5.38) in that G_w only contains $\widetilde{w}$ and not $\widetilde{T}$ and $\widetilde{C}$, and the second equality reflects the fact that the vorticity of a fluid element is conserved over time. If $m_0 \neq 0$, this means that the inviscid Orr mechanism would result in infinite gain as the optimizer chooses smaller and smaller k, which is the same limit that drives the transient growth mechanism described earlier. At this point one may wonder why the gain does not become infinite for cases with shear as $k \to 0$. To answer this question, we need to consider the time it takes for shear to tilt the wave into the upright position

$$t = \frac{m_0}{Sk} \ , \tag{5.72}$$

which is the time it takes for the vertical wavenumber m to decrease from m_0 initially to 0. We can make m_0 as small as we like, but in order to get infinite gain, k must approach 0 faster. This means that as $k \to 0$, the time until the infinite gain is realized becomes infinite. At this point, it becomes helpful to include the effects of viscosity. Since viscous forces would have an infinite amount of time to dampen the Orr mechanism, it is not immediately obvious whether infinite gain can be achieved in the presence of viscosity. We begin by considering the ODE for $\widetilde{w}$ in an unstratified two-dimensional case with viscosity

$$\frac{\mathrm{d}\widetilde{w}}{\mathrm{d}t} = \left(-Pr(k^2 + (m_0 - Skt)^2) + \frac{2Sk(m_0 - Skt)}{k^2 + (m_0 - Skt)^2} \right) \widetilde{w} \ . \tag{5.73}$$

This ODE can be obtained from (5.36) by neglecting $\widetilde{T}$ and $\widetilde{C}$. The analytical solution is

$$\widetilde{w}(t) = \widetilde{w}(0) \exp\left[-\int_0^t Pr(k^2 + (m_0 - Skt')^2) \ \mathrm{d}t' \right] \exp\left[\int_0^t \frac{2Sk(m_0 - Skt')}{k^2 + (m_0 - Skt')^2} \ \mathrm{d}t' \right] \ . \tag{5.74}$$

We know from our analysis of the inviscid problem that the maximum value of the second exponential is $(k^2 + m_0^2)/k^2$ and occurs when $t = m_0/(Sk)$. This value is the square root of the maximum gain from (5.71). We can evaluate the first integral, which expresses the influence of viscosity, at $t = m_0/(Sk)$ to complete the expression

$$\frac{\widetilde{w}(\frac{m_0}{Sk})}{\widetilde{w}(0)} = \exp\left[-\frac{(3k^2 m_0 + m_0^3)Pr}{3Sk} \right] \frac{k^2 + m_0^2}{k^2} \ . \tag{5.75}$$

This expression for the growth of the viscous Orr mechanism was also derived by Craik

& Criminale [66]. If we take the limit of (5.75) as $k \to 0$ with $m_0 > 0$, we see that the gain will become zero because the exponential decay dominates. However, if we choose a relation between k and m_0 of the form

$$k = Cm_0^n \tag{5.76}$$

where C and n are constants, and substitute that into (5.75), we obtain

$$\frac{\widetilde{w}(\frac{m_0}{Sk})}{\widetilde{w}(0)} = \exp\left[-\frac{(3C^2m_0^{2n-2}+1)Pr}{3SCm_0^{n-3}}\right]\frac{C^2m_0^{2n-2}+1}{C^2m_0^{2n-2}} \ . \tag{5.77}$$

The rightmost fraction in this equation shows us that if we wish to obtain infinite gain as $m_0 \to 0$, we need to choose $n > 1$, but this would mean that infinite time would be required to realize that infinite gain, seen in (5.72). Alternatively, we can choose $n = 1$ and have an arbitrarily large gain as $C \to 0$. However, (5.72) shows that after choosing $n = 1$ and substituting $k = Cm_0$, infinite time is required to produce the infinite gain as $C \to 0$. Either way, as long as $n < 3$, the exponential term will approach one as $m_0 \to 0$. Consequently, viscosity will not prevent the Orr mechanism from producing infinite gain, but infinite time will also be required to produce the infinite gain.

If we choose $n = 1$, we can construct a function that gives the maximum gain from the inviscid Orr mechanism as a function of t_{end}. Setting $k = Cm_0$ in (5.72) gives $C = 1/(St_{\text{end}})$. This is the C-value that corresponds to the wave with k and m_0 that the Orr mechanism can tilt into a fully upright position by time t_{end}. Setting $k = Cm_0$ and $C = 1/(St_{\text{end}})$ in (5.71) gives

$$G_w = (1 + S^2t_{\text{end}}^2)^2 \ . \tag{5.78}$$

In this paper, we study the effects of shear by setting $S = 0.1$. This means that the Orr mechanism will require a long time to produce large gain as $k \to 0$ and $m_0 \to 0$, even in the absence of viscosity. For the times that we considered, the growth of the settling or fingering instability was always larger than the growth of the Orr mechanism as $k \to 0$ and $m_0 \to 0$. We note that this does not imply that the Orr mechanism is generally irrelevant, as there are cases when it can enhance the gain caused by the instability. This will be discussed in sections 5.4.2 and 5.4.3.

5.4.2 Effect of shear on the fingering instability

To study the gain of the fingering instability with and without shear, we analyze the case of $Pr = 7$, $\tau = 100$, $R_\rho = 2$ and $V_p = 0$, for $S = 0$ and 0.1, respectively. Figure 5.2 shows the optimal gain G as a function of time t_{end}, along with the k- and m_0-values that produce this gain. Without shear, the optimally growing mode has $m = m_0 = 0$ and produces roughly exponential growth beyond the transient phase. The growth rate and most amplified k-value from linear stability theory [5], also shown in figure 5.2, agree closely with the gain obtained from the present analysis. Since the mode with $m = 0$ has no dependence on z, it is commonly referred to as the "elevator mode." With shear, the gain is smaller and $m_0 > 0$. Larger times t_{end} result in larger initial values m_0, so that the flow can spend most of the time interval over which the gain is evaluated near $m = 0$, where the fingering instability experiences maximum growth. Having $m_0 > 0$ also allows for the Orr mechanism to provide some additional growth. Since for $l = 0$ the shear reduces the gain of modes with $k > 0$, the discussion at the beginning of section 5.3 suggests that for the fingering case with shear optimal growth will occur for $k = 0$ and $l > 0$, which corresponds to a salt sheet. This is consistent with previous work on the interaction of the fingering instability with shear [50, 40, 41, 49].

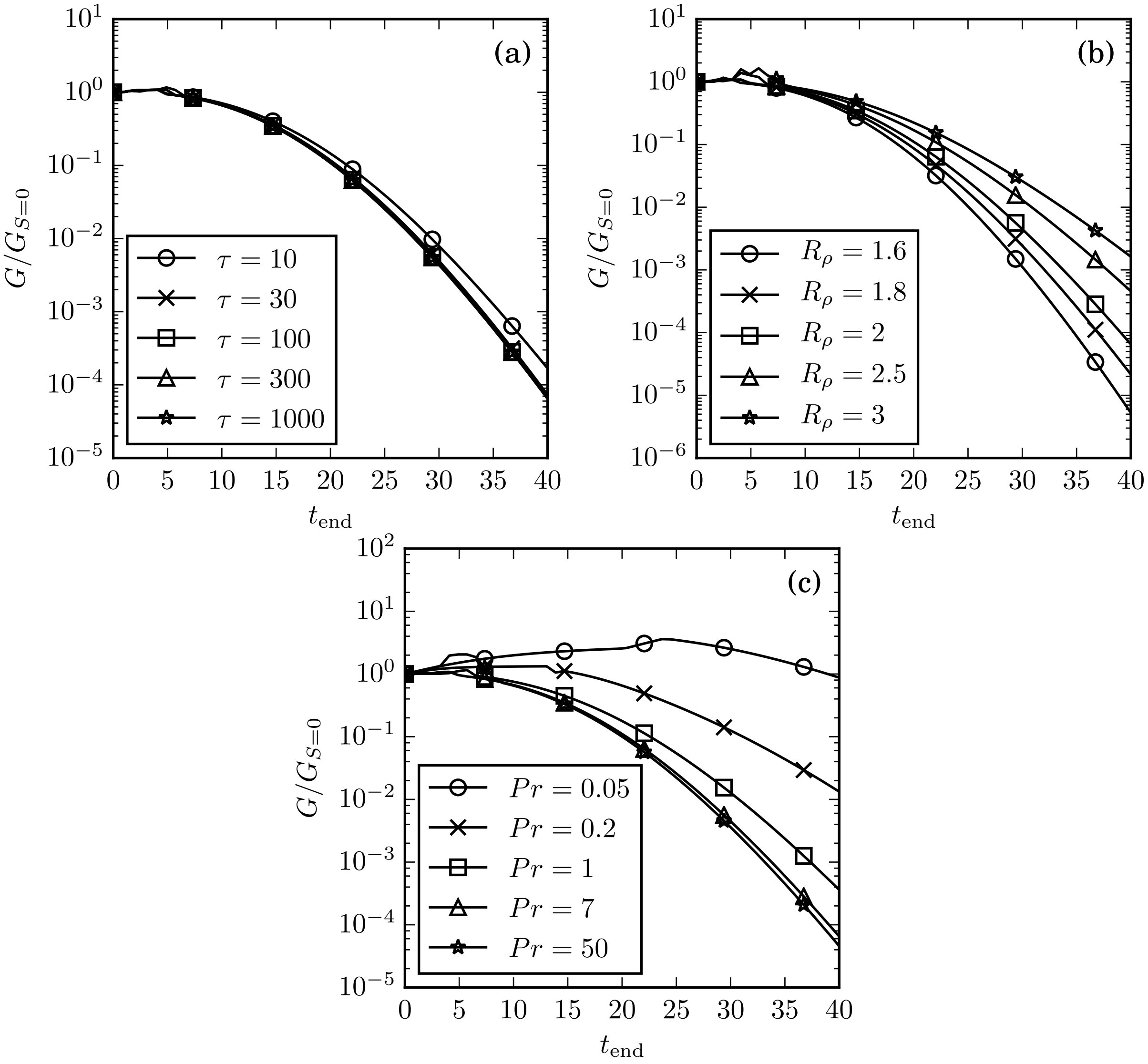

Figure 5.4: Ratio of sheared optimal gain with $S = 0.1$ to unsheared optimal gain for the fingering instability. Unless noted otherwise in the legend, the parameter values are $Pr = 7$, $\tau = 100$, $R_\rho = 2$ and $V_p = 0$.

Influence of τ and R_ρ

To determine how the damping effect of shear on the fingering instability depends on τ and R_ρ, we calculate the optimal growth for the base case parameters and varying τ- and R_ρ-values, for both $S = 0$ and 0.1. Figures 5.4a and b show the ratio of the sheared to the unsheared gain as a function of t_{end} for different τ- and R_ρ-values. Increasing τ

from 10 to 1,000 slightly increases the damping influence of shear. Similarly, lower values of R_ρ are affected somewhat more strongly by shear than higher values. Since lower τ and higher R_ρ correspond to weaker unsheared fingering, we can summarize these trends by stating that weaker fingering generally is affected less by the presence of shear.

These trends can be understood on the basis of the linear stability results for the case without shear. Figure 5.5 shows these linear stability results for a) the base case, b) the base case but with $\tau = 10$, and c) the base case but with $R_\rho = 3$. Without shear, as $t_{\text{end}} \to \infty$ the optimal growth will approach the fastest growing linearly unstable mode, as seen in figure 5.2. When shear is added, the vertical wavenumber m becomes a function of t, with $m(t) = m_0 - Skt$. The values that m takes between $t = 0$ and t_{end} are drawn as solid lines in figure 5.5. By approximating the growth of the sheared solution as locally exponential in time, we obtain

$$\frac{\mathrm{d}G}{\mathrm{d}t} = 2\sigma(t)G \ , \tag{5.79}$$

where G is the gain and $\sigma(t)$ the instantaneous growth rate from the linear stability analysis at $(k, m(t))$. The factor of 2 arises because the gain is the sum of the squares of the solution components. Taking the ratio of this approximation to the linear growth rate for the unsheared growth yields a damping coefficient

$$D(t_{\text{end}}) = \frac{G_{S=0.1}}{G_{S=0}} = \exp\left[2\left(\int_0^{t_{\text{end}}} \sigma(t) - \sigma_{max}\ \mathrm{d}t\right)\right] \ . \tag{5.80}$$

Figure 5.6 shows $D(t_{\text{end}} = 40)$ against the actual damping at $t_{\text{end}} = 40$ evaluated from the optimization calculations. Equation (5.80) reproduces the correct trend for the strength of the damping, which suggests that the trends of figure 5.4a-b are due to the fact that those parameter combinations for which σ depends more weakly on (k, m) are damped less by shear.

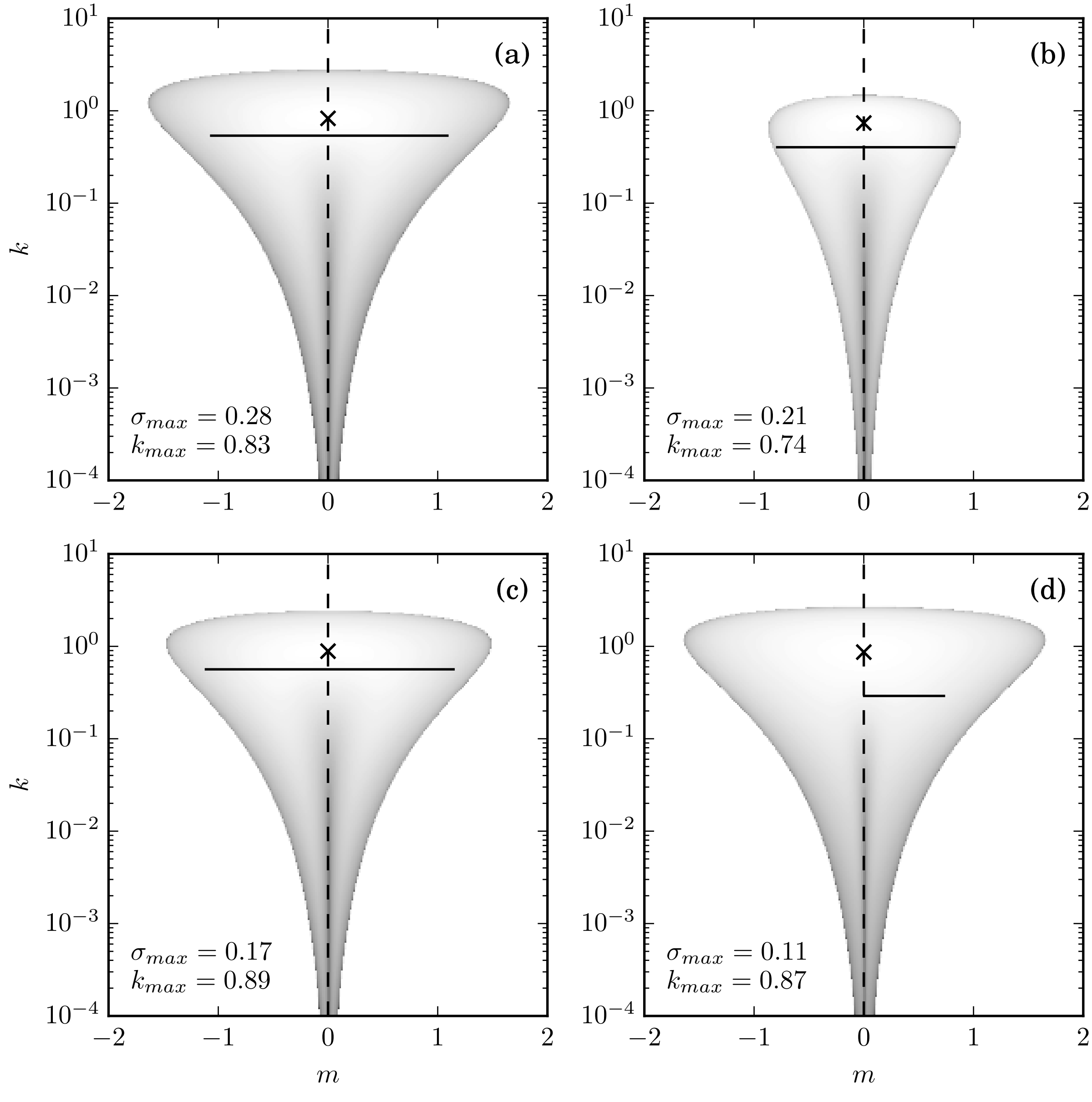

Figure 5.5: The unsheared case $S = 0$: linear stability analysis growth rate vs. horizontal wavenumber k and vertical wavenumber m for the parameter combinations: (a) base case of $Pr = 7$, $\tau = 100$, $R_\rho = 2$ and $V_p = 0$, (b) decreased $\tau = 10$, (c) increased $R_\rho = 3$, and (d) decreased $Pr = 0.05$. The shading is logarithmic, and the maximum growth rates are marked with an X. The horizontal black lines represent the paths of the non-modal optimal growth from $t = 0$ to t_{end} for $S = 0.1$ according to $m = m_0 - Skt$. (a-c): $t_{\text{end}} = 40$, (d) and $t_{\text{end}} = 25$.

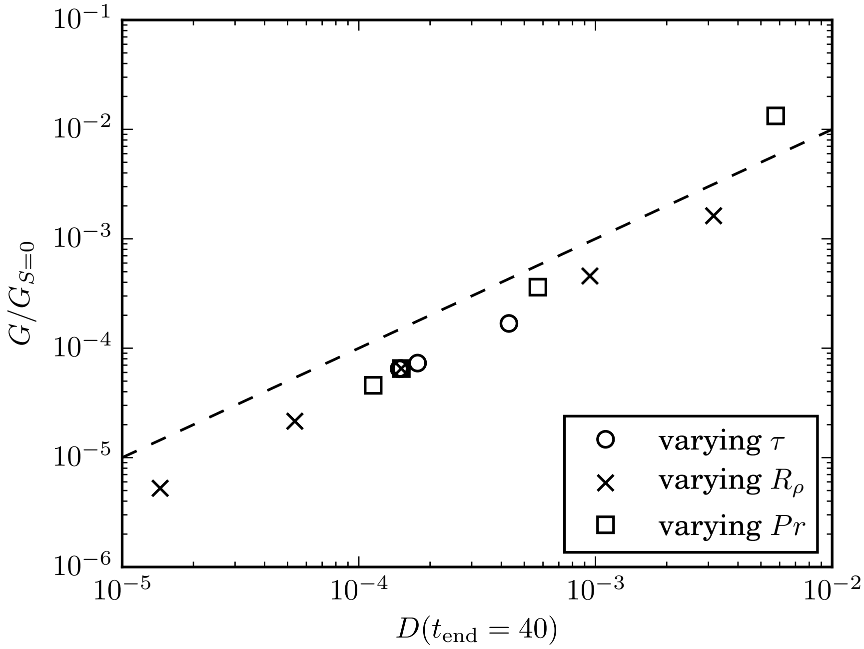

Figure 5.6: Actual damping $G(S)/G_{S=0}$ for $S = 0.1$ as a function of predicted damping (5.80) from assuming locally exponential growth as $m(t) = m_0 - Skt$ changes over time. The correct trend is recovered for all parameter combinations, although the predictions are a factor of 2-3 too small. Values of τ are 10, 30, 100, 300 and 1000. Values of R_ρ are 1.6, 1.8, 2, 2.5 and 3. Values of Pr are 0.2, 1, 7 and 50.

The effects of transient growth may still play a role in the imperfect agreement of figure 5.6, but they do not dominate the overall trends as τ and R_ρ are varied. In the presence of shear, transient growth affects the solution at all times since the local eigenmodes constantly change as a result of the time dependence of $m(t)$. In addition, the Orr mechanism provides a boost of $\widetilde{w}$ as m crosses zero, and subsequently causes extra damping of $\widetilde{w}$ as m moves away from zero.

According to (5.80), smaller values of $\sigma - \sigma_{max}$ reduce the damping effect of shear. Figures 5.7a and b show the dependence of $\sigma - \sigma_{max}$ on k (for $m = 0$) and on m (for $k = k_{max}$). Here k_{max} is the k-value for which σ_{max} occurs. Even though figure 5.4a indicates that $\tau = 10$ is damped less than $\tau = 1,000$, σ is reduced more for $\tau = 10$ along both of the paths shown in figures 5.7a and b. This apparent contradiction is resolved by the fact that for $\tau = 10$ the optimized growth path proceeds along a reduced value $k < k_{max}$, as seen in figure 5.5b. Although σ is reduced less for $\tau = 10$ along this path with $k < k_{max}$, this would not be hypothesized from figure 5.7b. The fact that σ is reduced more for $\tau = 10$ along $m = 0$ as k is reduced makes it difficult to produce a physical explanation why σ is reduced less along the optimal path for $\tau = 10$.

Influence of Pr

Figure 5.4c shows that shear has less of a damping effect on flows with with smaller Pr-values, and even produces additional transient growth when $Pr = 0.05$. As indicated by figure 5.6, the general trend can once again be explained in terms of linear stability analysis growth rates, with the exception of $Pr = 0.05$. Figure 5.7c shows that σ is more sensitive to m for high than for low Pr, which is consistent with the fact that high Pr flows get damped more. This allows us to formulate a physical argument for why there is less damping by shear when Pr is small.

We recall that the fingering instability is both driven and damped by diffusion, in the following sense. Deviations from the base state in both T and C contribute to vorticity generation. Since T is stably stratified, the T-related vorticity is stabilizing. Correspondingly, since C is unstably stratified, the C-related vorticity has a destabilizing influence. As the relative importance of diffusion grows with increasing k or m, the larger diffusivity of T causes the T-vorticity to be damped more than the C-vorticity, resulting in a net increase in destabilizing vorticity. In addition, as k is increased independently of m, the $(1, 2)$ and $(1, 3)$ terms in (5.36) show that vertical velocity generation grows proportionally to $k^2/(k^2 + m^2)$. This effect is influential since the interaction of the vertical velocity with the background T- and C-gradients drives the instability.

When Pr is reduced, vertical velocity generation and diffusion are both reduced. As the top row coefficients in (5.36) show, this results in smaller overall vertical velocity

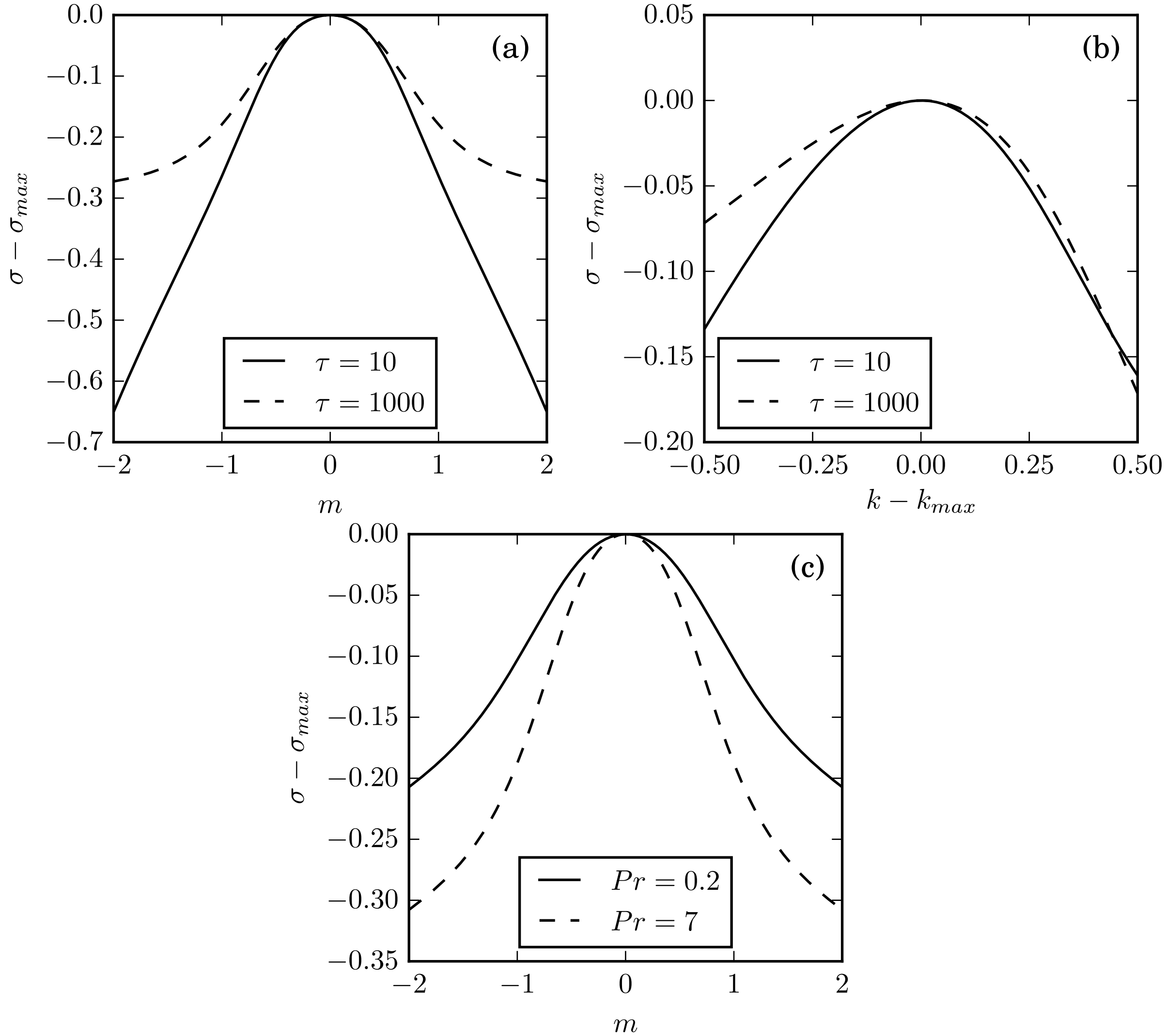

Figure 5.7: (a) $\sigma - \sigma_{max}$ as a function of m for $k = k_{max}$, where σ_{max} is the maximum growth rate and k_{max} is the value of k where σ_{max} occurs. (b) $\sigma - \sigma_{max}$ as a function of k with $m = 0$. (c) $\sigma - \sigma_{max}$ as a function of m with $k = k_{max}$ for two values of Pr. In (a) and (b), σ is more sensitive to k and m when $\tau = 10$ compared to $\tau = 1000$. Other parameters are $Pr = 7$, $R_\rho = 2$ and $V_p = 0$. In (c), σ is more sensitive to m when $Pr = 7$. The other parameters are $\tau = 100$, $R_\rho = 2$ and $V_p = 0$.

growth on the left hand side. To compensate, it becomes relatively more advantageous to increase the double-diffusive effect by increasing $|m|$. Increasing $|m|$ accomplishes three things. Firstly, it increases the importance of diffusion, which decreases the growth rate. Secondly, because of increased diffusion, there is also a stronger double-diffusive effect, which enhances the growth rate. Thirdly, it decreases the vertical velocity production terms $(1,2)$ and $(1,3)$ in (5.36), which decreases the growth rate. The overall effect of increasing $|m|$ is to decrease the growth rate. When Pr is small, increasing $|m|$ decreases the vertical velocity generation terms less relative to the changes in the other terms in (5.36), reducing the influence of one of the reasons why increasing $|m|$ lowers the growth rate. The fact that the overall growth rate is less sensitive to m when Pr is small causes shear to affect the solution growth less when Pr is small.

For $Pr = 0.05$ the sheared case grows more strongly than the unsheared one, as a result of the Orr mechanism. The solid black line in figure 5.5d indicates that for $Pr = 0.05$ and $t_{\text{end}} = 25$ we have $m(t_{\text{end}}) = 0$. This means that the Orr mechanism growth is at its strongest for $t = t_{\text{end}}$ when $Pr = 0.05$. The Orr mechanism can play a more prominent role in determining the optimal growth when Pr is low because this implies low viscosity. The reduced damping effect of viscosity on the Orr mechanism is reflected by the exponential term in (5.75). Equation (5.75) can also provide an estimate of the maximum gain from the Orr mechanism alone. Towards this end, if we assume that $\widetilde{T}$ and $\widetilde{C}$ are constant in time, the maximum gain from the Orr mechanism would be about one third the result of (5.75) squared. For the present case with $Pr = 0.05$ and $t_{\text{end}} = 25$, this evaluates to about 9, which is consistent with the results in figure 5.5d. For $Pr = 0.2$, the estimate is reduced to about 1.25, meaning that the Orr mechanism would provide much less of a boost. For $Pr \geq 0.2$, optimal growth is achieved by having $m(t)$ spend roughly equal amounts of time on either side of zero, as seen in figure 5.5. Since this path for $m(t)$ is twice as long, larger k can be accommodated with $\mathrm{d}m/\mathrm{d}t = -Sk$. Because these larger k-values produce stronger growth, their overall growth is higher without relying on the Orr mechanism.

5.4.3 Effect of shear on the settling instability

In order to investigate the effect of shear on the settling-driven instability [5], we set $\tau = 1$ to eliminate any double-diffusive effects. For the case of $Pr = 7$, $R_\rho = 2$ and $V_p = 1$, figure 5.8 shows that shear dampens the settling-driven instability, just as it dampens the fingering instability. Recall that the streamwise salt sheets discussed above in the context of the double-diffusive instability were oriented vertically, since the unsheared instability favors the $m = 0$ mode. For the settling-driven instability the situation is quite different. Since now $m \neq 0$ for the unsheared case, the "particle sheets" will be tilted in the spanwise direction. The linear stability analysis of [5] furthermore showed that the unsheared case favors two equally unstable modes with opposite wave slopes for the settling-driven instability. DNS simulations by the same authors indicated that both of these modes are present, resulting in a criss-cross pattern of waves. Hence we predict that in a three-dimensional flow with shear acting in the x, z-plane the initially dominant settling-driven instability mode will have the shape of this criss-cross pattern in the y, z-plane, while being invariant in the x-direction. This will give rise to "tube-like" structures, rather than sheets. In the following sections we examine the quantitative effect of shear on various aspects of the settling-driven instability.

Influence of V_p

To determine how the effect of shear depends on the setlling velocity, which acts as proxy for the particle size, we calculate the maximum gain with $S = 0$ and 0.1, and for $V_p = (1, 1.25, 1.5, 1.75, 2)$. The ratio of the sheared to the unsheared gain displayed in figure 5.9 demonstrates that the effect of shear on the settling-driven instability increases with V_p.

In order to explain this trend, we first review the mechanism behind the settling

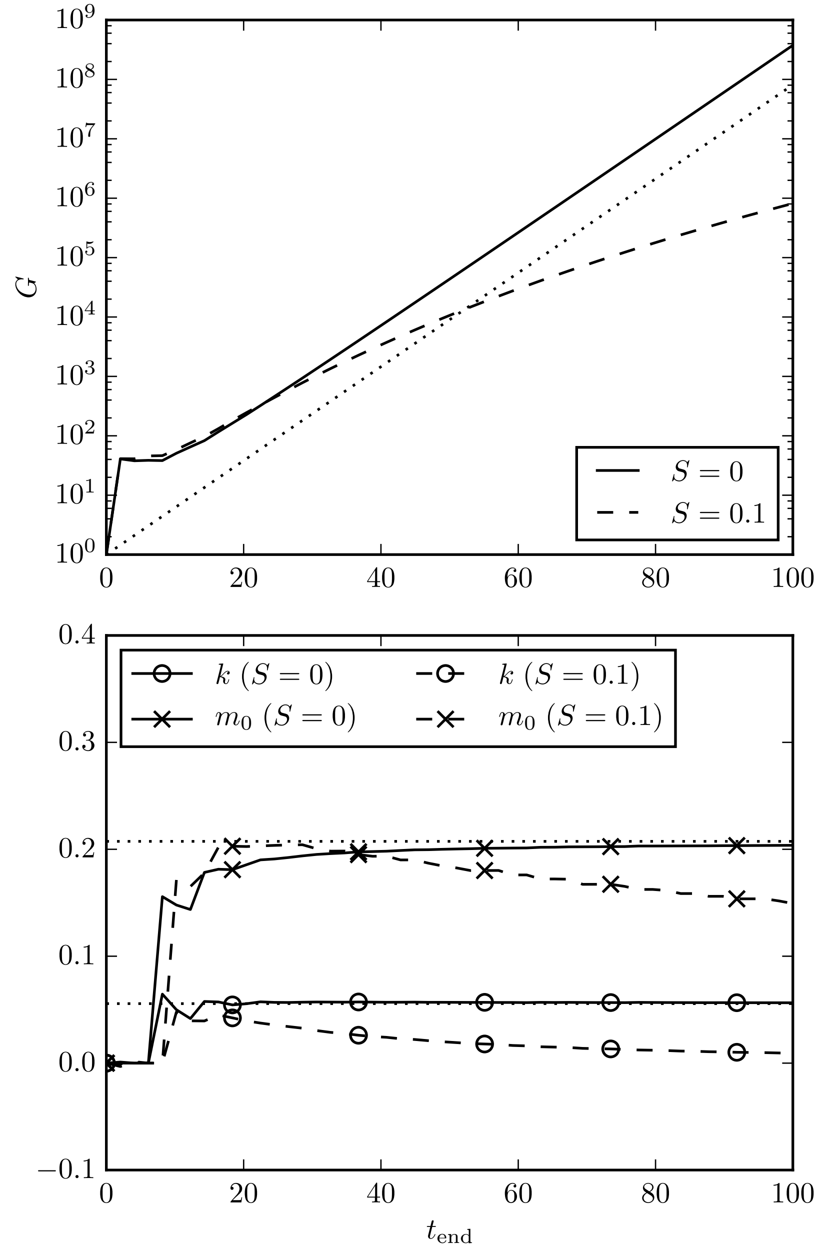

Figure 5.8: Optimized gain G and corresponding k and m_0 as a function of time interval $[0, t_{\text{end}}]$ for the settling instability. The other parameters are $Pr = 7$, $\tau = 1$, $R_\rho = 2$ and $V_p = 1$. The dotted lines indicate linear stability results for maximum growth rate and corresponding (k, m), in the absence of shear.

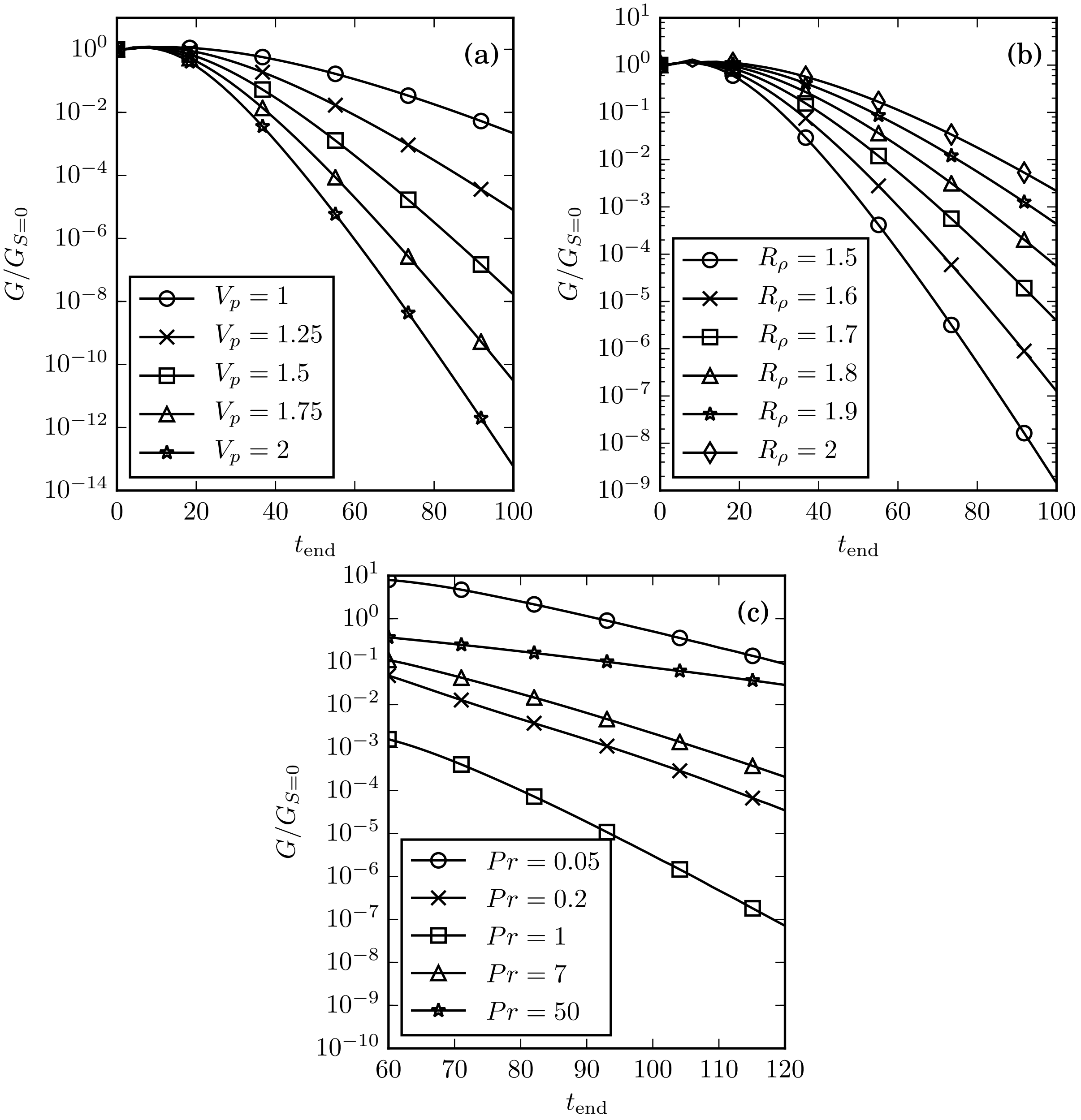

Figure 5.9: Ratio of sheared optimal gain with $S = 0.1$ to unsheared optimal gain for the settling instability with $\tau = 1$. Other parameters are (a) $Pr = 7$, $R_\rho = 2$, (b) $Pr = 7$, $V_p = 1$, (c) $R_\rho = 2$, $V_p = 1$.

driven instability as originally discussed in Alsinan *et al.*[5]. Again we have stabilizing T- and destabilizing C-vorticity. Since temperature contributes more strongly to the density, and the overall background density gradient is stable, the T-vorticity will outweigh the C-vorticity if the T- and C-perturbations have the same phase and diffuse at the same rate ($\tau = 1$), so that the system will be stable. When $V_p > 0$, on the other hand, a phase shift is introduced between the T- and C-perturbations, so that the stabilizing T-vorticity does not outweigh the destabilizing C-vorticity everywhere. This provides the conditions for an instability to develop.

Based on this explanation, it would be fair to wonder why $V_p > 0$ is needed for this instability to occur. In principle, a phase offset can be introduced in the initial perturbations of T and C, so that the T-vorticity does not stabilize the flow everywhere even when $V_p = 0$. But as we know from linear stability analysis, the resulting flow is still stable. The reason for this is that, even though an initial phase shift produces some transient growth, the resulting flow acts in such a way as to gradually reduce the phase offset between the T- and C-perturbations, so that these perturbations decay for long times. This is illustrated in figure 5.10, which shows the gain G and phase angle θ between the T- and C-perturbations as functions of time for a case with $V_p = 0$, $\tau = 1$, $k = 0.08$, $m = 0.2$ and an initial phase angle of $\theta(0) = -\pi/4$. The traditional linear stability analysis, such as applied by Alsinan *et al.*[5], captures only the long-term behavior.

We can further examine the source of this phase angle decay by considering an inviscid case without diffusion of either scalar, and in the absence of settling. In this scenario, the phase angle will decay initially, overshoot zero, reach a new maximum of opposite sign, decay again and overshoot zero to return to the initial position, only to restart the oscillation. Since there is no viscosity or diffusion, this oscillation is undamped. When viscosity and diffusion are added, the oscillations become damped with a viscous decay

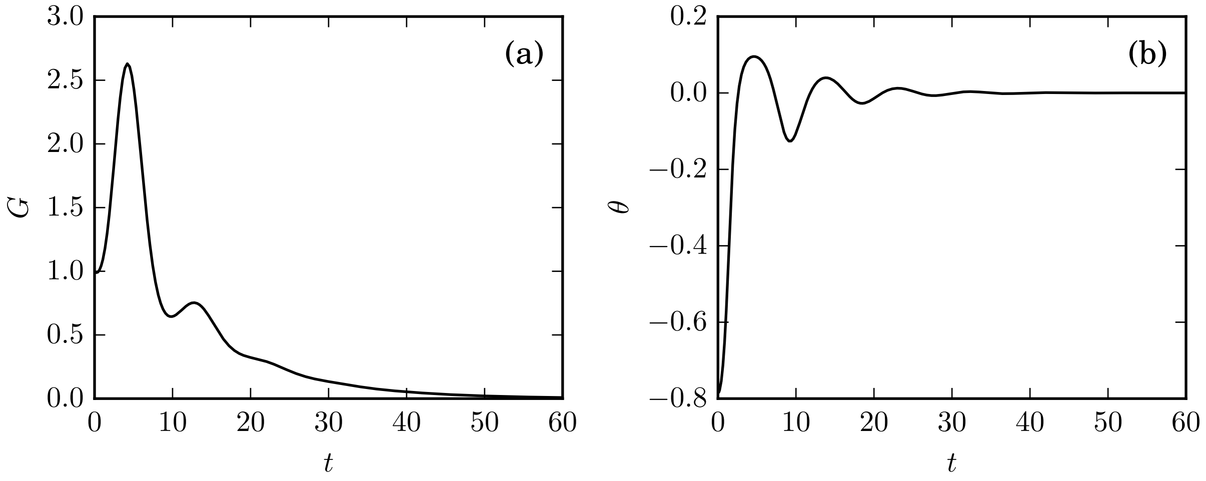

Figure 5.10: (a) Gain, as defined in (5.38), and (b) phase angle between temperature and particle perturbations as functions of time for $Pr = 7$, $\tau = 1$, $R_\rho = 2$, $V_p = 0$ and initial $\theta = -\pi/4$. There is initial, transient growth that decays as the phase angle decays without any sustained driving force to maintain it.

rate of $-(k^2 + m^2)$, according to the eigenvalues of the matrix in (5.36) with $S = 0$, $V_p = 0$ and $\tau = 1$. The two oscillatory eigenmodes with phase offset between T and C each decay with a rate of $-(1 + Pr)(k^2 + m^2)/2$. This demonstrates that if k or m are increased for the settling-driven instability, not only will viscous forces dampen the instability, but the phase offset which drives the instability will also have a stronger natural decay and therefore tend to be smaller.

The settling velocity V_p thus provides the mechanism that sustains the phase shift between the T- and C-perturbations, against its natural reduction in the absence of settling. We can get an idea of how strong the effect of V_p is by examining the rate of change of the phase angle between T and C when the C wave is settling with speed V_p. Assuming a plane wave of form $e^{ikx+imz+\sigma t}$, in order to obtain a vertical phase speed of V_p at x=const. we require $\sigma_i/m = V_p$, where the imaginary part of σ_i of the growth rate also represents the rate of change of the phase offset. Thus, the driving force for the phase offset is seen to be proportional to $V_p m$.

For a given V_p with $\tau = 1$, the growth of the settling instability is then governed by a balance of three mechanisms: a) the phase offset, governed by the balance of wave settling with strength $V_p m$ and phase offset decay with strength $(1 + Pr)(k^2 + m^2)/2$, b) viscosity and diffusion, proportional to $k^2 + m^2$, which dampen the perturbations, and c) $k^2/(k^2 + m^2)$, which affects the strength of the vertical velocity generated by the perturbations, according to (5.36). A smaller k implies an effectively weaker influence of viscosity along with a larger phase offset, but also weaker velocity generation, and thus can result in very slow growth.

Figures 5.11a and b show the linear stability growth rates for $V_p = 1$ and 2, in the absence of shear. When V_p increases, for $m \approx const.$ we can increase k and still have a sufficiently strong driving force $V_p m$ to maintain the phase offset, even though its natural decay increases. This larger k increases the effect of viscosity, but also the generation of vertical velocity. This allows modes with larger k to be unstable when V_p increases, so that the instability is shifted towards larger k, as seen in figures 5.11a and b.

We are now in a position to explain why the damping effect of shear is more pronounced for larger V_p. As for the fingering instability, this can be understood in terms of the linear stability growth rates for unsheared flows. In order to produce optimal growth, the values of (k, m) should remain inside the linearly unstable region as m decreases with time. Figures 5.11a and b indicate that this is indeed the case for $V_p = 1$ and 2. These figures also show that for larger V_p the maximum growth for the unsheared flow occurs at higher k. Recall that with shear $m(t) = m_0 - Skt$, so that m decreases more quickly for higher k, which means the flow spends less time in the unstable region. Consequently, the optimal growth with shear is found for k-values somewhat below the maximum unsheared gowth, for which the flow gets to spend more time in the unstable region. For $V_p = 2$ and shear, k decreases farther below the unsheared optimal k than for $V_p = 1$, so that the growth is reduced more strongly.

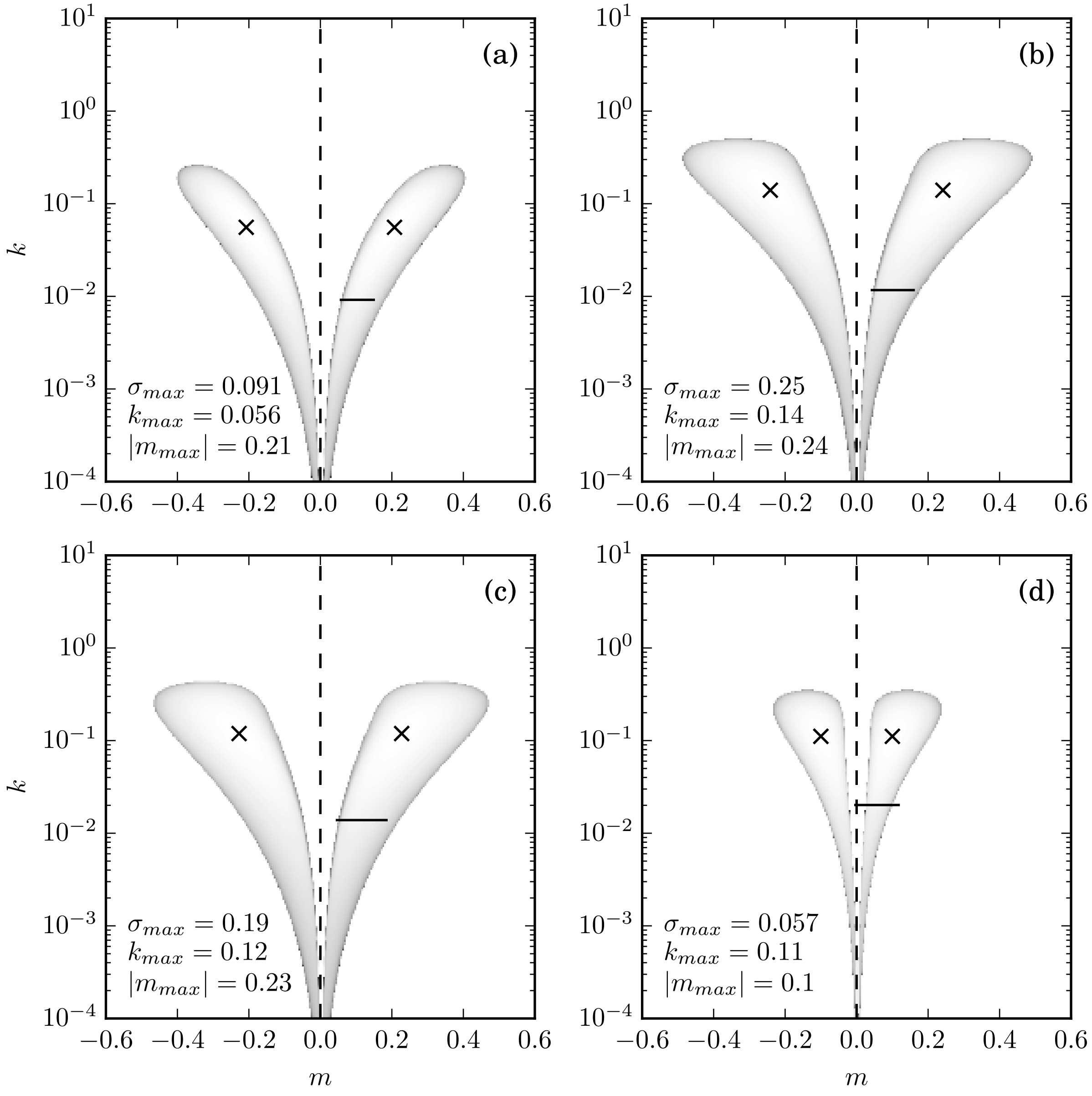

Figure 5.11: Linear stability growth rate vs. horizontal wavenumber k and vertical wavenumber m in the absence of shear, for parameters (a) base case of $Pr = 7$, $\tau = 1$, $R_\rho = 2$ and $V_p = 1$, (b) increased $V_p = 2$, (c) decreased $R_\rho = 1.5$ and (d) decreased $Pr = 0.05$. Shading is logarithmic. The maximum growth rates are marked with an X. The horizontal black lines represent the paths of the non-modal optimal growth when $S = 0.1$ and $t_{\text{end}} = 100$ (a-c), and $t_{\text{end}} = 60$ (d), as $m = m_0 - Skt$.

R_ρ	V_p	$\lvert\theta\rvert$
2	1	0.42
2	2	0.50
1.5	1	0.30

Table 5.1: Phase angle (radians) between temperature and particle concentration waves for the most unstable mode from linear stability analysis. Other parameters are $Pr = 7$ and $\tau = 1$.

Influence of R_ρ

Figure 5.9b shows that lower values of R_ρ are affected more strongly by shear than higher values. Figures 5.11a and c indicate that when R_ρ is decreased, the linear instability of the unsheared flow responds similarly to when V_p is increased, and the unstable region shifts toward larger k. To keep m in the unstable region over time for smaller R_ρ when shear is present, k needs to be reduced further below its unsheared maximum than for larger R_ρ, so that the growth is dampened more strongly.

The only remaining question is why for smaller R_ρ the instability shifts to larger k. Decreasing R_ρ increases the strength of the destabilizing C-vorticity relative to the stabilizing T-vorticity. This means that less phase offset is required to generate an instability for smaller R_ρ. Hence the instability shifts toward larger k-values, which generate more vorticity and faster growth, as long as k is not so large that viscosity becomes dominant or the phase offset too small. This relationship is reflected by table 5.1 which shows that, compared to the base case of $R_\rho = 2$ and $V_p = 1$, reducing R_ρ to 1.5 decreases the phase offset between the temperature and particle concentration perturbations for the most unstable mode. By contrast, holding $R_\rho = 2$ constant and increasing V_p to 2 drives the phase offset to larger values. This is consistent with the arguments of the previous section.

Influence of Pr

Figure 5.9c indicates that the strength of the shear's damping effect depends on Pr in a non-monotonic fashion. The damping is most pronounced for $Pr = 1$, while it decreases for both smaller and larger Pr-values. Consistent with our earlier observations, for $Pr = 0.05$ shear even causes additional growth for a range of t_{end}. We note that for some Pr-values the settling instability grows quite slowly, so that for $t_{\text{end}} < 60$ the initial transient growth mechanism is responsible for the maximum gain. Our interest, on the other hand, focuses on the effect of shear on the settling instability, so that we choose the range of t_{end} in figure 5.9c as $[60, 120]$ instead of $[0, 100]$.

The reduced damping when Pr is increased from 1 can be explained on the basis of arguments from the earlier sections. Recall that the strength of the natural phase offset decay is $(1+Pr)(k^2+m^2)/2$. This means that increasing Pr-values will result in smaller phase offsets and maximum growth rates for lower k-values. Although this is not shown in figure 5.11, we confirmed that as Pr increases from 1 to 7 to 50, the k-value of the fastest growing mode in the linear stability analysis decreases from 0.140 to 0.0557 to 0.0279. As before, a lower k for the unsheared instability leads to less damping in the presence of shear, as $m = m_0 - Skt$ is able to remain inside the linearly unstable region for longer times.

When Pr is decreased from 1, the reduced damping results from a combination of effects. Firstly, the k-value of the fastest growing linearly unstable mode decreases from 0.140 for $Pr = 1$, to 0.111 for $Pr = 0.05$. Velocity generation increases with k, but this effect is multiplied by Pr. When Pr becomes very low, increasing k no longer results in as large of an increase in velocity generation relative to the other terms in (5.36). While velocity diffusion also decreases with decreasing Pr, (5.36) shows that the overall growth of the velocity wave in the time derivative scales with Pr. It is important to keep in mind that while velocity diffusion decreases, scalar diffusion does not decrease. If this seems surprising, it is because of the way we have scaled the problem. The length scale is a diffusive scale based on the temperature diffusivity. Hence for a constant problem size, varying Pr means changing the viscosity of the fluid, not the diffusivity of the scalars. Since scalar diffusion is constant as Pr is decreased and velocity generation is less effective at large k for low Pr, it becomes relatively more costly for the instability to have a higher k. As k becomes smaller, the phase offset decay decreases. Consequently, the effect of diffusion can be further reduced by making m smaller as well, since less driving from the settling is needed to maintain the phase offset. In turn, smaller m results in stronger velocity production, which scales with $k^2/(k^2+m^2)$, as mentioned earlier. The overall effect of making Pr very small is to shift the unsheared instability toward slightly smaller k and significantly smaller m, as seen in figure 5.11d.

This leads to the second reason why damping is decreased for smaller Pr-values. Recall that the Orr mechanism produces maximum gain for $m = 0$ at $t = t_{\text{end}}$. Because for $Pr = 0.05$ the instability is located closer to $m = 0$ than for $Pr = 1$, as seen in figure 5.11d, it becomes easier for the Orr mechanism to have an impact, as m does not have to spend much time outside of the region of instability in order to reach zero. This is also illustrated in figure 5.11d, which shows the range of m-values over time for the optimally growing solution with $t_{\text{end}} = 60$ and $Pr = 0.05$. For the fingering instability the unstable region extends all the way to $m = 0$, as seen in figure 5.5. Nevertheless, the Orr mechanism is weaker for the fingering instability than for the settling-driven instability, since k is much larger for the fingering case. Equation (5.71) indicates that this limits the growth due to the Orr mechanism. Equation (5.75) furthermore shows that the viscous decay of the Orr mechanism is reduced for smaller Pr, which further enhances its importance. For $Pr = 0.05$ and $t_{\text{end}} = 60$, the estimate from section 5.4.2 of the maximum gain due to the Orr mechanism yields about 400. This suggests that, even though shear may dampen the settling-driven instability, the Orr mechanism may still result in enhanced overall growth for small Pr-values, consistent with figure 5.9c. For $Pr = 0.2$, the estimate yields a gain from the Orr mechanism alone of about 90. In summary, for $Pr < 1$ a further decrease of Pr will result in less damping, because the instability is located at lower k and the Orr mechanism will contribute more to its growth, thereby leading to the larger gains seen in figure 5.9c.

5.5 Discussion and Conclusions

The present investigation assesses the effects of shear on double-diffusive fingering and on the recently identified settling-driven instability by means of a transient growth analysis. Towards this end, it employs Kelvin waves within a linearized framework, so that the evolution of time-dependent waveforms in uniform shear can be considered. This approach allows us to eliminate the effects of boundaries and of shear-driven instability modes, so that the influence of shear on the above-mentioned instabilities can be analyzed in isolation.

Consistent with previous analyses by other authors, we find that shear dampens the fingering instability. Our analysis furthermore shows that shear also dampens the settling-driven instability mode. For both of these, the shear damping is stronger for parameter combinations that produce larger unsheared growth. These trends can largely be explained in terms of instantaneous linear stability results for the unsheared case. As the vertical wavenumber $m(t)$ changes with time, the path of $(k, m(t))$ taken by the tilting Kelvin wave results in lower average growth as compared to the maximum growth rate of the unsheared case. For both instabilities, low Pr-values result in less damping and an increased importance of the Orr mechanism. This stronger influence of the Orr mechanism can be traced to the smaller viscosity at lower Pr. For the settling-driven instability, lower Pr-values furthermore move the region of linear instability closer to $m = 0$, which strengthens the ability of the Orr mechanism to reinforce the instability.

Although shear dampens the growth of both the double-diffusive and the settling-driven instabilities, substantial growth may still occur during the linearized phase, as seen in figures 5.2 and 5.8, so that initially small perturbations can become sufficiently large for nonlinear effects to take over. This is consistent with the findings of Radko *et al.*[49] and Smyth & Kimura [41]. We expect a similar situation for the settling-driven instability, for which the shear dampening effect is of the same order, as seen in figures 5.4 and 5.9. However, this scenario will have to be analyzed in more depth by means of nonlinear simulations.

Appendix A

2D flow solver

A.1 Boussinesq

The two dimensional Boussinesq flow solver solves

$$\begin{aligned}\frac{\partial\omega}{\partial t}+\mathbf{u}\cdot\boldsymbol{\nabla}\omega &= \frac{1}{Re}\nabla^2\omega-\sum_n\alpha_n\frac{\partial c_n}{\partial x}\ , && \text{(A.1)}\\ \frac{\partial c_n}{\partial t}+\mathbf{u}\cdot\boldsymbol{\nabla}c_n &= \frac{1}{Pe_n}\nabla^2 c_n\ , && \text{(A.2)}\\ \nabla^2\psi &= -\omega\ , && \text{(A.3)}\end{aligned}$$

where ω is the vorticity, $\mathbf{u}=(u,v)$ is the veloctiy vector, Re is the Reynolds number, c_n is the nth concentration field, α_n is the coefficient for the influence of c_n on fluid density, Pe_n is the Péclet number for nth concentration field and ψ is the streamfunction. The vorticity is defined as

$$\omega=\frac{\partial v}{\partial x}-\frac{\partial u}{\partial y}\ , \tag{A.4}$$

and the streamfunction can be used to calculate velocity using

$$u=\frac{\partial\psi}{\partial y},\qquad v=-\frac{\partial\psi}{\partial x}\ . \tag{A.5}$$

Equations (A.1)-(A.2) are advanced in time using known values for u and v. When new values of u and v are needed, for example during a Runge-Kutta substep, (A.3) is used to find ψ, which can be used to obtain velocities using (A.5).

A.1.1 Horizontal Discretization

The code uses a pseudospectral Fourier method in the x-direction. The type of Fourier series selected is dependent on the desired boundary conditions for the left and right walls. If periodic boundaries are desired, (A.6) is used:

$$q = \sum_{k=0}^{N_x/2-1} \hat{q}_k e^{2\pi i k x/L_x} \ , \tag{A.6}$$

where q is one of (ω, c_n, u, v), $i = \sqrt{-1}$ and L_x is the length of the domain in the x-direction. The maximum frequency is the Nyquist frequency when the domain is sampled with N_x evenly spaced grid points. If slip walls with no scalar flux are desired, cosine and sine series are used:

$$q = \sum_{k=0}^{N_x-1} \hat{q}_k \cos\left(\frac{\pi k x}{L_x}\right), \qquad q = \sum_{k=1}^{N_x} \hat{q}_k \sin\left(\frac{\pi k x}{L_x}\right) \ . \tag{A.7}$$

Cosine series are used for c_n and v, while sine series are used for ψ, ω and u. From this point on, periodic boundaries and thus Fourier series defined in (A.6) are assumed, but only minor modifications are necessary to switch to slip boundaries.

Equations for the time evolution of $\hat{\omega}_k$ and $\hat{c}_{k,n}$ can be found by taking the appropriate

Fourier transform of (A.1)-(A.2). The result is:

$$\begin{aligned}\frac{\partial \hat{\omega}_k}{\partial t} &= -\widehat{\left(u\frac{\partial \omega}{\partial x}\right)}_k - \widehat{\left(v\frac{\partial \omega}{\partial y}\right)}_k + \frac{1}{Re}\left(-\frac{4\pi^2 k^2}{L_x^2}\hat{\omega}_k + \frac{\partial^2 \hat{\omega}_k}{\partial y^2}\right) \\ &\qquad - \sum_n \alpha_n \frac{2\pi i k}{L_x}\hat{c}_{k,n} \ , \qquad (A.8) \\ \frac{\partial \hat{c}_{k,n}}{\partial t} &= -\widehat{\left(u\frac{\partial c_n}{\partial x}\right)}_k - \widehat{\left(v\frac{\partial c_n}{\partial y}\right)}_k + \frac{1}{Pe_n}\left(-\frac{4\pi^2 k^2}{L_x^2}\hat{c}_{k,n} + \frac{\partial^2 \hat{c}_{k,n}}{\partial y^2}\right) \ . \qquad (A.9)\end{aligned}$$

The nonlinear terms are calculated using the pseudospectral method. This means that once we have a solution for $\hat{\omega}_k$ and $\hat{c}_{k,n}$ at a certain time, we use it to calculate u, v, $\partial\omega/\partial x$, $\partial\omega/\partial y$, $\partial c_n/\partial x$ and $\partial c_n/\partial y$ in physical space. The x-derivatives are calculated by multiplying by $2\pi i k/L_x$ in Fourier space and then performing an inverse FFT. The y-derivatives are calculated in Fourier space using the compact finite difference schemes discussed below before being converted into physical space using an inverse FFT. After all of the derivatives have been obtained in physical space, we calculate the convective terms in physical space and then use a FFT to transform the result back into Fourier space. This method is computationally efficient, but the primary drawback is that aliasing from the higher modes can lead to inaccuracy in the solution. In practice, we have found that any negative impact from this can be eliminated by using enough Fourier modes. Viscosity and diffusion naturally limit the magnitude of the higher Fourier modes, reducing the effects of aliasing. As long as the solution is adequately resolved by the Fourier modes, the higher modes are very weak and the effects of aliasing are minimal.

A.1.2 Vertical Discretization

The code uses compact finite differences [35] to discretize the y-direction. A centered, 8th-order scheme was selected for the interior of the domain. A centered 4th-order scheme was used for grid points one grid point away from the boundary and a one-sided 4th-order scheme was used on the boundaries. The compact finite schemes used by the code can be written

$$A_1\mathbf{f}' = B_1\mathbf{f} \ , \tag{A.10}$$

$$A_2\mathbf{f}'' = B_2\mathbf{f} \ , \tag{A.11}$$

where A_1, B_1, A_2 and B_2 are matrices and $\mathbf{f}$ is a vector containing the discretized function values. If A_1 or A_2 is the identity matrix, the scheme is reduced to a traditional finite difference scheme, also referred to as an explicit finite difference scheme. The elements of the matrices can be obtained using the formulas from Lele [35]. As an example, the first derivative on the interior points is calculated using

$$\beta f'_{i-2} + \alpha f'_{i-1} + f'_i + \alpha f'_{i+1} + \beta f'_{i+2} = a\frac{f_{i+1} - f_{i-1}}{2\Delta y} + b\frac{f_{i+2} - f_{i-2}}{4\Delta y} \tag{A.12}$$

$$\alpha = \frac{4}{9} \ , \quad \beta = \frac{1}{36} \ , \quad a = \frac{40}{27} \ , \quad b = \frac{25}{54} \tag{A.13}$$

This demonstrates the main advantage of compact finite differences over traditional finite differences. Eigth-order convergence is achieved with a stencil size of two grid points on either side of the central point. With traditional finite differences, a stencil size of four grid points on either side of the central point would be required to achieve 8th-order convergence. The smaller stencil size allows for higher order centered schemes to be used closer to the boundary, reducing the error there. Compact finite difference schemes also are generally more accurate on small scales relative to the grid spacing than traditional finite difference schemes [35], leading to greater overall accuracy, even if the rate of convergence is the same. These benefits come with the added cost of needing to solve a pentadiagonal matrix to find the values of the derivative. However, as we will see when discussing the time discretization, we would have to solve a pentadiagonal matrix for the second derivative even if a traditional finite scheme is used. There is still a small extra cost associated with using compact finite differences for the first derivative.

A.1.3 Time Discretization

The timestepping is done with a hybrid scheme [70] that uses Crank-Nicholson for the diffusion terms and a low-storage 3rd order Runge-Kutta method [14] for everything else. The timestepping process will be described here for vorticity (A.8), but the same process can be used for the scalar concentration fields with minor changes to account for the different equation (A.9).

We begin by combining all terms on the right hand side of (A.8) except the diffusion term, by setting

$$\hat{f}_k = -\widehat{\left(u\frac{\partial \omega}{\partial x}\right)}_k - \widehat{\left(v\frac{\partial \omega}{\partial y}\right)}_k - \sum_n \alpha_n \frac{2\pi i k}{L_x}\hat{c}_{k,n} \ , \tag{A.14}$$

and using this along with the compact finite difference scheme (A.11) to get

$$\frac{\mathrm{d}\hat{\boldsymbol{\omega}}_k}{\mathrm{d}t} = \frac{1}{Re}\left(-\frac{4\pi^2 k^2}{L_x^2} I + A_2^{-1}B_2\right)\hat{\boldsymbol{\omega}}_k + \hat{\mathbf{f}}_k \ . \tag{A.15}$$

The vectors $\hat{\boldsymbol{\omega}}_k$ and $\hat{\mathbf{f}}_k$ contain discretized points as a function of y. The dependence of the solution on x is contained in the different Fourier modes k. The governing equations are nonlinear, and the Fourier modes interact with each other through the nonlinear terms in $\hat{\mathbf{f}}_k$.

The low-storage Runge-Kutta scheme used here requires storage for two solutions – one to store the current solution and one to store a time derivative. Before a timestep begins, the solution storage contains the solution at time level n and the time derivative storage is unused. Using a superscript to denote time level, $\hat{\boldsymbol{\omega}}_k$ to denote the discrete values of the k-th Fourier mode as a function of y, and $\hat{\mathbf{g}}_k$ to denote the time derivative storage for the Runge-Kutta scheme, the outline of how to advance the solution from time level n to time level $n+1$ is as follows. It begins by storing the time derivative at time level n:

$$\hat{\mathbf{g}}_k \leftarrow \mathbf{f}_k^n \ . \tag{A.16}$$

The solution is then advanced to time level $n+1/3$ using a forward Euler step for the f-term and a Crank-Nicholson step for the diffusion term. After multiplying through by A_2, the equation to be solved is:

$$\begin{aligned}\left[\left(1+\frac{2\pi^2 k^2(\Delta t/3)}{L_x^2 Re}\right)A_2 - \frac{\Delta t/3}{2Re}B_2\right]\hat{\boldsymbol{\omega}}_k^{n+1/3} \\ = \left[\left(1-\frac{2\pi^2 k^2(\Delta t/3)}{L_x^2 Re}\right)A_2 + \frac{\Delta t/3}{2Re}B_2\right]\hat{\boldsymbol{\omega}}_k^n + \frac{\Delta t}{3}\hat{\mathbf{g}}_k \ .\end{aligned} \tag{A.17}$$

We note here that if an explict finite difference scheme was used, which would be equivalent to having A_2 equal to the identity matrix, we would still need to solve a matrix to advance the solution. Without using compact finite differences, solving a pentadiagonal matrix here would only afford us 4th-order accuracy, instead of the 8th-order accuracy we enjoy with compact finite differences. If 8th-order accuracy was desired using an explicit finite difference scheme, the matrix we would need to solve would have four more diagonals, nearly doubling the computational cost. The solution $\hat{\boldsymbol{\omega}}_k^{n+1/3}$ is calculated in place and overwrites $\hat{\boldsymbol{\omega}}_k^n$. The next step is to update $\hat{\mathbf{g}}_k$:

$$\hat{\mathbf{g}}_k \leftarrow -\frac{5}{9}\hat{\mathbf{g}}_k + \mathbf{f}_k^{n+1/3} \ . \tag{A.18}$$

We then step from time level $n + 1/3$ to $n + 3/4$ with the same process as before:

$$\begin{aligned}\left[\left(1+\frac{2\pi^2k^2(5\Delta t/12)}{L_x^2 Re}\right)A_2-\frac{5\Delta t/12}{2Re}B_2\right]\hat{\boldsymbol{\omega}}_k^{n+3/4}&\\ =\left[\left(1-\frac{2\pi^2k^2(5\Delta t/12)}{L_x^2 Re}\right)A_2+\frac{5\Delta t/12}{2Re}B_2\right]\hat{\boldsymbol{\omega}}_k^{n+1/3}&+\frac{15\Delta t}{16}\hat{\mathbf{g}}_k\ .\end{aligned} \tag{A.19}$$

We note that (A.18) shows that $\hat{\mathbf{g}}_k$ contains an approximation to 4/9 of a derivative, which when multiplied by $15\Delta t/16$ produces an approximation for the change in the f-terms over a time step of size $5\Delta t/12$. We then update $\hat{\mathbf{g}}_k$ once more,

$$\hat{\mathbf{g}}_k \leftarrow -\frac{153}{128}\hat{\mathbf{g}}_k + \mathbf{f}_k^{n+3/4}\ , \tag{A.20}$$

and use this to move the solution to time level $n + 1$,

$$\begin{aligned}\left[\left(1+\frac{2\pi^2k^2(\Delta t/4)}{L_x^2 Re}\right)A_2-\frac{\Delta t/4}{2Re}B_2\right]\hat{\boldsymbol{\omega}}_k^{n+1}&\\ =\left[\left(1-\frac{2\pi^2k^2(\Delta t/4)}{L_x^2 Re}\right)A_2+\frac{\Delta t/4}{2Re}B_2\right]\hat{\boldsymbol{\omega}}_k^{n+3/4}&+\frac{8\Delta t}{15}\hat{\mathbf{g}}_k\ ,\end{aligned} \tag{A.21}$$

which completes the timestep process.

A.1.4 Poisson Equation

The discretized Poisson equation (A.3), after multipling through by A_2, is

$$\left(-\frac{4\pi^2k^2}{L_x^2}A_2 + B_2\right)\hat{\boldsymbol{\psi}}_k = -\hat{\boldsymbol{\omega}}_k\ . \tag{A.22}$$

This means $\hat{\psi}$ can be found from $\hat{\omega}$ by solving N_x pentadiagonal matrices, where N_x is the number of Fourier modes.

A.2 Non-Boussinesq

Since the non-Boussinesq version of the code uses many of the same numerical techniques as the Boussinesq version, only the differences are highlighted here. The non-Boussinesq version of the code solves

$$\begin{aligned}
\frac{\mathrm{D}\omega}{\mathrm{D}t} &= \frac{1}{\rho}\frac{\partial \rho}{\partial y}\frac{\mathrm{D}u}{\mathrm{D}t} - \frac{1}{\rho}\frac{\partial \rho}{\partial x}\frac{\mathrm{D}v}{\mathrm{D}t} + \frac{1}{\rho Re}\nabla^2\omega - \frac{1}{(1-\sigma)\rho}\frac{\partial \rho}{\partial x} && \text{(A.23)}\\
\frac{\mathrm{D}\rho}{\mathrm{D}t} &= \frac{1}{Pe}\nabla^2\rho && \text{(A.24)}\\
\nabla^2\psi &= -\omega && \text{(A.25)}
\end{aligned}$$

where $\mathrm{D}/\mathrm{D}t = \partial/\partial t + \mathbf{u}\cdot\boldsymbol{\nabla}$ is the material derivative, $\sigma \in [0,1]$ is the density ratio and $\rho \in [\sigma, 1]$ is the density. There are two major differences from the Boussinesq case. The first is that all of the terms in the ω-equation are now nonlinear. Because of this, the low-storage Runge-Kutta scheme is used for all terms, and there is no hybrid scheme with the Crank-Nicholson method. After these equations are transformed into Fourier space, all nonlinear terms are calculated in physical space using the pseudospectral method as described for the Boussinesq case. The second major difference is the presence of u and v time derivatives on the right hand side of the equation for ω. We discretize these time derivatives with forward differences, meaning that an iterative method is required to step (A.23) forward in time. For a forward Euler timestep, which could be a substep in a Runge-Kutta method, ω is advanced using guesses for $\partial u/\partial t$ and $\partial v/\partial t$. The new value of ω is used to find the new u and v, which are then used to make better guesses for $\partial u/\partial t$ and $\partial v/\partial t$. This process is repeated until convergence.

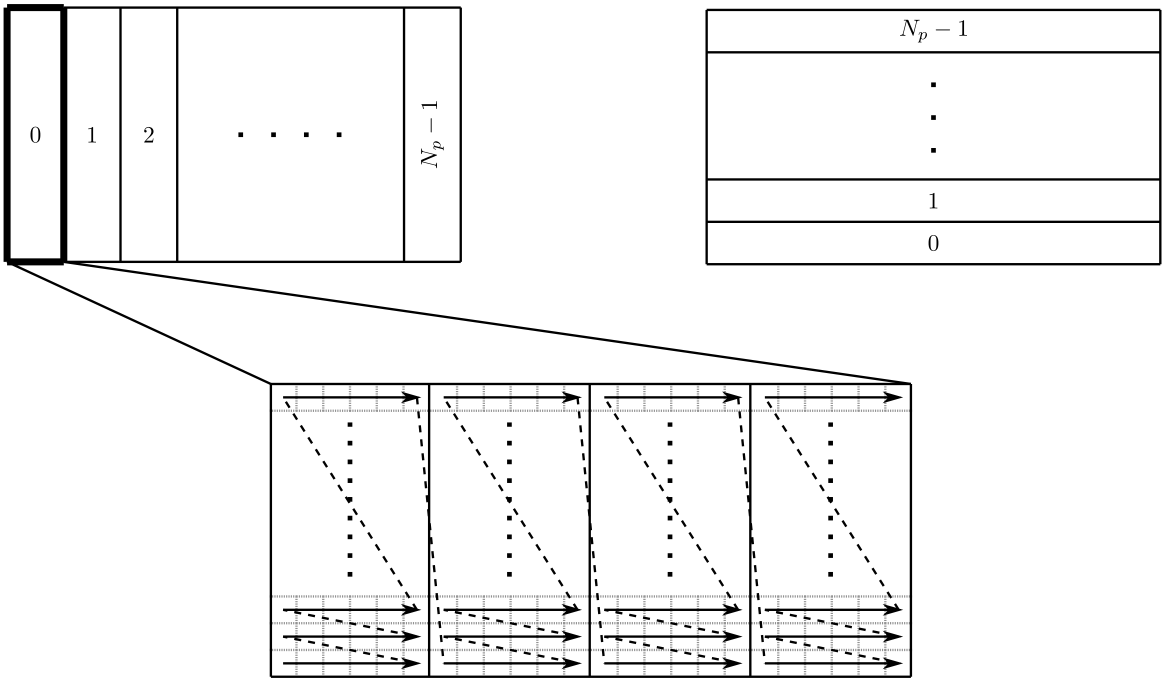

Figure A.1: Vertical slice (top-left) and horizontal slice (top-right) data layouts for N_p processors, numbered $(0, 1, ..., N_p - 1)$. The bottom part shows the memory order inside one processor domain in the vertical slice layout. Data is arranged into sub–columns, with row-major ordering inside each sub-column. The memory order when the data is in the horizontal slice layout is row-major.

A.3 Parallelization and Performance Considerations

Our code is parallelized with MPI. Two data layouts, illustrated in the top of figure A.1, are used during the calculations. In the top right of that figure, each processor owns a slice of the data that spans the entire domain in the horizontal direction. This data layout is used for calculating forward and inverse Fourier transforms. Fourier transforms are done using *FFTW* [71], widely recognized as a leading library for the efficient computation of FFTs. Although *FFTW* provides functionality to perform a distributed memory FFT, even load balancing among the processors is only achieved if the number of Fourier modes is even divisible by the number of processors squared. Since this is a fairly restrictive condition, we chose to do the FFTs with all of the data required for each

FFT on the same processor, so that no communication is required between processors during the computation of the FFTs. After finishing the FFTs, the code transposes the data to the layout shown in the top left of figure A.1. In this layout, each processor owns a slice of data that spans the entire domain in vertical direction. This vertical slice layout is used when the code needs to solve a pentadiagonal matrix for timestepping, finding derivatives or solving the Poisson equation. This strategy of transposing the data between the two layouts described is not new and is used internally by $FFTW$ when performing a two dimensional FFT.

When the data is in the vertical slice layout, the data elements within each processor are not arranged in a pure column-major fashion, as might be expected from a transpose operation. The memory order of the data elements within one processor domain is shown in the bottom of figure A.1. The data is arranged into row-major sub-columns that are generally 16 or 32 double-precision floats wide. This data layout has many benefits for overall code performance compared to a pure columnwise layout. To begin, the transpose process that switches the overall layout from horizontal slices to vertical slices and vice-versa is slightly cheaper. Once the data is in the vertical layout, the sub-column arrangement also allows for vectorization of the computations. This means that two or even four operations can be done for the price of one, depending on the CPU. When solving a pentadiagonal matrix, the sub-column layout also allows the CPU to make use of out-of-order execution. In a pure column-major layout, each step of the solution of a pentadiagonal matrix depends on the previous step, so each mathematical operation must wait for the previous one to finish before beginning. This is known as a dependency chain. In the sub-column layout we use, multiple pentadiagonal matrices can be worked on at once. While the CPU is waiting for a mathematical operation on one matrix to complete, it can begin working on a mathematical operation on a different matrix, breaking the dependency chain.

At this point, one might wonder why sub-columns are better than simply putting the data into a row-major layout inside each vertical slice. The answer has to do with CPU caches. When solving a pentadiagonal matrix using the Thomas algorithm, as is done often in our code, the data access pattern travels up a column during the forward elimination phase, and then travels back down the column during the backsubstitution phase. Solving fewer matrices at once increases the fraction of each matrix that can be stored in cache and used for speedy computation in the backsubstitution phase. Solving fewer matrices at once, however, does not preclude the pure row-major format from being used. The benefits of using sub-columns over a pure row-major format are better prefetching and eliminated cache thrashing. As a CPU loads data from different memory locations, it keeps track of these locations and looks for patterns. If it can find a pattern, it will predict what parts of memory will be demanded by future loads and begin loading them into CPU cache prematurely. The easiest pattern to predict is purely sequential access, and this pattern provides the best prefetching performance. Although the memory access pattern generated when solving pentadiagonal matrices in the sub-column format is not sequential, it more closely resemebles sequential access compared to if a pure row-major format had been used. The second benefit of the sub-column format is eliminated cache thrashing. When data is loaded from memory into CPU cache, there are only a certain number of cache addresses that are allowed to be used. The cache addresses allowed are determined by the memory address of the data. Since the number of processors and the number of grid points in each direction are usually powers of two, if the data was arranged in a pure row-major format, each row would be competing for the same cache addresses on most CPUs. This would drastically reduce the effective size of the cache, and is known as cache thrashing. Cache thrashing can be eliminated by bringing each row of data for the matrices being solved simultaneously closer together in memory, which is what the sub-column format does.

In summary, smaller sub-columns make better use of CPU cache and larger sub-columns make better use of CPU vectorization and out-of-order operation. The ideal performance is achieved by choosing a moderate sub-column width, which is usually smaller than the number of columns owned by each processor.

Appendix B

Additional vorticity model calculations

B.1 Extension of the non-Boussinesq vorticity model to 3D flows

The steady-state Euler equation can be written in conservative form as

$$\boldsymbol{\nabla} \cdot (\rho \boldsymbol{u}\boldsymbol{u}) + \boldsymbol{\nabla} p \quad = \quad \rho \mathbf{g} \ . \tag{B.1}$$

We define L as the z-component of the curl of (B.1). We take y as the vertical direction so that $\mathbf{g} = (0, -g, 0)$, and denote the velocity components by $\boldsymbol{u} = (u, v, w)$. Then we can write $L = \nabla \cdot \mathbf{q}$, where

$$\mathbf{q} = \begin{pmatrix} q_x \\ q_y \\ q_z \end{pmatrix} = \begin{pmatrix} g\rho + \partial_x(uv\rho) + \partial_z(vw\rho) + \frac{1}{2}\partial_y[\rho(v^2 - u^2)] \\ -\partial_y(uv\rho) - \partial_z(uw\rho) + \frac{1}{2}\partial_x[\rho(v^2 - u^2)] \\ 0 \end{pmatrix} . \tag{B.2}$$

Here $\mathbf{q}$ is arbitrary up to a gauge transformation, so that we can add the curl of any vector field to $\mathbf{q}$ and still have $L = \nabla \cdot \mathbf{q}$. We have used this choice so that $q_z = 0$.

If the system is two-dimensional or periodic in the spanwise direction, then on applying the divergence theorem there is no boundary in the z-direction, so that there will be no contribution from q_z. If side walls are present, we need to integrate q_z on the walls. However, the integral is zero, so that again there is no contribution.

Now consider q_y on the basal and top surfaces where $v = 0$. Using the continuity equation,

$$q_y = -u\rho\partial_y v - \partial_z(uw\rho) - \tfrac{1}{2}\partial_x(\rho u^2) = u\rho\partial_z w - \partial_z(uw\rho) - \tfrac{1}{2}u^2\partial_x\rho \ . \tag{B.3}$$

When we integrate with respect to z, the $\partial_z(uw\rho)$ term will be zero whether the system is periodic or has sidewalls. All of these terms are likely to be small in the limit of time averaging, low diffusion and high Reynolds number. This follows for the $u\rho\partial_z w$ term in the periodic case through symmetry arguments, although in the presence of sidewalls there may be some mean contribution.

Finally, we have the q_x term to consider. The y-integration of $\frac{1}{2}\partial_y(\rho v^2)$ will be zero, since v vanishes on the top and basal surfaces. Integration of $\partial_z(vw\rho)$ in z results in zero for both periodic boundaries and sidewalls ($w = 0$). With these simplifications, q_x can be written as

$$q_x = g\rho + \partial_x(uv\rho) - \tfrac{1}{2}\partial_y(\rho u^2) \ . \tag{B.4}$$

In the same manner as in section 2.2.2, we assume that the integration in y and z of $\partial_x(uv\rho)$ is zero. Then

$$q_x = g\rho - \tfrac{1}{2}\partial_y(\rho u^2) \ , \tag{B.5}$$

so that we recover the same result for three dimensions as we had in two dimensions.

B.2 Vorticity flux deviations for the primitive variable approach

An equation corresponding to (2.41) for the vorticity approach will now be derived for the primitive variable approach in two dimensions. We start with the conservative equations

$$\begin{aligned} \partial_t(\rho u) + \partial_x(\rho u^2) + \partial_y(\rho uv) + \partial_x P - \mu\nabla^2 u &= 0 \; , && \text{(B.6)} \\ \partial_t(\rho v) + \partial_x(\rho uv) + \partial_y(\rho v^2) + \partial_y P - \mu\nabla^2 v + \rho g &= 0 \; . && \text{(B.7)} \end{aligned}$$

Taking the z-component of the curl, dividing by $\rho_1 U_b^2$ and integrating over $BCDE$ gives

$$E_t^* + \frac{1}{\rho_1 U_b^2} \oint \mathbf{q} \cdot \hat{\mathbf{n}} \, \mathrm{d}l + E_\mu^* = 0 \; , \tag{B.8}$$

where

$$\mathbf{q} = \left(\begin{array}{c} gp + \partial_x(\rho uv) + \frac{1}{2}\partial_y(\rho(v^2 - u^2)) \\ -\partial_y(\rho uv) + \frac{1}{2}\partial_x(\rho(v^2 - u^2)) \end{array} \; , \right) \tag{B.9}$$

and $U_b = \sqrt{g(1-\sigma)H}$ is the buoyancy velocity. The terms E_t^* and E_μ^* are given by

$$E_t^* = \iint \boldsymbol{\nabla}^* \times (\partial_t(\rho^* \mathbf{u}^*)) \, \mathrm{d}A^* \; , \tag{B.10}$$

$$E_\mu^* = -\frac{1}{Re} \iint \boldsymbol{\nabla}^* \times (\nabla^{*2} \mathbf{u}^*) \, \mathrm{d}A^* \; . \tag{B.11}$$

Integrating the second term in (B.8), and using the fact that $v = 0$ on the top and bottom walls, as well as $u_C = u_D$, gives

$$\begin{aligned}\oint \mathbf{q}\cdot\hat{\mathbf{n}}\,\mathrm{d}l &= \int_{DE+BC} \frac{1}{2}u^2\partial_x\rho\,\mathrm{d}x + \int_{EB+CD} g\rho\,\mathrm{d}y + \int_{EB+CD} \partial_x(\rho u v)\,\mathrm{d}y \\ &\quad -\frac{1}{2}\rho_B u_B^2 + \frac{1}{2}\rho_E u_E^2\ . \end{aligned} \tag{B.12}$$

The vorticity flux is defined as

$$\begin{aligned}\Omega &= \int_{EB} u(\partial_x v - \partial_y u)\,\mathrm{d}y \\ &= \int_{EB} u\partial_x v\,\mathrm{d}y - \int_{EB}\frac{1}{2}\partial_y(u^2)\,\mathrm{d}y \\ &= \int_{EB} u\partial_x v\,\mathrm{d}y - \frac{1}{2}(u_B^2 - u_E^2)\ . \end{aligned} \tag{B.13}$$

Consequently,

$$\begin{aligned}-\frac{1}{2}\rho_B u_B^2 + \frac{1}{2}\rho_E u_E^2 &= \frac{1}{2}\rho_E(u_E^2 - u_B^2) + \frac{1}{2}u_B^2(\rho_E - \rho_B) \\ &= \rho_E\Omega - \rho_E\int_{EB} u\partial_x v\,\mathrm{d}y + \frac{1}{2}u_B^2(\rho_E - \rho_B)\ . \end{aligned} \tag{B.14}$$

Substituting (B.14) into (B.12) gives

$$\begin{aligned}\oint \mathbf{q}\cdot\hat{\mathbf{n}}\,\mathrm{d}l &= \int_{DE+BC} \frac{1}{2}u^2\partial_x\rho\,\mathrm{d}x + \int_{EB+CD} g\rho\,\mathrm{d}y + \int_{EB+CD} \partial_x(\rho u v)\,\mathrm{d}y \\ &\quad +\rho_E\Omega - \rho_E\int_{EB} u\partial_x v\,\mathrm{d}y + \frac{1}{2}u_B^2(\rho_E - \rho_B)\ . \end{aligned} \tag{B.15}$$

We can divide by $\rho_1 U_b^2$ and substitute this back into (B.8). Since $\rho_E = \rho_1$ for a top current,

$$\begin{aligned}\frac{1}{\rho_1 U_b^2}\oint \mathbf{q}\cdot\hat{\mathbf{n}}\,\mathrm{d}l &= \int_{DE+BC}\frac{1}{2}u^{*2}\partial_x\rho^*\,\mathrm{d}x^* + \int_{EB+CD}\frac{\rho^*}{1-\sigma}\,\mathrm{d}y^* \\ &\quad+\int_{EB+CD}\partial_x(\rho^* u^* v^*)\,\mathrm{d}y^* + \Omega^* - \int_{EB} u^*\partial_x v^*\,\mathrm{d}y^* \\ &\quad+\frac{1}{2}u_B^{*2}(1-\rho_B^*)\ . \end{aligned} \tag{B.16}$$

The second integral on the RHS can be evaluated piecewise

$$\begin{aligned}\int_{EB+CD}\frac{\rho^*}{1-\sigma}\,\mathrm{d}y^* &= \frac{1}{1-\sigma}((1-h^*)+\sigma h^* - 1) \\ &= \frac{1}{1-\sigma}(h^*(\sigma-1)) \\ &= -h^* \\ &= -\Omega_C^*\ . \end{aligned} \tag{B.17}$$

We can define the error in this piecewise evaluation such that

$$\int_{EB+CD}\frac{\rho^*}{1-\sigma}\,\mathrm{d}y^* = E_C^* - \Omega_C^*\ . \tag{B.18}$$

Substituting (B.18) into (B.16) and then employing this in (B.8) gives an equation for Ω^*:

$$\begin{aligned}\Omega^* &= \Omega_C^* - E_C^* - E_t^* - E_\mu^* - E_a^* \\ &\quad-\frac{1}{2}u_B^{*2}(1-\rho_B^*) - \int_{DE+BC}\frac{1}{2}u^{*2}\partial_x\rho^*\,\mathrm{d}x^* + \int_{EB}u^*\partial_x v^*\,\mathrm{d}y^*\ , \end{aligned} \tag{B.19}$$

where

$$E_a^* = \int_{EB+CD} \partial_x(\rho^* u^* v^*)\,\mathrm{d}y^* \ . \tag{B.20}$$

Although (B.19) contains some terms that are very similar to those in (2.41), it is generally more complicated, so that in chapter 2 of this work we chose to evaluate the deviations from the model using the vorticity approach.

Appendix C

Derivation of energy budget

We begin by taking the dot product of (3.5) and velocity $\mathbf{u}$ to obtain

$$\left(\partial_0 u_i\right) u_i + \left(u_j \partial_j u_i\right) u_i = -\left(\partial_i P\right) u_i + \frac{1}{Re}\left(\partial_j \partial_j u_i\right) u_i - \left(\rho \hat{e}_2\right) u_i \ . \tag{C.1}$$

Making use of the continuity equation (3.4) gives a transport equation for $u_i^2/2$

$$\partial_0 \left(\frac{u_i^2}{2}\right) + u_j \partial_j \left(\frac{u_i^2}{2}\right) = -\partial_i \left(P u_i\right) + \frac{1}{Re}\left[\partial_j \partial_j \left(\frac{u_i^2}{2}\right) - \left(\partial_j u_i\right)\left(\partial_j u_i\right)\right] - \rho u_2 \ . \tag{C.2}$$

Integrating over the area of the domain and making use of continuity and the divergence theorem yields

$$\begin{aligned} \partial_0 \int \frac{u_i^2}{2} \mathrm{d}A + \int \left(u_j \frac{u_i^2}{2}\right) \hat{n}_j \mathrm{d}S = \frac{1}{Re}\left[\int \frac{\partial}{\partial \hat{n}} \left(\frac{u_i^2}{2}\right) \mathrm{d}S - \int \left(\partial_j u_i\right)\left(\partial_j u_i\right) \mathrm{d}A\right] \\ - \int \rho u_2 \ \mathrm{d}A \end{aligned} \tag{C.3}$$

Because of the no mass flux and free slip boundary conditions, the mechanical energy balance simplifies to

$$\partial_0 \int \frac{u_i^2}{2} \mathrm{d}A + \int \rho u_2 \mathrm{d}A + \frac{1}{Re} \int \left(\partial_j u_i\right)\left(\partial_j u_i\right) \ \mathrm{d}A = 0 \ . \tag{C.4}$$

We define gravitational potential energy as

$$E_p = \int \rho x_2 \mathrm{d}A \ . \tag{C.5}$$

The time derivative of E_p is

$$\frac{\mathrm{d}E_p}{\mathrm{d}t} = \int x_2 \frac{\partial \rho}{\partial t} \mathrm{d}A = \int x_2 \left(-u \cdot \nabla \rho + \frac{\mathrm{D}\rho}{\mathrm{D}t} \right) \mathrm{d}A = \int \rho u_2 \mathrm{d}A + \int x_2 \frac{\mathrm{D}\rho}{\mathrm{D}t} \ \mathrm{d}A \ . \tag{C.6}$$

By rearranging this, we obtain

$$\int \rho u_2 \mathrm{d}A = \frac{\mathrm{d}E_p}{\mathrm{d}t} - \int x_2 \frac{\mathrm{D}\rho}{\mathrm{D}t} \ \mathrm{d}A \ . \tag{C.7}$$

By substituting (C.7) into (C.4), we arrive at

$$\partial_0 \int \frac{u_i^2}{2} \mathrm{d}A + \frac{\mathrm{d}E_p}{\mathrm{d}t} - \int x_2 \frac{\mathrm{D}\rho}{\mathrm{D}t} \ \mathrm{d}A + \frac{1}{Re} \int \left(\partial_j u_i\right) \left(\partial_j u_i\right) \ \mathrm{d}A = 0 \ . \tag{C.8}$$

Integrating in time, one obtains

$$\int \frac{u_i^2}{2} \mathrm{d}A + E_p - \int_0^t \int x_2 \frac{\mathrm{D}\rho}{\mathrm{D}t} \ \mathrm{d}A \ \mathrm{d}t + \frac{1}{Re} \int_0^t \int \left(\partial_j u_i\right) \left(\partial_j u_i\right) \ \mathrm{d}A \ \mathrm{d}t = \text{const.} \tag{C.9}$$

Bibliography

[1] Z. Borden and E. Meiburg, *Circulation based models for Boussinesq gravity currents*, *Phys. of Fluids* **25** (2013), no. 10.

[2] N. Konopliv, S. Llewellyn Smith, J. McElwaine, and E. Meiburg, *Modelling gravity currents without an energy closure*, *J. Fluid Mech.* **789** (2016) 806829.

[3] N. Konopliv and E. Meiburg, *Double-diffusive lock-exchange gravity currents*, *J. Fluid Mech.* **797** (2016) 729764.

[4] B. Schulte, N. Konopliv, and E. Meiburg, *Clear salt water above sediment-laden fresh water: Interfacial instabilities*, *Phys. Rev. Fluids* **1** (5, 2016) 012301.

[5] A. Alsinan, E. Meiburg, and P. Garaud, *A settling-driven instability in two-component, stably stratified fluids*, *J. Fluid Mech.* **816** (3, 2017) 243–267.

[6] T. von Kármán, *The engineer grapples with nonlinear problems*, *B. Am. Math. Soc.* **46** (08, 1940) 615–683.

[7] T. Benjamin, *Gravity currents and related phenomena*, *J. Fluid Mech.* **31** (1, 1968) 209–248.

[8] C. Pozrikidis, *Introduction to Theoretical and Computational Fluid Dynamics.* Oxford University Press, 1997.

[9] P. Saffman, *Vortex Dynamics.* Cambridge University Press, 1992.

[10] R. Lowe, J. Rottman, and P. Linden, *The non-Boussinesq lock-exchange problem: Part 1. Theory and experiments*, *J. Fluid Mech.* **537** (8, 2005) 101–124.

[11] V. Birman, J. Martin, and E. Meiburg, *The non-Boussinesq lock-exchange problem: Part 2. High-resolution simulations*, *J. Fluid Mech.* **537** (8, 2005) 125–144.

[12] J. McElwaine, *Rotational flow in gravity current heads*, *Philos. Trans. A Math. Phys. Eng. Sci.* **363** (2005), no. 1832 1603–1623.

[13] C. Chen and E. Meiburg, *Miscible displacements in capillary tubes: Influence of Korteweg stresses and divergence effects*, *Phys. Fluids* **14** (2002), no. 7 2052–2058.

[14] J. Williamson, *Low-storage Runge-Kutta schemes*, *J. Comput. Phys.* **35** (1980), no. 1 48–56.

[15] H. Anjum, J. McElwaine, and C. Caulfield, *The instantaneous froude number and depth of unsteady gravity currents*, *J. Hydr. Res.* **51** (2013), no. 4 432–445.

[16] J. Simpson, *Gravity Currents in the Environment and the Laboratory.* Cambridge University Press, 2nd ed., 1999.

[17] M. Ungarish, *An Introduction to Gravity Currents and Intrusions.* CRC Press - Taylor & Francis Group, 2009.

[18] P. Linden, *Gravity currents – theory and laboratory experiments*, in *Buoyancy-Driven Flows* (E. Chassignet, C. Cenedese, and J. Verron, eds.), pp. 13–51. Cambridge University Press, 2012.

[19] H. Huppert and J. Simpson, *The slumping of gravity currents*, *J. Fluid Mech.* **99** (8, 1980) 785–799.

[20] H. Huppert, *Gravity currents: a personal perspective*, *J. Fluid Mech.* **554** (5, 2006) 299–322.

[21] C. Härtel, E. Meiburg, and F. Necker, *Analysis and direct numerical simulation of the flow at a gravity-current head: Part 1. Flow topology and front speed for slip and no-slip boundaries*, *J. Fluid Mech.* **418** (2000) 189–212.

[22] M. Cantero, S. Balachandar, and M. Garcia, *High-resolution simulations of cylindrical density currents*, *J. Fluid Mech.* **590** (2007) 437–469.

[23] E. Meiburg, S. Radhakrishnan, and M. Nasr-Azadani, *Modeling gravity and turbidity currents: Computational approaches and challenges*, *App. Mech. Rev.* **67** (2015), no. 4 040802.

[24] V. Alavian, G. Jirka, R. Denton, M. Johnson, and H. Stefan, *Density currents entering lakes and reservoirs*, *J. Hydraulic Engr.* **118** (1992), no. 11 1464–1489.

[25] S. Legg, *Overflows and convectively-driven flows*, in *Buoyancy-driven Flows*, pp. 203–239. Cambridge University Press New York, 2012.

[26] A. Law, W. Ho, and S. Monismith, *Double diffusive effect on desalination discharges*, *J. Hydraulic Engr.* **130** (2004), no. 5 450–457.

[27] R. Sparks, R. Bonnecaze, H. Huppert, J. Lister, M. Hallworth, H. Mader, and J. Phillips, *Sediment-laden gravity currents with reversing buoyancy*, *Earth and Planetary Science Letters* **114** (1993), no. 2 243–257.

[28] E. Meiburg and B. Kneller, *Turbidity currents and their deposits*, *Ann. Rev. Fluid Mech.* **42** (2010) 135–156.

[29] T. Radko, *Double-Diffusive Convection.* Cambridge University Press, 2013.

[30] H. Huppert and J. Turner, *Double-diffusive convection*, *J. Fluid Mech.* **106** (5, 1981) 299–329.

[31] A. Traxler, S. Stellmach, P. Garaud, T. Radko, and N. Brummell, *Dynamics of fingering convection. Part 1: Small-scale fluxes and large-scale instabilities*, *J. Fluid Mech.* **677** (2011) 530–553.

[32] S. Stellmach, A. Traxler, P. Garaud, N. Brummell, and T. Radko, *Dynamics of fingering convection. Part 2: The formation of thermohaline staircases*, *J. Fluid Mech.* **677** (2011) 554–571.

[33] T. Maxworthy, *The dynamics of double-diffusive gravity currents*, *J. Fluid Mech.* **128** (3, 1983) 259–282.

[34] J. Yoshida, H. Nagashima, and W. Ma, *A double diffusive lock-exchange flow with small density difference*, *Fluid Dynamics Research* **2** (1987), no. 3 205 – 215.

[35] S. Lele, *Compact finite difference schemes with spectral-like resolution*, *J. Comp. Phys.* **103** (1992), no. 1 16 – 42.

[36] P. Burns and E. Meiburg, *Sediment-laden fresh water above salt water: nonlinear simulations*, *J. Fluid Mech.* **762** (1, 2015) 156–195.

[37] R. Henniger, D. Obrist, and L. Kleiser, *High-order accurate solution of the incompressible Navier-Stokes equations on massively parallel computers*, *J. Comp. Phys.* **229** (2010), no. 10 3543–3572.

[38] A. Wray, *Very low storage time-advancement schemes*, tech. rep., NASA Ames Research Center, 1986.

[39] S. Kimura and W. Smyth, *Direct numerical simulation of salt sheets and turbulence in a double-diffusive shear layer*, *Geophysical Research Letters* **34** (2007), no. 21.

[40] W. Smyth and S. Kimura, *Instability and diapycnal momentum transport in a double-diffusive, stratified shear layer*, *J. Phys. Oceanogr.* **37** (6, 2007) 1551 – 1565.

[41] W. Smyth and S. Kimura, *Mixing in a moderately sheared salt-fingering layer*, *J. Phys. Oceanogr.* **41** (7, 2011) 1364 – 1384.

[42] K. Winters, P. Lombard, J. Riley, and E. D'Asaro, *Available potential energy and mixing in density-stratified fluids*, *J. Fluid Mech.* **289** (4, 1995) 115–128.

[43] R. Tailleux, *Thermodynamics/dynamics coupling in weakly compressible turbulent stratified fluids*, *ISRN Thermodynamics* **2012** (1, 2012).

[44] P. Linden and T. Shirtcliffe, *The diffusive interface in double-diffusive convection*, *J. Fluid Mech.* **87** (8, 1978) 417–432.

[45] M. Worster, *Time-dependent fluxes across double-diffusive interfaces*, *J. Fluid Mech.* **505** (4, 2004) 287–307.

[46] N. Didden and T. Maxworthy, *The viscous spreading of plane and axisymmetric gravity currents*, *J. Fluid Mech.* **121** (8, 1982) 27–42.

[47] B. Ruddick, O. Phillips, and J. Turner, *A laboratory and quantitative model of finite-amplitude thermohaline intrusions*, *Dyn. Atm. Oceans* **30** (1999), no. 2–4 71–99.

[48] F. Necker, C. Härtel, L. Kleiser, and E. Meiburg, *High-resolution simulations of particle-driven gravity currents*, *Int. J. Multiphas. Flow* **28** (2002), no. 2 279–300.

[49] T. Radko, J. Ball, J. Colosi, and J. Flanagan, *Double-diffusive convection in a stochastic shear*, *J. Phys. Oceanogr.* **45** (2015), no. 12 3155–3167.

[50] P. Linden, *Salt fingers in a steady shear flow*, *Geo. & Astro. Fluid Dyn.* **6** (1974), no. 1 1–27.

[51] J. Parsons, J. Bush, and J. Syvitski, *Hyperpycnal plume formation from riverine outflows with small sediment concentrations*, *Sedimentology* **48** (2001), no. 2 465–478.

[52] P. Burns and E. Meiburg, *Sediment-laden fresh water above salt water: Linear stability analysis*, *J. Fluid Mech.* **691** (1, 2012) 279–314.

[53] X. Yu, T. Hsu, and S. Balachandar, *Convective instability in sedimentation: Linear stability analysis*, *J. Geophys. Research: Oceans* **118** (2013), no. 1 256–272.

[54] X. Yu, T. Hsu, and S. Balachandar, *Convective instability in sedimentation: 3-d numerical study*, *J. Geophys. Research: Oceans* **119** (2014), no. 11 8141–8161.

[55] A. Karimi and A. Ardekani, *Gyrotactic bioconvection at pycnoclines*, *J. Fluid Mech.* **733** (10, 2013) 245–267.

[56] J. Turner, *Double-diffusive intrusions into a density gradient*, *J. Geophys. Research: Oceans* **83** (1978), no. C6 2887–2901.

[57] B. Ruddick and J. Turner, *The vertical length scale of double-diffusive intrusions*, *Deep Sea Research Part A. Oceanographic Research Papers* **26** (1979), no. 8 903–913.

[58] T. Mulder and J. Syvitski, *Turbidity currents generated at river mouths during exceptional discharges to the world oceans*, *J. Geol.* **103** (1995), no. 3 285–299.

[59] M. Stern, *The salt-fountain and thermohaline convection*, *Tellus* **12** (1960), no. 2 172–175.

[60] J. Turner, *Double-diffusive phenomena*, *Ann. Rev. Fluid Mech.* **6** (1974), no. 1 37–54.

[61] P. Segre, F. Liu, P. Umbanhowar, and D. Weitz, *An effective gravitational temperature for sedimentation*, *Nature* **409** (2001) 594–597.

[62] J. Reali, P. Garaud, A. Alsinan, and E. Meiburg, *Layer formation in sedimentary fingering convection*, *J. Fluid Mech.* **816** (2017) 268–305.

[63] L. Kelvin, *Stability of fluid motion: Rectilinear motion of viscous fluid between two parallel plates*, *Phil. Mag.* **24** (1887), no. 5 188–196.

[64] G. Rosen, *General solution for perturbed plane Couette flow*, *Phys. Fluids* **14** (1971), no. 12 2767–2769.

[65] T. Shepherd, *Time development of small disturbances to plane Couette flow*, *J. Atmos. Sci.* **42** (1985), no. 17 1868–1872.

[66] A. Craik and W. Criminale, *Evolution of wavelike disturbances in shear flows: A class of exact solutions of the Navier-Stokes equations*, *P. Roy. Soc. Lond. A Mat.* **406** (1986), no. 1830 13–26.

[67] E. Knobloch, *On the stability of stratified plane Couette flow*, *Geophys. Astro. Fluid* **29** (1984), no. 1-4 105–116.

[68] M. Gunzburger, *Adjoint equation-based methods for control problems in incompressible, viscous flows*, *Flow Turbul. Combust.* **65** (12, 2000) 249–272.

[69] R. Lindzen, *Instability of plane parallel shear flow (toward a mechanistic picture of how it works)*, *Pure Appl. Geophys.* **126** (3, 1988) 103–121.

[70] C. Canuto, M. Hussaini, A. Quarteroni, and T. Zang, *Spectral Methods: Fundamentals in Single Domains.* Springer-Verlag Berlin Heidelberg, 2006.

[71] M. Frigo and S. Johnson, *The design and implementation of FFTW3*, *Proceedings of the IEEE* **93** (2005), no. 2 216–231. Special issue on "Program Generation, Optimization, and Platform Adaptation".